IMPROVED TITANIUM DIOXIDE PROMOTED PHOTOCATALYST FOR DEGRADATION OF POLLUTANT IN WATER

EMY MARLINA BINTI SAMSUDIN

INSTITUTE OF GRADUATE STUDIES
UNIVERSITY MALAYA
KUALA LUMPUR

2016

IMPROVED TITANIUM DIOXIDE PROMOTED PHOTOCATALYST FOR DEGRADATION OF POLLUTANT IN WATER

EMY MARLINA BINTI SAMSUDIN

THESIS SUBMITTED IN FULFILLMENT OF THE REQUIREMENTS FOR THE DEGREE OF DOCTOR OF PHILOSOPHY

INSTITUTE OF GRADUATE STUDIES
UNIVERSITY MALAYA
KUALA LUMPUR

2016

UNIVERSITY OF MALAYA

ORIGINAL LITERARY WORK DECLARATION

Name of Candidate: Emy Marlina Binti Samsudin

Registration/Matric No: HHC130006

Name of Degree: Doctor of Philosophy (Ph. D)

Title of Thesis: Improved Titanium Dioxide Promoted Photocatalyst for Degradation of Pollutant in Water

Field of Study: Chemical Engineering (Catalysis)

I do solemnly and sincerely declare that:

(1) I am the sole author/writer of this Work;
(2) This Work is original;
(3) Any use of any work in which copyright exists was done by way of fair dealing and for permitted purposes and any excerpt or extract from, or reference to or reproduction of any copyright work has been disclosed expressly and sufficiently and the title of the Work and its authorship have been acknowledged in this Work;
(4) I do not have any actual knowledge nor do I ought reasonably to know that the making of this work constitutes an infringement of any copyright work;
(5) I hereby assign all and every rights in the copyright to this Work to the University of Malaya ("UM"), who henceforth shall be owner of the copyright in this Work and that any reproduction or use in any form or by any means whatsoever is prohibited without the written consent of UM having been first had and obtained;
(6) I am fully aware that if in the course of making this Work I have infringed any copyright whether intentionally or otherwise, I may be subject to legal action or any other action as may be determined by UM.

Candidate's Signature　　　　　　　　　Date: 5th May 2016

Subscribed and solemnly declared before,

Witness's Signature　　　　　　　　　Date: 5th May 2016

Name: Afsalina Che kob @Yaacob

Designation: Project Officer, UM

ABSTRACT

The quality of drinking water is testified to be satisfactory in most developed countries. However, the United Nations has reported that 783 million people do not have access to safe drinking water. Furthermore, only 1% of available water resources can be used as drinking water. One of the most common pollutants found in drinking water is atrazine herbicide. Malaysia, being an active player in agriculture consumes large quantity of atrazine and other pesticides. Atrazine is classified as low toxic herbicides but prolong consumption leads to cardiovascular and mutagenic effects. The current technology is via granulated activated carbon (GAC) however it leads to leaching, non-selective and waste disposal costs. An alternative effective method is by photocatalytic degradation using semiconductor photocatalyst. The key factor for a successful photocatalytic activity is to sustain large concentrations of surface active radicals to oxidize pollutants into simpler and less hazardous substance. In photocatalysis, TiO_2 is a preferred semiconductor as it is cheap, photo-active, stable and is non-toxic. However, the photocatalytic ability of TiO_2 is limited to only a small fraction of solar light (4%) and hence hampers its activity. Numerous efforts are initiated to improve TiO_2 properties which include anion doping and most recent hydrogenation of TiO_2. Nevertheless, the photocatalytic activity of anion-doped TiO_2 was only accessible under UV and visible light. In addition, hydrogenated TiO_2 was reported to possessed rapid electrons and holes recombination although the optical response was extended towards the infra-red region. In this work, hydrogenated F-doped TiO_2 showed remarkable enhancement for the photocatalytic degradation of atrazine by a factor of ~8.5 relative to as prepared TiO_2. Within 180 min of photocatalytic activity, more than 95 % of 0.5 mg/l atrazine was removed. Atrazine removal was shown to exceed those of N,F co-doped TiO_2 (85 %), hydrogenated TiO_2 (70 %), N-doped TiO_2 (70 %), F-doped TiO_2 (40 %) and F127-TiO_2 (35 %). F-doped TiO_2 was prepared using pluronic F127 as surfactant and

trifluoroacetic acid as the fluorine precursor, followed by hydrogenation at 500 °C and 1 atm to obtain hydrogenated F-doped TiO_2. Acid catalyzed sol-gel method was used to prepare F-doped TiO_2 and other photocatalysts as it allows efficient control of purity, homogeneity, crystal phase and particle size. In addition, sol-gel method does not require needs of special equipment and can be conducted at low temperature. Hydrogenated F-doped TiO_2 showed enhanced solar light absorption with ability to absorb light in the UV, visible and infra-red region. The sustainability of photo-generated electrons and holes on the photocatalyst surface enables larger formation of active surface radicals. Furthermore, the synergy between hydrogenation and F-doping modifies the morphology, crystal structure, surface charge, hydrophilicity, defects and surface area which were shown to favor the photocatalytic activity. High photocatalyst reusability up to 10th cycles was achieved. Hydrogenated F-doped TiO_2 could serve as a new potential photocatalyst and thus supports the water industry for the abatement of recalcitrant organic pollutants. Furtherance, this leads to the possibility in providing safe drinking water by adapting a more sustainable and feasible approach.

ABSTRAK

Kualiti air minum dilaporkan memuaskan di kebanyakan negara maju. Walaubagaimanapun, Pertubuhan Bangsa-Bangsa Bersatu telah melaporkan 783 juta penduduk tidak mendapat air minuman yang bersih. Tambahan pula, hanya 1 % daripada sumber air sedia ada boleh digunakan sebagai air minuman. Salah satu racun pencemar yang paling biasa dijumpai di dalam air minuman adalah atrazine racun herba. Malaysia ialah negara yang aktif dalam bidang pertanian dan menggunakan kuantiti atrazine yang banyak. Atrazine diklasifikasikan sebagai racun yang mempunyai ketoksikan yang rendah tetapi penggunaan jangka masa panjang membawa kesan kepada kardiovaskular dan mutagen. Pada masa ini, atrazine ditapis dengan menggunakan karbon aktif dalam bentuk granular (GAC). Walaupun ianya berkesan, GAC mengalami kelemahan seperti larut lesap, maka GAC bukan pilihan terbaik dan juga melibatkan kos tambahan untuk pelupusan sisa. Satu kaedah alternatif yang berkesan dalam merawat atrazine dalam air adalah dengan melalui keadah fotopemangkinan menggunakan bahan semikonduktor. Kelebihan utama menggunakan keaedah fotopemangkinan adalah penghasilan radikal aktif yang banyak pada permukaan mangkin untuk mengoksidakan bahan pencemar organik kepada bahan yang kurang berbahaya. Dalam fotopemangkinan, TiO_2 adalah mangkin pilihan kerana ia adalah murah, foto-aktif, bersifat lengai dan tidak mencemar alam sekitar. Walau bagaimanapun, keupayaan foto pemangkinan TiO_2 adalah terhad kepada cahaya ultra ungu (UV) iaitu hanya 4% daripada cahaya matahari. Dengan itu, pelbagai usaha telah dilakukan untuk memperbaiki sifat-sifat TiO_2 seperti memasukkan anion dan melakukan penghidrogenan. Aktiviti fotopemangkinan yang telah dimasukkan dengan anion TiO_2 adalah aktif dibawah sinaran UV dan cahaya nampak. Di samping itu, hidrogenasi TiO_2 dilaporkan mengalami kelemahan seperti penggabungan elektron di dalam lohong elektron yang berlaku dengan pantas walaupun keaktifannya dapat

dilanjutkan daripada cahaya nampak sehingga rantau infra-merah. Dalam tesis ini, hidrogenasi F-TiO$_2$ menunjukkan aktiviti fotopengmangkinan atrazine yang ketara sehingga $\sim$ 8.5 kali berbanding dengan TiO$_2$ konvensional. Dalam tempoh 180 min aktiviti foto pemangkinan , lebih daripada 95 % daripada 0.5 mg/l atrazine telah dibuang. Penyingkiran atrazine telah ditunjukkan untuk melebihi N,F bersama didopkan TiO$_2$ (85 %), hidrogenasi TiO$_2$ (70 %) , N-didopkan TiO$_2$ (70 %) , F-didopkan TiO$_2$ (40 %) dan F127 -TiO$_2$ (35 %). F-TiO$_2$ disediakan melalui F127 pluronic sebagai surfaktan dan asid trifluoroasetik sebagai pelopor fluorin, dan melalui proses hidrogenasi pada 500 °C dan 1 atm untuk mendapatkan hidrogenasi F-TiO$_2$. Hidrogenasi F-TiO$_2$ menunjukkan peningkatan penyerapan cahaya solar dengan keupayaan untuk menyerap sinaran UV, cahaya namapak dan infra-merah. Keberkesanan hidrogenasi F-TiO$_2$ disebabkan oleh elektron foto yang dihasilkan dan lohong pada permukaan mangkin bagi mengelakkan elektron tersebut kembali bersatu semula. Maka ini membolehkan pembentukan lebih banyak radikal aktif di permukaan mangkin. Tambahan pula, sinergisme antara penghidrogenan dan F-didopkan telah mengubah morfologi, struktur hablur, caj permukaan, hidrofilik, kecacatan dan permukaan lalu meningkatkan aktiviti fotopengmangkinan. Laporan menunjukkan fotopengmangkinan yang tinggi boleh dan dapat digunapakai semula sebanyak kitaran kesepuluh. Oleh itu, hidrogenasi F-TiO$_2$ boleh dijadikan sebagai fotopengmangkinan baru yang berpotensi dalam industri rawatan air. Kesimpulannya, mangkin ini dapat digunakan dalam teknologi rawatan air untuk menyediakan air minuman yang bersih dengan pendekatan yang lebih lestari dan tersaur.

ACKNOWLEDGEMENT

Syukur Alhamdulillah to the Al-mighty Allah Subhanahu Wa Ta'ala

I dedicated my thesis to the most important people in my life,

for their unconditional love, wisdom and encouragement.

My parents.

Heartfelt appreciation to both of my supervisors for their patience and guidance,

Dr Juan Joon Ching and Professor Wan Jefrey Basirun.

This journey would not have been merrier without the presence of

my two best teachers,

Professor Centi Gabriele and Subrata Saha.

Millions of thanks to the rest of nanotechnology and catalysis research centre (Nanocat)

team for their hard work and dedication on behalf of all postgraduate students.

Thank you.

With love to the moon and back,

Emy Marlina Binti Samsudin

TABLE OF CONTENTS

LIST OF FIGURES

LIST OF TABLES

LIST OF SYMBOLS AND ABBREVIATIONS

$C_8H_{14}ClN_5$	:	2-chloro-4-(ethylamino)-6 (isopropylamino)-s-triazine
Abs	:	Absolute
Al_2O_3	:	Aluminum oxide
etc	:	And so forth
Å	:	Angstrom
a.u	:	Arbitrary unit
atm	:	Atmospheric
At %	:	Atomic percent
ATR	:	Atrazine
θ	:	Bragg's angle
BET	:	Brunauer-Emmett-Teller
Cds	:	Cadmium sulfide
C	:	Carbon
CO_2	:	Carbon dioxide
CHNS	:	Carbon, hydrogen, nitrogen and sulphur
CNT	:	Carbon nanotube
C_3N_4	:	Carbon nitride
°C	:	Celsius
CCD	:	Central composite design
CVD	:	Chemical vapor deposition
Cr	:	Chromium
Co	:	Cobalt
CB	:	Conduction band
Cu	:	Copper
DSC	:	Differential scanning calorimetry

DRUV-Vis	:	Diffuse reflectance ultraviolet-visible
e^-	:	electron
eV	:	Electron volt
EDX	:	Energy Dispersive X-Ray
EtOH	:	Ethanol
EISA	:	Evaporation induced self-assemble
SA_{ext}	:	External surface area
FESEM	:	Field emission scanning electron microscopy
F	:	Fluorine
FTIR	:	Fourier transformed infrared
FWHM	:	Full width at half maxiumum
⍰	:	Gamma
Au	:	Gold (Aurum)
g/l	:	Gram per litre
GAC	:	Granulated activated carbon
HPLC	:	High pressure liquid chromatograph
HR-TEM	:	High resolution transmission electron microscope
h	:	hour
h^+	:	hole
H_2	:	Hydrogen
OH^-	:	Hydroxyl ion
$\cdot OH$	:	Hydroxyl radical
Fe	:	Iron
Fe_2O_3	:	Iron (III) oxide
IEP	:	Isoelectric point
JCPDS	:	Joint Committee on Powder Diffraction Standards

LUX	:	Luminescence units
Mn	:	Manganese
MS	:	Mass spectroscopy
MCL	:	Maximum contaminant level
Mn	:	Manganese
mHz	:	megaHertz
mPa	:	megaPascal
Mg/l	:	Milligram per litre
min	:	minute
CH_4	:	Methane
e.g.	:	For example
Mo	:	Molybdenum
nm	:	Nanometre
NDRC	:	Natural Resources Defense Council
Ni	:	Nickel
Nb	:	Niobium
N	:	Nitrogen
O^{2-}	:	Oxide
O_2	:	Oxygen molecule
ppb	:	Parts per billion
ppm	:	Parts per million
%	:	Percentage
O_2^{2-}	:	Peroxide
P	:	Phosphorus
PL	:	Photoluminescence
Pt	:	Platinum

pH	:	Potential of hydrogen
H^+	:	Proton
k	:	Rate constant
RSM	:	Response surface methodology
rpm	:	Rotation per minute
Ru	:	Rubidium
SAED	:	Selected area electron diffraction
Ag	:	Silver (Argentum)
SHE	:	Standard hydrogen electrode
S	:	Sulphur
O_2^-	:	Superoxide
$\cdot O_2^-$	:	Superoxide anion radical
S.A	:	Surface area
i.e.	:	That is
TGA	:	Thermal gravimetric analysis
SnO_2	:	Tin (IV) oxide
Ti	:	Titanium
TiO_2	:	Titanium dioxide
TTIP	:	Titanium isopropoxide
TFA	:	Trifluoroacetic acid
UV	:	Ultraviolet
VB	:	Valence band
V	:	Vanadium
WO_3	:	Tungsten trioxide
H_2O	:	Water
W	:	Watt

λ	:	Wavelength
Wt %	:	Weight percent
WHO	:	World Health Organization
XRD	:	X-Ray diffraction
XPS	:	X-Ray photoelectron spectroscopy

LIST OF APPENDIX

CHAPTER 1: INTRODUCTION

1.1 Global water scenario

Water resources are abundant and renewable, however only less than 1% of available water resources can be utilized as drinking water (Tarver, 2008). These limited water resources include ground water, springs, aquifers, rivers and hyporheic zones. All processed drinking water must adhere to the national drinking water regulations for maximum contaminant level (MCL) for physical, chemical, bacteriological and radioactivity. Although the quality of drinking water is satisfactory in most developed countries (Rosborg, Nihlgard, Gerhadsson, & Sverdrup, 2006), 783 million people does not have access to safe drinking water (Wall, 2012). In addition, the hectic industrial growth worldwide, especially in textile, pharmaceutical and agriculture, has led to various types of recalcitrant contaminants into the water system (Harris & McCartor, 2011). Thus it is crucial that the contaminated water should be treated effectively before being disposed into the environment or delegated to consumers for daily use.

1.2 Pesticides as water pollutant

In 1968, a Nobel laureate, Norman Borlaug initiated green revolution to maximize crop production by using pesticides such as herbicides, insecticides and fungicides (Ahmad, Tan, & Abd Shukor, 2008). In general, pesticides are toxic chemical agents that are released intentionally into the environment to prevent, weaken, destroy, or otherwise discourage pests. Each pesticide is designed for a specific target and the usage depends on the severity of the problem. There are many categories of pesticides which include organophosphate, carbamate, organochlorine, pyrethroid and sulfonylurea. This approach has decreased the world starvation significantly (Dawe, Stamoulis, & Wiebe, 2011). However, the continuous usage of these chemicals results in unintended serious public health and environmental problems. In Figure 1.1, more than half a million of population in Central America are at risks due to pesticide pollution. Figure 1.2 showed

the widespread usage of pesticides globally from 2005 to 2009. The country consuming largest amount of pesticides includes Bahamas, Colombia, and Mauritius and followed by Japan, Chile, China, Netherlands and Malaysia.
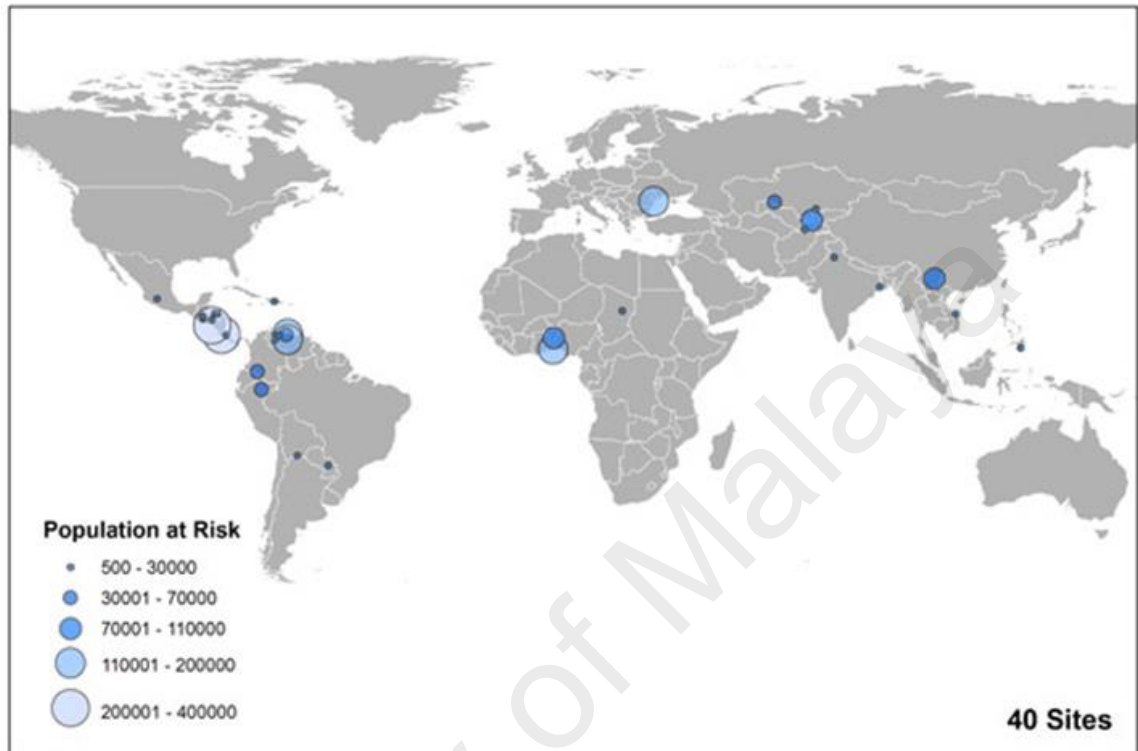
Figure 1.1: Population at risk due to pesticide contamination in 2011
(Harris & McCartor, 2011)
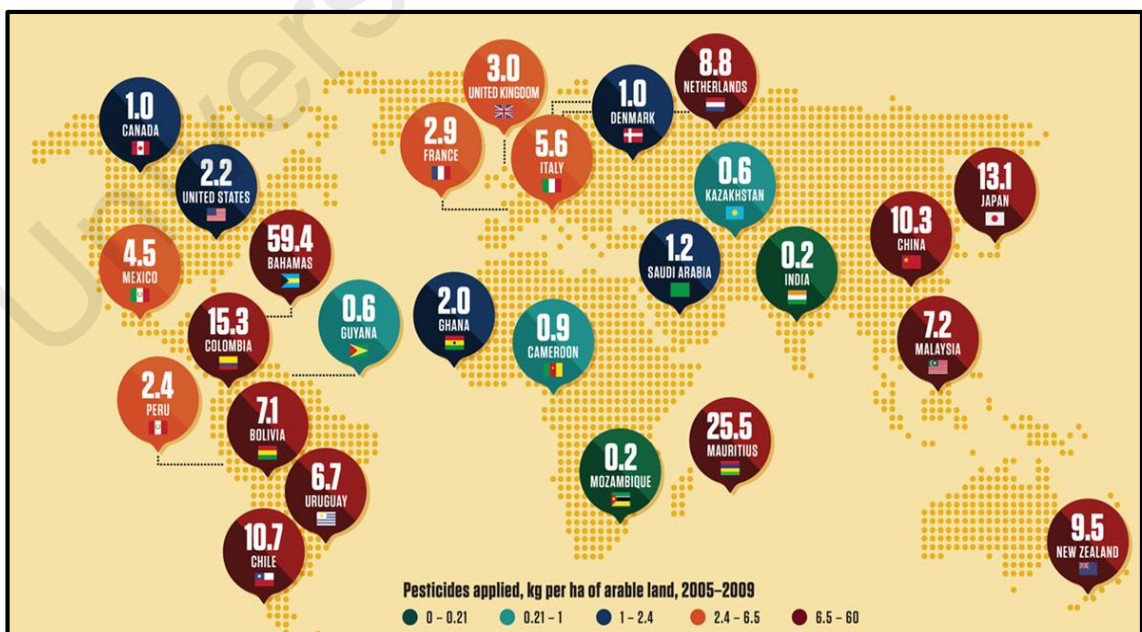
Figure 1.2: Usage of pesticides worldwide from 2005 to 2009 in kg per hectares of arable lands (Plummer, 2013)

1.2.1 Atrazine herbicide
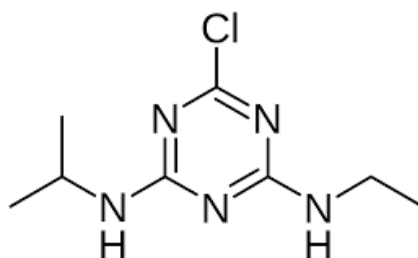
Figure 1.3: Molecular structure of atrazine compound, $C_8H_{14}ClN_5$

A recalcitrant drinking water pollutant includes atrazine herbicide (2-chloro-4-(ethylamino)-6 (isopropylamino)-s-triazine) (Figure 1.3) and is widely used to control the growth of broadleaf and grassy weeds as it is both effective and inexpensive (Ahmad et al., 2008). Atrazine is applied directly to the soil and is easily washed off by the rain into a nearby water bodies or percolate through the soil into the ground water wells. Atrazine is also relatively stable in soil and aquatic environments (soil half-life of 4 to 57 weeks). Even though atrazine is classified as low toxic herbicides, its large consumption has ranked it the most common herbicides in surface water and ground water (Plakas, Karabelas, Wintgens, & Melin, 2006).

In Malaysia, out of 33 million hectares of land, 6.6 million hectares are used for the agricultural activities (20% of total area) (Olayini, Ramli, & Sood, 2013). This crop includes oil palm, cocoa, rubber, tobacco, pepper, paddy, fruits and vegetables for local consumption and export purposes. Atrazine is the most widely used pesticides in Malaysia (Ahmad et al., 2008). Given that 99 % of water supplies are from the rivers, and 1 % from groundwater (Azlan, Khoo, Idris, Ismail, & Razman, 2011), it is crucial that the source of drinking water is efficiently treated and abides to the national drinking water quality standards according to World Health Organization (WHO) guidelines.

In 2010, the Natural Resources Defense Council (NRDC) in the United States raised an issue regarding the continuous threat of atrazine towards drinking water supplies (Wu, Xing, Tian, Zhang, & Chen, 2010). It is recently reported that high doses of

atrazine induces abnormalities and deformities in non-target organisms (Ahmad et al., 2008). A person who drinks water exceeding the maximum permitted concentration of atrazine of 3 ppb for several years could experience problem with their cardiovascular system. In other words, low concentration of atrazine pollutant in drinking water could cause severe health repercussions. Atrazine has been detected in the drinking water supplies in the United States originating from runoffs herbicides used on row crops (Beutler & Shaer, 2013). Figure 1.4 showed the estimated atrazine usage in one part of the United States in year 1992 and 2013 (*National Water-Quality Assessment (NAWQA) Program*, 2013).
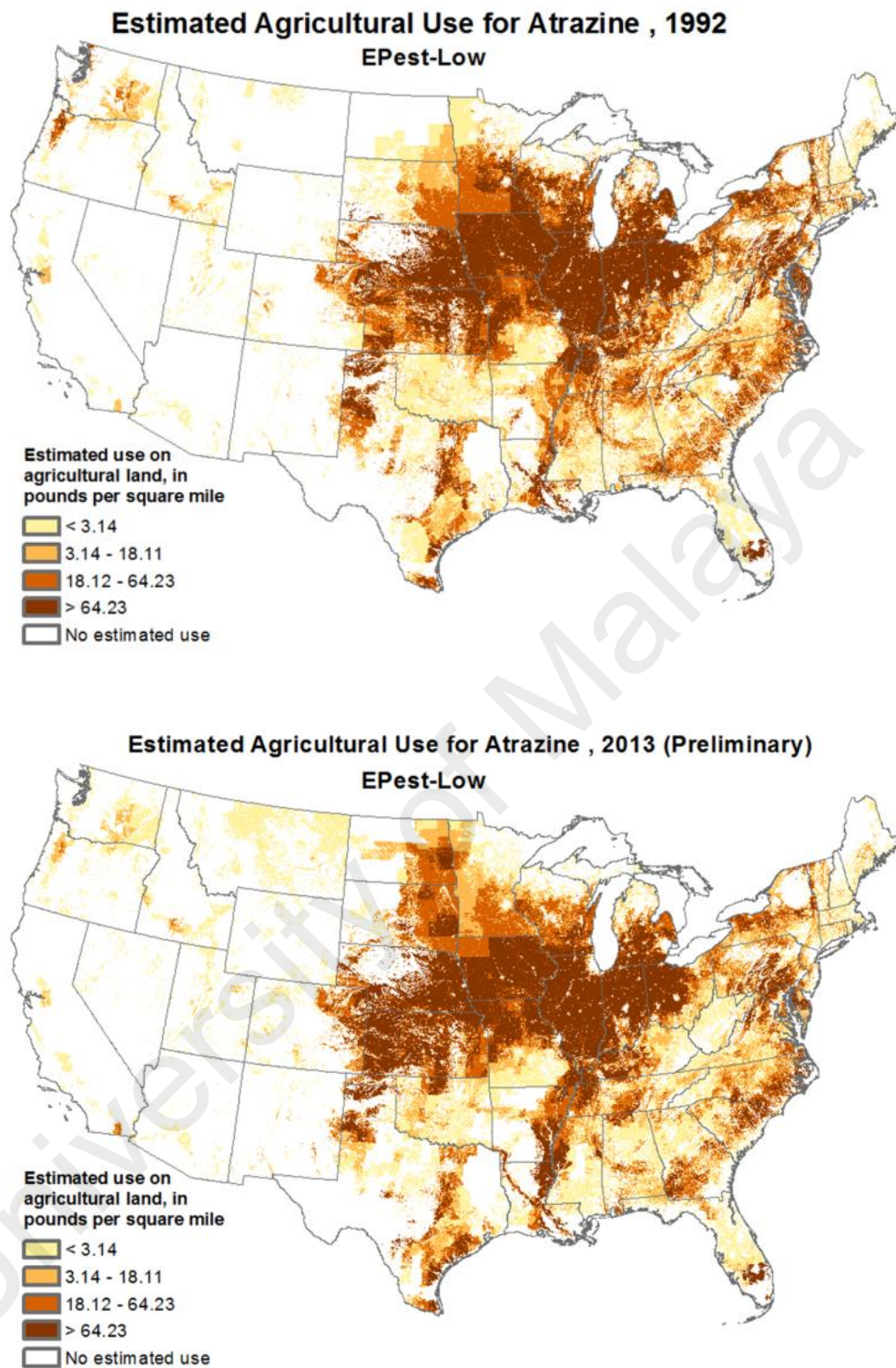
Figure 1.4: Estimated agricultural use for atrazine in year 1992 and 2013 in the United States

1.3 Relevant research on water treatment technology

There are numerous developed technologies to treat water containing atrazine which includes incineration, reverse osmosis, electro-dialysis, chemical degradation, immobilized enzyme based technology and phytoremediation (Pathak & Dikshit, 2011). However, these approaches are either costly, time consuming or generate toxic by-products and therefore are less feasible. A more recent approach which includes ultrasonic destruction, dissipation and photocatalytic degradation has been introduced (Collings & Gwan, 2010; Konstantinou & Albanis, 2003). According to WHO, granulated activated carbon (GAC) is efficient in removing atrazine from water to as low as 0.1 ppb in concentration (Zadaka, Nir, Radian, & Mishael, 2008). For a drinking water system, the efficiency of current technology to remove atrazine to the allowable limit has always been a main concern. Although current technology by GAC is effective in treating contaminated water containing atrazine, there is a probability of GAC leaching. In addition, atrazine is physically absorb on GAC and has a tendency to desorb and re-enters the aqueous environment. GAC being non-selective also reduces its efficiency in targeting specific organic pollutants. Therefore, stand-alone water treatment technologies comprised of GAC is not adequate. Among various methods, photocatalytic degradation using TiO_2 is most effective in treating variety of refractory organic pollutants (Schneider et al., 2014). The photocatalytic degradation of atrazine using TiO_2 has been studied since 1990 and until today, the research progress is still ongoing (Ahmad et al., 2008; Konstantinou & Albanis, 2003; Pathak & Dikshit, 2011; Plakas et al., 2006; Ribaudo & Bouzaher, 1994; Wu, Quirindongo, Sass, & Wetzler, 2010; Zadaka et al., 2008).

1.3.1 Photocatalytic treatment using titanium dioxide, TiO_2

Titanium dioxide, TiO_2 is a widely investigated semiconductor due to its versatility, low cost, stable and environmental friendly. Previous works demonstrates the application of TiO_2 in photocatalysis, photovoltaic, water splitting, sensors and CO_2 reduction for fuel generation (Park, Park, Kim, & Choi, 2013). TiO_2 is one of the preferred semiconductors for water purification due to its strategic redox position relative to other semiconductor like Fe_2O_3, SnO_2 and WO_3 (Gratzel, 2001). There are various methods to synthesize TiO_2 which includes sol-gel, hydrothermal, solvothermal, chemical vapor deposition (CVD), spray pyrolysis, electrodeposition, sonochemical, microwave, spin coating and evaporation induced self-assemble (EISA) (Balasubramanian, Dionysiou, Suidan, Baudin, & Laine, 2004; Gratzel, 2001; Li et al., 2014; Oshani, Marandi, Rasouli, & Farhoud, 2014; Su, Hong, & Tseng, 2004). Amongst all synthesis method, sol-gel via alkoxide route has many other advantages relative to other methods such as homogeneity, purity and flexibility in introducing dopants at the molecular level (Pookmanee & Phanichphant, 2009).

1.4 Problem statement

The photocatalytic activity of conventional TiO_2 to degrade pollutant is limited due to its wide band gap and inefficient electrons and holes separation (Shon et al., 2008). As a result, numerous studies are initiated to improve TiO_2 properties. Efforts includes metal doping (Cu, Co, Ni, Cr, Mn, Mo, Nb, V, Fe, Ru, Au, Ag, Pt, etc.), non-metal doping (N, S, C, P, etc.), dye sensitization, heterogeneous composites (Al_2O_3, WO_3, CdS, etc.), hybridization with nano-materials (CNTs, fullerenes, graphene, zeolites, etc.) and dye-sensitization and surface adsorbates (phosphates, surfactants, polymers, etc.) (Gupta & Tripathi, 2011; Mohamed, McKinney, & Sigmund, 2012; Park et al., 2013; Shon et al., 2008; Zaleska, 2008). A more recent attempt includes creating surface disorders by hydrogenation, while preserving the crystallite core in TiO_2 (Chen, Liu,

Yu, & Mao, 2011). With respect to the above, enhanced photocatalytic activity are observed with an increased light utilization from 4% (UV light) to 45% (visible light). However, the remaining portion of the solar light (infra-red) is left unharnessed. The photocatalytic activity of TiO_2 is proportional to the amount of light absorbed (Chen, Li, Grätzel, Kostecki, & Mao, 2012). Thus, it is important to design TiO_2 that is able to absorb wider range of solar light and simultaneously efficient separation of electrons and holes.

The photodegradation of atrazine using TiO_2 has been investigated since 1990. However, these investigations focused on the photocatalytic process parameters rather than the properties and type of TiO_2 used. The photocatalysts used includes commercial anatase TiO_2 (Hequet, Gonzalez, & Cloirec, 2001; Ruslimie, Razali, & Khairul, 2011), commercial Degussa P25 (Pelizzeti et al., 1990; Zahraa, Sauvanaud, Hamard, & Bouchy, 2003), S-TiO_2 (Liu, Cheng, Sheng, & Li, 2009) and N,F-TiO_2 Some of the work on the photodegradation of atrazine involves Fenton reagents and oxidants (Andersen et al., 2013; Barndõk, Peláez, Han, & Platten, 2013). In depth investigation between TiO_2 physico-chemical properties (i.e. morphology, crystal structure, crystal phase, size, etc.) are limited. Furthermore, the photocatalytic studied on atrazine are mostly conducted under UV light irradiation. There is also a necessity to design a solar-drive photocatalyst that possess superior properties for enhance photodegradation activity and less dependency on additional chemicals (Fenton reagent, oxidants, etc.). As a result, there is a need to improve TiO_2 limitations and its corresponding photocatalytic activity towards atrazine degradation.

1.5 Research objectives

This main research focus is to develop an efficient photocatalyst for photodegradation of atrazine. The general objectives are as follows:

i. To design TiO_2 photocatalyst that is photo-active with capability to absorb wide range of solar light and possesses efficient electrons and holes separation

ii. To evaluate the newly developed photoactive catalyst for the photodegradation of atrazine pollutant

1.5.1 Specific research objectives

i. To prepare surfactant-based TiO_2 using non-ionic Pluronic F127 template

ii. To mono-doped TiO_2 using nitrogen, N and fluorine, F anions

iii. To dual-doped TiO_2 using both nitrogen, N and fluorine, F anions

iv. To hydrogenate un-doped TiO_2

v. To hydrogenate all prepared anion mono-doped and dual-doped TiO_2

vi. To characterize the physicochemical properties of synthesized TiO_2 photocatalysts with FESEM, EDX, HR-TEM, BET, XRD, RAMAN, PL, FTIR, TGA, DSC and XPS

vii. To evaluate the newly developed TiO_2 photoactive catalyst for the photodegradation of atrazine pollutant under solar light irradiation

1.6 Scope of work

In order to enhance the photocatalytic activity under solar light irradiation, TiO_2 are synthesized and modified via sol-gel method, anionic dopant and hydrogenation. This study was divided into three phases. **Phase I** involves photocatalyst preparation via sol-gel method in the presence of nonionic surfactant to synthesis TiO_2. Then, TiO_2 photocatalysts were modified by doping with anionic dopants namely N, F to improve

solar light absorption and delay the electrons and holes recombination. The selected anionic doped TiO_2 photocatalysts were subjected to hydrogenation. Hydrogenation is expected to further increase the solar light absorption and improved the catalytic surface activity via surface defects.

In summary, nine (9) types of photocatalysts were prepared below.

i. TiO_2 (without pluronic F127 surfactant)

ii. TiO_2 (with pluronic F127 surfactant, namely F127-TiO_2)

iii. Anionic doped TiO_2 (N-doped TiO_2 (N-TiO_2), F-doped TiO_2 (F-TiO_2) N and F co-doped TiO_2 (N,F-TiO_2))

iv. Hydrogenated TiO_2 (H-TiO_2)

v. Hydrogenated anionic doped TiO_2 (Hydrogenated N-TiO_2 (HN-TiO_2), Hydrogenated F-TiO_2 (HF-TiO_2) and Hydrogenated N,F-TiO_2 (HNF-TiO_2))

Phase II involves photocatalysts characterization in order to evaluate the physico-chemical properties. The characterization was conducted with thermal gravimetric analysis (TGA), differential scanning calorimetry (DSC), Field emission scanning electron microscope (FESEM), Electron diffractive X-Ray (EDX), Brunner-Emmet-Teller (BET), Zeta Potential (ZP), High resolution-transmission electron microscope (HR-TEM) and Selected area electron diffraction (SAED), X-Ray powder diffractogram (XRD), Raman spectroscopy, Fourier transformed infra-red spectroscopy (FTIR), Diffuse reflectance-ultraviolet visible spectroscopy (DR-UV vis), Photoluminescence spectroscopy (PL) and X-Ray photoelectron spectroscopy (XPS).

Phase III involves evaluating the photocatalytic activities of the prepared photocatalysts for the photodegradation of atrazine pollutant under solar light irradiation. The degradation products were analyzed by UV-Vis spectrophotometer and

high pressure liquid chromatography-mass spectroscopy (HPLC-MS & HPLC-MS/MS). The photocatalytic degradation pathway of atrazine into cyanuric acid was proposed.

1.7 Research novelty

The research approach is designed to cater a newly designed photocatalyst that is able to maximize solar light absorption. The modified surface properties of the catalyst using combination of synergies from anion-doped and hydrogenation process facilitates efficient charge carriers migration to the catalyst surface with high improved lifetime. To the best of our knowledge, this is the first time TiO_2 is modified using this strategy. The anionic dopant on TiO_2 coupled with hydrogenation has significantly enhanced the photocatalytic degradation of atrazine under solar light irradiation. Subsequently, this revolutionized greater possibility in treating drinking water by adapting a more sustainable and feasible approach.

1.8 Thesis organization

This thesis consisted of five (5) chapters namely (1) introduction, (2) literature review, (3) methodology, (4) results and discussion and (5) conclusion and recommendation.

Chapter 1 consists of current environmental issue related to wastewater treatment especially on recalcitrant drinking water pollutant such as atrazine herbicide. The limitation of the wastewater treatment on atrazine herbicide has been clearly described and thus the objectives, scope of work and research novelty were explained.

Chapter 2 critically emphasized on the state of art with respect to previous and latest research scenarios of wastewater treatment on atrazine. The research gaps of photocatalysis treatment on atrazine was also identified and explicitly explained.

Chapter 3 embodied the methodology adapted to fulfill the scope of work and research targets. The method of preparing a series of photoactive catalyst namely TiO_2 (with and without surfactant), anion-doped TiO_2 and hydrogenated TiO_2 were

explained. The sol gel technique was chosen to synthesize all of the photocatalysts. The selected anions for doping include nitrogen, N and fluorine, F and hydrogenation of the photocatalysts were performed at atmospheric condition at desired time and temperature. The equipments and the analysis parameters such as FESEM, EDX, HR-TEM, BET, XRD, FTIR, PL, Raman, TGA, DSC and XPS were clearly explained. The procedure for the photocatalytic degradation activity of atrazine such as instrument setup, process parameters and sampling were discussed. The analysis procedure and instruments used for analyzing the degradation products were emphasized.

Chapter 4 consisted of results and discussions of the physicochemical properties of the synthesized photocatalysts namely TiO_2 (without surfactant), TiO_2 (with surfactant), N-doped TiO_2, F-doped TiO_2, N,F co-doped TiO_2, hydrogenated TiO_2 and hydrogenated F-doped TiO_2. Characterizations of individual prepared photocatalysts were discussed separately in this section. Section 4.1, 4.2, 4.3, 4.4, 4.5 and 4.6 discussed the physicochemical properties of surfactant modified TiO_2, N-doped TiO_2, F-doped TiO_2, N,F co-doped TiO_2, hydrogenated TiO_2 and hydrogenated F-doped TiO_2 photocatalysts, respectively. The photocatalytic activities of the photocatalysts were discussed in detail in section 4.7 to 4.9.

Chapter 5 summarized the research findings and their implications were concluded. In section 5.1, the parameters influencing the photocatalytic activity were discussed. Among the synthesized photocatalysts, the most active photocatalyst for the photodegradation of atrazine was concluded. The proposed degradation pathways for atrazine were elaborated as well. In section 5.2, the future work was discussed to further enhance the photocatalytic activity.

CHAPTER 2: LITERATURE REVIEW

2.1 Photocatalyst and photocatalysis

The pioneering work of Fujishima and Honda (1972) revealed the possibility of water splitting using a simple electrochemical cell supported-TiO_2 semiconductor setup. This had initiated tremendous interests amongst researchers on the application of metal oxides in the energy sector. Since then, intensive research on semiconductors such as TiO_2, ZnO and even C_3N_4 are investigated for the application of H_2 and CH_4 generation, air and water purification and solar cells (Hashimoto, Irie, & Fujishima, 2006).

The word photocatalysis consists of two parts, "photo" and "catalysis". Catalysis is a process where a material is used to modify the rate of a chemical reaction by reducing the activation energy. The material is known as a catalyst and is not altered or consumed in the end of the reaction. Photocatalysis is a reaction similar to catalysis but under the influence of light in order for catalyst activation. In photocatalysis, the catalyst is known as the photocatalyst. Thus, photocatalyst is a material that acts as a catalyst by altering the rate of a chemical reaction under light exposure (Fujishima, Rao, & Tryk, 2000).

2.2 Band structure

The ability to photo-excite electrons in any crystalline semiconductor using an external source of energy is the key factor for any photo-based application. These electrons populate in an energy band, which is a collection of individual energy levels of electrons surrounding each atom. In an isolated atom, electrons only have discrete energy levels. However in a crystalline solid, these energy level splits into many divisions due to the atomic interactions and creates continuous band of allowed energy states such as the valence and conduction band (Figure 2.1). The valence band is made of occupied molecular orbitals and has an energy level lower than the conduction band. The conduction band is higher in energy and is generally empty. The distance between

the valence band and conduction band in a semiconductor is term as the band gap where the Fermi level lies (50 % probability of occupied states) (Zeghbroeck, 2011).
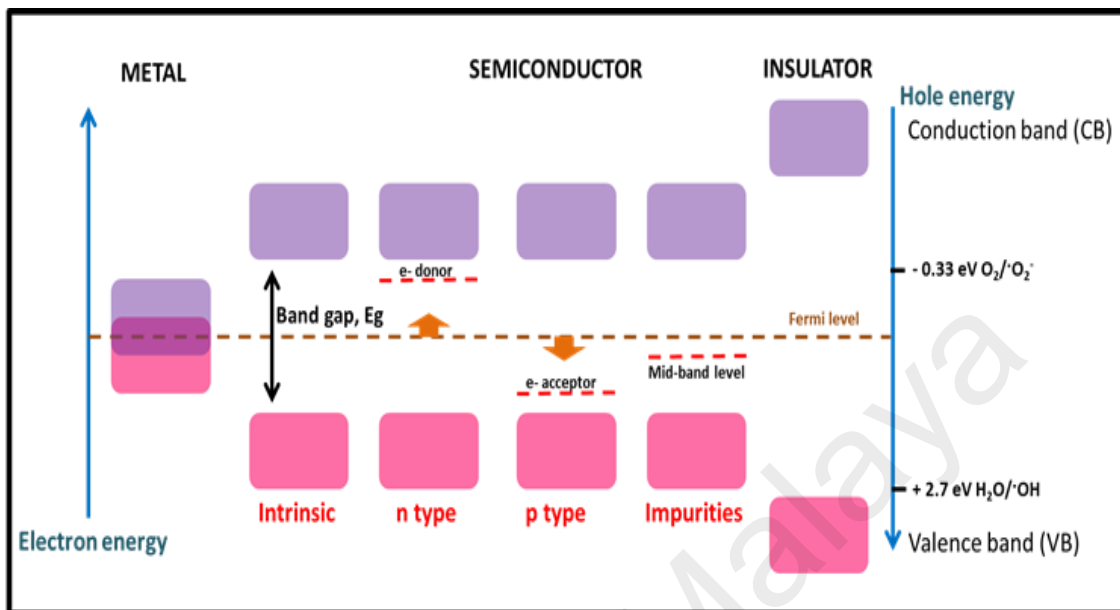
Figure 2.1: Valence and conduction band of metal, semiconductor and insulator

There are many types of semiconductor with varying energy band position and band gap energy (Figure 2.2). In an intrinsic semiconductor, the Fermi level lies in the mid gap. The Fermi level for extrinsic semiconductor such as the n-type and p-type shifts towards the conduction band and valence band, respectively (Zeghbroeck, 2011). Thus with this aspects, metal and insulator cannot be used as a photocatalyst due to the less strategic position of bands. In a metal solid, the electron flows freely due to bands overlapping and Fermi level is already positioned in the conduction band. For insulators, the wide band gap (exceeding ~9 eV) requires large amount of energy to be photo-excited (Brune, Hellborg, Whitlow, & Hunderi, 1997; Zeghbroeck, 2011).
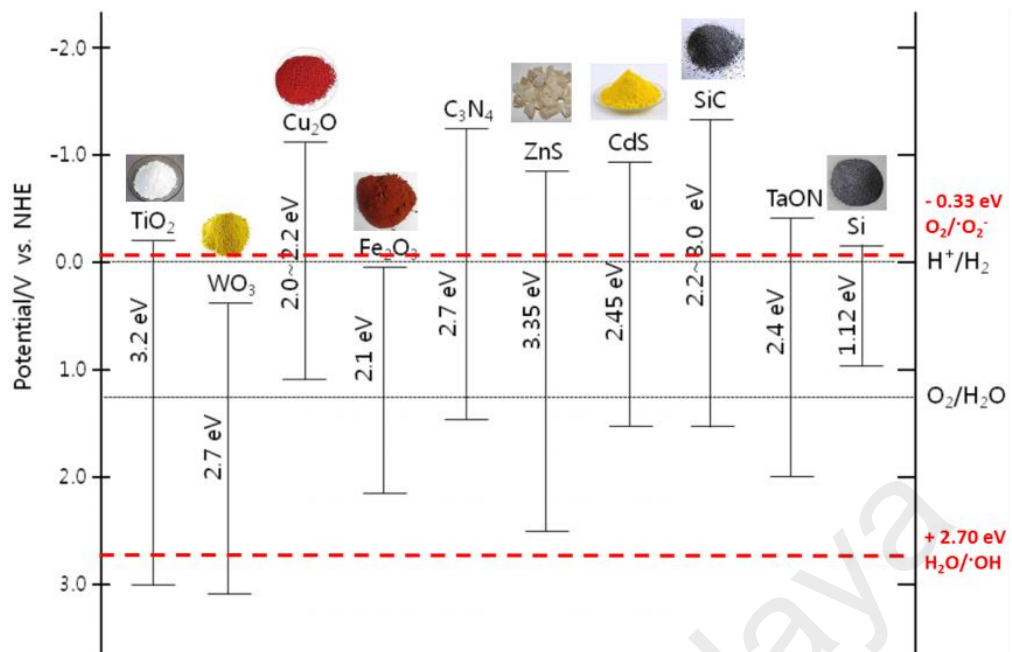
Figure 2.2: List of semiconductors and band gap positions (Hyeun, 2013)

2.3 Mechanism of photocatalyst

In a semiconductor photocatalyst, absorption of energy equal or greater than the band gap excites the electrons, e^- in the valence band towards the conduction band, leaving a positive hole, h^+. The electrons and holes may also recombine in the bulk or surface of the photocatalyst (Figure 2.3)
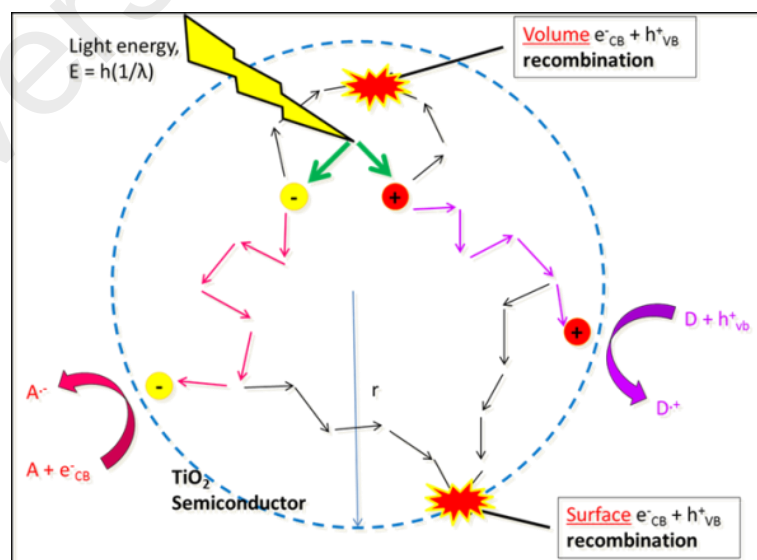
Figure 2.3: Bulk (volume) and surface electrons and holes recombination in a photocatalyst
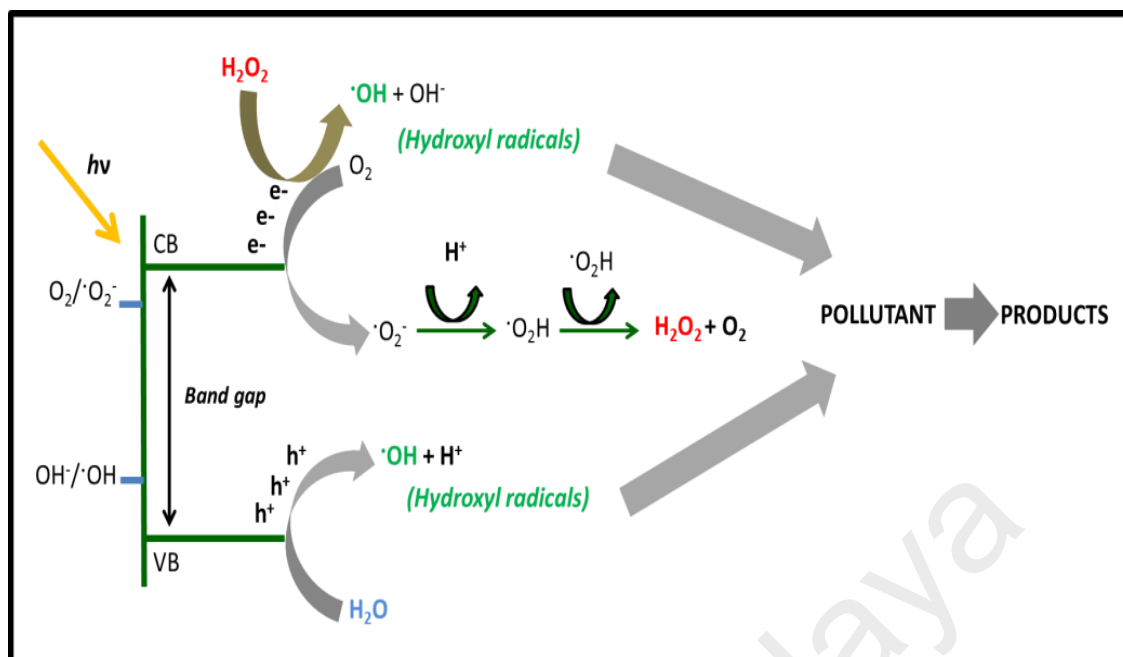
Figure 2.4: Photocatalytic degradation mechanisms of TiO_2
(Samsudin, Hamid, Juan, Basirun, & Kandjani, 2015)

Contrary, the non-recombined charge carriers migrates to the catalyst surface and reacts with an electron acceptor (O_2) and donor (H_2O). In humid or aqueous environment, the positive holes (at the conduction band) react with absorbed water molecules or hydroxyl ions and forms hydroxyl radicals, $\cdot OH$. These radical in turn oxidizes organic pollutants and is termed as indirect oxidation. Direct oxidation occurs when the organic pollutant is oxidized directly by the conduction band holes. The photo-excited electrons at the valence band react with absorbed oxygen and forms superoxide anion radicals, $\cdot O_2^-$. These radical in turn reduces organic pollutant and is termed as indirect reduction. Direct reduction occurs when the organic pollutant is reduced directly by the valence band electrons. In a photocatalytic activity, $\cdot OH$ radicals are mostly favored due to its high oxidizing potential relative to other radical such as superoxide anion radicals, $\cdot O_2^-$ (Gaya, 2014; Zeghbroeck, 2011). The photocatalyst degradation mechanism is illustrated in Figure 2.4 and Table 2.1.
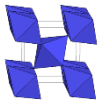
Table 2.1: Principle of a photocatalyst and radical formations

PATH		DESCRIPTION	MECHANISM
Photo-excitation of semiconductor			
	(1)	Electron-hole pair generation (energy equal or greater than band gap)	Semiconductor $+ h\nu \rightarrow e^-_{CB} + h^+_{VB}$
	(2)	Electron-hole pair recombination	$e^-_{CB} + h^+_{VB} \rightarrow TiO_2 +$ heat
Reaction at the conduction band			
	(1)	An electron can migrate to the catalyst surface and directly reduces absorbed organic pollutant	$D + e^-_{cb} \rightarrow \cdot D^-$ Organic pollutant $+ e^-_{cb} \rightarrow$ reduced species (direct)
	(2)	An electron can migrate to the catalyst surface and reduce absorbed oxygen molecules and forms superoxide anion radicals	$O_2 + e^-_{CB} \rightarrow O_2^{\cdot-}$ Organic pollutant $+ O_2^{\cdot-} \rightarrow$ reduced species (indirect)
	(3)	Formation of hydroxyperoxyl radical from superoxide anion radicals via a reductive pathway	$OO^{\cdot-} + H^+ \rightarrow \cdot OOH$
	(4)	Formation of hydrogen peroxide Formation of hydrogen peroxide and oxygen	$\cdot OOH + H^+ \rightarrow H_2O_2$ $\cdot OOH + \cdot OOH \rightarrow H_2O_2 + O_2$
	(5)	Formation of hydroxyl radical	$H_2O_2 + e^-_{CB} \rightarrow OH^- + \cdot OH$ Organic pollutant $+ \cdot OH \rightarrow$ reduced species (indirect)
Reactions at the valence band			
	(1)	A hole can migrate to the catalyst surface and directly oxidizes absorbed organic pollutant	$D + h^+_{vb} \rightarrow D^{\cdot+}$ Organic pollutant $+ h^+_{vb} \rightarrow$ oxidized species (direct)
	(2)	A hole can migrate to the catalyst surface and oxidize absorbed water molecules or surface hydroxyls and forms hydroxyl radicals	$H_2O + h^+_{vb} \rightarrow \cdot OH + H^+$ Organic pollutant $+ \cdot OH \rightarrow$ oxidized species (indirect)

2.4 Properties of titanium dioxide, TiO$_2$ semiconductor

Titanium dioxide, TiO$_2$ which belongs to the transition metal oxide group occurs in the form of three naturally occurring polymorphs which are tetragonal anatase, rutile and orthorhombic brookite (Carp, Huisman, & Reller, 2004). Rutile is the most stable, whereby anatase and brookite can be transformed into rutile due to their metastable properties (Gupta & Tripathi, 2011). When titanium ion paired with an oxide ligand forming TiO$_2$, there will be splitting of d-orbitals on titanium due to electron repulsions (Rozhkova & Ariga, 2015). The color of intrinsic TiO$_2$ origins from the value of d-splitting energy of titanium ions when paired with oxide ligands, where all absorbed visible light is reflected to govern the color of a white metal oxide. The properties of each TiO$_2$ polymorph are illustrated in Table 2.2.

Table 2.2: Properties and application of TiO$_2$
(Gupta & Tripathi, 2011; Paola, Bellardita, & Palmisano, 2013)

Properties	Anatase	Rutile	Brookite
Crystal structure	Tetragonal	Tetragonal	Orthorhombic
Lattice constant (Å)	*a = b = 3.784* *c = 9.515*	*a = b = 4.5936* *c = 2.9587*	*a = 9.184* *b = 5.447* *c = 5.154*
Density (g/cm^3)	3.79	4.13	3.99
Ti-O bond length (Å)	1.937 (4) 1.965 (2)	1.949 (4) 1.980 (2)	1.87 to 2.04
O-Ti-O bond angle	77.7° 92.6°	81.2° 90.0°	77.0° to 105°
Refractive index	2.56, 2.48	2.61, 2.90	2.58, 2.70
Band gap (eV)	3.05 to 3.23	2.98 to 3.02	3.1 to 3.4
Application	Photocatalyst, Pigments	Solar cells, Optics, Pigments, cosmetics	Difficult to prepare

2.5 TiO$_2$ versus other materials as a photocatalyst

In TiO$_2$, the valence band is composed of O 2p orbitals hybridizing with the Ti 3d orbitals, while the conduction band solely contains Ti 3d orbitals. The intrinsic position of the valence and conduction band in TiO$_2$ is strategically located for the redox activity of most organic pollutant (Hyeun, 2013). Furthermore, the energy level at the valence band is positive enough to oxidize absorbed water molecules or hydroxyl ions. The energy level at the conduction band is also negative enough to reduce absorbed molecular oxygen. Both the former and latter process generates active surface radicals for the degradation activity. In addition, the intrinsic band gap of TiO$_2$ is small enough to be photo-excited under UV light irradiation (Carp et al., 2004). Referring to Figure 2.2, the valence and conduction band of other semiconductors such as WO$_3$, Fe$_2$O$_3$ and Cu$_2$O do not lies within a strategic redox location as observed for TiO$_2$ although the band gap value is smaller.

Apart from strategic band position and band gap value, a good photocatalyst should be non-toxic, photo-stable and cost effective. In an aqueous environment, CdS and PbS

semiconductor have been reported to undergo photo-corrosion and leaching of toxic heavy metals (Colmenares et al., 2009). ZnO has almost similar band position and band gap as TiO_2, but ZnO is unstable and readily dissolves in water, forming $Zn(OH)_2$ on the ZnO particle surface (Chen, 2008; Rovelli & Thampi, 2015). With time, this will deactivate the catalyst. Thus, TiO_2 is close to being an ideal photocatalyst as it is photo-stable with energy bands strategically located for redox activity under UV light irradiation.

2.6 Design of TiO₂ as a photocatalyst

The remarkable physico-chemical properties of TiO_2 has triggered research outbursts, especially in the field involving energy-conversion applications such as photocatalysis, fuel generation, CO_2 reduction, electro chromic devices and solar cells (Carp et al., 2004; Zaleska, 2008). Contrariwise, the application of conventional TiO_2 for practical and commercial point of view are still limited, particularly in photocatalysis due to the wide band gap of 3.2 eV anatase TiO_2 (Asahi, Morikawa, Ohwaki, Aoki, & Taga, 2001). The photocatalytic activity of TiO_2 is a surface-driven catalytic mechanism and the rate is influenced by the concentration of surface radicals such as hydroxyl radicals ($\cdot OH$) and superoxide anion radicals ($\cdot O^{2-}$) (Gaya & Abdullah, 2008; Zaleska, 2008). Thus the mobility of charge carriers towards the catalyst surface, and the ability of the catalyst to absorb photons are two important aspects when designing TiO_2 (Park et al., 2013). High sustainability of charge carriers on the catalyst surface facilitates larger production of radicals. Moreover, wider absorption of light by TiO_2 generates larger concentration of radicals (Chen et al., 2012). These radicals in return, oxidize organic pollutants into simpler and less hazardous substance. Numerous strategies are employed to enhance the photocatalytic activity of TiO_2, which includes using surfactant, metal and non-metal doping, heterogeneous composites (WO_3, SiO_2, Al_2O_3, etc.), hybridization with nano-materials (graphene, zeolites), dye anchoring and

19

very recently, hydrogenation (Carp et al., 2004; Chen et al., 2011; Gaya & Abdullah, 2008; Gupta & Tripathi, 2011; Li et al., 2014; Mohamed et al., 2012; Oshani et al., 2014; Shon et al., 2008; Yu et al., 2008; Zaleska, 2008).

2.6.1 Surfactant-based TiO₂

The usage of surfactant for the preparation of mesoporous silica was first initiated by Mobil in 1992 (Luo, Wang, & Yan, 2003). Similar analogy is introduced in preparing mesoporous TiO_2 which significantly affects the morphology, size, porosity and surface area. TiO_2 prepared without surfactant leads to poorly structured materials due to dense inorganic chains as a result of less controlled hydrolysis and condensation process (Shahini, Askari, & Sadrnezhaad, 2011) . The preparation of TiO_2 using alkyl phosphate surfactant via sol-gel initiated by Antonelli & Ying (1995) sparks interests as an alternative approach towards enhancing the properties of TiO_2. Since then, various surfactants are used, which includes phosphates, ionic surfactants, non-ionic surfactants, amines and block co-polymers for the preparation of mesoporous TiO_2 (Agarwala & Ho, 2009; Antonelli & Ying, 1995; Deng et al., 2010; Gajjela, Ananthanarayanan, Yap, Gratzel, & Balaya, 2010; Smarsly et al., 2008; Yu et al., 2008). Smarsly et al (2008) used titanium tetrachloride ($TiCl_4$) and PHB-PEO block co-polymer to prepare TiO_2 thin film by dip coating and straight thermal treatment technique. The prepared TiO_2 thin film showed highly organized mesoporous anatase films, with 10 nm pore diameter, reportedly larger than previously reported ordered mesostructure crystalline TiO_2. Agarwala and Ho (2009) prepared TiO_2 thin film by dip coating and thermal treatment using titanium (IV) ethoxide ($Ti(OEt)_4$) and pluronic F123 as titanium precursor and structure direction agent respectively. The surfactant-based TiO_2 thin film showed anatase crystal structure with high degree of crystallinity and quasi-hexagonal ordered pores between 8-10 nm. It is worth to note that the pores of TiO_2 collapsed at higher thermal treatment temperature of 550 °C, hence balancing of the synthesis procedure is

crucial to optimize TiO$_2$ surface properties, regardless of the presence of a structure directing agent. (Li et al., 2014) prepared TiO$_2$/SiO$_2$ hybrid photocatalyst films by evaporation induced self-assembly (EISA) technique using titanium (IV) isopropoxide (TTIP) and tetraethyl orthosilicate (TeOS) as the metal precursor and poly(styrene-b-2-vinyl pyridine-b-ethylene oxide as the surfactant. Mesoporous and thermal stable hybrid photocatalyst was obtained with uniform pore size which showed superior photocatalytic activity. In another work, cetyltrimethylammonium bromide (CTAB) was employed in preparing TiO$_2$ and enhanced surface area and high crystallinity was observed (Peng, Zhao, Dai, Shi, & Hirao, 2005). Spray drying method of pre-dissolved titanium (IV) isopropoxide (TTIP) in HCl acid and pluronic F127 in ethanol were used to produced mesoporous spherical TiO$_2$ with large surface areas (Oveisi, Suzuki, Beitollahi, 2010). The addition of pluronic F127 during sol-gel does not affect the final pH of the solution and thus the rate of hydrolysis and condensation remains unaffected (Mahata, Mahato, Nandi, & Mondal, 2011; Sung, Ho, Kim, Cho, & Oh, 2010).

2.6.2 Doping

Doping of TiO$_2$ using metal and non-metal has been an important approach in band gap engineering to improve the optical response of the catalyst. Transition metal doping includes manganese (Mn), iron (Fe), cobalt (Co), nickel (Ni) and copper (Cu) while non-metal doping includes boron (B), nitrogen (N), phosphorus (P), Sulfur (S) and halogen groups (Zaleska, 2008) . For substitution doping, the dopants will either replace the metal or oxide centers of TiO$_2$, and results to an energy shifts in the valence or conduction bands (Orikawa, Sahi, & Hwaki, 2001). However, for interstitially doped TiO$_2$, mid-band energy levels are formed and are usually attributed to defects such as oxygen vacancies and reduced Ti^{4+} centres (Viswanathan & Krishanmurthy, 2012).

2.6.2.1 Metal loaded-TiO₂

Fe-doped TiO_2 was prepared by using wet impregnation method and iron nitrate as the precursor from 0.5 to 5.0 wt % concentration (Naṿo et al., 1998). Large particle size and smaller specific surface area was observed which does not benefit the photocatalytic activity. Another initiative in preparing Fe-doped TiO_2 using similar Fe-source but via co-precipitation method proved otherwise (Ganesh et al., 2012). Enhanced photocatalytic activity was observed and attributed to the reduced band gap from 3.2 to 2.2 eV, which allowed visible light absorption. Furthermore, the presence of Fe in TiO_2 was believed to stabilize the doped TiO_2 in the form of anatase. Ni-doped TiO_2 thin film was prepared by chemical solution deposition method. The optical response shifted towards the visible region. The addition of nickel in TiO_2 also resulted to the growth of rutile crystal phase (Lim et al., 2005). In another work, Ni-doped TiO_2 was prepared using sol-gel and nickel nitrate (Ni $(NO_3)_2$. $6H_2O$) as the dopant precursor. Improved particle uniformity and less aggregation was observed (Teimouri, Aberoomand, Moradi, Zhalechin, & Piramoon, 2012). Degussa P25 was doped with copper between 0 and 5 wt % using a non-transferred plasma torch system (Tsai, Hsi, Kuo, Chang, & Liou, 2013). It was observed that the mass ratio of anatase decreased at higher Cu-loading. Cu-doped TiO_2 prepared at 5 wt % loading demonstrated largest optical shift towards the visible light, relative to Degussa P25. V-doped TiO_2 was prepared using hydrothermal method and V_2O_5 / HCl as the metal precursor from 0.1 to 0.9 % in concentration (Thuy, Van, & Hai, 2012). The catalyst showed single anatase crystal phase and visible light absorption. The improved optical response was attributed to the formation of lattice disorders and also charge-transfer transitions from the d-d orbitals of vanadium to the conduction band of TiO_2. It has been widely reported that for metal-doped TiO_2, the Fermi level within TiO_2 band gap shifts towards the valence band,

where the effective mass is the lowest (Supriyo Bandyopadhyay, 2002). This leads to an alteration on the intrinsic band gap of TiO_2 and enables wider solar light absorption.

2.6.2.2 Non-metal

Non-metal doping into TiO_2 such as P, N, S and many others promotes visible light absorption via band gap engineering (Zaleska, 2008). Out of all non-metal doping, doping with nitrogen has been numerously reported to yield the best photocatalytic activity amongst other non-metal doped TiO_2 (Ananpattarachai, Kajitvichyanukul, & Seraphin, 2009). Various source of nitrogen dopants are studied which includes urea, triethylamine, diethylamine, ammonia, hydrazine and melamine, in which different binding chemistry of nitrogen in TiO_2 are observed (Zhang, Zou, Lewis, & Dionysio, 2014). Similar choice of dopant, for example triethlyamine showed different properties of TiO_2 and thus the nature of doping relies greatly on the synthesis procedure (Ananpattarachai et al., 2009; Gole, Stout, Burda, Lou, & Chen, 2004; Wang et al., 2006). It also showed that low and high nitrogen loading favored interstitial and substitutional TiO_2 doping, respectively. Contrary to cationic doping (i.e. transition metals), anionic doping do not form deep localized *d* states which acts as charge recombination centres (Asahi et al., 2001). Nitrogen doping is also widely reported to cause red optical shift towards visible light response. One possible reason is the overlapping of O 2p and N 2p energy level and subsequent band gap narrowing (Zhang et al., 2014).

Pure single anatase crystal phase of P-doped TiO_2 was prepared using phosphoric acid as the precursor via sol-gel method (Gopal et al., 2012). Similar to N-doped TiO_2, the optical response is red shifted towards the visible light. The particle size also decreased. Furthermore, the XPS analysis confirmed replacement of Ti^{4+} ion with P^{5+} ions forming Ti-O-P bonds. S-doped TiO_2 thin film was prepared using carbon disulfide via chemical vapor deposition method and showed visible light absorption (Dunnill et

al., 2009). Due to the larger atomic radii of sulfur, doping into TiO$_2$ has been reported to be difficult as compared to N-doping (Klaus, 2016). Furthermore, it has been reported that the crystallinity of S-doped TiO$_2$ reduced and thus perturbed the electron mobility, to some point. Tongpool and Setwong (2008) heat treated thiourea with TiO$_2$ at 450 °C for the preparation of S-doped TiO$_2$. Interestingly, the photocatalytic activity were shown to enhance and also worsens, depending on the total effects of S-doping with respect to optical response, surface area, hole mobility and blocking of active sites. In addition, S-doped TiO$_2$ prepared using Degussa P25 showed presence of anatase and rutile crystal phase while S-doped TiO$_2$ prepared using TiO$_2$ (Smith supply) showed presence of single anatase crystal phase. The as-prepared TiO$_2$ using tetraisopropyl orthotitanate via sol-gel method showed presence of anatase and brookite. However, the mechanism of the different crystal phase growth was not stressed. Contrary to metal-doped TiO$_2$, the Fermi level within TiO$_2$ band gap for non-metal doped TiO$_2$ shift towards the conduction band, where the effective mass is the lowest (Supriyo Bandyopadhyay, 2002). Thus, the intrinsic band gap of TiO$_2$ is altered and enables absorption of wider solar light region.

Among the non-metal dopants, application of fluorine as a capping agent and/or dopant in TiO$_2$ is effective to enhance the photocatalytic activity. This is because fluorine is capable of modifying TiO$_2$ structure, hydrophilicity, surface charge, exposed facets, porosity, surface area and thermal stability (Lv, Yu, Cui, Chen, & Li, 2011; Wang, Chen, Ma, Zhu, & Zhao, 2009). In F-doped TiO$_2$, the fluoride ions are physically adsorbed on the catalyst surface forming $\equiv$Ti-F bonds or could either substitute oxygen atom in TiO$_2$ lattice forming -Ti-F-Ti- bonds. Fluorine-doped TiO$_2$ is an excellent structure directing agent and promotes the growth of high energy {001} facets (Zhou et al., 2008). In addition, the synergy between {001} and {101} facets in TiO$_2$ is proven to promote efficient charge carriers separation as a result of surface hetero-junction (Yu,

Jeon, & Kim, 2015). The high electronegativity of fluorine and enhance surface acidity in F-doped TiO_2 also improves the separation of electrons and holes (Dozzi, Andrea, Ohtani, Valentini, & Selli, 2013). As a result of charge imbalance between fluoride ions (-1) and oxide ions (-2), the excess positive charge is neutralized by hydroxide ions by forming surface adsorbed hydroxyl groups ($\equiv$Ti-OH) (Ho, Yu, & Lee, 2006). In F-doped TiO_2, the doped fluoride ion is highly stable due to its high redox potential ($\cdot$F/F-) of 3.6 V vs NHE (Yu, Wang, Cheng, & Su, 2009), and is not easily oxidized by the valence band holes.

Up to date, the most widely applied method to fabricate F-doped TiO_2 is by hydrothermal process, followed by spray pyrolysis, vapor phase fluorination and very few, sol-gel method (Dozzi et al., 2013; Ho et al., 2006; Kwamman & Smith, 2012; Li et al., 2005; Lv et al., 2011; Zhou et al., 2008). Ho et al (2006) prepared $TiO_{2-x}F_x$ by hydrothermal method and obtained visible-driven photocatalytic activity attributed to the extrinsic absorption triggered by oxygen vacancies. Previous works also used hydrothermal method to prepare flower-like $F-TiO_2$ and showed improved photocatalytic activity due to {001} facets enhancement (Ong, Tan, Chai, Yong, & Mohamed, 2014). The larger surface of Ti-O-Ti angle in {001} relative to {101} facets results in destabilized and very reactive O 2p states and thus benefits the photocatalytic activity (Yu, Low, Xiao, Zhou, & Jaroniec, 2014).

However, excessive {001} facets in TiO_2 could act as photo-generated electrons and holes recombination centre (Wang et al., 2015). Xiang & Yu, 2011 obtained highly porous flower-like $F-TiO_2$ with intense UV light absorption, high exposure of reactive {001} facets and improved photocatalytic activity. Still, hydrothermal method suffers major drawbacks such as high-energy consumptions and requirement of special conditions (Yu et al., 2014). Furthermore, the usage of hydrofluoric acid to prepared F-

TiO$_2$ is highly toxic and corrosive (Ma et al., 2010). Thus, preparing F-doped TiO$_2$ using a safer, easier and less costly method is much favorable.

2.6.2.3 Co-doping

The idea of combining two dopants for the preparation of co-doped TiO$_2$ has gained vast attention as an alternative to improve the photocatalytic activity (Jusof Khadidi & Hamid, 2013; Kumar et al., 2013). Co-doping can be prepared using transition metal and non-metal dopants, lanthanoids and non-metal dopants or two non-metal dopants. For example, the synergy between nitrogen and fluorine in N,F co-doped TiO$_2$ facilitates superior visible light photocatalytic activity due to modified color centre, smaller band gap, enhanced crystallinity, oxygen vacancies, larger surface area and inhibition of electrons and holes recombination (Li & Liu, 2008; Yu et al., 2014).

Li & Liu (2008) also observed retardation of anatase to rutile crystal phase in the presence of nitrogen and fluorine in TiO$_2$. Ce, N co-doped TiO$_2$ was prepared using sol-gel method and showed improved photocatalytic activity, surpassing the performance of non-doped and N-doped TiO$_2$ (Liu, Tang, Mo, & Qiang, 2008). This observation is attributed to the significant optical response to 500 nm (visible light) and also, additional presence of active sites (Ti^{3+}) on the catalyst surface.

2.6.3 Metal deposition

Transition metals, especially noble metals such as platinum (Pt), Palladium (Pd), Gold (Au) and Silver (Ag) that are chemically deposited on TiO$_2$ surface are shown to improve charge carriers separation in TiO$_2$ by acting as electron scavengers (He & Yao, 2006). These noble metals can be deposited via photodeposition process, thermal deposition, physical vapor deposition and also via chemical reduction of the noble ion species on TiO$_2$ surface (Nainani, Thakur, & Chaskar, 2012). Analogous to surface fluorination, metal deposited on the surface of TiO$_2$ generates greater electron flux on the catalyst surface and thus catalyzes the generation of surface radicals. Subsequently,

larger concentration of surface radicals enables faster degradation of organic pollutant, and thus elevates the photocatalytic activity. Apart from improved electron flux on the catalyst surface, Nainani et al (2012) observed narrowing of band gap and improved visible light absorption of Ag-deposited TiO_2, relative to Merck pure anatase TiO_2. Pd-deposited TiO_2 was prepared using commercial TiO_2 and showed smaller particle size and improved electrons and holes separation (Ahmed, Ivanova, Hussein, & Bahnemann, 2014). Despite the superior catalytic activity as a result of improved catalyst properties, this approach is less feasible due to the high cost of noble metals.

2.6.4 Hydrogenation

A recent breakthrough in developing solar-driven TiO_2 is via hydrogenation of TiO_2. Chen et al (2011) published a report discussing the properties of hydrogenated TiO_2 and its relation towards dye photodegradation and photocatalytic water splitting process. Up to date, various hydrogenation methods are available which includes pressurized hydrogen gas chamber (Chen et al., 2013), high temperature atmospheric hydrogenation (Ramchiary & Samdarshi, 2014), plasma enhanced chemical vapor deposition (Yan et al., 2014) and by alumina reduction (Wang et al., 2013). Hydrogenation is a clean process and do not form additional impurity level, contrary to doped TiO_2 (Wei, Yaru, Chunhua, & Zhongzi, 2012). The photocatalytic activity of hydrogenated TiO_2 is reported to improve due to the formation of surface disorders, which acts as active sites and thus, enhance the mobility of electrons (Zhu et al., 2012). Surface disorders are created by the termination of surface dangling bonds with hydrogen ions (hydride intermediate) (Chen et al., 2013).

Hydrogenation of TiO_2 is a surface modification phenomenon and does not perturb the crystalline core of TiO_2. Yan et al (2014) hydrogenate commercial Degussa P25 by plasma enhanced hydrogenation treatment and obtained high photocatalytic activity due to efficient electrons and holes separation attributed to the present of surface disorders.

Hydrogenation of TiO_2 affects the color of the catalyst as a result of surface disorders and is significantly influenced by the availability of surface dangling bonds (Leshuk et al., 2013). Hydrogenated TiO_2 also demonstrates dramatic change towards TiO_2 ability to absorb UV, visible and infrared light. Hydrogenated commercial Degussa P25 was prepared using pressurized hydrogen gas chamber and demonstrated high photocatalytic activity due to enhanced solar light absorption, high crystallinity and change of catalyst color from white to black (Lu, Dai, Jin, & Huang, 2011). Some work attributes the enhancement of solar light absorption to the presence of band tail states from the valence band to the conduction band (Chen et al., 2013; Wang et al., 2013; Yan et al., 2014). Others attribute to the formation of surface disorders and defects (Wei et al., 2012). Surface and bulk oxygen vacancies and Ti^{3+} are also observed in hydrogenated TiO_2 (Chen et al., 2013). The enhancements in photocataytic activity using hydrogenated TiO_2 relative to other conventional modified TiO_2 are mainly due to its superior light absorption and presence of surface disorders as additional active sites (Lin et al., 2014). However, Leshuk et al (2013) showed worsens photocatalytic activity in hydrogenated TiO_2 due to small specific surface area and excessive oxygen vacancies acting as charge carrier traps. Therefore, hydrogenation can be a promising method with a proper synthesis method.

2.6.5 Other modifications

Band gap engineering to cater for wider solar light absorption can be achieved by nano-compositing TiO_2 with another metal oxide or semiconductor such as Cu_2O, ZrO_2, SiO_2, Al_2O_3, WO_3, SnO_2, doped-TiO_2, C_3N_4 and many more (Hu, Lu, Chen, & Zhang, 2013; Zaleska, 2008). Previous reports observed enhanced charge carriers mobility via the formation of surface hetero-junctions between the composites and also band gap narrowing (Liu, Wu, Liu, & Jiang, 2010). Another strategy includes dye sensitization of TiO_2 surface by physisorbed or chemisorbed dyes to increase the sensitivity towards

solar light absorption and is widely used for solar cell application (Gupta & Tripathi, 2011). Depending on the nature of the dye, it can either inject holes into the particles, or more commonly electrons upon photo-excitation of the catalyst. However, the drawback of dyes is the self-photo-degradation forming intermediates which could deteriorates the catalyst reusability over time (Wu, Lin, Zhao, Hidaka, & Serpone, 1999). Hybridizing TiO_2 with materials such as graphene, carbon nanotube, fullerene and zeolites are also able to improve electrons mobility and thus the photocatalytic reaction (Xiang, Yu, & Jaroniec, 2012).

Clearly, there are advantages and disadvantages of each modification method and thus synergies formation via combination of two or more strategies are favorable. This combination can result to improved photocatalytic activity. Compared to cationic dopant, anionic dopant eliminates charge carriers recombination due to deep localized d states found in metal dopants. Furthermore, decorating the catalyst surface with an electronegative anion dopant significantly improve the surface properties. Meanwhile, hydrogenation is a very effective method to widen solar light absorption. Therefore, the synergies of anionic dopant and hydrogenation will dramatically enhance the photocatalytic activity by the lower charge carrier recombination rate and favorable surface properties, as well as the ability to increase the photonic efficiency under wider solar light absorption.

2.7 Synthesis of TiO_2

Over the recent years, numerous synthesis methods of TiO_2 have been introduced which includes sol-gel, hydrothermal, solvothermal, chemical vapor deposition, spray pyrolysis, electrochemical, sonochemical, and microwave (Byranvand, Kharat, Fatholahi, & Beiranvand, 2013). Different synthesis method affects the nucleation and growth of TiO_2 and, hence its properties such as morphology (nanoparticles, nanorods, nanotubes, nanoflakes, nanoflowers), size, particle uniformity, crystal structure and

surface reactivity (active sites such as defects and facets) (Wang, He, Lai, & Fan, 2014). Powdered nanoparticles are generally prepared by sol-gel, hydrothermal and solvothermal method whereby thin films and nanotubes by electrochemical, chemical vapor deposition and spray pyrolysis method. Both sonochemical and microwave method can be used to compliment the conventional preparation method, however its sensitivity towards the change in the physical and chemical properties of TiO_2 should be addressed.

2.7.1 Sol-gel

Nano-sized TiO_2 is widely prepared using room temperature sol-gel method as this method allows efficient control of its purity, homogeneity and composition (Su et al., 2004). According to Paul and Choudhury (2013), tailoring of certain TiO_2 properties such as morphology, size and porosity is possible by sol-gel as it is carried out in solution. Moreover, sol-gel method also does not require the necessity of special equipment (Pillai, McCormack, & Colreavy, 2007). TiO_2 prepared using sol-gel method is shown to yield high photocatalytic activity as well (Santana-Aranda, M.Moran-Pineda, Hernandez, & Castillo, 2005). Vijayalaxmi & Rajendran, 2012 observed smaller particle size with better crystallinity of TiO_2 using sol-gel relative to hydrothermal method, prepared at the same condition. In a sol-gel method, the physico-chemical properties of TiO_2 are greatly influence by the type and ratio of titanium precursor, solvent, water and pH condition and thus affect the rate of hydrolysis and condensation illustrated below.

Hydrolysis

$M\,(OR)_n + H_2O \rightarrow M\,(OR)_{n-1}(OH) + ROH$ <div style="float:right">Eq. (2.1)</div>

Condensation

$M\,(OR)_n + M\,(OR)_{n-1}(OH) \rightarrow M_2O(OR)_{2n-n} + ROH$ <div style="float:right">Eq. (2.2)</div>

Poly-condensation

$2M\,(OR)_{n-1}(OH) \rightarrow M_2O(OR)_{2n-n} + H_2O$ <div style="float:right">Eq. (2.3)</div>

Overall Reaction

$$M(OR)_n + (n/2)(H_2O) \rightarrow MO_{(n/2)} + nROH \qquad \text{Eq. (2.4)}$$
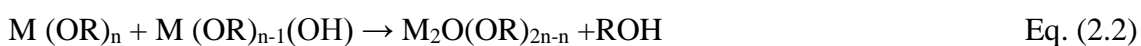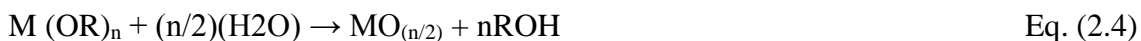
The type of titanium precursor used in preparing TiO_2 includes titanium tetra-butoxide, titanium tetra-isopropoxide, titanium tetra-chloride, titanium tetra-ethoxide and others. Different source of Ti-precursor influence TiO_2 morphology (Vijayalaxmi & Rajendran, 2012). Furthermore, larger particle size is obtained using Ti-precursor with more reactive ligands due to its less steric hindrance during the hydrolysis and condensation process. Larger particle size of TiO_2 was observed using titanium tetra-ethoxide relative to titanium tetra-isopropoxide and titanium tetra-butoxide. Moreover, largest surface area of TiO_2 is obtained using titanium tetra-isopropoxide (Simonsen & Søgaard, 2009).

The pH during sol-gel influences the growth of TiO_2 whereby at neutral pH range, TiO_2 is highly unstable and tends to agglomerates (Sung et al., 2010). Therefore sol-gel is best prepared under acid-catalyzed or base-catalyzed reaction. Sayilkan and Asilturk (2005) emphasized on the importance of HCl as a stabilizer for the formation of anatase crystal phase at low temperature. The formation of anatase and rutile crystal phase is favored at low acidity and high acidity respectively. Low acidity coupled with large Ti-ligands results to slow hydrolysis and thus gel is formed rather that precipitation (Loryuenyonga, Angamnuaysiria, Sukcharoenponga, & Suwannasria, 2012).

In addition, uncontrolled precipitation during sol-gel leads to the formation of rutile. Small size TiO_2 particle with enhanced surface area is observed for TiO_2 prepared at acidic condition (Santana-Aranda et al., 2005). Sung et al (2010) observed TiO_2 as powder and granular form, prepared at basic and acidic condition respectively. The type of solvent used also influences the type of crystal polymorphs in TiO_2 (Luo et al., 2003).

In a sol-gel method, the ageing and calcination duration, as well as temperature, plays a significant role towards TiO_2 crystal growths and final particle size (Shahini et al., 2011). High ageing temperature is observed to decrease the surface area of TiO_2.

Furthermore, recent work demonstrates that the order of chemical mixing during sol-gel significantly influences the morphology, crystal structure, size and optical properties of TiO_2 (Samsudin et al., 2015). Although sol-gel method governs many advantages as mentioned earlier, any slight changes in the experimental conditions would yield different catalyst properties. Thus, care during the sol-gel process should be taken when reproducing TiO_2 using this method.

2.7.2 Hydrothermal method

Differently from sol-gel, the preparation of TiO_2 by hydrothermal method is conducted in a closed system (steel pressure vessels autoclaves with or without Teflon liners) under controlled pressure (P < 10 mPa) and temperature (T < 200 °C) using aqueous mixture as the solvent. The type of aqueous solvent includes deionized water, NaOH and inorganic salts (Wang et al., 2014). The pressure during the hydrothermal process is greatly influenced by the operated temperature and type of solvent used (Byranvand et al., 2013). The process includes crystal growth and transformation, phase equilibrium and the formation of fine nano-crystals (Wang et al., 2014)

Different pH condition enables tuning of TiO_2 shapes ranging from nanoparticles, nanorods and nanotubes during hydrothermal process (Byranvand et al., 2013). Hydrothermal method also generates TiO_2 with consistent homogeneity, purity and small particle size (Kasuga, Hiramatsu, Hoson, Sekino, & Niihara, 2007). A typical hydrothermal process would require mixing of titanium precursor with the desired solvent, and is treated in an autoclave at high temperature. The obtained precipitate is washed with deionized water and dispersed in acid, before undergoing calcination to formed well-defined nanoparticles of TiO_2 (Wang et al., 2014).

Kim and Kwak (2007) evaluated the properties (crystallinity, surface area and photocatalytic activity) of TiO_2 prepared by sol-gel and sol-gel supported hydrothermal method. Without the calcination of both catalysts, the hydrothermally prepared TiO_2

showed good crystallinity with anatase structure whereby, as-synthesized sol-gel showed amorphous and semi-crystalline phase. Furthermore, larger surface area was observed in the former. Prior to calcination, the crystallinity of both catalysts were enhanced with increased particle size. Nevertheless, higher calcination temperature increased the band gap and was sufficient for only UV light absorption. It was observed that the photocatalytic activity of TiO_2 prepared via hydrothermal method demonstrated better photocatalytic activity than sol-gel method due its larger surface area and higher crystallinity.

Employing concentrated hydrochloric acid (HCl) as the morphological/ crystallographic controlling agent and titanium n-butoxide as Ti precursor, TiO_2 nanostructure was synthesized using hydrothermal method for a duration of 36 h (Phan et al., 2009). The resulting TiO_2 resulted pure anatase crystal phase and mixed of anatase and rutile phase using low and high concentration of HCl, respectively. Another interesting observation is the tuning of TiO_2 morphology from cubic-like nanoparticle (low HCl dosage) to flower-like nanoparticle (medium HCl dosage), and then followed by cauliflower and ball-like aggregates made of rod-plates (high HCl dosage).

2.7.3 Solvothermal method

Solvothermal method is almost similar to hydrothermal, except that non-aqueous organic solvents are used instead of water-based solvent. The organic solvent includes alcohol, toluene, acetone and carboxylic acid (Wang et al., 2014). Thus, higher temperature and pressure can be applied when using this method. Solvothermal method also showed better catalyst properties relative to hydrothermally prepared TiO_2 with respect to size, uniformity, agglomeration and crystal phase (Chen et al., 2012). Furthermore, calcination of the catalyst is not necessary as crystalline TiO_2 is readily formed during the dissolution-precipitation process in the autoclave chamber. High crystalline TiO_2 using solvothermal method was observed due to the low dielectric

constant of the organic solvents used. This give rise to a decreased in the solubility of TiO$_2$, which limits the dehydration process and thus formation of smaller highly crystalline nanoparticles (Lucky, Sui, Lo, & Charpentier, 2010)

Commercial TiO$_2$ powder was mixed with absolute ethanol and sodium hydroxide, and was heated in a Teflon-line autoclave at 200 °C for 1 to 2 days. The synthesized TiO$_2$ nanoparticles possessed anatase crystal phase with mixed morphologies of rod-like and flat particles (Almajdalawi et al., 2013). Although there was no calcination step, the dried nanoparticles showed high crystallinity. Another work utilized a lower boiling point solvent (ketone) to prepare TiO$_2$ photocatalyst by solvothermal method (Nam, Yang, & Duc, 2013). It was observed that morphology of TiO$_2$ were greatly affected by the types of solvent used; nanotubes for methyl ethyl ketone solvent and nanoparticles/nanowires for methyl ethyl ketone/ acetone solvent. In terms of optical properties, the former showed smaller band gaps of 3.21 eV while the latter, at 3.45 eV.

Although hydrothermal and solvothermal is a promising method to generate high crystalline TiO$_2$ with various morphologies, the use of an autoclave is less cost effective. . In addition, a relatively long time is required to obtained the target reaction temperature in the autoclave, which may already induced a pre-reaction and difficulty to separate the nucleation stage from the crystal growth stage of TiO$_2$ (Chen, Yu, Shin, & Yoo, 2010).

2.7.4 Chemical vapor deposition (CVD)

The preparation of TiO$_2$ thin films by condensing heated gas and depositing it as solid film on a hot substrate is achieved by chemical vapor deposition method (CVD). CVD are normally used to form surface coatings of various materials in order to improve its mechanical, electrical, optical, resistivity and thermal properties (Wang et al., 2014). The properties of TiO$_2$ thin films prepared by CVD are controlled by the gas flow rate and composition, temperature, pressure and also the chamber geometry. A

more enhanced CVD process would involve the use of ions, photons, plasmas, lasers or combustion reactions to increase the solid deposition rates (Warwick, Dunnill, Goodall, Darr, & Binions, 2011).

TiO_2 thin film was prepared using low-temperature atmospheric-pressure CVD method in air (Maruyama & Tabata, 1990). The heated gas were produced by heating isopropyl alcohol solutions of titanium tetraacetylacetonate and the chemical reaction products were deposited as thin film on a borosilicate glass substrate. It was observed that the temperature of the substrate determines the crystallinity of the deposited anatase TiO_2, where an amorphous solid film was obtained at temperature below 500 °C.

Glass coated TiO_2 thin film was prepared using CVD method. It was observed that the crystal grain size increased with the substrate temperature (Sun et al., 2008). Differently from sol-gel thin film formation on the substrate, the possibility of sodium ion diffusion from the glass to the TiO_2 film is eliminated by using CVD as this method can eliminate the necessity of annealing process. TiO_2 crystallinity and growth of crystal phase can be controlled by manipulating the substrate temperature. Hence, photocatalytic efficiency of the glass coated TiO_2 thin film prepared using CVD method is preserved. However, the formation of crystal grains requires higher substrate temperature whereby substrate temperature of 400 °C showed a net structure with no apparent grain boundaries (Brinker & Schunk, 1992).

2.7.5 Spray pyrolysis

Spray pyrolysis method is analogous to chemical vapor deposition method but the formation of thin film on the substrate is achieved by spraying a solution on a heated substrate, instead of condensation of heated gas. Spray pyrolysis method also does not require a complicated vacuum system and sputtering as in the case of CVD (Okuya, Nakade, & Kaneko, 2002). Previous work demonstrated that the smoothness and crystallinity of the prepared TiO_2 thin films are less likely to be affected by the

difference between spray pyrolysis and CVD process (Conde-Gallardo et al., 2005). In spray pyrolysis, the selection of solution contains other components which are volatile at the temperature of deposition. Furthermore, to control the homogeneity and growth of thin films on the substrate, a combination of spray pyrolysis with ultrasonic technique to generated aerosols droplets are desired. Spray pyrolysis is used to prepare thin film materials for different application, which includes electrodes in solar cells, gas sensors and photocatalyst (Oja, Mere, Krunks, Solterbeck, & Es-Souni, 2004).

TiO_2 films was prepared by spray pyrolysis using a mixture of titanium isopropoxide (precursor), ethanol (solvent) and acetylacetone (stabilizer) (Oja et al., 2004). The mixture was sprayed on a heated substrate using pulsed solution feed at a temperature ranged from 300 to 500 °C, whereby the thickness of the film can be controlled by the number of spray pulses. The characterization results showed presence of pure anatase crystal phase using a substrate temperature of 500 °C. Annealing at 700 °C result to the growth of rutile crystal phase.

Similar observations were reported for the preparation of TiO_2 thin film using spray pyrolysis method whereby amorphous phase is observed at temperature below 500 °C (Abou-Helal & Seeber, 2002; Conde-Gallardo et al., 2005). In addition, it was also observed that manipulating the deposition temperature and time did not caused any band gap modification. However, the visible light transmission was greater at higher deposition temperature as a result of better surface crystallinity. Enhanced film thickness and porosity was also achieved at longer deposition time which improved the catalytic activity of the thin film.

2.7.6 Sonochemical

In a sonochemical method, the chemical reactions of the starting materials proceed in the presence of high frequency ultrasonic waves. Sonochemical method is usually used to control and improve the properties of the prepared photocatalyst, particularly its

morphology and size, by generating ultrasonic waves. This method is widely applied for materials including alloys, oxides, colloids and carbides (Wang et al., 2014). In a liquid solution, the ultrasonic waves create cavitation gas vacuole which violently forms, grows, collapses and adiabatically generates intense local heating (~5000 K) and high pressure (500 atm). Such change in the temperature and pressure in a closed system enables morphology tuning of the TiO_2 nano-particles. In addition, previous work demonstrated that smaller particle size of TiO_2 is achievable using higher sonication power, due to the formation of shockwaves via sonochemical method (Hassanjani-Roshan, Kazemzadeh, Vaezi, & Shokuhfar, 2011). The condition created by the energetic collapse of gas vacuoles leads to the hemolytic bond breakage of solvent (i.e H_2O) and forms radicals (H^+, OH^-), and thus may lead to different reaction pathways and mechanism.

TiO$_2$ prepared using sol-gel and sol-gel with sonochemical method was also studied (Choi, Cho, Kim, & Lee, 2011). Involving the sonochemical step did not induce any change in the crystal phase, but reduces the particle size from 20 nm to 10nm. The larger surface area of the latter elevated the photocatalytic degradation activity by a minimal increase of 28.7 % only.

The formation of brookite crystal phase was observed for the preparation of TiO_2 using surfactant-assisted sonochemical method (Yu, Zhang, & Yu, 2002). It was also observed that the ratio of brookite in TiO_2 increased under ultrasonic influence, but in the absence of a surfactant, the ordered mesostructure of the catalyst deteriorated. The particle size and surface area of TiO_2 prepared using surfactant-assisted sonochemical method reduced and increased respectively, relative to the commercial Degussa P25 sample. Although sonochemical method enables fine tuning of TiO_2 particle size, the temperature of the sonicator during the synthesis step requires close monitoring as any

change in the temperature as a result of gas cavitation might change the physical and chemical behavior of the chemical reaction and photocatalyst properties.

2.7.8 Microwave

Microwave assisted method is a rapid synthesis technique with high productivity via homogeneous heating and requires less stringent process conditions, relative to other conventional synthesis methods which requires complex chemical mixtures and longer reaction time (Wang et al., 2015). Microwaves are a form of electromagnetic radiation, with principal frequencies of microwave heating between 900 to 2450 MHz (Wang et al., 2014). The low production cost, coupled with high energy conversion efficiency results to greater interests in using microwave assisted method for dye-sensitized solar cells application, in order to subside the conventional silicon-based solar cells (Hong-en Wang et al., 2011). The microwave method can be used together with hydrothermal and solvothermal process by inducing localized and uniform heating in the autoclave, rather than heat being transferred from the autoclave wall to the liquid mixture which requires longer process duration.

Nano-crystalline TiO_2 was prepared via microwave hydrothermal method using urea (precipitating agent) and titanium (IV) chloride, $TiCl_4$ which was diluted with ice-cold distilled water to form $TiOCl_2$ (Murugan, Samuel, & Ravi, 2006). The mixture was hydrothermally heated in a Teflon-lines autoclave and uniform direct solution heating was achieved using microwave digestion system for 2 to 6 min. The obtained TiO_2 contained 90 % of anatase crystal phase, which simply illustrates the efficiency of microwave hydrothermal method in producing anatase TiO_2 within a short time. The rapid crystal growth observed was attributed to the localized high temperature induced by the microwave radiation. The synthesized TiO_2 were observed to be agglomerated, as evidenced by the TEM image.

Anatase TiO$_2$ photo-anodes was prepared using thiobenzoate complex of titanium in two different solvent, benzyl alcohol and ethanol which was exposed to microwave irradiation for 10 to 30 min (Dar, Chandiran, Grätzel, Nazeeruddin, & Shivashankar, 2014). Both TiO$_2$ samples displayed pure tetragonal anatase phase, which is highly suitable for solar cells application. However, both samples demonstrated lower photon to current efficiency, and is attributed to the aggregation of small particle size and reduced surface area.

Rao and Rajendar (2015) used room-temperature ionic liquid to synthesize TiO$_2$ nanoparticles by microwave methods. Agglomeration of hexagonal pure anatase TiO$_2$ was obtained with an average particle size of 23 nm. Although rapid processing time is achieved via microwave assisted method, the major drawback is the uncontrolled particle agglomeration in most cases which reduces the exposed surface area, particularly for absorbing dyes used in dye-sensitized solar cells application.

2.7.9 Anodic oxidation

Anodic oxidation, or also called anodization is widely used to fabricate *in situ* nanotubes for various anodizing metals such as titanium (Ti), aluminum (Al), zirconium (Zr) and niobium (Nb) via electrochemical conversion that forms an oxide film or foil (Wang et al., 2014). Contrary to nanotubes constructed via hydrothermal method, the preparation of nanotubes by anodization was reported to be more uniform, highly ordered and vertically oriented (Gong et al., 2001). In a typical electrochemical cell, anodizing metals are used as the anodes and undergo oxidation process to form metal oxides in a fluoride-based electrolyte such as hydrofluoric acid (HF) and sodium fluorine (NaF). Platinum (Pt), silver (Ag) or graphite (crystalline C) is usually used as the electrons receiver (cathode) at a potential between 10 to 25 V (Varghese, Mor, Grimes, Paulose, & Mukherjee, 2004). The shape and dimension of the nanotubes can be controlled by adjusting the pH (using organic or inorganic acids), electrolyte, voltage

and bath temperature (Su & Zhou, 2011). Anodization process using polar organic electrolytes and operating at high pH results to low dissolution chemical rate, and thus yields longer nanotubes arrays (Yang, Luo, Cai, & Yao, 2010).

A two steps anodization method was used to fabricate highly ordered TiO_2 nanotubes by using Ti foil and graphite as anode and cathode respectively and ethylene glycol and aqueous ammonium fluoride, NH_4F as the electrolyte (Li, Zhang, Guo, Yu, & Zhang, 2009). In the first step, Ti foil was anodized, and the layer of formed nanotubes was then removed by ultrasonification to expose the glossy underlying Ti surface. The second step involves anodizing at similar conditions to grow well aligned nanotubes, using the imprints nanotubes patterns from earlier step. By varying the anodizing voltage, two sets of TiO_2 nanostructures were observed which were classified as lotus-root shaped and bamboo shaped nanotubes. Similar observation was also observed in previous work, whereby anodizing voltage at 20 V governs well aligned nanotubes and non-uniform nanotubes with varied wall thickness at 30 V (Sreekantan, Hazan, & Lockman, 2009).

2.7.10 Electrodeposition

Electrodeposition, similarly to electroplating or electrophoretic deposition utilizes an electric field to deposits migrated ions in a solution onto an electrode (Wang et al., 2014). Typically, a solution containing metal salts is immersed in an electrolyte where the metallic ions are reduced and deposited at the cathode. This method is simple, easily controlled and enables the formation of homogeneous coating (Hanaor, Michelazzi, Leonelli, & Sorrell, 2012). For scale-up of transparent TiO_2 thin film for industrial use, electrodeposition method is preferred relative to chemical vapor deposition method as this method allows larger surface area coverage of substrate (Karuppuchamy, Andou, & Endo, 2012).

A three electrodes system containing an aqueous solution of 0.1 M $K_2[TiO(C_2O_4)_2]$ and 1 M Hydroxylamine at pH 8 (adjusted by using KOH) was used in the preparation of TiO_2 thin film using potential range from -1.0 V to -1.2 V (vs. Ag/AgCl). The working electrode includes ITO-coated glass, platinum foil as the counter electrode and Ag/AgCl as the reference electrode. The electrodeposited film was further calcined in air to enhance the crystallinity of TiO_2 thin film (Karuppuchamy et al., 2012).

The electrodeposition of TiO_2 nanoparticles on multiwalled carbon nanotube (working electrode) using platinum and Ag/AgCl as the counter and reference electrode respectively, was employed with a working potential of -0.1 V (vs. Ag/AgCl) and 30 min deposition time. The electrolyte contained 3 M KCl solution with hydrogen peroxide and 10 mmol/L Ti $(SO_4)_2$ (Jiang & Zhang, 2009).

The combination of electrodeposition and anodic aluminum oxide (AAO) templating method showed highly ordered TiO_2 nanotube arrays consisted of pure anatase crystal phase, with uniform length and wall thickness (Wang, Song, Liu, Yao, & Zhang, 2013). In this work, the electrodeposition was conducted at 25 °C, using platinum as the counter electrode in a three electrodes system and potential range from 0.8 to 1.0 V (vs. Ag/AgCl). The electrolyte was composed of 0.1 M $TiCl_3$ in deionized water, and the pH is maintained at 2 using sodium carbonate. AAO was used as the working electrode with one side of the electrode sputtered with a layer of Au film.

Among all of the preparation methods, sol-gel method is a widely employed technique as it can be conducted at relatively low temperature with simple equipment setup. Furthermore, the properties of the photocatalyst can be easily tuned by modifying the reaction parameters such as pH, solvent, temperature and duration during the synthesis process. Sol-gel method also allows efficient control of the photocatalyst purity, homogeneity and composition.

2.8 Application of TiO₂ for water treatment

The photocatalytic degradation of toxic wastes in contaminated water has been intensively studied using various forms of TiO_2 which includes nanopowders, nanotubes and TiO_2 deposited as thin films (Wang et al., 2014). Removing toxic substances in contaminated water by photocatalytic degradation increases water reusability and environmental sustainability, particularly towards aquatic species. Furthermore, the removal of harmful materials in drinking water sources enables safe consumption. The advantage of using TiO_2 is that the photodegradation process generally leads to the formation of harmless minerals, CO_2 and H_2O (Gaya, 2014). TiO_2 is highly effective in degrading organic pollutants such as dye, persistence organic pollutants and pesticides (Carp et al., 2004). The applications of TiO_2 are further elaborated in section 2.8.1.

There are many parameters which affect the photocatalytic degradation activity in an aqueous system which includes type of photocatalyst, initial pollutant concentration, catalyst loading, medium pH, dissolved and aerated oxygen concentration, Fenton reagents, light intensity and wavelength and spectators component (impurities). Optimization of these degradation parameters has been taken into account for various photodegradation studies in order to design an effective and sustainable treatment processes (Ahmed, Rasul, Martens, Brown, & Hashib, 2010). For the photocatalytic degradation of dyes, high initial dye concentration limits the formation of ·OH radicals on the catalyst surface. This is due to the adhesion of larger quantity of dyes covering the active sites of the catalyst and reduces the formation of radicals from the oxidation of absorbed surface hydroxyls. The path length for photons to diffuse through the dyes molecules and reaching the catalyst surface for photo-excitation also decreased, whereby in low concentration, the effect is reversed (Neppolian, Choi, & Sakthivel, 2002).

The classic toxic substances in contaminated water are categorized into manufacturing and processing plants, and also agriculture industries (Bhatkhande, Pangarkar, & Beenackers, 2002). The wastes commonly detected in wastewater from the manufacturing and processing plants includes heavy metals, formaldehyde (dyes), nitrobenzene, phenols, polychlorinated biphenyl (PCBs) and polycyclic aromatics hydrocarbon (PAHs). Contaminants coming from the agriculture industries include organophosphorus pesticides and atrazine. The chemicals used in the agriculture industries particularly those with direct contact with soil, have been reported to percolate through soil and contaminate nearby water bodies and drinking water wells (Aktar, Sengupta, & Ashim, 2009).

Pesticides are one of the largest source of toxic water pollutants (Harris & McCartor, 2011). These claims were based on the estimated number of people affected by the pollutant and globally identified polluted sites, where the concentration of pollutants had exceeded the water regulation standards. In addition, textile dyes are also reported as one of the largest sources of water pollutant, whereby the disposed dyes into the water bodies (river, sea) are not ready biodegradable (Arora, 2014).

2.8.1 Photocatalytic degradation of textile dyes

At present, it is estimated that more than 100,000 different dyes and pigments are available commercially (azo dyes represents about 70 % on weight basis). The production rate of dyes per year is over 1 million tons which composed of 50 % textile dyes whereby 20 % of the produced dyes are discharged into nearly water bodies as it is difficult to remove dyes completely from the waste streams by conventional wastewater treatment (Arora, 2014). Dyes', having high stability towards biodegradation becomes a threat to the ecological system and leads to poor aesthetic condition.

The photocatalytic degradation of dyes has been employed as an alternative method to clean up dye containing polluted water (Bhatkhande et al., 2002). This strategy

differs from the time consuming biological method such as microbial degradation, adsorption by microbial biomass, dye decolorization and bioremediation. In a photocatalytic degradation of dye, the pollutant is rapidly destroyed with the aid of UV or solar light irradiation.

As dyes are present in the form of anionic and cationic, the isoelectric point (IEP) of the photocatalyst plays an important factor which influences the overall photocatalytic activity. For most TiO_2 photocatalyst, the reported IEP is approximately at pH 6.4 (Stewart, 2009). Thus the absorption onto TiO_2 surface for anionic (negatively charged) and cationic (positively charged) dyes is favored at acidic and alkaline environment respectively.

The applications of bare and modified TiO_2 towards the photocatalytic degradation of the dyes pollutant are shown in Table 2.3.

Table 2.3: Using TiO$_2$ for the removal of dyes in contaminated water

Photocatalyst	Extrinsic modification	Model pollutant	Experiment setup	Major observation	Reference
Commercial Degussa P25	None	Reactive blue 4	Pollutant concentration = 1 x 10^{-4} to 5 x 10^{-4} M Catalyst dosage = 2 g/l Light source = Solar light	• ~ 98 % dye removal at 1 x 10^{-4} M dye concentration in 24 h • ~ 32 % dye removal at 5 x 10^{-4} M dye concentration in 24 h • Reactive blue 4 molecules were degraded to CO$_2$, SO$_2^{-4}$, NO$_3^-$, NH$_4^+$ and H$_2$O • Follows first order kinetics	(Neppolian et al., 2002)
Light yellow N doped TiO$_2$ nanopowders	Anionic dopant (Nitrogen, N)	Acid orange 7 (AO7) Procion red MX-5B (MX5B) Reactive black 5 (RB5)	Pollutant concentration = 0.03 mM (all dyes) Catalyst dosage = 10 mg/l Light source = Direct solar light (low intensity light source, with an average 120 W/m^2)	• Using un-calcined N-doped TiO$_2$ results to 53 % AO7, MX5B and RB5 dye removal in 30 min and complete decolorization in 240 min • Using calcined N-doped TiO$_2$ results to 70 % AO7, MX5B and RB5 dye removal in 60 min and complete decolorization in 180 min • All dyes showed only 8 % in TOC reduction in 60 min, and rapidly increased to 60 % within 120 min • Slow TOC reduction was attributed to the transformation of smaller organic intermediates such as phenols, aldehydes and acetic acids • All dyes did not act as electron injector to TiO$_2$ as the position of HUMO LUMO is within the band gap of N-doped TiO$_2$ • Follows first order reaction	(Liu, Chen, Li, & Burda, 2005)

Table 2.3: (Continued)

Photocatalyst	Extrinsic modification	Model pollutant	Experiment setup	Major observation	Reference
N,S co-doped TiO_2 nanopowder	Anionic mono-doping (Sulphur, S) and Anionic co-doping (Nitrogen, N and Sulphur, S)	Methyl orange (MO)	Pollutant concentration = 10 mg/l Catalyst dosage = 0.1 g/l Light source = 18W low-pressure Hg lamp as UV-light and sunlight as UV-Vis light source	• N,S co-doped TiO_2 showed best activity under both UV and visible light, followed by mono doped S-TiO_2 and least activity by un-doped TiO_2 • Almost complete color removal and dye mineralization is observed in 120 min (UV light) and 720 min (vis light) for N,S co-doped TiO_2 • The presence of doped S in TiO_2 as chemisorbed SO_4^{2-} increased the surface acidity and acts as Bronsted acidic sites and Lewis acid sites; enhanced oxygen and dye absorption • The presence of doped N triggered surface oxygen vacancies and visible light absorption • The synergy between N and S enhanced the photocatalytic activity of 10 mg/l methylene orange dye	(Wei, Ni, & Cui, 2008)
Commercial TiO_2 anatase	None	Direct yellow 9	Pollutant concentration = 80 μmol/l Catalyst dosage = 1.5 g/l Light source = Solar Light (300–800nm with intensity 500 W/m^2) pH = 2, 7 and 10	• Complete dye mineralization in 120 min • Degradation rate decreased from 0.0282/min to 0.0183/min from pH 2 to pH 10	(Regulska, Małgorzata Bruś, & Karpińska, 2013)

Table 2.3: (Continued)

Photocatalyst	Extrinsic modification	Model pollutant	Experiment setup	Major observation	Reference
Ag-deposited TiO$_2$ nanopowder	Metal deposition (Silver, Ag at 1% molar ratio)	Methylene blue (MB)	Pollutant concentration = 25 to 100 mg/l Catalyst dosage = 0.5 to 1.5 g/l Light source = 15 W UV lamp (254 nm) pH = 5, 7 and 9	• Based on response surface methodology result, the optimum values of the three independent variables were catalyst loading of 0.99 g/l, dye concentration of 57.68 mg/l and pH of 7.76 • The optimum condition is expected to decolorized and mineralized methylene blue dye at 95.7 % in 120 min	(Sahoo & Gupta, 2012)
Surface disordered TiO$_2$ nanopowder	Hydrogenation	Methylene blue (MB)	Pollutant concentration = n/a Catalyst dosage = 0.5 g/l Light source = 18W visible light with wavelength > 400 nm	• Anatase to rutile ratio of 0.67 showed 15 times higher photocatalytic activity under the visible light, relative to non-hydrogenated Degussa P25 catalyst • Complete dye mineralization in 75 min using hydrogenated TiO$_2$ • High activity in hydrogenated TiO$_2$ is attributed to the narrowing of band gap (to ~ 2.8 eV) and efficient electrons and holes separation • Follows first order reaction	(Ramchiary & Samdarshi, 2014)
Black TiO$_2$ nanopowder	Hydrogenation	Rhodamine B (RhB)	Pollutant concentration = 2 mg/l Catalyst dosage = 0.2 g/l Light source = 50 W simulated solar light	• Hydrogenated TiO$_2$ showed better activity than commercial Degussa P25 • Complete dye mineralization in 50 min using hydrogenated TiO$_2$ • High activity is attributed to the formation of oxygen vacancies, Ti-H surfaces as absorption sites and narrowing of band gap (to ~2.8 eV)	(Teng et al., 2014)

2.8.2 Photocatalytic degradation of pesticides

Pesticides can be categorized into different types based on its mode of action. Approximately 1 to 2.5 million tons of pesticides are mainly used in the agriculture sector, where 40 % are herbicides and the remaining 60 % are insecticides and fungicides (Fenner, Canonica, Wackett, & Elsner, 2013). The accumulations of these chemicals are a potential threat to the aquatic system as the natural degradation process of biotic (via selective microorganism) and abiotic (via chemical reaction) in the environment faces some constraint (Mc Murray, Dunlop, & Byrne, 2006). A potential threat, for example, is monocrotophos which is a widely used insecticides and is categorized as an endocrine disrupting chemical and pose threats to the reproduction of humans and animals (Avasarala, Tirukkovalluri, & Bojja, 2011).

The photocatalytic degradation of pesticides using TiO_2, particularly triazine herbicides are widely employed in many research studies (Konstantinou & Albanis, 2003). Generally, the photocatalytic degradation of organic pollutants results to the formation of CO_2 and H_2O (Gaya & Abdullah, 2008). However, in the case of triazine herbicides, total mineralization does not occur and cyanuric acid is observed as a non-toxic, end-product (Mc Murray et al., 2006). Similar to insecticides such as acephate and dimethoate, the photocatalytic degradation using TiO_2 leads to the release of SO_4^{2-} and NO_3^- as inorganic intermediates, while glyphosate insecticides liberates NO_3^- and PO_4^{3-} (Echavia, Matzusawa, & Negishi, 2009).

The applications of bare and modified TiO_2 towards the photocatalytic degradation of the pesticides pollutants are shown in Table 2.4.

Table 2.4: Using TiO_2 for the removal of pesticides in contaminated water

Photocatalyst	Extrinsic modification	Model pollutant	Experiment setup	Major observation	Reference
TiO_2 Degussa P25	None	Herbicides (Atrazine, Simazine, Triethazine, Prometon, Prometryn)	Pollutant concentration = Atrazine, 25 mg/l Simazine, 3 mg/l Triethazine, 15 mg/l Prometon, 25 mg/l Prometryn, 25 mg/l Catalyst dosage = 0.5 g/l Light source = 1500 W xenon lamp	• Atrazine and other s-triazine herbicides are completely removed in 20 min • Organic carbon (TOC) was still observed after 900 min for all degraded pollutant; thus showed incomplete mineralization • Formation of cyanuric acid as the stable end-product of atrazine and other s-triazine pollutants	(Pelizzeti et al., 1990)
TiO_2 – Polyvinyl alcohol (PVA) polymer composite	Polymer composite	Fungicides (Thiram)	Pollutant concentration = 1×10^{-4} to 5×10^{-4} mol/l Catalyst dosage = 100 mg immobilized on PVA Light source = 125 W high pressure Hg lamp (UV light) and 50 W halogen lamp (visible light) Others = air (source of oxygen) aeration throughout the experiment	• Under UV light irradiation, Thiram was degraded by 47% • Under visible light irradiation, Thiram was degraded by 0.3 % • Thiram is completely removed in 150 min • Adsorption study confirmed no presence of adsorbed Thiram on TiO2-PVA composite • The photocatalytic degradation rate constant decreased at higher initial pollutant concentration • Thiram is completely removed in 150 min • The degradation end-products includes CO_2, NO_3^- and SO_4^{2-} • Follows first order rate reaction	(Thakare & Bhave, 2005)

Table 2.4: (Continued)

Photocatalyst	Extrinsic modification	Model pollutant	Experiment setup	Major observation	Reference
TiO$_2$ (Degussa P25)-indium doped tin oxide (ITO) thin film	None	Herbicides (Atrazine)	Pollutant concentration = 20 mg/l Catalyst dosage = 1.60 to 0.19 mg/cm^2 Light source = 9W UV-A fluorescent lamp or 9W UV-B fluorescent lamp	• 20 mg/l of atrazine is completely removed in 200 min in the presence of air or oxygen • Organic carbon (TOC) was still observed at the end of 200 min, thus atrazine is not completely mineralized • Formation of cyanuric acid as the stable end-product of atrazine mineralization • Optimum catalyst loading was at 1.1 mg/cm^2	(Mc Murray et al., 2006)
TiO$_2$ immobilized on silica gel	None	Insecticide (Acephate, dimethoate, glyphosate)	Pollutant concentration = Acephate, 0.1 mM Dimethoate, 0.1 mM Glyphosate, 0.1 mM Catalyst dosage = 14.0 g in spiral glass tube Light source = 6 W black light fluorescent UV lamp Others = Oxygen aeration at 100 ml/min	• 100 % acephate and dimethoate removal at 105 min and 60 min, respectively was achieved by photocatalytic reaction • 100 % glyphosate removal at 60 min was achieved by adsorption and photocatalytic reaction • Incomplete mineralization after 120 min, showing 69 %, 86 % and 52% TOC reduction for acephate, dimethoate and glyphosate • For dimethoate, released of NO$_2^-$ as an intermediate of NO$_3^-$ was observed • Toxic intermediates such as methamidophos and omethoate were not present • Follows first order reaction	(Echavia et al., 2009)

Table 2.4: (Continued)

Photocatalyst	Extrinsic modification	Model pollutant	Experiment setup	Major observation	Reference
Mg-doped TiO_2 nanopowder	Cationic doping using alkaline earth metal (Magnesium, Mg at 1 wt%)	Insecticide (mono crotophos, MCP)	Pollutant concentration = 15.0 to 90.0 mM Catalyst dosage = 0.1 to 1.1 g/l Light source = 400 W visible light using UV filtered high pressure Hg vapor lamp pH = 3 to 8	• For the photocatalytic degradation of MCP, the optimum conditions are at catalyst loading (0.5 g/l), initial pollutant concentration (50.0 mM) and at pH 3 • Released of PO_4^{3-} as final degradation product • The rate of formation of PO_4^{3-} in the solutions is used to express the rate of MCP degradation	(Avasarala, Tirukkovalluri, & Bojja, 2016)
TiO_2 nanopowder	None	Herbicides (Atrazine)	Pollutant concentration = 5 mg/l Catalyst dosage = 0.2 g/l Light source = UV light (302 nm)	• Photolysis of atrazine was not observed • 70.6 % atrazine removal in 240 min • Formation of atrazine intermediates was not emphasized	(Ruslimie et al., 2011)
N,S co-doped TiO_2 nanowires	Anionic co-doping (Nitrogen, N and Sulphur, S)	Herbicides (Atrazine)	Pollutant concentration = 5 mg/l Catalyst dosage = 1 g/l Light source = 15 W fluorescent lamp with UV block filter of 420 nm	• 63 % of atrazine mineralization in 360 min • Degradation of atrazine was mainly driven by ·OH radicals and VB holes • Visible light activity was driven by band gap narrowing due to N and S co-doping • High reusability rate of 5 cycles • Follows first order reaction	(Zhang, Wu, & Liu, 2014)

Photocatalyst	Extrinsic modification	Model pollutant	Experiment setup	Major observation	Reference
Degussa P25 TiO$_2$ modified with metallic nanoparticles	Co-catalyst (Gold, Au; Copper, Cu and Nickel, Ni)	Herbicides (Atrazine)	Pollutant concentration = 25 mg/l Catalyst dosage = 1 g/l Light source = 2 W low power UV lamp Others = Air aeration at 100 ml/min	• 48 % atrazine mineralization using bare Degussa P25 in 300 min • More than 60 % atrazine mineralization using Au-deposited TiO$_2$ (most active catalyst) in 300 min • Au remained as metallic state, but Cu and Ni was oxidized during the photocatalytic activity	(Santacruz-Chavez, Oros-Ruiz, Prado, & Zanella, 2015)
TiO$_2$ nanopowder	Cationic doping with transition metal (Iron, Fe) Non-metal doping with (Silicon, Si)	Fungicides (Carbendazim)	Pollutant concentration = 8 mg/l Catalyst dosage = 0.5 to 2.0 g/l Light source = 20W UV black florescent lamps and sunlight Doped Fe = 1 wt% to 4 wt% Doped Si = 3 wt%, 7 wt%, 9 wt%	• Optimum concentration of dopants which showed maximum degradation of carbendazim is at 2 wt % for Fe-doped TiO$_2$ and 5 wt % for Si-doped TiO$_2$ • Fe-doping significantly improve the catalytic activity under visible light with an optimal catalyst dosage of 1 g/l • Above the optimal catalyst dosage, a decreased in the degradation rate was observed • This is attributed to the effect of light scattering by the increased of suspension opacity, and thus reduced number of available active sites • The maximum degradation for carbendazim under sunlight irradiation is 98 % for both Fe-doped and Si-doped TiO$_2$	(Kaur, Sraw, Wanchoo, & Toor, 2016)

2.8.2.1 Photocatalytic degradation pathway of atrazine pollutant

For the photocatalytic degradation of atrazine, the pollutant is degraded into non-hazardous cyanuric acid. Atrazine degradation pathway is illustrated in Figure 2.5 (Konstantinou, Sakellarides, Sakkas, & Albanis, 2001; Mc Murray et al., 2006; Parra, Elena Stanca, Guasaquillo, & Ravindranathan Thampi, 2004; Pelizzeti et al., 1990; Zahraa et al., 2003). The photocatalytic degradation of atrazine was investigated with the addition of oxidants (peroxymonosulfate and persulfate) under simulated solar light using N,F-TiO$_2$ film (Andersen et al., 2013). The result showed synergic effects by combining the photocatalytic films with oxidants by producing higher concentrations of radicals and increased degradation rate. The intermediate degradation products of atrazine were observed, but no detection of cyanuric acid. This could be due to the limited surface area of N,F-TiO$_2$ films to generate sufficient electron/hole pairs for photo-oxidation of atrazine molecules and limited contact area between the catalyst and pollutant. It has been found that complete mineralization of atrazine was seldom achieved and a stable end by-product, cyanuric acid, was often observed (Konstantinou et al., 2001; Mc Murray et al., 2006; Minero, Pelizzetti, Malato, & Blanc, 1996; Parra et al., 2002; Pelizzeti et al., 1990; Ruslimie et al., 2011). However, complete mineralization of atrazine was observed by the addition of fluoride ions to a TiO$_2$ suspension (Oh & Jenks, 2004). The interpretation of the effect, in agreement with previous works was the formation of homogeneous phase hydroxyl radicals (Minero et al., 1996). On TiO$_2$/F, but in the pH range 2-6, the reaction occurs almost entirely via homogeneous hydroxyl radicals due to the unavailability of surface-bound hydroxyl in the presence of fluoride ions. The reaction is related to hydroxyl radicals formed in homogeneous phase due to leached F$^-$ ions.

There are numerous methods of preparing and modifying TiO$_2$ to increase the photocatalytic activity. Based on literature survey, there is no report on the synergistic

effect of anion dopant and hydrogenation for photocatalytic degradation of atrazine. In this study, the synergistic effect of anion dopant and hydrogenation will enhance the photodegradation of atrazine because of improved physical and chemical properties such as morphology, crystal structure, charge carriers mobility, surface defects, electronic band structure and optical response. As a result, hydrogenated anion-doped TiO$_2$ photocatalyst could serve as a new potential photocatalyst and supports the photocatalytic industry for the abatement of atrazine.
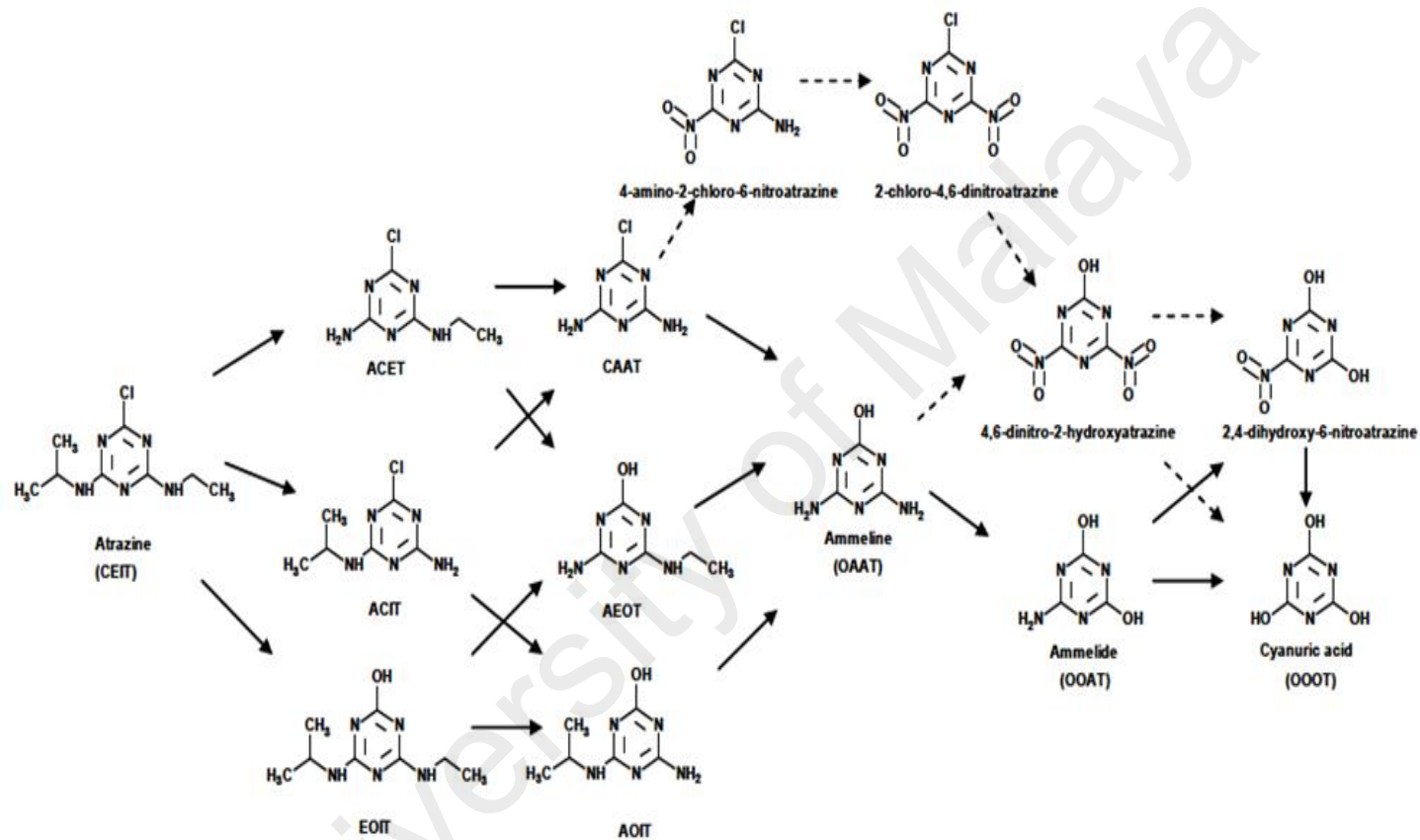
Figure 2.5: Atrazine degradation pathway using TiO$_2$ photocatalyst
(López-Muñoz, Aguado, & Revilla, 2011)

CHAPTER 3: METHODOLOGY

3.1 Research design

In this study, TiO_2 photocatalysts were prepared via sol-gel method in the presence and absence of non-ionic surfactant. Subsequently, the surfactant based- TiO_2 photocatalysts were modified by mono-doping and dual-doping using nitrogen (N) and fluorine (F) precursor. The surfactant-based un-doped and anion-doped TiO_2 were subjected to hydrogenation process to produce hydrogenated photocatalysts. The physical and chemical properties of prepared photocatalysts powder were characterized using FESEM, EDX, HR-TEM, BET, XRD, FTIR, Raman, PL, DRUV-Vis, Zeta Potential, TGA, DSC and XPS. The photocatalytic activity was also evaluated under solar light using atrazine herbicides as the model water pollutant. An overview of the work flowchart is displayed in Figure 3.1.
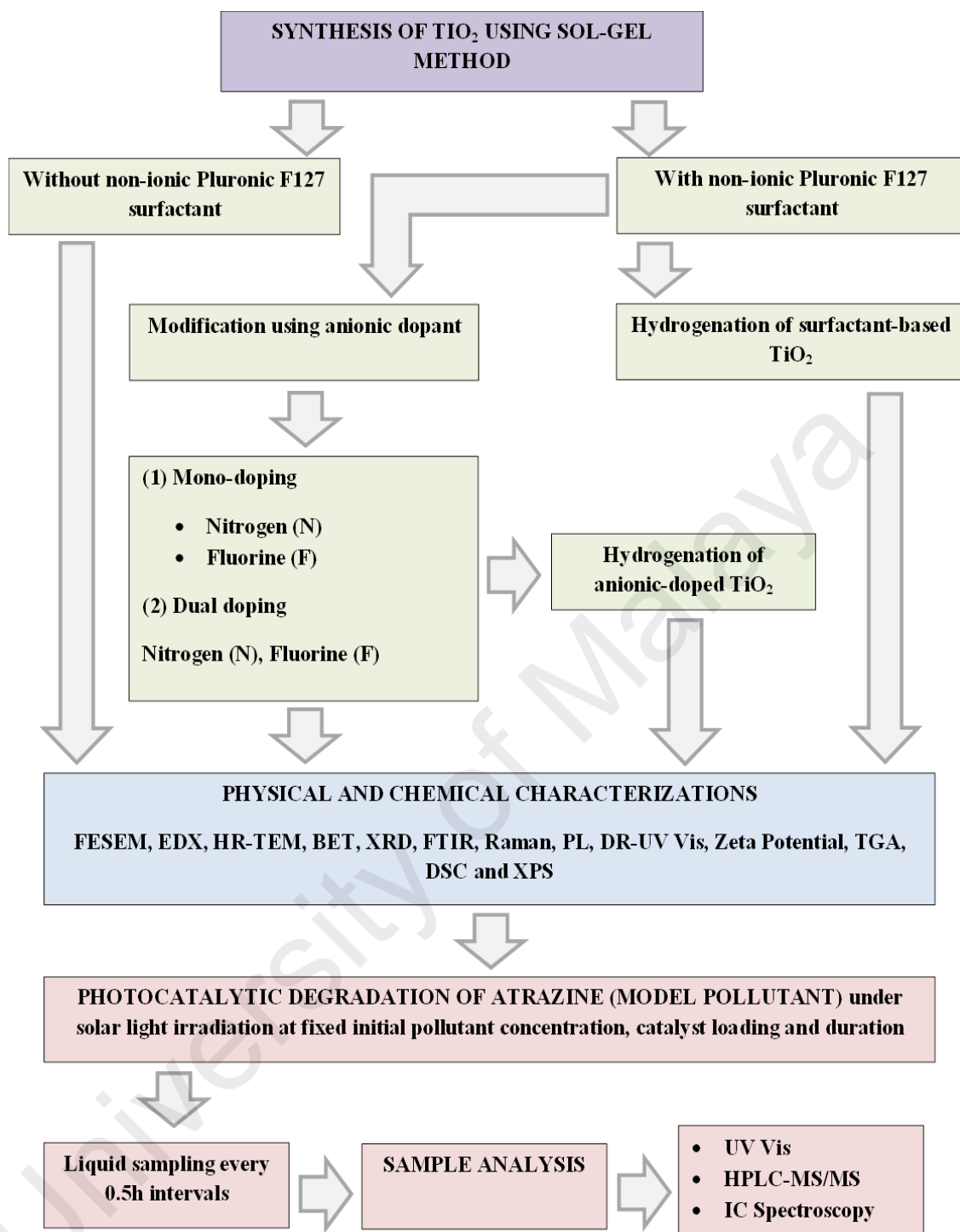
Figure 3.1: Overview of the research methodology

3.2 Materials

All the chemicals used were purchased from Sigma Aldrich without further pre-treatment. Titanium isopropoxide (TTIP, 97 %), concentrated hydrochloric acid (37 %), ethanol (95 %), absolute ethanol (99 %) and non-ionic surfactant pluronic F127 were used in the catalyst synthesis step. The source of nitrogen and fluorine precursors was triethylamine (98 %), trifluoroacetic acid (99 %) and ammonium fluoride (98 %). Pure hydrogen gas (99.99 % purity) was purchased from Linde Sdn Bhd. Atrazine (98%) was used as a pollutant model to evaluate the photocatalytic degradation activity. Milli-Q deionized water was used throughout the experimental work.

3.3 Preparation of TiO$_2$ photocatalysts

The importance of precursor and chemicals point of introduction during the sol-gel significantly influenced the final crystallinity and crystal structure of TiO$_2$, and thus careful consistencies was taken during the synthesis steps. Nine types of modified TiO$_2$ photocatalyts were prepared using the molar ratio in Table 3.1 and the flowchart is illustrated in Figure 3.2.

Table 3.1: Molar ratio of prepared photocatalysts

Titanium Isopropoxide (TTIP)	Pluronic F127 surfactant	Hydrochloric acid (HCl)	Absolute ethanol	Deionized water
1.0	0.005	0.5	15	40

The calculated amount of chemicals required is displayed in Table 3.2. In section 3.3.1, the preparation steps for non-ionic surfactant-based TiO$_2$ are described followed by section 3.3.2, for anionic doping of TiO$_2$. The remaining two sections, 3.3.3 and 3.3.4 described the preparation method for hydrogenated TiO$_2$ and hydrogenated anion-doped TiO$_2$ respectively.
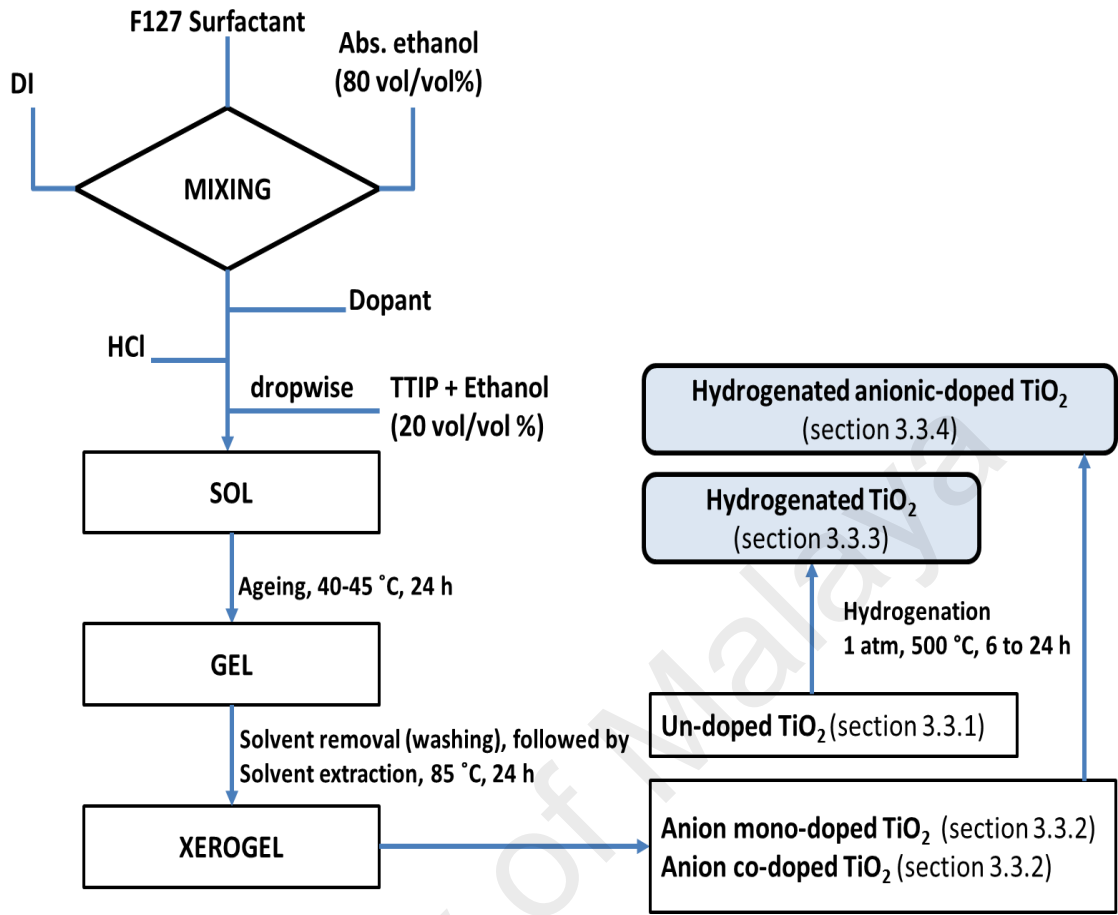
Figure 3.2: Preparation of photocatalysts

Table 3.2: Amount of chemicals required using the molar ratio in Table 3.1 for the preparation of photocatalysts

Chemicals	TiO$_2$ (without surfactant)	TiO$_2$ (with surfactant)	N-doped TiO$_2$		F-doped TiO$_2$		N,F co-dopedTiO$_2$	
TTIP	10.31 ml							
EtOH	81.83 ml							
Pluronic F127		2.21 g						
HCl (37%)	Adjusted to obtain pH 3.5±0.2 (Appendix A)							
DI water	8.00 ml							
Triethylamine (99%)			0.5	2.47 ml				
			1.0	4.93 ml				
			1.5	7.40 ml				
			2.0	9.86 ml				
			2.5	12.33 ml				
Trifluoroacetic acid (98%)					0.5	1.36 ml		
					1.0	2.71 ml		
					1.5	4.06 ml		
					2.0	5.42 ml		
					2.5	6.84 ml		
Ammonium fluoride (98%)							0.5	0.66 g
							1.0	1.32 g
							1.5	1.98 g
							2.0	2.65 g
							2.5	3.31 g

59

3.3.1 Surfactant-modified TiO$_2$

Two types of mixtures were prepared; Mixture A & B. Mixture A consisted of 16.34 ml (20 vol/ vol %) of total absolute ethanol and deionized water. The pH of mixture A was maintained at 3.5±0.2 by using HCl. Mixture B consisted of 65.59 ml (80 vol/ vol %) of total absolute ethanol and was premixed with TTIP precursor for 5 min. Subsequently, mixture B was added drop-wised into mixture A and sol was formed. The sol was aged at 45 °C overnight to form a cloudy white gel. The gel was washed several times using deionized water and then followed by ethanol (95 %). The samples were dried at 85 °C for 24 h and subsequently grinded into fine powder form. To obtain nano-crystalline TiO$_2$, the samples were calcined under continuous air flow at 500 °C for 6h. The air flow-rate and heating rate were set at 16 ml/min and 0.5 °C/min. For surfactant-based TiO$_2$, pluronic F127 powder was added into mixture A and was stirred vigorously for 5 min until pluronic F127 powders were dissolved. The addition of pluronic F127 does not temper the final pH of the solution and thus similar pH of 3.5±0.2 was applied using HCl. Subsequently, similar ageing, washing, drying and calcination process were repeated.

3.3.2 Anion-doped TiO$_2$

The initial molar ratios of anion precursors were 0.5, 1.0, 1.5, 2.0 and 2.5. For the preparation of anion doped TiO$_2$, the source of precursor was added into mixture A. Mixture A consisted of 16.34 ml (20 vol/ vol %) of total absolute ethanol and deionized water. The pH was then adjusted to 3.5±0.2. Mixture B consisted of 65.59 ml (80 vol/vol %) of total absolute ethanol and was premixed with TTIP precursor for 5 min. Mixture B was added drop-wised into mixture A and sol was formed. Prior to 24 h ageing process at 45 °C, the gel was washed, dried and calcined using the same procedure mentioned in section 3.3.1. The anions include trifluoroacetic acid (fluorine

precursor), triethlyamine (nitrogen precursor) and ammonium fluoride (nitrogen and fluorine precursor).

3.3.3 Hydrogenated TiO$_2$

Surfactant-modified TiO$_2$ was prepared using similar procedures as described in section 3.2.1 and was further subjected to hydrogenation process at atmospheric pressure from room temperature to 500 °C at a heating rate of 10 °C/min. The samples were hydrogenated for 6, 12 and 24 h under continuous flow of pure hydrogen gas at 16 ml/ min. The prepared hydrogenated TiO$_2$ were denoted as H6-TiO$_2$ (6h, hydrogenation), H12-TiO$_2$ (12h, hydrogenation) and H24-TiO$_2$ (24h, hydrogenation).

3.3.4 Hydrogenated anion-doped TiO$_2$

Hydrogenated anion-doped TiO$_2$ was prepared using anion-doped TiO$_2$. The photocatalyst representing F-doped TiO$_2$ was further hydrogenated at atmospheric pressure from room temperature to 500 °C at a heating rate of 10 °C/min. The samples were hydrogenated for 6, 12 and 24 h using continuous flow of pure hydrogen gas at 16 ml/min. The prepared hydrogenated F-doped photocatalysts were denoted as HF6-TiO$_2$ (6 h, hydrogenation), HF12-TiO$_2$ (12 h, hydrogenation) and HF24-TiO$_2$ (24 h, hydrogenation). The photocatalyst representing N-doped TiO$_2$ and N,F co-doped TiO$_2$ were hydrogenated using similar condition for 12 h and were denoted as HN12-TiO$_2$ and HNF12-TiO$_2$ respectively.

3.4 Photocatalytic degradation activity and assessment

3.4.1 Atrazine stock solution

A 5 mg/l stock solution of atrazine was prepared by dissolving 0.0025 g atrazine in 0.5 L of deionized water. The solution was vigorously stirred in darkness for 24 h and stored in a clean amber colored bottle in a cool dry place and away from direct sunlight

or heat. Four different concentrations of atrazine solution at 0.5, 1.0, 1.5 and 2.0 mg/l were prepared by dilution method using 5 mg/l of stock solution (Appendix B). The wavelength and light absorption intensity were verified by using UV Vis.

3.4.2 Photocatalytic reactor setup

The photocatalytic reactor used was a stirred tank photo-reactor (STR) equipped with 100 ml pyrex tubes and a circulating water bath to maintain the temperature during reaction. Two sources of light are used, UV with mercury lamp light (6-20 W, $\lambda < 350$ nm) and solar visible light with xenon arch lamp (150 W, Lux = 10,000, λ from 200 to 1000 nm). In order to evaluate the activity under visible light, the UV portion of the solar light was filtered.
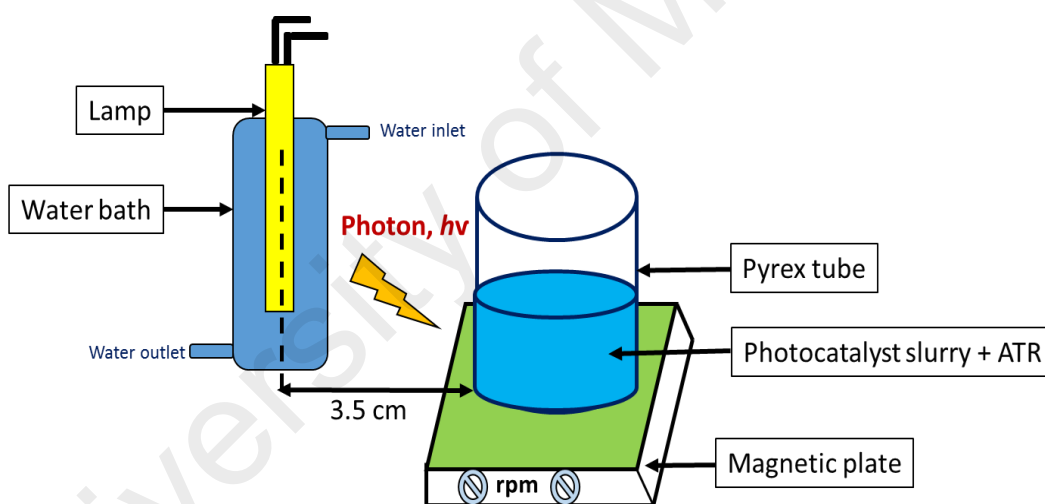
Figure 3.3: Schematic diagram of photocatalytic reactor setup

3.4.3 Photocatalytic degradation activity

To standardize the process parameters for the photocatalytic degradation of atrazine such as catalyst loading and initial atrazine concentration, a preliminary catalytic activity study was initiated. The range of atrazine concentration was from 0.5 to 2.0 mg/l while catalyst loading from 0.1 to 1.5 g/l. In this work, the photodegradation was conducted without additional of strong chemical oxidant such as hydrogen peroxide and the natural pH was used without adjustment throughout the experiments. Thus the

relationships between the photocatalytic activities and photocatalyst properties are well correlated. Initially, the catalyst was stirred in the absence of light to allow optimum atrazine absorption onto the catalyst surface. The results on atrazine removal by simple adsorption on the photocatalysts were verified. In all experiment, the stirring rate was fixed at 400 ± 20 rotation per minute (rpm).

3.4.4 Product analysis

Liquid samples were taken every 0.5 h and analyzed by UV-Vis analyzer (Perkin Elmer, Lambda 35). The maximum wavelength of atrazine was fixed at 222.5 nm with calculated R^2 of 0.9986 (Appendix C). For catalyst reusability test, identical conditions were employed. HPLC-MS was also used to analyze for atrazine and cyanuric acid concentration using Agilent Zorbax column C-18 with two separate mobile phases (Appendix D). For atrazine, the mobile phase used was 66 : 34 % v/v H_2O (DI) : MeCN. The flow rate was fixed at 1.0 ml/min and the wavelength, λ was set at 213 nm. The volume of the sample injected was 20 µl at 20 °C. For cyanuric acid, the mobile phase used was 95 : 5 % v/v NaH_2PO_4: MeOH. The flow rate was fixed at 0.5 ml/min and the wavelength, λ was set at 213 nm. The volume of the sample injected was 20 µl at 20°C. The intermediates products was analyzed using Agilent 6400 Series Triple Quadrupole in positive mode using electrospray ionization (ESI) and Agilent Zorbax StableBond-C18 reversed phase column (4.6 mm ID x 250 mm, 5 µm). The samples were analyzed in full scan mode (1 spectra/s) with flow rate of 0.5 ml/min and runtime of 20 min to determine the MS/MS data. The LC separation method followed isocratic elution using 95 % H_2O (DI) and 5 % MeCN at pH 2.7. Agilent mass hunter workstation (MHW) was used to qualitatively interpret the HPLC-MS/MS spectrum.

For the photocatalytic activity involving F-doped TiO_2, N,F co-doped TiO_2 and hydrogenated F-doped TiO_2, the liquid samples was also analyzed for the presence of F^-

ions as a result of probable leaching from the catalyst using ion chromatograph (IC) spectrometer (APHA 4110B method).

The rate of reaction was determined according to the equation below where k is the order of rate constant (min^{-1}), $[ATR]_t$ and $[ATR]_o$ are atrazine concentration at time t and t=0, respectively.

$$-\frac{d[ATR]}{dt} \equiv \text{ rate} = k\ [ATR] \qquad\qquad \text{Eq. (3.1)}$$

$$\ln\frac{[ATR]_t}{[ATR]_\circ} = -kt \text{ or } \ln[ATR]_t = -kt + \ln[ATR]_o \qquad\qquad \text{Eq. (3.2)}$$

3.5 Characterization of the photocatalysts

In order to understand the physical and chemical characterizations of the prepared photocatalysts, various instruments were used which includes morphology (FESEM, HR-TEM), composition (EDX, CHNS), textural properties (BET), crystal properties (XRD), chemical structure (Raman, FTIR), recombination and defects (PL), surface charge and isoelectric point, IEP (Zeta potential), optical response (DRUV Vis), thermal stability (TGA, DSC) and surface chemical state (XPS). From section 3.5.1 to 3.5.13, the principle and analysis procedures of individual characterizations were discussed.

3.5.1 Field emission scanning electron microscopy (FESEM)

3.5.1.1 Background of FESEM

Field emission scanning microscope (FESEM) analyzed the topographical of a sample with unlimited depths by using high-energy beam of electrons emitted from field emission gun. The exited electrons from the field emission gun are confined into focused monochromatic beam using metal orifice and magnetic lenses. The detectors of

electrons which are placed in the microscope are used to collects signals to generate the sample's image. Different from conventional scanning electron microscope (SEM), FESEM generates vivid images with spatial resolution 3 to 6 times greater.

3.5.1.2 Sample analysis procedure

FESEM Quanta FEI 200F was used to analyze the surface morphology, size and particles distribution. The sample was dispersed in ethanol and sonicated in an ultrasonic bath at room temperature for 2 min to obtain a clear cloudy suspension. One drop was carefully fixed on a carbon tape and was left to dry overnight in a desiccator prior to analysis. Both low (5 kV) and high (10 kV) were employed to give the best resolution. Magnification from 50 k to 200 k was used.

3.5.2 Energy dispersive X-ray (EDX)

3.5.2.1 Background of energy dispersive X-ray (EDX)

Energy dispersive X-ray (EDX) that is incorporated with FESEM instrument is used to determine the elemental composition on the material surface within 500 nm in thickness. EDX is able to distinguish all elements in the order of 0.1 percent and is limited to elements having an atomic number greater than boron. X-rays are generated from the atoms when an electron beams from the FESEM scans across the sample surface. The energy of the individual X-rays is the characteristics of the elements that generate it.

3.5.2.2 Sample analysis procedure

The elemental composition was determined using INCA software. The analysis was conducted per area basis. For EDX, similar sample preparation as FESEM was employed.

3.5.3 Carbon, hydrogen, nitrogen and oxygen (CHNS) analyzer

3.5.3.1 Background of CHNS analyzer

CHNS analyzer is an effective tool to measure the elemental composition of carbon (C), hydrogen (H), nitrogen (N) and sulphur (S) in both organic and inorganic sample by thermal combustion process. Both oxidation and reduction process occurs during the thermal combustion process using oxygen and high purity copper, respectively. For CHNS analyzer, the detection limit is 0.05 wt % (500 ppm).

3.5.3.2 Sample analysis procedure

The weight percent of the elements in the sample was analyzed using CHNS Perkin Elmer, 2400 series II (CHNS mode). Prior to CHNS analysis, the sample was grinded into fine powder and dried in a desiccator overnight. 2 mg of the dried sample was placed in a tin capsule before placing it in the auto sampler. In the reaction chamber, the sample underwent completed combustion at 990 °C under oxygen. The leaving gas then underwent reduction at 500 °C in silica tubes packed with copper granules and then, transported using high purity Helium as the carrier gas to the chromatographic system for analysis.

3.5.4 High resolution transmission electron microscopy (HR-TEM)

3.5.4.1 Background of HR-TEM

High resolution transmission electron microscopy (HR-TEM) is widely used to evaluate the sample crystallinity, crystal size, crystal structure, surface defects and lattice spacing at atomic scale. This instrument utilized both the transmitted and scattered beams to generate an interference image, and can be as small as the unit cell of crystals. This instrument generally consists of more than one condenser lenses to focus the electron beams on the sample, objective lens to form diffraction patterns and

intermediates lenses for image magnification on the screen. Different from conventional TEM, HR-TEM has higher power of lattice resolution.

3.5.4.2 Sample analysis procedure

HR-TEM analysis was conducted using JEM-2100F at an accelerating voltage of 200 keV. A small amount of fine powder sample was dispersed in ethanol and sonicated for 0.5 min in an ultrasonic bath at room temperature. Using a disposable pipette, one drop of the suspension was carefully dropped on a 400 square mesh copper grid (3.05 mm) and dried at 40 °C in an oven for 3 days prior to analysis.

3.5.5 Brunner-Emmet-Teller (BET)

3.5.5.1 Background of BET

BET is used to analyze the textural properties such as surface area, pore size, pore shape and pore volume of the sample. BET is a multilayer adsorption process whereby non-corrosive gases (such as nitrogen, carbon dioxide, argon, etc.) are used to evaluate the adsorption of gas molecules on the solid surface. The degree of adsorption depends on several factors such as pressure, temperature and solid-gas interactions. After reaching the saturation pressure, the sample is removed from the gas environment and is heated to release adsorbed gas from the material and quantified. The collected data is displayed as BET isotherm which plots the amount of gas adsorbed with the relative partial pressure. There are 5 types of adsorption isotherms which are Type I, II, III, IV and V.

3.5.5.2 Sample analysis procedure

The textural properties of the samples were analyzed using nitrogen adsorption-desorption analyzer TriStar II 3020 series, Microactive 2.0. Prior to BET analysis, 1 g of the solid sample was dried in an oven at 60 °C for 2 h to remove any trapped

moistures. The sample was then placed in a 6 mm glass cell and degassed in a vacuum chamber, operating at 350 °C for 6 h to remove remaining moisture and possible contaminants. The sample was measured using relative pressure range of 0.01-0.90 P/P_o. The microporosity (external surface area, SA_{ext}) of the sample was also determined using the equation in **section 3.6.1**.

3.5.6 X-Ray powder diffraction (XRD)

3.5.6.1 Background of XRD

XRD is widely employed to analyze the crystallinity, crystal phase, crystal ratio, planes and lattice spacing of any crystalline substance. It a non-destructive test based on scattered waves mutually reinforcing one another. When an X-Ray beam hits a crystalline atom, the electrons around the atom oscillate with similar frequency as the incoming beam. As the atoms in a crystal are arranged in a periodic pattern, the combining waves formed constructive interference. Thus well-defined diffracted X-Ray beams are formed when leaving the sample at various directions.

3.5.6.2 Sample analysis procedure

XRD analysis was conducted using Bruker AXS D8 advanced diffractometer at 40 kV and 40 mA. The step size was 0.2° per second and Cu Kα radiation (α = 1.5406Å) was used. The Bragg angle was analyzed from 10° to 80°. Prior to the analysis, the sample was grinded into fine powder and was closely packed in a sample holder. The sample surface was smoothened by using a non-leaching glass slide. The obtained XRD patterns were evaluated using High Score-Plus software and the diffraction peaks were matched against the JCPDS standard reference patters. Spurr's and Scherrer's equations were employed to calculate the crystal phase ration and size respectively. In addition, the XRD data was also extracted into a Williamson-hall equation and the lattice strain of the samples were determined.

3.5.7 Fourier transformed infra-red spectroscopy (FTIR)

3.5.7.1 Background of FTIR

FTIR is widely used to determine the functional group in solid or liquid samples. The analysis is based on the ability of the molecules to absorb light in the infra-red region and generates vibrational frequencies. The absorption corresponds to the bonds presents, which is the ratio of the sample spectrum to the background spectrum of the IR.

3.5.7.2 Sample analysis procedure

The FTIR spectrum was analyzed using Bruker Vertex 80/80v with frequency ranging from 4000 to 400 cm^{-1}. The sample was prepared in pellet form using KBr and was grinded into fine powder before compressed using hydraulic support at 30 MPa. The analysis was conducted in drift mode for rough surface sample.

3.5.8 PL-Raman spectroscopy

3.5.8.1 Background of PL-Raman

Raman spectroscopy is generally employed to analyze the chemical structure of inorganic materials. Raman spectroscopy is based on scattering of light by the vibrating molecules as a result of interaction between the monochromatic laser beam and molecules of the sample. The Raman spectrum is constructed using the scattered light which has a different frequency from the incident light. This is also referred as inelastic scattering. Thus, Raman spectra are formed due to the inelastic collision between the incident monochromatic beam and molecules of the sample. Photoluminescence (PL) is a non-destructive test to evaluate the electronic structure of a material by photon absorption-emission process. The PL spectrum is widely employed to understand the mobility of charge carriers (electrons and holes) and also intrinsic defects. By

combining Raman and PL analysis, both the vibrational and electronic properties of the material can be evaluated using one instrument.

3.5.8.2 Sample analysis procedure

An in-built PL-Raman spectroscopy (Renishaw LabRam confocal Raman microscope with 325 nm line of a continuous He–Cd laser at room temperature) was used to analyze chemical structure of the sample. The sample was grinded into fine powder before analysis. The Raman data was further extracted to estimate the concentration of exposed facets using the equation in section 3.6.5.

3.5.9 Diffuse reflectance-ultraviolet visible spectroscopy (DR-UV Vis)

3.5.9.1 Background of DR-UV Vis

DR-UV Vis is widely used to observe the optical properties of liquid and solid materials by quantifying the amount of absorbed and scattered light. The material is placed between a light source and a photodetector and the difference in intensity of the beam of light before and after passing through the sample is measured. These measurements are compared at each wavelength to determine its absorption spectrum.

3.5.9.2 Sample analysis procedure

DR-UV Vis was conducted using Agilent Cary 100 model with a diffuse reflectance accessories. The sample was grinded into fine powder and was packed firmly in a solid holder. The surface of the sample was smoothened using a glass slide. The sample was analyzed using a double beam spectrometer. The lamp used was tungsten halogen with light source between 190 and 900 nm. The slit width was fixed at 2 nm. The band gap of the sample was determined using Kubelka-Munk function as shown in section 3.6.6.

3.5.10 Zeta Potential (ZP)

3.5.10.1 Background of Zeta Potential

Zeta potential is used to determine the surface charge, particle agglomeration, particle size distribution and isoelectric point (IEP) of a material. An electrical double layer is formed due to the interaction between the net charge of the particle surface and ions in the surrounding. Thus when a particle shifts position, the ions within the boundary follows. The potential that exists at this boundary is termed as zeta potential. The intensity of zeta potential indicates the material stability in a colloidal system. Generally, a material with zeta potential between +30 mV and -30 mV are considered unstable. Zeta potential can be used to determine the isoelectric point (IEP) of a material as well, which is the pH when the zeta potential value is at 0 mV. At this condition, the material is unstable due to extensive coagulation and flocculation.

3.5.10.2 Sample analysis procedure

The isoelectric point (IEP) of the sample was analyzed using Malvern ZetaSizer Nano instrument. The sample was grinded into fine powder and dispersed in ethanol. Then it was sonicated in an ultrasonic batch for 0.5 min before transferring it into a liquid cuvette. The analysis was conducted via pH titration mode using suitable titrating reagents for pH ranging from 3 to 11. From the zeta potential graph, the pH intercept at zero zeta potential represents the isoelectric point (IEP) of the sample.

3.5.11 Thermal gravimetric analysis (TGA)

3.5.11.1 Background of TGA

Thermal gravimetric analysis (TGA) is used to determine the change in the material physical and chemical properties as a function of increasing temperature or time. It is generally employed for materials that exhibit either mass loss or gain as a result of

decomposition or oxidation process. The instrument continuously measure the weight of the sample as it is gradually heated up to a maximum temperature of 2000 °C. TGA can also be coupled with FTIR and mass spectroscopy gas analysis.

3.5.11.2 Sample analysis procedure

The thermal stability of the sample was determined using Mettler-Toledo TGA/SDTA851e instrument. Approximately 50 mg of the sample was placed in an alumina crucible and heated from room temperature up to 700 °C using heating rate of 5 °C/min and constant air flow of 50 ml/min. The change in mass over temperature was plotted and the point of thermal stability of the sample was identified.

3.5.12 Differential scanning calorimetry (DSC)

3.5.12.1 Background of DSC

Differential scanning calorimetry (DSC) is used to determine the enthalpies during a chemical reaction and at which temperature does this change occurs. An inert material such as alumina or empty aluminum pan is used as the reference, and the temperature of both the sample and reference are increased at a constant rate. The range of temperature lies between -160 °C and 600 °C. As DSC is conducted at constant pressure, the heat flow is regard as the enthalpy change. Software is built in conjunction with DSC instrument for data analysis such as Star e evaluation software.

3.5.12.2 Sample analysis procedure

The energy profile of the sample was determined using Mettler-Toledo DSC 882e instrument. Approximately 50 mg of the samples was placed in an aluminum DSC pan. The sample was analyzed from room temperature up to 500 °C using a heating rate of 10 °C/min and constant air flow at 50 ml/min. The energy profile was plotted as a function of temperature and the exothermic and endothermic points were identified.

3.5.13 X-ray photoelectron spectroscopy (XPS)

3.5.13.1 Background of XPS

X-ray photoelectron spectroscopy (XPS) is used to characterize the surface chemical state of a material from 1 to 12 nm in depth. The chemical element and nature of the chemical bond between these elements can be detected except for hydrogen and helium. In XPS, the material is irradiated with sufficient energy of X-rays to excite the electrons away from the nuclear attraction force of an element into the vacuum state. In the vacuum state, the electron analyzer measures the kinetic energy and produces an energy spectrum of intensity versus binding energy. Each of the energy peaks on the spectrum represents a specific element.

3.5.13.2 Sample analysis procedure

The binding energy of different elements in the sample was determined using Thermo Scientific K-alpha instrument. The sample was pressed into tablets before analysis. The analysis was carried out using a non-monochromatized Mg Kα (photon energy of 1253.6 eV). A flat gold (Si/10nm Ti/200nm Au) was used as the substrate and reference. The XPS core levels were aligned to the C1s binding energy (BE) of 285 eV.

3.6 Calculation

3.6.1 Microporosity

The external surface area, SA_{ext} of the sample was calculated using t-plot external surface area divided by the Langmuir surface area (Galarneau, Villemot, Rodriguez, Fajula, & Coasne, 2014).

3.6.2 Spurr's equation

Spurr's equation was used to determine the crystal ratio of individual phases in a mixed anatase and rutile TiO$_2$ (Spurr & Myers, 1957).

$$f_A = 1/(1+1.26 \times I_R/I_A) \hspace{3cm} \text{Eq. (3.3)}$$

Where f_A is the weight fraction of anatase, $f_R = 1 - f_A$ is the weight fraction of rutile, I_A is the intensity of maximum anatase phase peak {101} and I_R is the intensity of maximum rutile phase peak {110}. The scattering coefficient used was 1.26.

3.6.3 Scherrer's equation

Scherrer's equation was used to determine the crystallite size of nano TiO$_2$ crystals and is not applicable for grains larger than 0.01 to 0.02 μm (Patterson, 1939).

$$\tau = K \lambda / \beta \cos \theta \hspace{3cm} \text{Eq. (3.4)}$$

Where τ is the mean size of the ordered (crystalline) domains, K is a dimensionless shape factor, λ is the X-ray wavelength, β is the line broadening at half the maximum intensity (FWHM) and θ is the Bragg angle. The dimensionless shape factor has a typical value of 0.9, but varies with the actual shape of the crystallite. The value of 0.9 generally represents spheres particles, but is also valid for cubes, tetrahedral and octahedral particles.

3.6.4 Williamson-Hall Plot

The XRD peak was exploited to estimate the average crystal lattice strain of the prepared TiO$_2$ samples by plotting $\beta \cos \theta/\lambda$ versus $\sin \theta/\lambda$ where β is the line broadening at half the maximum intensity (FWHM), θ is the diffraction angle of first four intense XRD peaks and λ is the XRD wavelength (Prabhu & Rao, 2014). From this

plot, the slope represents the effective value of lattice strain and the intercept represents the effective crystallite size.

3.6.5 Calculation of high energy {001} facets by Raman

The Raman spectrum was exploited to estimate the percentage of high energy exposed {001} facets in the TiO_2 crystal structure by dividing the Raman peak intensity of A1g (~ 515 cm^{-1}) and Eg (~144 cm^{-1}) (F. Tian, Zhang, Zhang, & Pan, 2012).

3.6.6 Kubelka-Munk's equation

The band gap of prepared TiO_2 was estimated using Kubelka-Munk's theory for powder samples (Rosendo López & Gómez, 2012). By plotting [F (R$_\infty$) hν]$^{1/r}$ versus hν, the intercept between the linear extrapolation of the graph and the baseline results to the value of the band gap (eV). The reflectance function, F(R) was determined directly from Agilent Cary 100 instrument or can be calculated using Eq. 3.3.

$$F(R_\infty) = (1-R_\infty)2/2R_\infty = k/s \qquad \text{Eq. (3.5)}$$

Where R is the reflectance, k is the absorption coefficient, s is the scattering coefficient, h is the Planck's constant and ν is the frequency. The value of r used was 2 for indirect allowed transition. Other r values includes 1/2 (direct allowed transition), 3/2 (direct forbidden transition) and 3 (indirect forbidden transition).

CHAPTER 4: RESULTS AND DISCUSSIONS

In this chapter, the prepared photocatalysts namely TiO$_2$ (without surfactant) **(Section 4.1)**, TiO$_2$ (with surfactant @ F127-TiO$_2$) **(Section 4.2)**, N-doped TiO$_2$ **(Section 4.3)**, F-doped TiO$_2$ **(Section 4.4)**, N,F co-doped TiO$_2$ **(Section 4.5)**, hydrogenated TiO$_2$ **(Section 4.5)**, and hydrogenated F-doped TiO$_2$ **(Section 4.6)** were discussed. Physicochemical properties such as appearance, morphology, crystallinity, crystal phase, size, textural properties, chemical structure and composition, facets, optical response, charge carriers mobility, and surface chemical state were determined. The photocatalysts were evaluated for the photocatalytic degradation of atrazine. The relationship between photocatalytic activity and photocatalysts characteristics was also studied and discussed in **Section 4.7 and 4.8.**

4.1 Surfactant-modified TiO$_2$ (F127-TiO$_2$)

4.1.1 Morphology and textural properties

TiO$_2$ prepared without and with pluronic F127 is labeled as TiO$_2$ and F127-TiO$_2$ respectively. The morphology of the prepared photocatalyst was examined under field emission scanning electron microscope (FESEM) at 100,000x magnification (Figure 4.1). Distinctive modification on particle size and structure change was observed. Significant reduction of particle size occurs from an average size of 50-100 nm (Figure 4.1a) to 20-30 nm (Figure 4.1b). Different structures and sizes were observed in TiO$_2$, while the homogeneity enhances in F127-TiO$_2$, with smaller uniform size of tetragonal bipyramid structures. In this work, pluronic F127 was shown to significantly influence the growth, particle size and homogeneity. The comparison of morphology was also valid as similar synthesis procedure and ageing duration was used. Ageing temperature and duration during the sol-gel process significantly affects the growth of particles and determines the final particle size of the catalyst (Shahini et al., 2011). Furthermore,

76

pluronic F127 has no effect towards the solution pH, hence the rate of TTIP hydrolysis

and Ti-O-Ti condensation/poly-condensation remains unaffected (Sung et al., 2010).
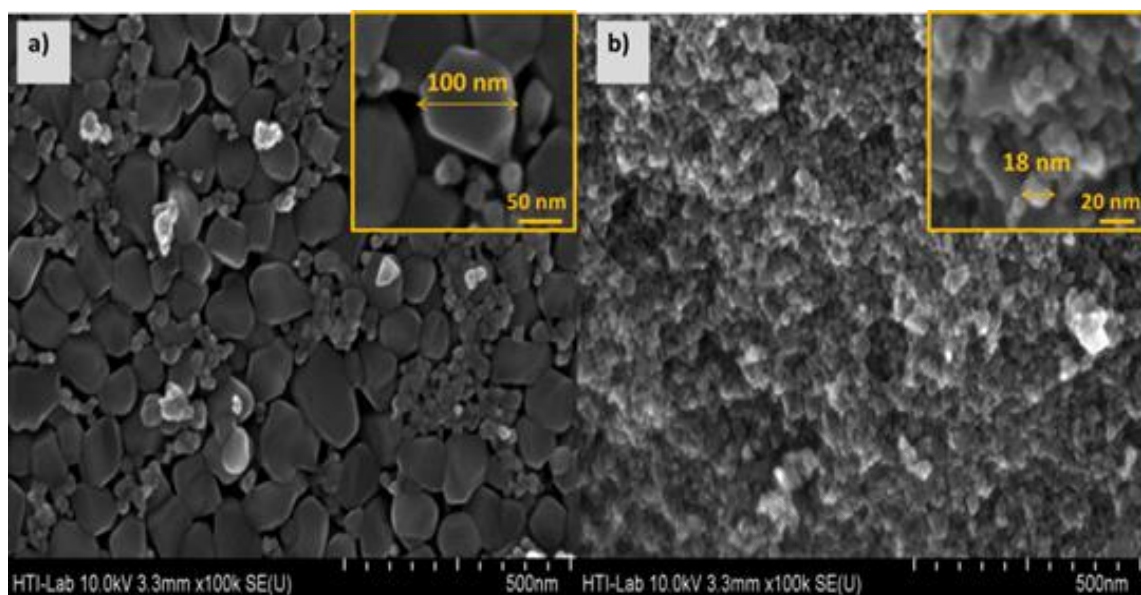
Figure 4.1: Morphology of a) TiO_2 and b) F127-TiO_2 at 100,000x magnification using FESEM analysis with inset images each at higher resolution scale

Albeit minimal change in TiO_2 atomic stoichiometry was observed (Table 4.1),

larger oxygen content was observed in F127-TiO_2. Aforementioned, EDX analysis is

limited to surface elemental composition and is statistically based on selected area,

hence does not represent the total atomic concentration in TiO_2.

Table 4.1: Elemental composition (atomic %) by EDX for TiO_2 and F127-TiO_2

Element	Atomic No	TiO_2 (%)	F127-TiO_2 (%)
Ti	22	37.95	31.79
O	8	62.05	68.21
	Total	100.00	100.00

High resolution transmission electron microscope (HR-TEM) shows vivid lattice

spacing of 0.352 nm in TiO_2 and 0.235 nm in F127-TiO_2 corresponding to anatase (101)

plane and (001) plane respectively (Figure 4.2a-b) (Han, Kuang, Jin, Xie, & Zheng,

2009). The usage of Pluronic F127 in the synthesis of TiO_2 was able to promote the

growth of {001} facets, proven by the presence of truncated tetragonal bipyramid

structures (square shapes) as shown in Figure 4.2b, as opposed to the less reactive {101} facet represented by tetragonal bipyramid structures (spheres with blunt edges and rhombuses) as shown in Figure 4.2a (Ichimura, Mack, Usmani, & Mars, 2012). The geometrical of a single crystal consisting of flat and square surfaces represents {001} facets, while trapezoidal surfaces represents {101} facets (Ong et al., 2014). Furthermore, smaller particle size facilitates good photocatalytic activity due to higher degree of reactive oxygen species (ROS) formed such as hydroxyl radical, hydroxyl ion, oxygen ion, superoxide anion radicals and hydrogen peroxide (Lee et al., 2012). Large concentration of radicals facilitates the photocatalytic activity.
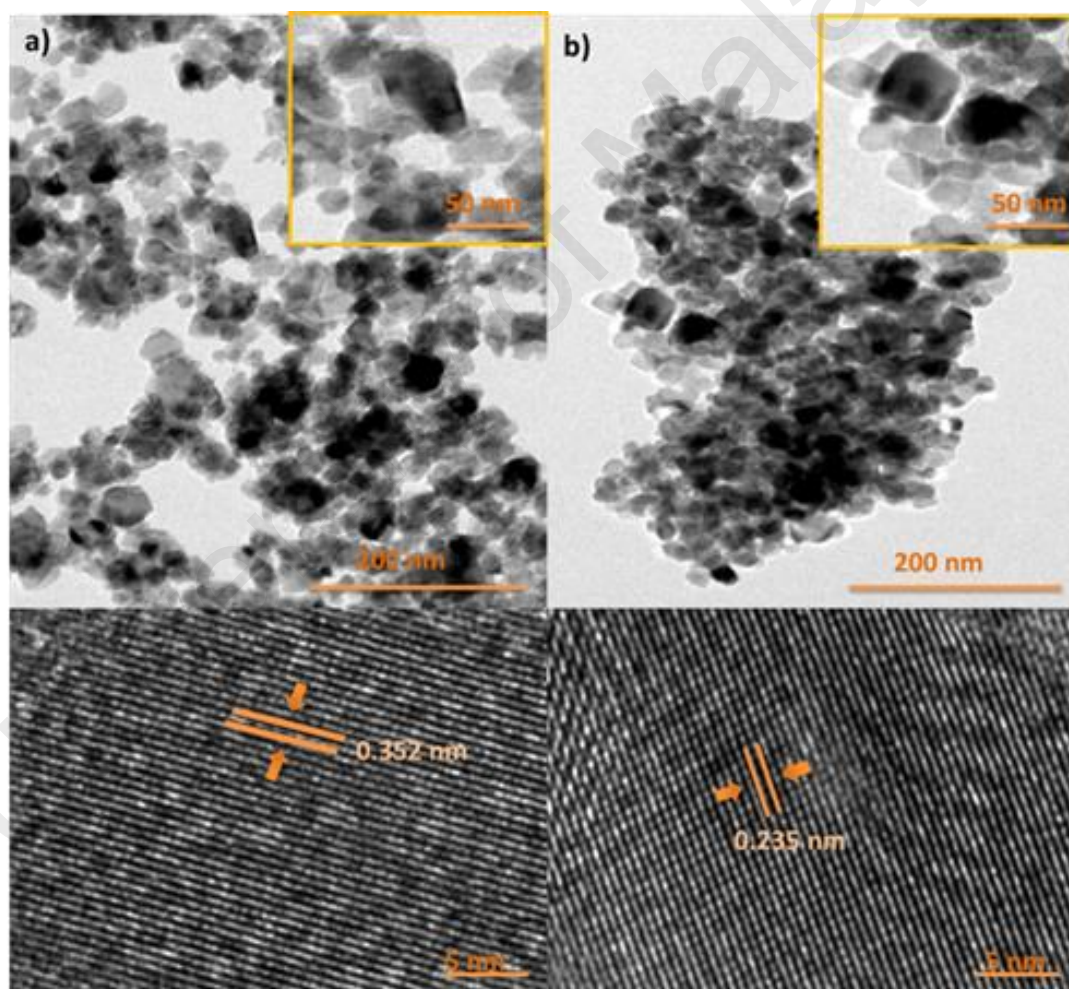
Figure 4.2: HR-TEM image and lattice spacing of a) TiO_2 with 0.352 nm (101) plane and b) F127-TiO_2 with 0.235 nm (001) plane

Nitrogen adsorption and desorption isotherms showed linear isotherms of type IV for both TiO_2 and F127-TiO_2 (Figure 4.3) conforming to uniform mesoporous structure.

In this work, the calcination temperature played a major role in TiO_2 crystallization process as well as maintaining the integrity of the formed pores.
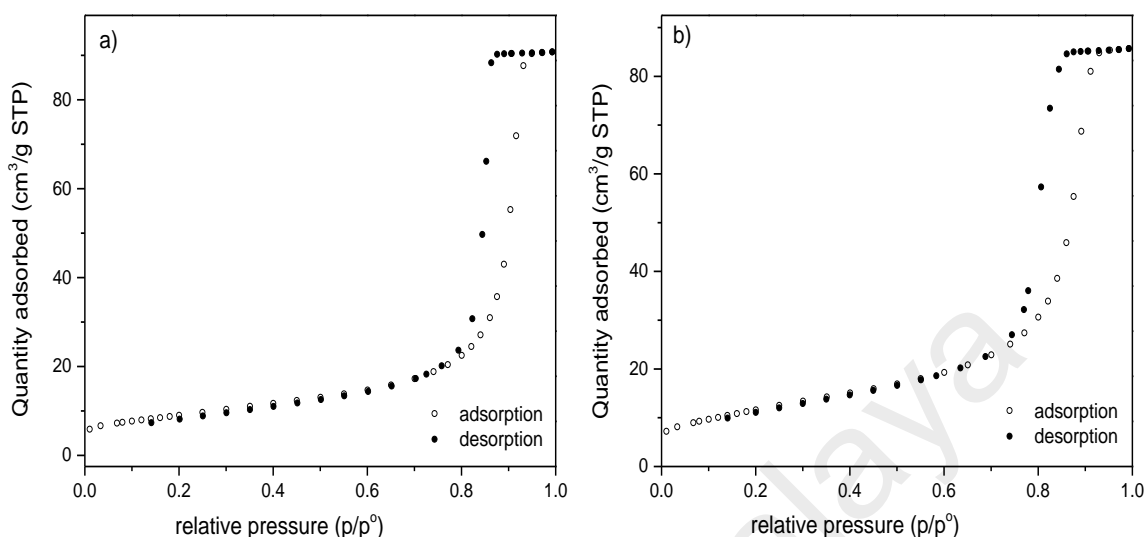
Figure 4.3: Nitrogen adsorption/desorption linear isotherms plot of a) TiO_2 and b) F127-TiO_2

Based on the calculated microporosity value (expressed as external surface area, SA_{ext}), F127-TiO_2 showed higher value of microporosity thus contributed to the larger surface area of F127-TiO_2 (Table 4.2) and smaller crystallite size of anatase (Table 4.3). In this work, Pluronic F127 showed less effect on the cumulative pore volume but narrows the pore width from 17.3 nm to 11.1 nm. The sharp increased between 0.5 and 0.7 relative partial pressure of nitrogen absorption in both photocatalyst as a result of capillary condensation, represents good particles homogeneity (Gajjela et al., 2010).

Table 4.2: Textural properties of TiO_2 and F127-TiO_2

Catalyst	BET surface area, m^2/g	SA_{ext}, ratio	Cumulative pore vol., cm^3/g	Average pore width, nm
TiO_2	30.46	0.551	0.132	17.3
F127-TiO_2	38.77	0.990	0.133	11.1

Table 4.3: Corresponding FWHM, cystallite size and phase composition (XRD analysis) and percentage of exposed {001} facets (Raman analysis) of TiO$_2$ and F127-TiO$_2$

Catalyst	Plane & Corresponding FWHM				Crystallite size, nm		Percentage (%) of crystal phase		Percentage (%) of exposed {001} facets
	(110)	(101)	(004)	(200)	Rutile	Anatase	Rutile	Anatase	
TiO$_2$	0.1574	0.1378	0.1574	0.3936	52.0	59.0	32.53	67.47	5.36
F127-TiO$_2$	0.1181	0.3542	0.4723	0.2755	69.3	23.0	34.50	65.50	7.63

4.1.2 Thermal stability

The thermal stability of F127-TiO$_2$ was evaluated by observing the change of weight and energy with respect to temperature. Figure 4.4a illustrates several steps of weight loss and its derivatives until a thermal stability was reached. Initially, the major weight loss in amorphous F127-TiO$_2$ was completely removed below 200 °C. This was confirmed by two endothermic peaks at 118 °C and 186 °C in Figure 4.4b and was attributed to organic solvent and internal hydroxyl group removal. The weight loss observed from 200 °C until approximately 500 °C represents removal of pluronic F127 template and other remaining organic solvents. Above 500 °C, the amorphous F127-TiO$_2$ reached its thermal stability confirming with no further weight loss. The crystallization of F127-TiO$_2$ was shown to occur at 251°C from amorphous to anatase structure (D. Eder & Windle, 2008), and further crystallization or/and phase transformation at 378 °C and 425 °C. In this work, to cater for catalyst uniformity and for the sake of direct comparison of the final physico-chemical properties of both catalysts, the same thermal treatment temperature and other condition (pH, ageing temperature and duration, water/solvent ratio, thermal treatment duration) were applied.
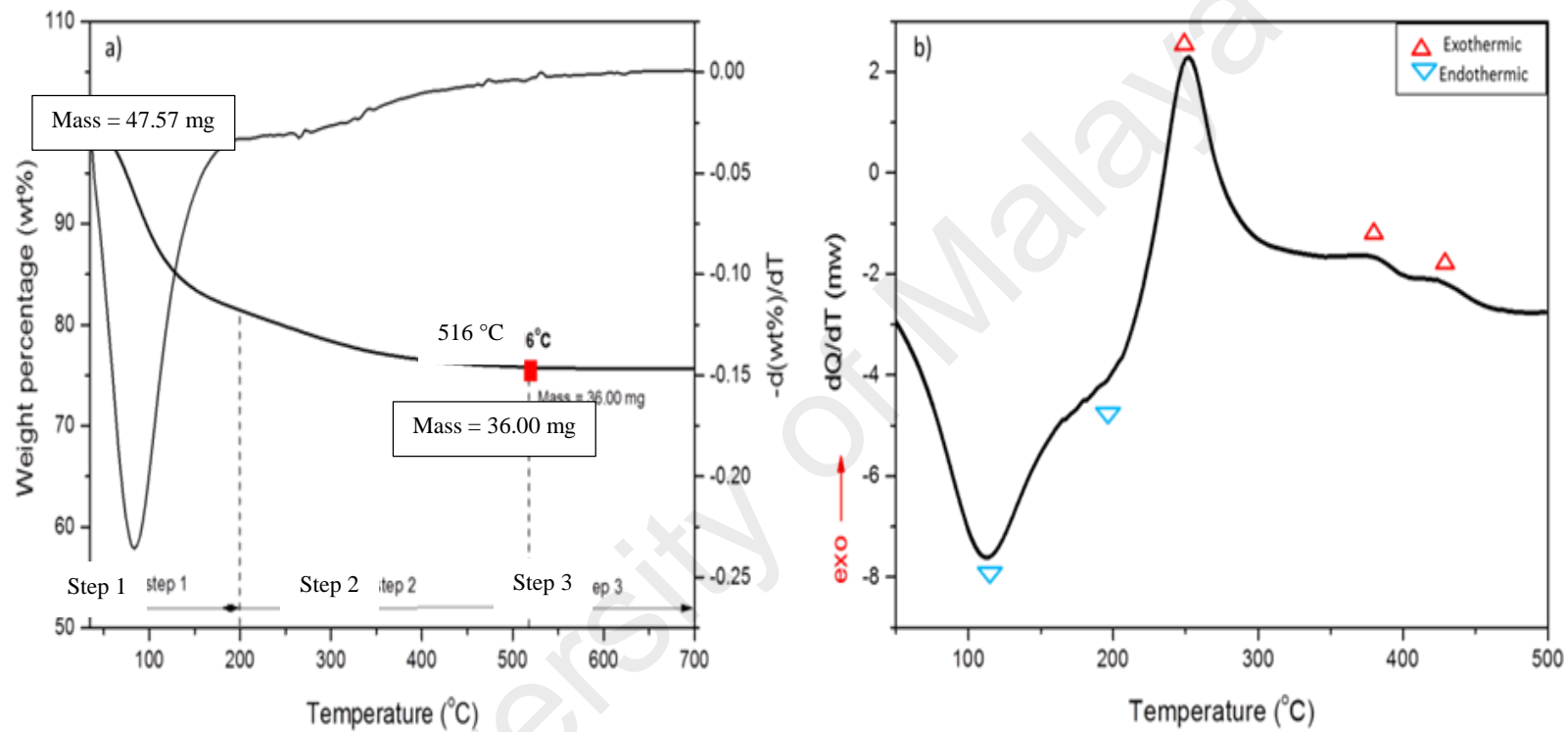
Figure 4.4: a) Weight loss (wt %) and derivative curve –d (wt %)/dT versus temperature plots of F127-TiO$_2$ (Sample was analyzed before calcination at 500 °C) and b) Energy profile of F127-TiO$_2$ (Sample was analyzed before calcination at 500 °C)

4.1.3 Structure and crystallinity

Both XRD spectra showed mixed anatase and rutile crystal phases with diffraction pattern matching JCPDS 73-1764 (anatase) and JCPDS 34-0180 (rutile) (Figure 4.5, Table 4.3). The pH used during TiO_2 sol-gel preparation significantly affects the formation and stability of TiO_6 (octahedral) polymer network. An acid or base catalyzed sol-gel reaction affects the type of polymorphs and degree of TiO_2 crystallinity. Sung et al (2010) observed different crystal phases and ratio of TiO_2, calcined under different temperature ranging from 200 to 500 °C prepared using similar type of HCl acid. In their study, TiO_2 was prepared at pH 3.92 and calcined at 500°C. A single anatase phase was obtained. As mixed phase consists of anatase and rutile was obtained in this work using similar calcination temperature, the differences could be influenced by the concentration of acid (protons), competition between olation and oxolation during network formation, ageing time and type of solvent/precursor.
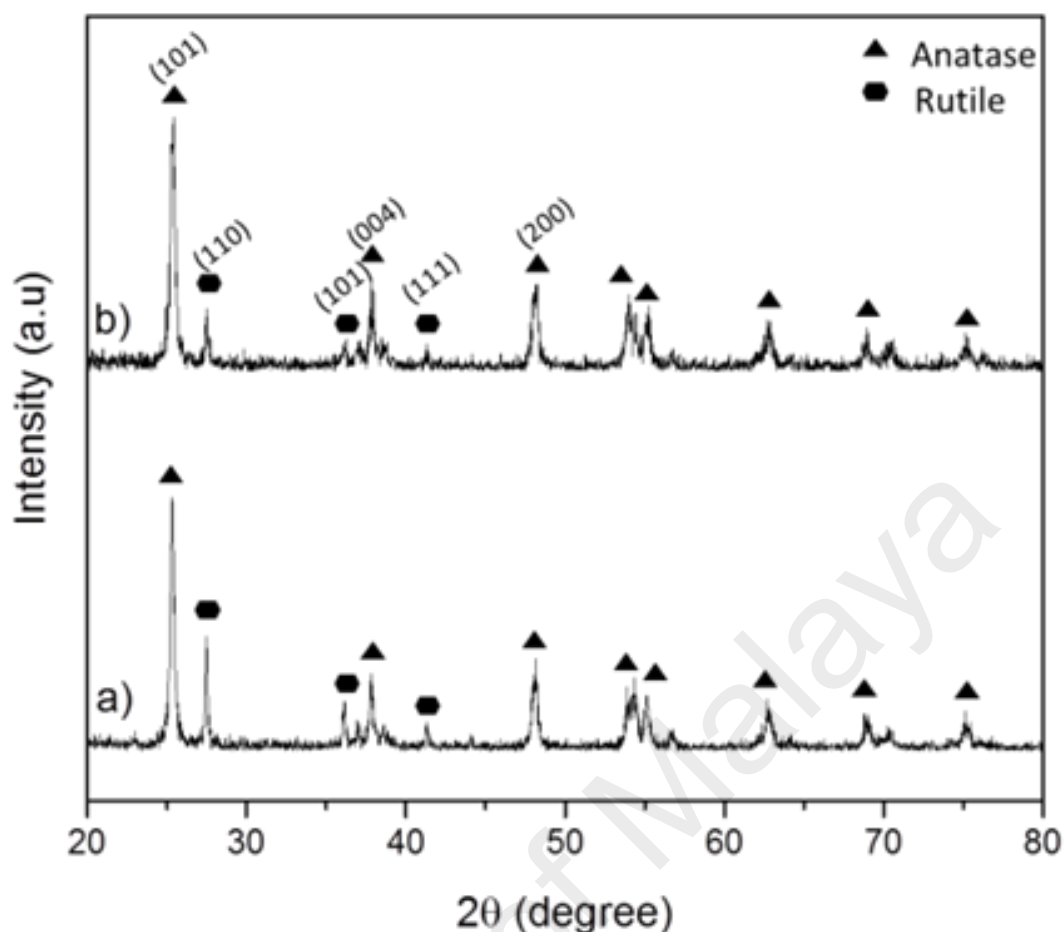
Figure 4.5: X-ray diffraction (XRD) spectra of a) TiO_2 and b) F127-TiO_2

There is no new XRD peak and change in the crystal ratio observed in F127-TiO_2 relative to TiO_2. Comparing this two XRD spectra, drastic broadening of (101) anatase peak was observed from FWHM of 0.1378 to 0.3542 of TiO_2 and F127-TiO_2 respectively. This was attributed to smaller anatase crystallite size from 59 nm (TiO_2) to 23 nm (F127-TiO_2) estimated using Debye-Scherer's equations (Patterson, 1939). Interestingly, rutile crystallite size increased by ~17 nm in F127-TiO_2 and was confirmed from the narrowing of FWHM of (110) plane. This suggests that pluronic F127 did not have much effect on the crystal phase ratio, but a major impact on the particle size, crystallite size, especially towards anatase crystal structure. It is worth to note that similar solvent (ethanol) was used in the preparation of both photocatalysts, as the type of solvent significantly affect TiO_2 crystal polymorphs (Luo et al., 2003). The

change in TiO$_2$ crystal phase ratio is crystallite size dependent, and applied for crystallite size below ~14 nm. However, the crystallite size of anatase observed in this work was 23 nm. Anatase has a weaker thermodynamic stability compared to rutile, hence less change in the crystallite size was expected for rutile than of anatase. Another point to consider was the change of shape which was evaluated by the thickness in [001] direction and length in [100] direction corresponding to the FWHM of (004) and (200) diffraction peaks, respectively. As pluronic F127 is a structure directing agent, a significant change in the shape of both photocatalysts was not surprising. The FHWM of (004) diffraction peaks broadened from 0.1574 to 0.4723 and the FHWM of (200) diffraction peaks narrowed from 0.3936 to 0.2755 for TiO$_2$ and F127-TiO$_2$ respectively. This simply demonstrates that the thickness in [001] direction reduces and length in [100] direction increases in F127-TiO$_2$.
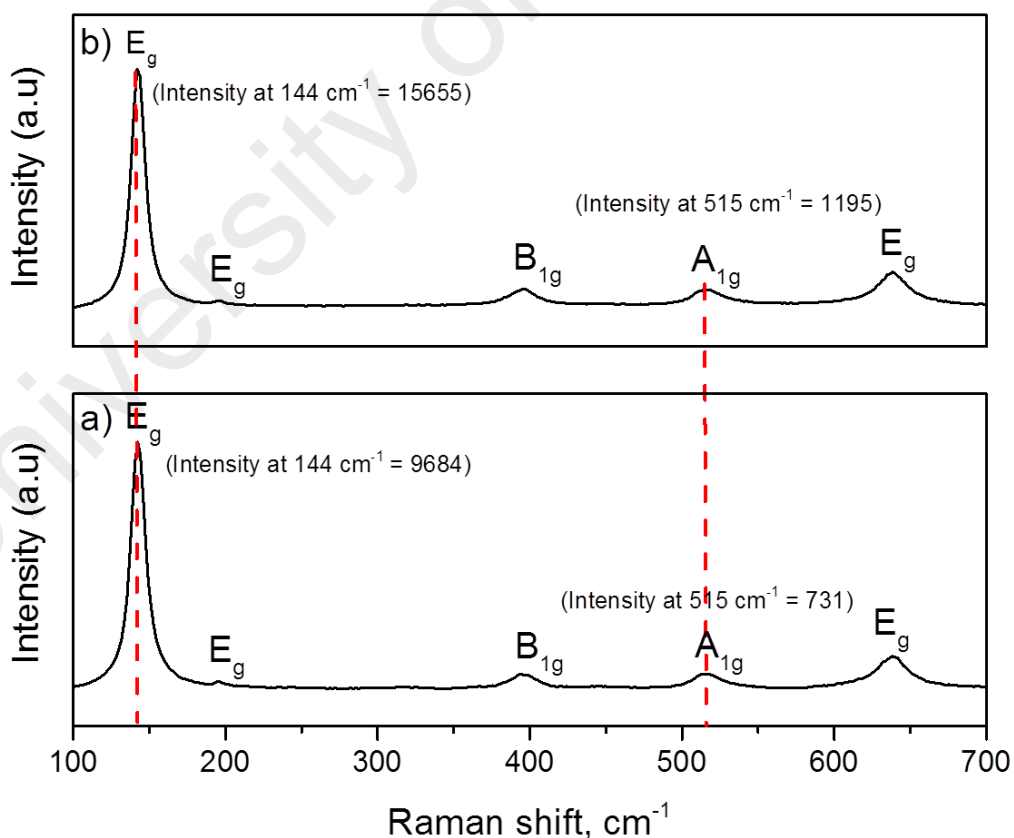
Figure 4.6: Raman spectra of a) TiO$_2$ and b) F127-TiO$_2$

The chemical structure of TiO$_2$ and F127-TiO$_2$ confirms that it is of TiO$_2$ based on the assigned Raman vibration peaks (Figure 4.6). However, only anatase structure was

observed following the symmetric stretching vibration (E_g at 144 cm^{-1},195 cm^{-1} and 637 cm^{-1}), symmetric bending vibration (B_{1g} at 395 cm^{-1}) and anti-symmetric vibration (A_{1g} at 515 cm^{-1}) (Samsudin et al., 2015). Although XRD showed approximately 30 wt % of rutile in both photocatalysts, no obvious rutile band at 608 cm^{-1} was present in the Raman spectra. This is an implication that Raman was effective in showing the presence of TiO$_2$ but not the definite crystal structure. Another important data extracted from Raman is the percentage of high energy anatase {001} facets (F. Tian et al., 2012). As observed, the change of shape in F127-TiO$_2$ (Figure 4.1) consist larger exposure of high energy {001} facets from 5.36 % to 7.63 %. Higher percentage of exposed high energy {001} facets in TiO$_2$ favors the photocatalytic activity (Han et al., 2009).

4.1.4 Light absorption and photoluminescence behavior

Both of the photocatalysts showed effective band gap narrowing, enabling absorption of visible light as opposed to only UV light (Figure 4.7). This was observed before in TiO$_2$ consisting of anatase and rutile crystal phase mixures (Oshani et al., 2014). There were less band gap differences between TiO$_2$ and F127-TiO$_2$ although the band gap of F127-TiO$_2$ was smaller by 0.03 eV. In previous studies, band gap was shown to be crystallite size dependent, whereby, smaller crystallite size leads to larger band gap due to quantum size effect (Reddy, Manorama, & Reddy, 2003). However, the range of crystallite size that caused this effect is still not very clear. In this study, there was a significant reduction of anatase crystallite size and increment of rutile crystallite size. If quantum size effect was applicable, a significant difference in band gap would be apparent as there was a drastic crystallite size differences between both photocatalysts.

As this is not observed, the cause of band gap differences is closely related to the morphology and composition of anatase and rutile crystal structure, whereby the different arrangement of TiO$_6$ (octahedral) rutile units affects its final optical properties.

The higher mass density and more pronounced localization of 3d states of rutile results to a smaller band gap and is more pronounced in F127-TiO$_2$ due to the larger rutile ratio (Scanlon et al., 2013).
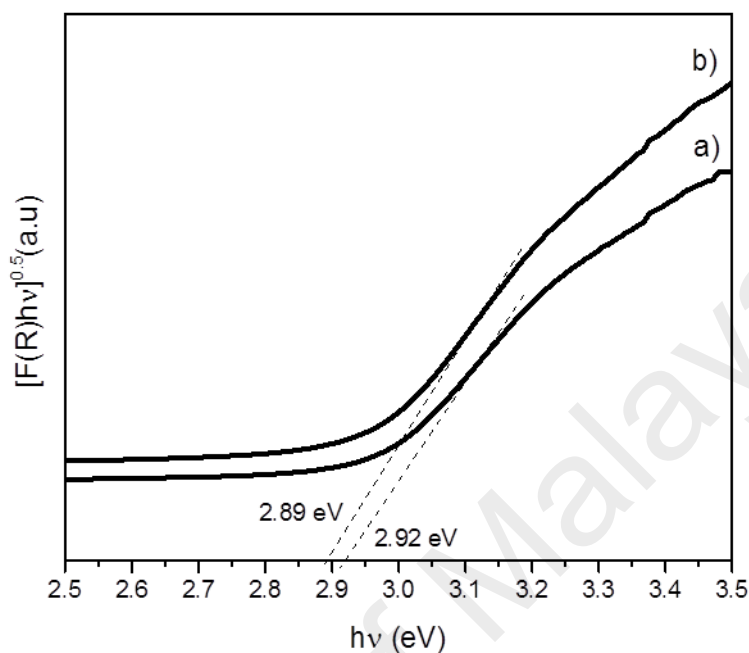
Figure 4.7: Band gap of a) TiO$_2$ and b) F127-TiO$_2$ calculated using Kubelka-Munk function

In a mixed phase TiO$_2$, the modified band alignment creating n-p hetero-junction between rutile and anatase facilitates the surface redox reaction via narrowing of band gap as opposed to a single anatase phase and thus, improved charge carriers separations (Hanaor & Sorell, 2010; Scanlon et al., 2013). Although, the electronic structure of TiO$_2$ anatase crystal phase favors the formation of surface-adsorbed hydroxyl radicals, it is less hydrophilic as compared to rutile due to its lower surface energies (Hanaor & Sorell, 2010). Despite TiO$_2$ rutile crystal phase being UV-Vis photo-active, the larger grain size of rutile increases the tendency of electrons and holes pair recombination, thus is less likely to produce high concentration of active radicals for the photocatalytic degradation activity (Jiang et al., 2010). The combination of rutile and anatase crystal phases facilitates larger availability of surface trapped electrons and holes to react with absorbed O$_2$ and H$_2$O for radical formation (Oshani et al., 2014). Furthermore, mixed

phase TiO$_2$ is activated under both UV and visible light region of the solar spectrum. However, the photocatalytic activity depends on other factors as well such as grain and crystallite size, morphology, facets, surface free energy and defects.

The photoluminescence (PL) was used to evaluate the radiative recombination pathway and decay rate constant of trapped electrons with valence band holes. In principle, TiO$_2$ should not show a band gap PL as it is an indirect band gap semiconductor. However, illumination with UV light (excitation wavelength of 365 nm) results in broad visible PL. There was a significant difference in the PL intensity between TiO$_2$ and F127-TiO$_2$, as observed in Figure 4.8a,b. In the former photocatalyst, electrons and holes recombination was greatly favored corresponding to the numerous trapped states observed at 450 nm, 500 nm and 530 nm respectively. Meanwhile there were less trapped states observed in F127-TiO$_2$ at 450 nm and 530 nm (Figure 4.8b). This was a possible indication that pluronic F127 contributed towards the hindrance effect of electrons and holes recombination due to morphology changes. The photo-excited electrons and holes in F127-TiO$_2$ have greater capability to migrate to the catalyst surface for radical formation. If we analyzed closely, both photocatalysts consists of almost similar crystal ratio of anatase and rutile, hence the PL intensity changes as a result of rutile content was not the main contribution to the difference in the PL spectra (Ruslimie et al., 2011).
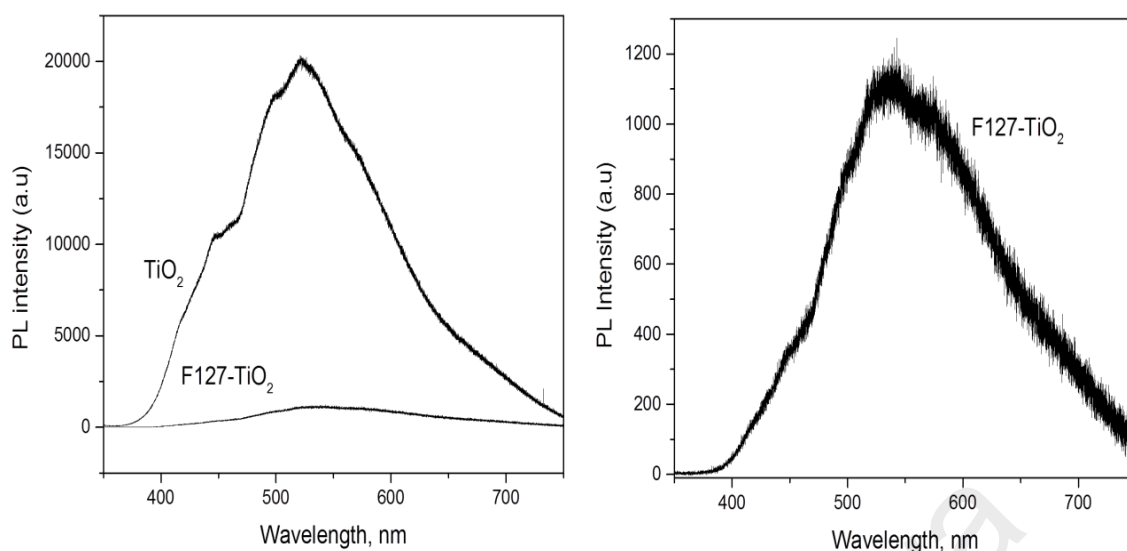
Figure 4.8: a) Photoluminescence (PL) spectra of TiO_2 and $F127$-TiO_2 and b) PL Inset of $F127$-TiO_2

Figure 4.9 illustrates the radiative recombination pathway schematic diagram by extracting the information from Figure 4.8a. In Figure 4.9, three defects centres were proposed based on three PL peaks corresponding to different wavelengths. The wavelength at 450 nm corresponds to self-trapped electrons (usually around 415 nm) and defects sites (500 nm and 530 nm). No emission peak was observed at 650 nm belonging to another defect sites observed in single anatase TiO_2 (Chaudhary, Srivastava, & Kumar, 2011). The change of crystallite size, particle size and morphology coupled with an increment of exposed high energy {001} facets in F127-TiO_2 contributes to a positive effect by inhibiting electrons and holes recombination through fewer defect centres and thus facilitates the photocatalytic activity (Dozzi et al., 2013). It is previously reported that smaller crystallite size reduces the intensity of the PL peaks, governing enhanced electrons and holes separation (Wang, Widiyastuti, Ogi, Lenggoro, & Okuyama, 2007). The drastic decrement of anatase crystallite size in F127-TiO_2 from 59 nm to 23 nm was one of the factors responsible for the low PL intensity (Figure 4.8b). Bulk oxygen vacancy also influences the ability of a photocatalyst to absorb light, i.e. visible light, however, an excess amount leads to a

decreased in the photocatalytic degradation activity as it serves as charge carrier traps (Tan et al., 2014). This could, however, be correlated with the low PL intensity of F127-TiO$_2$, due to fewer bulk oxygen vacancies and greater surface oxygen vacancies.
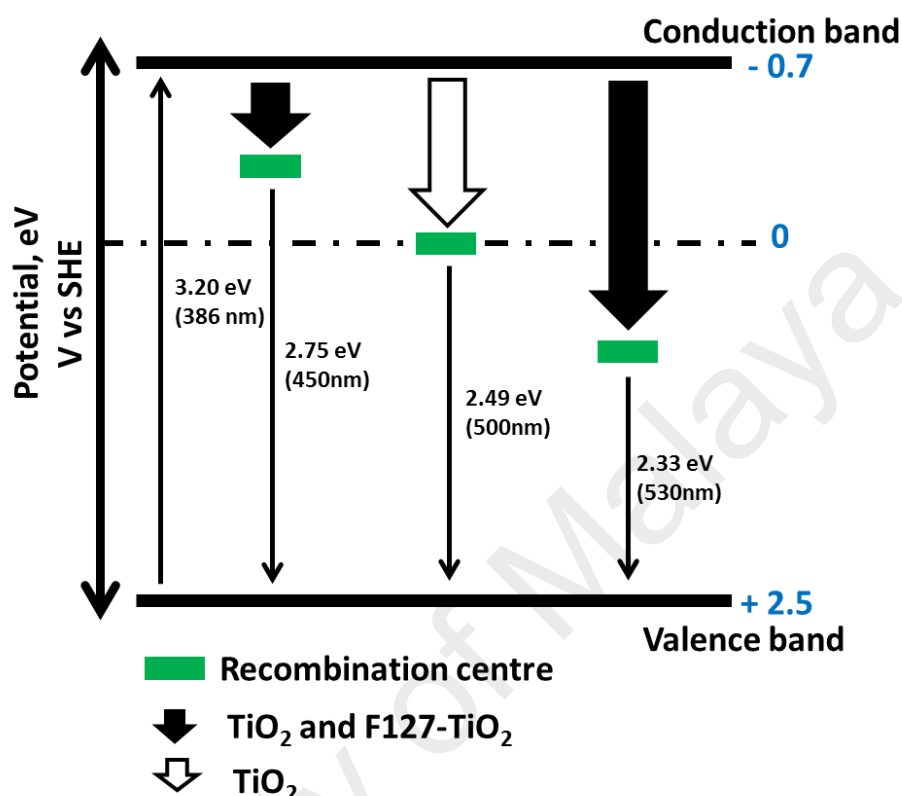
Figure 4.9: Recombination pathway schematic diagram for TiO$_2$ and F127-TiO$_2$

4.1.5 Surface characterization

XPS was used to evaluate the chemical state of TiO$_2$ and F127-TiO$_2$. The binding energy, E_g of Ti 2p$_{3/2}$ and Ti 2p$_{1/2}$ at 459 eV and 464 eV, respectively, represents Ti^{4+} (Figure 4.10) (Xiong, Li, Yang, & Yu, 2012). There was a difference of 0.1 eV between Ti 2p of both photocatalysts, slightly shifting towards lower E_g in F127-TiO$_2$. This was an indication that Ti in O-Ti-O bond in F127-TiO$_2$ was more electron rich as compared to TiO$_2$. In other reported work, the shifting of Ti 2p towards lower E_g indicated foreign atom substitution in Ti-O-Ti bond, forming doped TiO$_2$ such as O-Ti-C (Lin, Zheng, Xie, Zhu, & Xie, 2007). There was an absence of E_g around 457.7 eV, which is a characteristic of surface Ti^{3+} (Xiong et al., 2012).

Similar E_g at 530.1 eV and 531.7 eV were observed for O 1s in TiO_2 and F127-TiO_2, corresponding to lattice O^{2-} and surface-bound hydroxyl, OH respectively. There was no presence of absorbed H_2O at E_g of 532.7 eV for both photocatalysts (Liu et al., 2008). The surface-bound hydroxyls, OH were formed as a byproduct from the thermal treatment process of un-calcined TiO_2 under the influence of air or oxygen following the below reaction (Karaman, Sariipek, Koysuren, & Yildiz, 2013).

$$TTIP + O_2 \rightarrow TiO_2 + 4C_3H_6 + 2H_2O \qquad \text{Eq. (4.1)}$$

The position of valence band (VB) edge in Figure 4.10 was estimated by linear extrapolation of the peaks to the baseline. Clearly shown, VB of TiO_2 was positioned at ~3.0 eV and the VB position of F127-TiO_2 was blue shifted close to ~2.0 eV, indicating narrowing of band gap or presence of impurities states (Cui et al., 2014). This observation was closely related to Ti^{3+} and oxygen vacancies (Wang, Lu, Ni, Su, & Xu, 2012).

However, referring to the calculated band gap using Kubelka-Munk function, the band gap of TiO_2 and F127-TiO_2 were 2.92 eV and 2.89 eV, respectively, which showed less deviation as opposed to the significant shift of valence band edge. It is believed that a wide defect energy state belt was formed within the band gap of F127-TiO_2 which contributed to visible light absorption and enhancement of the photocatalytic activity.

Interestingly, the crystal ratio of anatase and rutile in both photocatalysts remained almost similar at 70 wt % anatase and 30 wt % rutile. Several works reported that the type and ratio of TiO_2 crystal phase significantly affects the position of the valence and conduction band, thus the band gap (Zaleska, 2008). As there was no significant change in the crystal phase ratio, the change of VB position in F127-TiO_2 was assumed to be due to the larger presence of oxygen vacancies and Ti^{3+} defects.
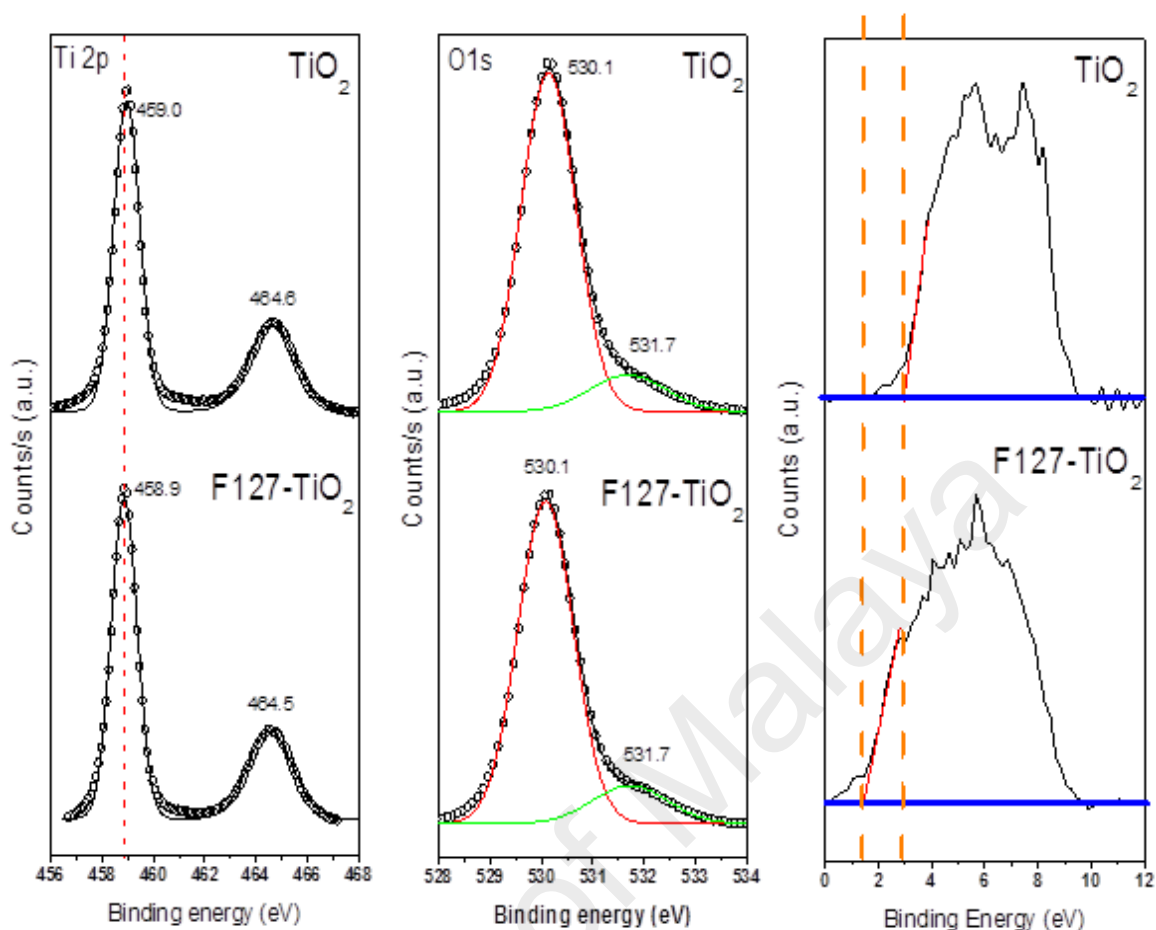
Figure 4.10: XPS spectra of TiO_2 and F127-TiO_2

4.2 Nitrogen-doped TiO_2 (N-TiO_2)

4.2.1 Morphology and textural properties

TiO_2 prepared without and with nitrogen was labeled as TiO_2 and NX-TiO_2 (X =1, 2, etc.) respectively. Nitrogen was successfully doped in TiO_2 in the range of 8-17 wt % as shown in Table 4.4. The nitrogen content in CHNS appeared slightly higher than by EDX, as CHNS measures the total bulk nitrogen while EDX measures the nitrogen presence on the surface of N-TiO_2. In the prepared photocatalyst, no change in color is observed and the catalysts remained as white powder. This implies that the probability of interstitially doped N or chemisorbed γ-N_2 in TiO_2 is greater, as color change is usually attributed to substituted doping (Sun, Qiao, Sun, & Wang, 2008).

92

Table 4.4: Atomic and weight percentage of nitrogen in N-TiO$_2$

[a] Initial N Molar Concentration	Sample Marking, NX-TiO$_2$	[b] Amount of N doped (wt %) in TiO$_2$	[c] Amount of N doped (wt%) in TiO$_2$
0.0	N0	0.00	0.00
0.5	N1	8.71	9.05
1.0	N2	10.32	11.03
1.5	N3	11.29	12.00
2.0	N4	13.99	13.71
2.5	N5	16.56	16.99

[a] Source of N from triethylamine precursor
[b] Amount of N successfully doped in TiO$_2$ (EDX analysis)
[c] Amount of N successfully doped in TiO$_2$ (CHNS analysis)

The FESEM images of un-doped and N-TiO$_2$ possessed agglomerates of spherical particles with an average particle size of 27 nm to 37 nm (Figure 4.11). Although it is observed that N-precursor have a minimal effect on the size and shape of the particles, there was a slight increment of particle size in N-doped TiO$_2$ prepared at lower nitrogen load. This could be partially due to the larger size of nitrogen atomic radius as compared to the oxygen atomic radius in doped TiO$_2$. This observation contradicts to previous work where a significant decreased in the particle size was observed in N-doped TiO$_2$ (Sathish, Viswanathan, Viswanath, & Gopinath, 2005). At higher nitrogen loading, the particles agglomeration appeared less, thus homogeneity and dispersibility of the particles were enhanced. This was clearly revealed in HR-TEM images (Figure 4.12) whereby N1-TiO$_2$ appeared more dispersed as compared to N0-TiO$_2$. Both samples shows irregular crystal size ranging from 11 nm to 22 nm, whereby larger crystallite size was observed in doped TiO$_2$.
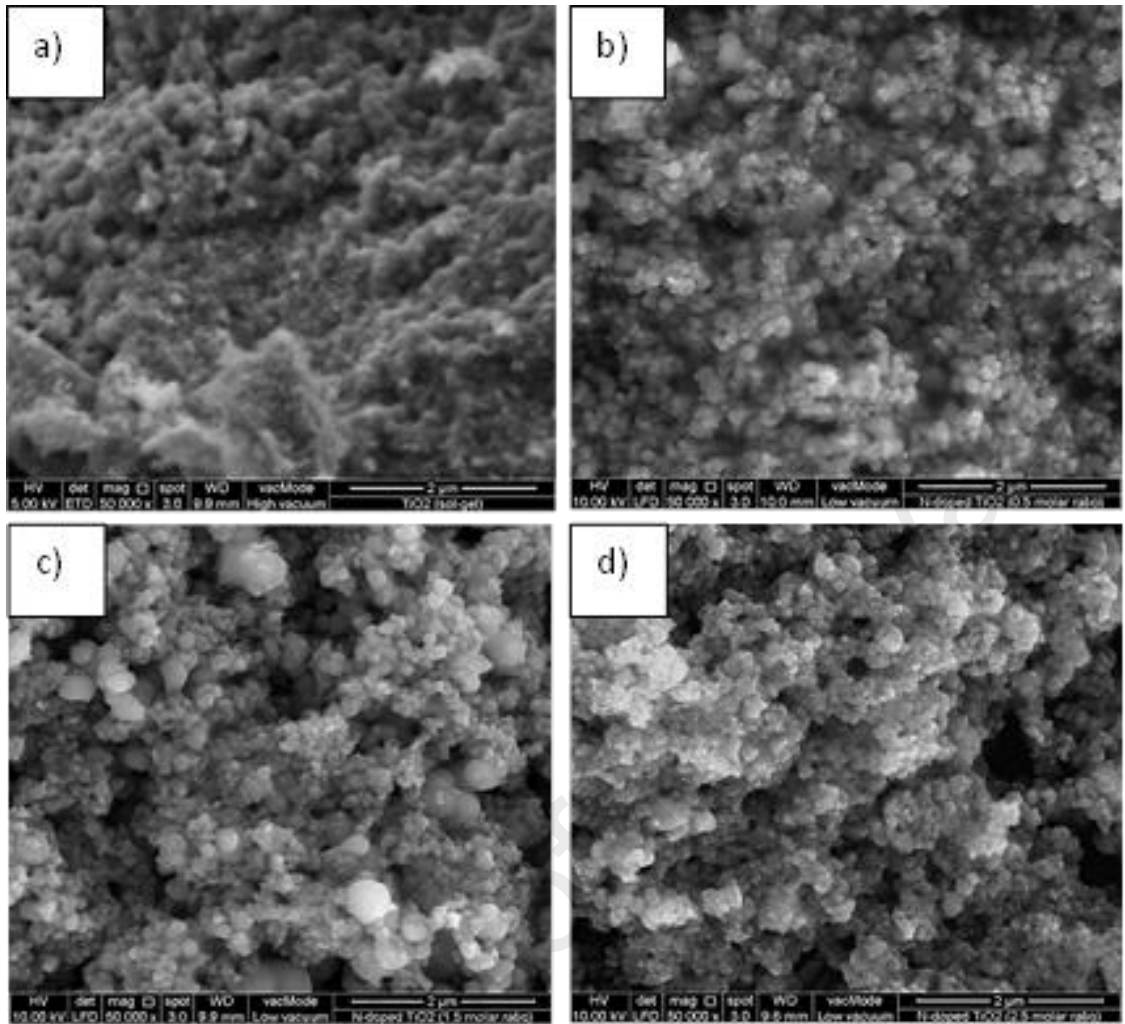
Figure 4.11: FESEM images of a) un-doped TiO_2 (N0-TiO_2), b) N1-TiO_2, c) N3-TiO_2 and d) N5-TiO_2 at 50,000x magnification
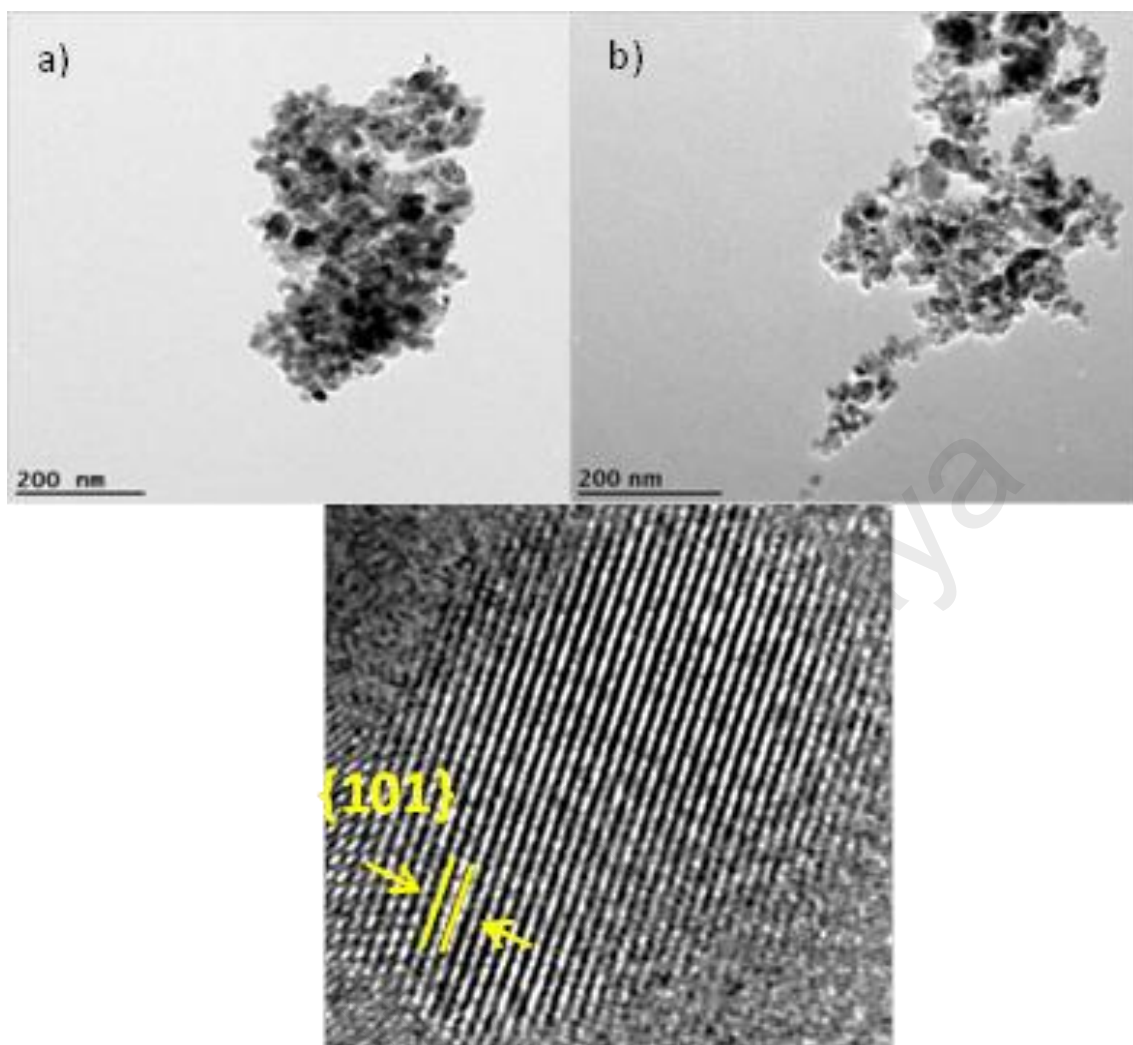
Figure 4.12: HR-TEM images of TiO$_2$ powders for a) N0-TiO$_2$, b) N1-TiO$_2$ and c) lattice spacing of anatase phase for N1-TiO$_2$

The BET specific surface area and porosity presented in Table 4.5 showed less influence on the change of porosity after nitrogen doping, as compared to the specific surface area. The nitrogen absorption-desorption isotherms in Figure 4.13 showed strong interaction of isotherm type IV and narrowed distribution of uniform mesoporous pores in the range of 2 nm to 50 nm (Xiang, Yu, Wang, & Jaroniec, 2011).
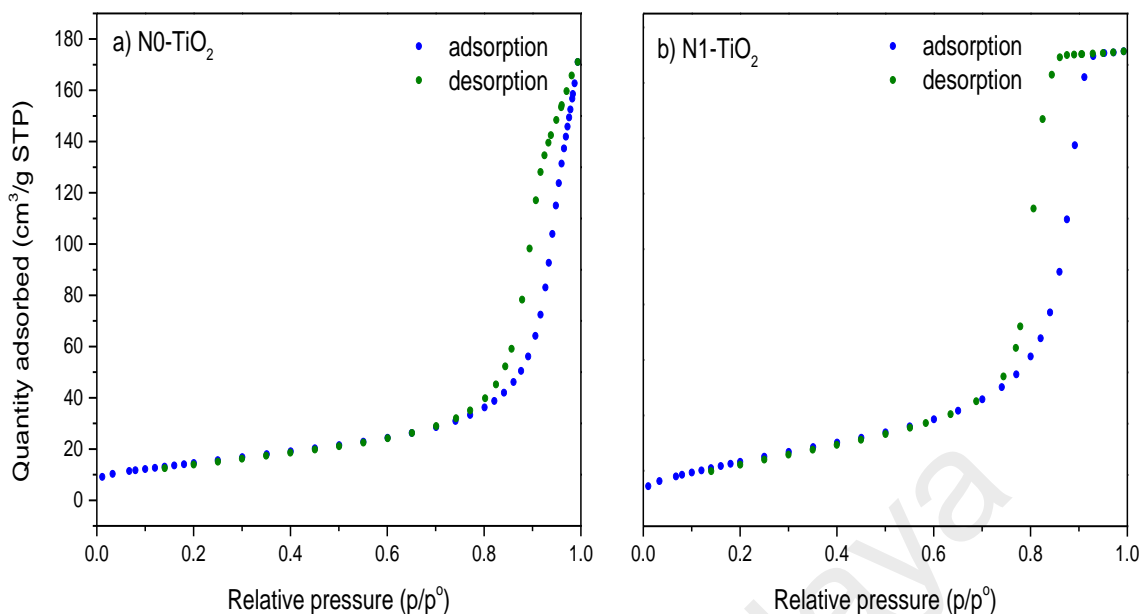
Figure 4.13: Nitrogen adsorption-desorption linear isotherm (Type IV) for a) N0-TiO$_2$ and b) N1- TiO$_2$

4.2.2 Structure and crystallinity

Un-doped TiO$_2$ consisted of two crystal phases, namely anatase and rutile (Table 4.5). Interestingly, all doped TiO$_2$ showed predominant anatase phase and enhanced crystallinity under all synthesis condition. A major peak corresponding to (101) anatase plane is observed at angle 25°, followed by minor peaks at 37°, 47°, 54°, 55°, 62°, 69°, 70° and 75° and is based on JCPDS 731764 (Figure 4.14).

During the sol-gel process, the crystal growth rate exceeded the nucleation rate as a result of N-dopant introduction. The presence of nitrogen in TiO$_2$ inhibits the condensation of spiral chain of anatase TiO$_6$ octahedral to linear chain of rutile TiO$_6$ octahedral. This can be seen from the disappearance of rutile major plane (110) at 27° angle after the addition of nitrogen. Similar observation was reported whereby the addition of nitrogen improved the thermal stability of the catalyst by increasing the temperature required for rutile phase formation (Ananpattarachai et al., 2009). It was further observed that nitrogen doped in TiO$_2$ affects the full width of half maximum (FWHM), an indication of crystal size changes and lattice distortion (Figure 4.15). At

low nitrogen loading, there was a significant narrowing of FWHM, and the crystal size

increased from 23 nm to 34 nm. The drastic change in the crystal size, however, did not

affect the lattice spacing as shown in Table 4.5 and were observed by others (Bae, Yun,

Ahn, & Kim, 2010). All crystallite size were calculated by Scherer's formula using the

highest intensity peak of the predominant phase (Patterson, 1939).

Table 4.5: Crystal phase, crystallite size, band gap, surface area and porosity of un-doped and N-TiO$_2$

Sample	Weight fractions of phase (%)		Average crystallite size, nm	d spacing	Band gap	BET surface area	Porosity
	Anatase	Rutile		Å	eV	m^2/g	cm^3/g
N0	94	6	23.0	3.50	3.00	48.98	0.235
N1	100	-	34.5	3.50	2.92	30.32	0.221
N2	100	-	34.5	3.50	2.93	26.61	0.245
N3	100	-	29.6	3.51	2.89	34.88	0.113
N4	100	-	29.6	3.51	2.93	38.78	0.134
N5	100	-	23.0	3.49	2.86	55.02	0.269
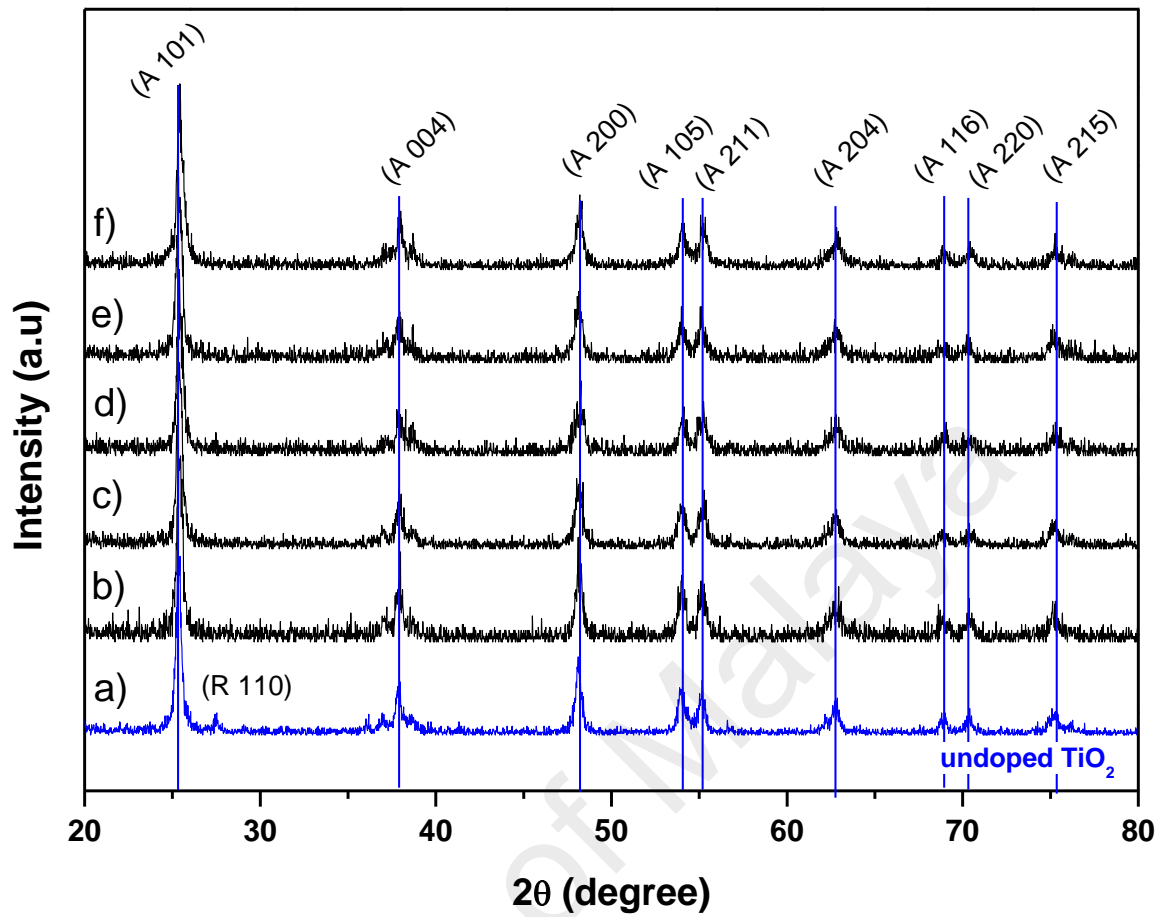
Figure 4.14: XRD spectra showing the crystal structure of a) N0-TiO$_2$, b) N1-TiO$_2$, c) N2-TiO$_2$, d) N3-TiO$_2$, e) N4-TiO$_2$ and f) N5-TiO$_2$
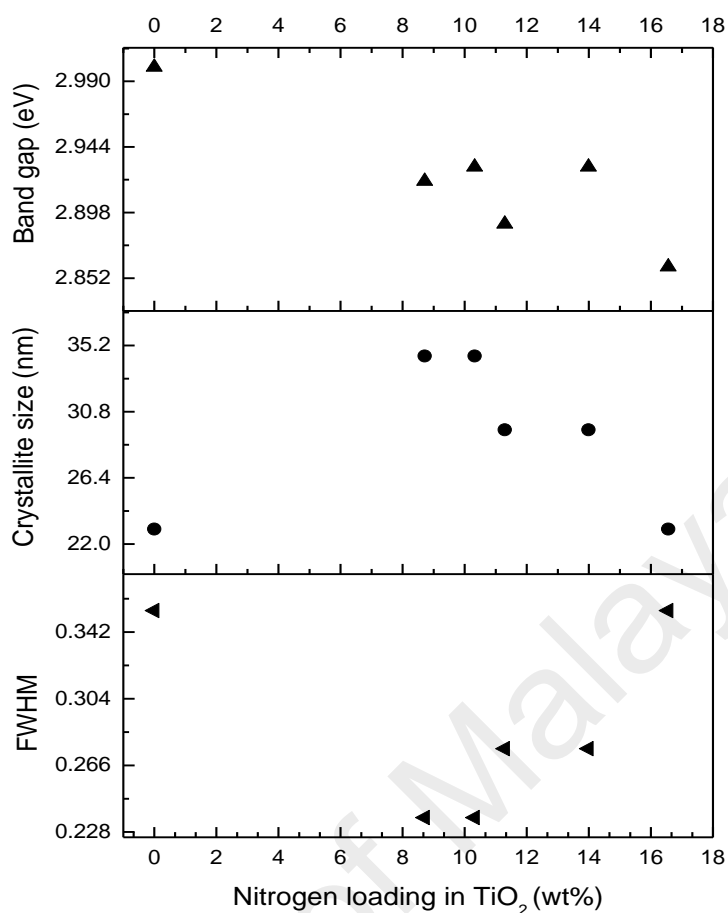
Figure 4.15: Effect of FWHM, crystallite size and band gap alterations at different loading of nitrogen in TiO₂

4.2.3 Chemical composition

All prepared photocatalysts showed significant anatase phase with major bands at 144 cm^{-1} (E_g), 395 cm^{-1} (B_{1g}), 515 cm^{-1} (A_{1g}) and 637 cm$_{-1}$ (E_{1g}) (Figure 4.16). A weak, but apparent Raman band of anatase was shown at 195 cm^{-1} (E_g). In all N-doped TiO₂, no remarkable rutile band at 446 cm^{-1} (E_g) was observed and supports our observation in the X-ray diffraction (XRD) spectrum. Although rutile phase was present in un-doped TiO₂, no significant rutile band can be seen in the Raman spectra. In previous work, N-TiO₂ was also prepared using different N : Ti atomic ratios by solvothermal method and showed predominant anatase bands in the Raman spectra (Yang, Jiang, Shi, Xiao, & Yang, 2010). It was observed that the amount of nitrogen loaded in TiO₂ influences the size of the particles. Higher nitrogen loading results to a red Raman shift,

indicating smaller particles size (Figure 4.17). This observation was in good agreement with those shown in the XRD data.
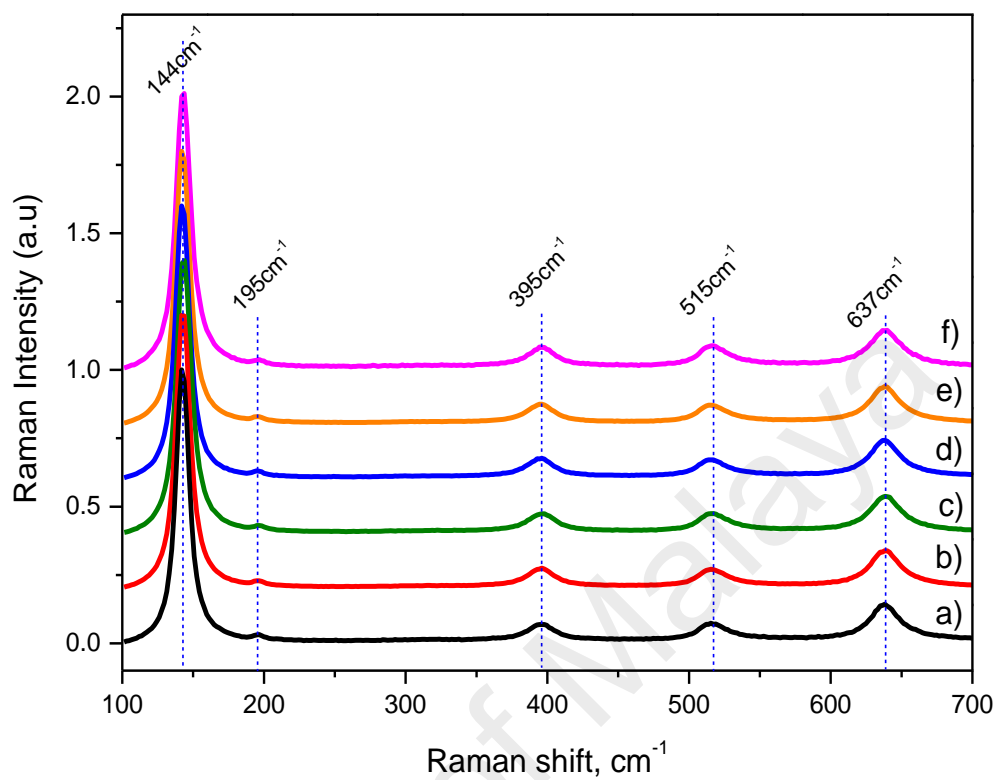
Figure 4.16: Raman spectra of a) N0-TiO$_2$, b) N1-TiO$_2$, c) N2-TiO$_2$, d) N3-TiO$_2$, e) N4-TiO$_2$ and f) N5-TiO$_2$
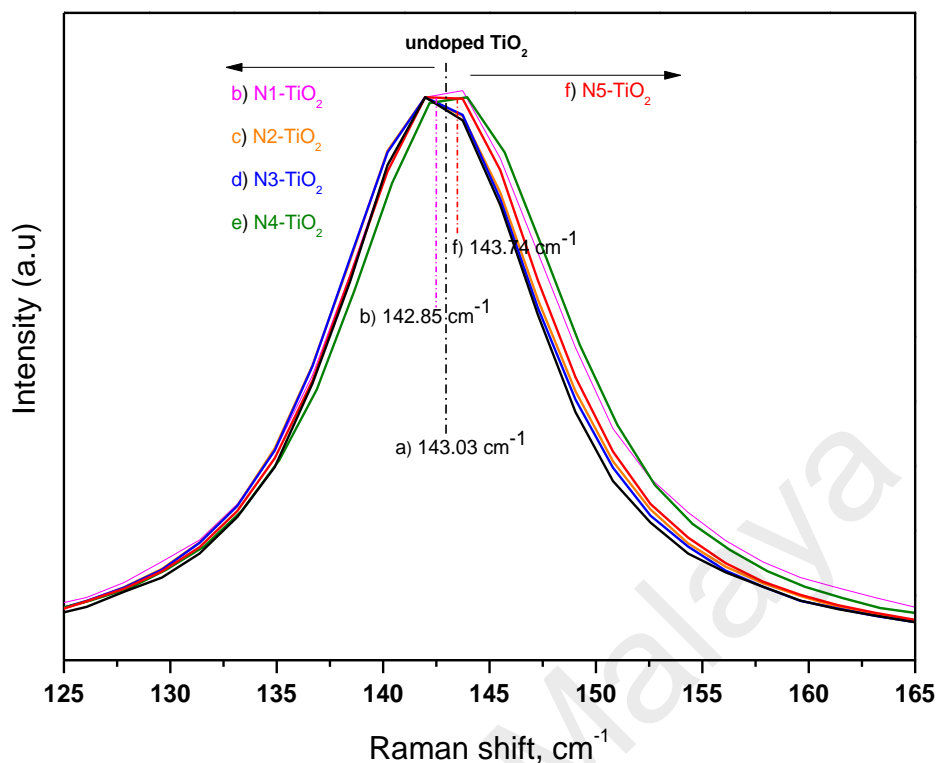
Figure 4.17: Raman localized spectra of a) N0-TiO$_2$, b) N1-TiO$_2$, c) N2-TiO$_2$, d) N3-TiO$_2$, e) N4-TiO$_2$ and f) N5-TiO$_2$

FTIR analysis was used to analyze the presence of nitrogen in TiO$_2$ prior to doping at different loading. In Figure 4.18a-b, similar spectra were observed in both un-doped and N-doped TiO$_2$ around 2363-2360 cm^{-1} and 700-400 cm^{-1} which corresponds to absorbed CO$_2$ (Tian, Qian, Hu, Sun, & Du, 2012) and Ti-O stretching and Ti-O-Ti bridging stretching mode (Umar, Yusri, Rahman, Saad, & Salleh, 2012), respectively. The enlarged FTIR spectra from 1700 to 1200 cm^{-1} revealed significant differences between both catalysts (Figure 4.18c). N-doped TiO$_2$ possessed multiple peaks within this region which corresponds to surfaced absorbed nitrogen at 1463-1384 cm^{-1} (Yang et al., 2010) and lattice nitrogen at 1632 cm^{-1}, 1546 cm^{-1}, 1338 cm^{-1} and 1255 cm^{-1} (Livraghi et al., 2006).
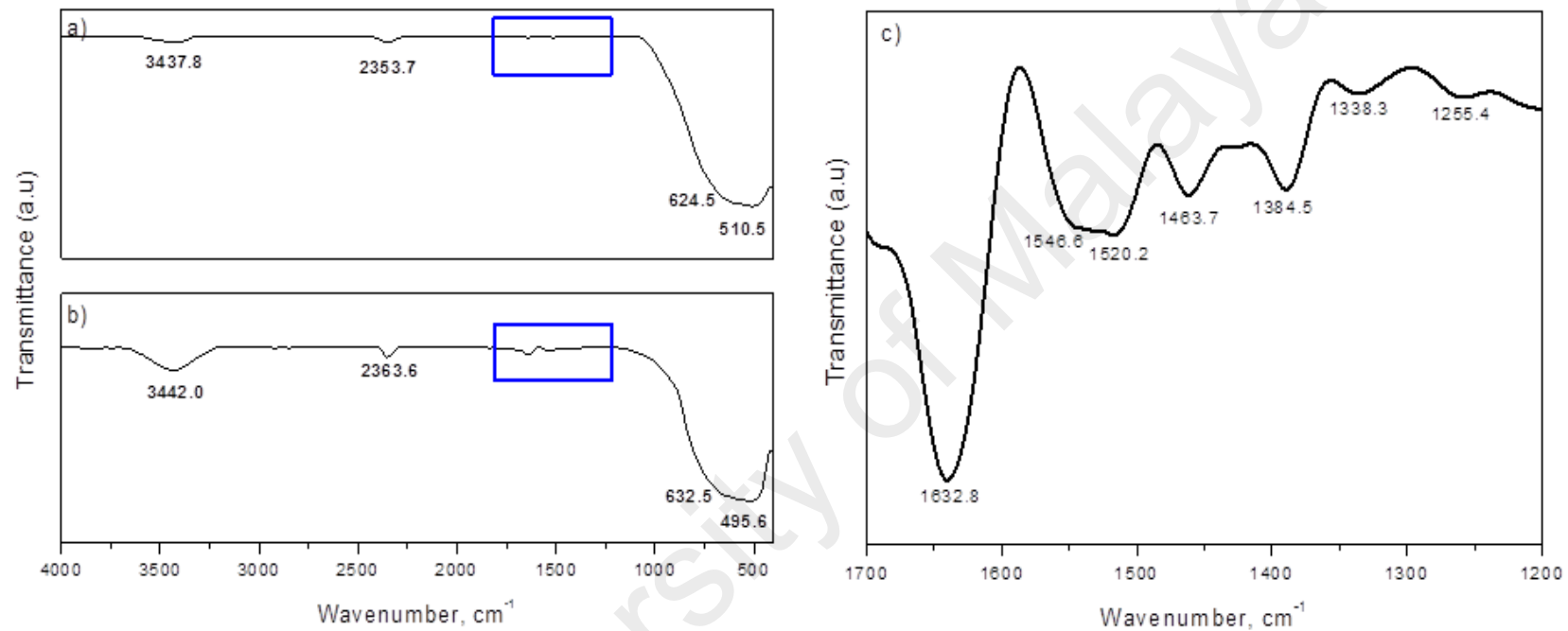
Figure 4.18: FTIR spectra of a) N0-TiO_2, b) N1-TiO_2 and c) enlarged FTIR spectra of figure 4.18b) from 1200 cm^{-1} to 1700 cm^{-1}

4.2.4 Surface characterization

In Figure 4.19, no nitrogen signal was detected in un-doped TiO_2. In N-doped TiO_2, the binding energy, E_g of N 1s spectra was observed at 400.4 eV and no other E_g was present between 395 to 399 eV and above 400.4 eV. From previous work, interstitial nitrogen showed E_g around ~400 to 402 eV, 399.6 eV and 399.8 eV (Emeline, Kuznetsov, Rybchuk, & Serpone, 2008; Wang et al., 2009) In addition, molecularly chemisorbed γ–N_2 showed E_g around ~400 to 402 eV (Hu, Wang, Zhang, Zhang, & Liu, 2014). It is still unclear on the nature of N 1s present at E_g of ~400 to 402 eV, as whether nitrogen was doped interstitially or present as chemisorbed N_2 or mutually. The difference in E_g and XPS intensity for each reported work were influenced by the selection of dopant (Ananpattarachai et al., 2009) and catalyst preparation routes (Wang et al., 2009). In this work, triethylamine was used as the source of nitrogen precursor.
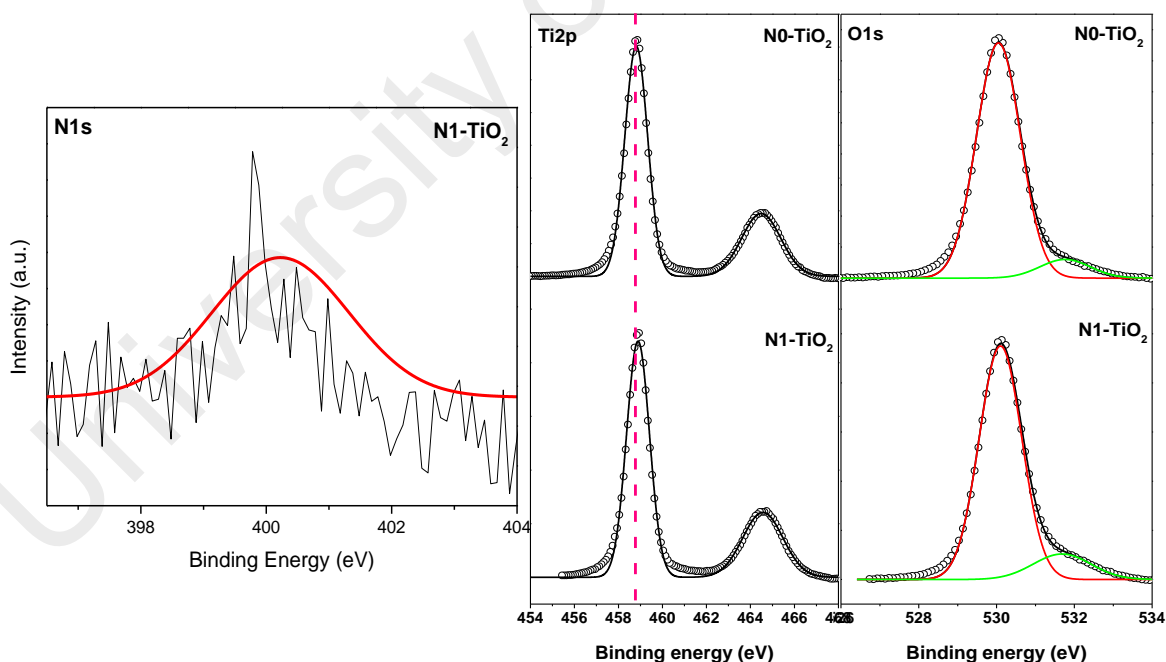
Figure 4.19: XPS Spectra of N 1s, Ti 2p and O 1s of N0-TiO_2 and N1-TiO_2

Ananpattarachai et al (2009) used similar dopant in preparing N-TiO$_2$ and obtained E$_g$ at 402.5 eV, which was assigned to nitric oxide or nitrogen monoxide (NO) and nitrite (NO^{2-}), corresponding to an interstitial doped nitrogen in TiO$_2$. Hu et al (2014) also incorporated triethylamine as N-precursor in synthesizing N-TiO$_2$. Interestingly, it was reported that the point of dopant introduction during the sol-gel process determines the final state of N 1s formed in TiO$_2$. Molecularly chemisorbed N$_2$ are generally present if the crystallization process of TiO$_2$ occurs before the introduction of nitrogen and shows N 1s E$_g$ around 400.5 and 401.4 eV. Similar broad N1s XPS emission was also observed in other reported work (Nosaka, Matsushita, Nishino, & Nosaka, 2005), however strong correlation could not be made as different preparation procedures was employed. Viswanathan & Krishanmurthy (2012) reviewed that low nitrogen loading in TiO$_2$ generally consists of E$_g$ of N 1s spectra within ~396-397 eV while for high nitrogen loading at ~400 eV, however no quantification was mentioned. In this work, the reported E$_g$ of N1s peak at ~400.4 eV was attributed to interstitial nitrogen in the TiO$_2$ matrix or chemisorbed molecular γ-N$_2$. For the latter, TiO$_2$ was doped at high nitrogen loading, however, no significant change in the crystal phase and lattice spacing were observed (Table 4.5). This suggests the presence of chemisorbed molecular γ-N$_2$ on the surface of TiO$_2$. As the amount of nitrogen doped in TiO$_2$ increased, the crystallinity of TiO$_2$ decreased. Observations made from FTIR (Figure 4.18) supports the presence of O-Ti-N bonds as clear demarcation of lattice nitrogen was observed especially in the magnified FTIR spectrum from 1200 – 1700 cm^{-1}. This could be attributed to O-Ti-N in the bulk of the doped photocatalyst as XPS did not detect any E$_g$ for surface substituted nitrogen. N-H bond and NO$_X$ were not present in N1-TiO$_2$ due to the absence of E$_g$ around 398.7 eV and above 403 eV respectively (Wang et al., 2009). This was further supported by the FTIR spectrum in Figure 4.18c, as ammonia (N-H) band was not present. A slight negative shift of E$_g$ in Ti 2p$_{3/2}$ between un-doped TiO$_2$

and N-doped TiO_2 was observed in previous work when nitrogen substitutes for oxygen atom in TiO_2 lattice (Cong, Zhang, Chen, & Anpo, 2007). The change of E_g was due to the difference of electronegativity of nitrogen and oxygen atom in N-Ti-O linkage, causing partial electron transformation from N to Ti as oxygen is more electronegative than nitrogen, thus increasing the electron density of Ti. However, this was not observed in this study hence the probability of surface substituted nitrogen in TiO_2 is less likely. Based on Ti 2p spectra, the E_g of the photoelectron peak illustrates the existence of Ti^{4+} species in the TiO_2 nanostructures (Stewart, 2009). The two de-convoluted O 1s peaks remained unchanged for both un-doped and N-doped TiO_2 at 530.0 eV and 531.7 eV. The former represents metallic oxide (Ti-O) and the latter represents surface hydroxyl, -OH and was in agreement with the IR frequency observed in N0-TiO_2 and N1-TiO_2 at 3437.8 cm^{-1} and 3442 cm^{-1} respectively. No absorbed H_2O at ~532.7 eV was detected in the XPS peak (Liu et al., 2008). The presence of nitrogen in TiO_2 increased the number of hydroxyl sites and enhanced the hydrophilicity of the catalyst. The hydroxyl peaks observed in both FTIR (Figure 4.18) and XPS (Figure 4.19) analysis were more significant in N1-TiO_2 as compared to N0-TiO_2. Previous work also showed that nitrogen in TiO_2 facilitates the wettability of the catalyst surface, thus benefits the photocatalytic activity (Morikawa et al., 2005).

4.2.5 Light absorption and photoluminescence behavior

The UV-Vis spectra of un-doped and N-doped TiO_2 photocatalyst prepared at different nitrogen loading are presented in Figure 4.20. The corresponding band gap was estimated using Kubelka-Munk function (Table 4.5). A significant increase of light absorption towards lower photons energy level was observed for all N-doped TiO_2, extending the absorption coverage towards 550 nm of the visible light region.
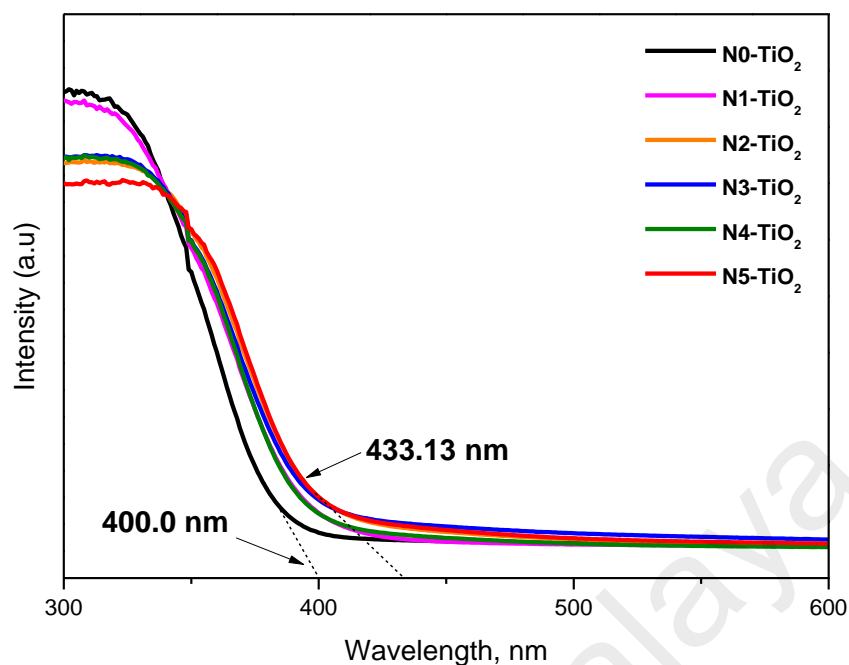
Figure 4.20: Absorption spectra for all prepared photocatalysts at different nitrogen loading

This was due to the additional impurity level created within the band gap, thus causing a shift of the Fermi level closer to the conduction band and thus narrowing of the band gap. This was further supported by Xiang et al (2011) whereby from the first principle density functional theory (DFT) calculation, interstitial N-precursor can induced local states above the valence band and was responsible for visible light response. According to Tian et al (2012), substituted nitrogen in the TiO_2 forms a narrow N 2p band, which overlapped with O 2p orbital, promoting greater electrons mobility from the valence band to the conduction band during photo-excitation. However, XPS data clearly showed no presence of substituted nitrogen in the TiO_2 lattice forming Ti-N-Ti linkages, but probable interstitial doping and chemisorbed γ-N_2.

Apart from that, the formation of oxygen vacancies to compensate for overall charge balance played an important role towards the narrowing of band gap as well. The formation of oxygen vacancies in N-doped TiO_2 facilitates wider light absorptions above 500 nm (Zhang et al., 2014) and was in good agreement with XPS and FTIR

results. Furtherance, nitrogen existence in TiO_2 induces the formation of oxygen vacancies (Wu, Lin, & Lin, 2013). Despite the remarkable improvement of photonic efficiency, the fate of electrons and holes during photo-excitation determines the overall photoactivity mechanism. The incorporation of nitrogen in TiO_2 shows broad visible emission around 530 nm, which affects the electrons and holes recombination rate (Figure 4.21). At high nitrogen loading, the photoluminescence intensity increases due to increasing number of oxygen vacancies and defect sites. Excessive oxygen vacancies acts as electrons and holes recombination centres and thus reduces the amount of surface radicals, giving rise to high photoluminescence intensity (Tian et al., 2012). It was observed that electrons and holes recombination were inhibited at low nitrogen loading due to fewer charge trapping sites, hence facilitates better photocatalytic activity. The PL peak at 450 and 500 nm indicates defects presence in the N-doped TiO_2 and could act as new adsorption centers (Li et al., 2005). Furthermore, the PL peaks showed broad spectrum, which was an indication of oxygen vacancies.
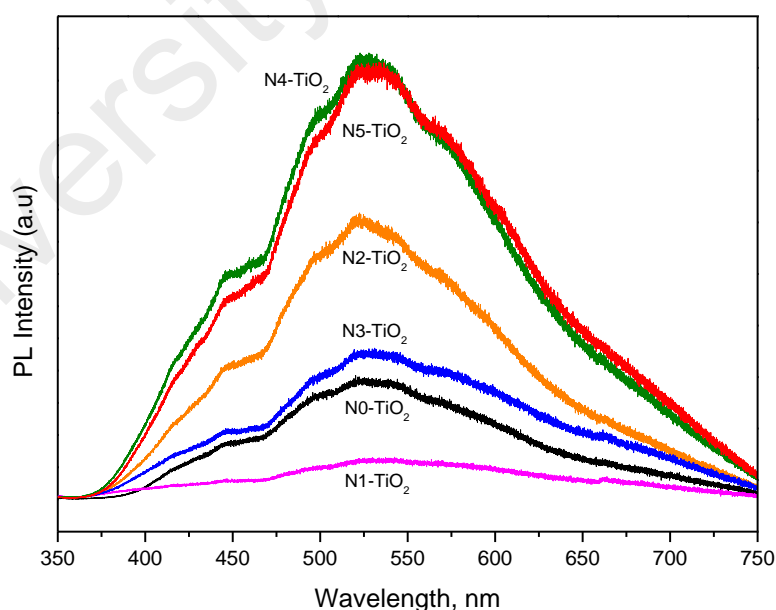
Figure 4.21: Photoluminescence spectra for all prepared photocatalyst at different nitrogen loading

4.3 Fluorine-doped TiO$_2$ (F-TiO$_2$)

4.3.1 Morphology and textural properties

The morphology and composition of all prepared photocatalysts were examined under FESEM at 200,000x magnification and EDX respectively (Figure 4.22, Table 4.6). Agglomeration of sphere shape particles dominated the structure of both un-doped and F-doped TiO$_2$, and was more severe in F1-TiO$_2$. The particles were most dispersed in F3-TiO$_2$. This imply that different fluorine concentration doped in TiO$_2$ affects its surface charges and hence, its dispersion. The size of F-doped TiO$_2$ was also larger by 10 to 30 nm relative to F0-TiO$_2$ (Table 4.7). In overall, the particles of un-doped TiO$_2$ have smooth edges comparative to more defined edges of F-doped TiO$_2$. Mixed morphologies of spheres and compressed truncated tetragonal bipyramids were observed in F4-TiO$_2$. Less significant change in morphology was observed for other F-doped TiO$_2$.
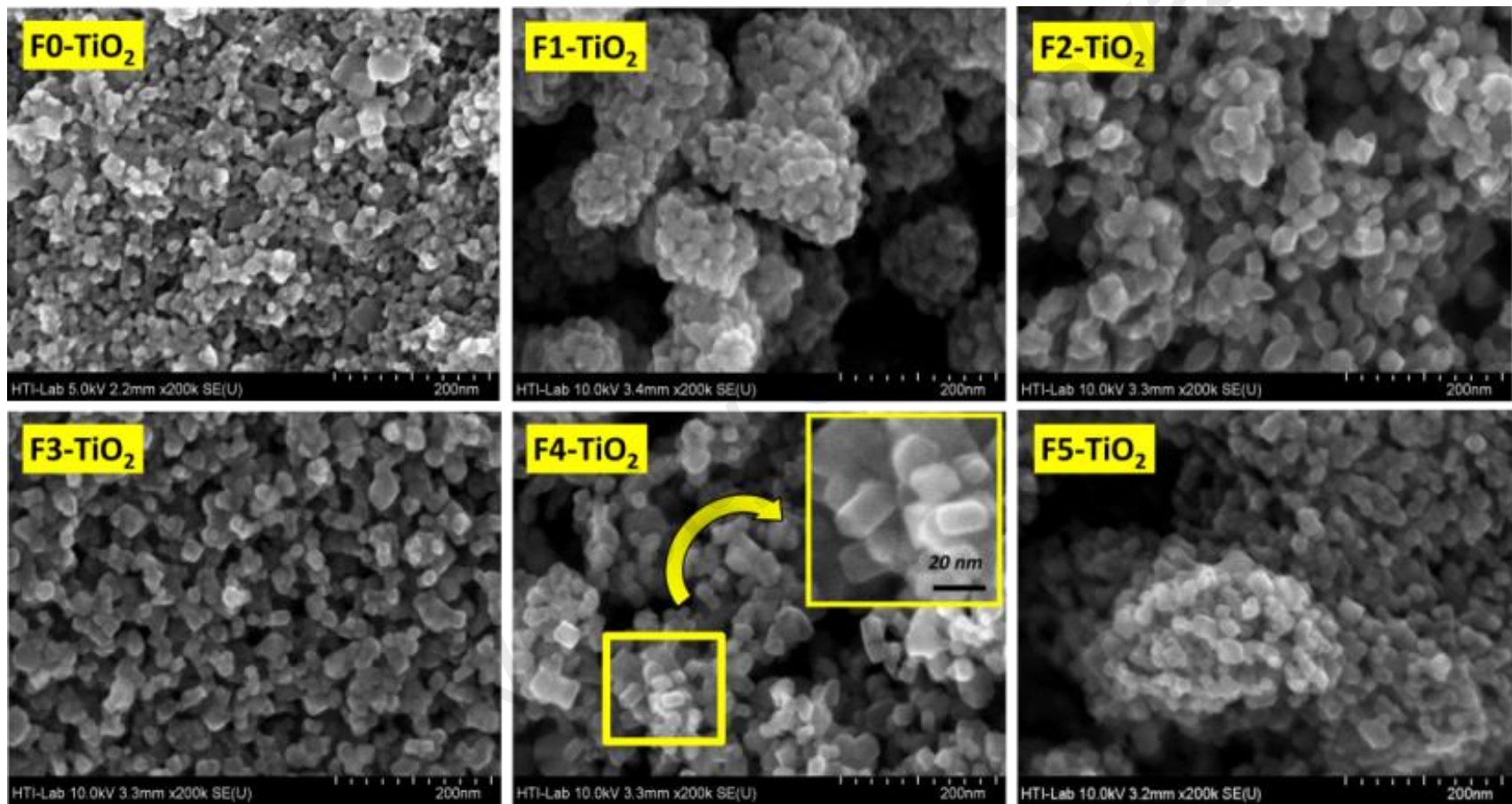
Figure 4.22: Morphology of un-doped TiO$_2$ (F0-TiO$_2$) and F-doped TiO$_2$ at 200,000x magnification

Table 4.6: Elemental composition (%) by EDX in F-TiO$_2$

Catalyst	Atomic composition (%)			Stoichiometric ratio	
	Titanium (Ti)	Oxygen (O)	Fluorine (F)	Titanium (Ti)	Oxygen (O)
F0-TiO$_2$	31.79	68.21	-	1.00	2.14
F1-TiO$_2$	34.67	64.84	0.49	1.00	1.87
F2-TiO$_2$	22.29	76.87	0.84	1.00	3.44
F3-TiO$_2$	24.15	74.39	1.46	1.00	3.08
F4-TiO$_2$	22.89	75.28	1.82	1.00	3.28
F5-TiO$_2$	22.95	75.01	2.04	1.00	3.27

[a] FESEM analysis (Voltage 10kV, high vacuum)

Fluorine acts as a morphology controlling agent and influences the direction of crystal growth (Liu et al., 2010). The change of TiO_2 structure after adding fluorine is related to the change of surface energy of the nanocrystals (Bourne & Davey, 1976; Chen, Jiang, Geng, Zhu, & Yang, 2008). In this work, trifluoroacetic acid (TFA) was opted as fluorine precursor due to the non-labile C-F bonds, instead of highly hazardous hydrofluoric acid. Relative to hydrofluoric acid, TFA has larger acid dissociation constant (stronger acid), and generate ions easily in an aqueous environment. Nevertheless, in TFA, the fluoride ions dissociates in the form of bulky CF_3COO^- ions, thus direct contact between F^- ions and titanium oxo-polymer (O-Ti-O) during crystal growth process are limited to a certain extent, if compared to hydrofluoric acid and NH_4F. The accessibility of F^- ions during crystal growth influences the structure of F-doped TiO_2. This explains why less drastic changes in the morphology of F-doped TiO_2 were observed (Figure 4.22) if compared to the flower-like, cubic shape and hollow TiO_2 box prepared using hydrofluoric acid (Ong et al., 2014).

It is worth to mention that the insertion of fluorine in TiO_2 does not necessarily require the presence of oxygen vacancy (Czoska et al., 2008). Interestingly, the atomic concentration of oxygen in F-doped TiO_2 increased especially in F1-TiO_2 and onwards (Table 4.6) and was attributed to the residual thermal degradation products of fluorine precursor (Jollie & Harrison, 1997; Samsudin, Hamid, Juan, & Basirun, 2015). Previous work also observed increased oxygen content in TiO_2 prepared using pluronic F127 (Samsudin, Hamid, Juan, & Basirun, 2015). In addition, substituted fluorine atoms in TiO_2 lattice caused charge imbalance due to different oxidation state of oxygen and fluorine (Yu, Jiaguo, Wingkei, Zitao, & Lizhi, 2002). To compensate, the excess positive charge was neutralized by hydroxide ions by forming surface adsorbed hydroxyl radicals (Li et al., 2005). This could also contribute to the increment of oxygen atomic concentration on the surface of F-doped TiO_2. In addition, adsorbed

TFA was thermally degraded at 245 $^{\circ}$C and 325 $^{\circ}$C respectively and formed chemisorbed trifluoroacetate complex on TiO_2 surface (Yu, Ho, Yu, Hark, & Iu, 2003). Regardless, it is expected that most of unreacted TFA was removed in all F-doped TiO_2 prepared in this work, as the calcination temperature applied in this study was 500 °C. The decrement of surface area in F-doped TiO_2 (Table 4.7) evidenced crystal growth to larger size and the decrement of pore volume could be associated with pore blockage. Similar decrement in surface area in F-doped TiO_2 using TFA was also observed before (Yu et al., 2003). In Figure 4.23, F-doped TiO_2 remained and follow a type IV nitrogen adsorption-desorption linear isotherm (Brunauer-Deming-Deming-Teller classification) and indicates presence of mesoporous structure (2 to 50 nm) (Xiang & Yu, 2011). The shape of hysteresis loop changed from type H1 to type H3 in un-doped and F-doped TiO_2, respectively. The distinctive difference observed in Figure 4.23 indicates change in morphology and pore shapes from cylindrical to slits (Xiang et al., 2011).

Table 4.7: Particle size and textural properties of F-TiO_2

Catalyst	Average particle size, nm	Multilayer surface area, m^2/g	External surface area ratio, SA_{ext}	Cumulative pore volume, cm^3/g	Average pore width, nm
F0-TiO_2	10-30	38.77	0.9900	0.133	11.1
F1-TiO_2	10-50	26.61	0.1682	0.245	36.9
F2-TiO_2	10-50	23.32	0.0753	0.114	19.7
F3-TiO_2	10-50	17.51	0.1064	0.066	15.4
F4-TiO_2	10-50	24.65	0.2750	0.120	20.1
F5-TiO_2	10-50	31.21	0.0064	0.120	15.8
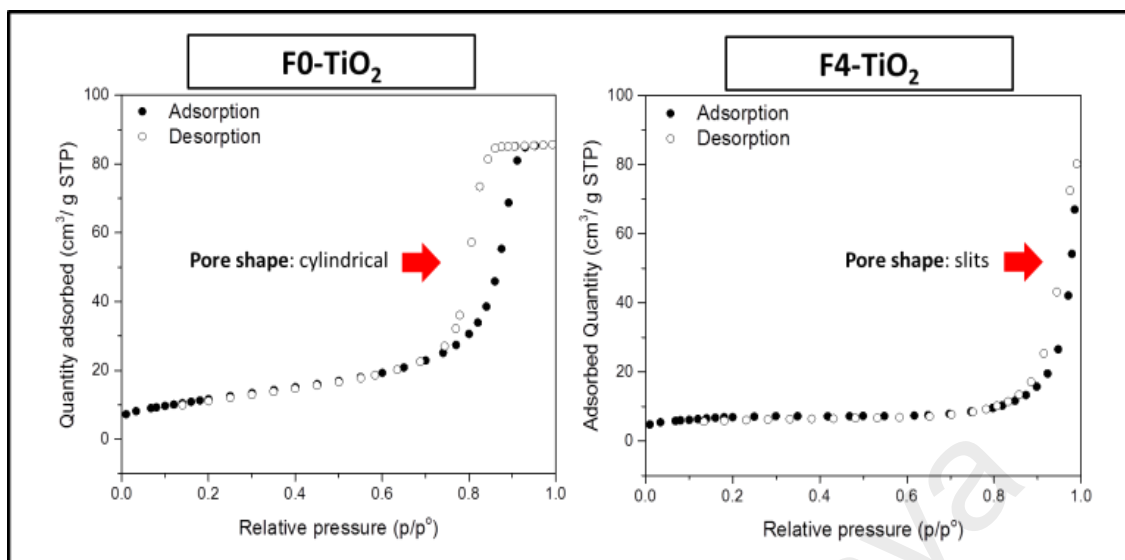
Figure 4.23: Nitrogen adsorption-desorption linear isotherm plot of un-doped TiO$_2$ (F0-TiO$_2$) and F4-TiO$_2$

4.3.2 Structure and crystallinity

The crystal structure and lattice spacing of un-doped and F-doped TiO$_2$ were observed under HR-TEM (Figure 4.24a,b). Lattice spacing of 0.351 nm was clearly observed in both photocatalysts (Inset, Figure 4.24a,b), representing (101) plane of anatase (Segomotso, Niu, Nasir, Tian, & Zhang, 2013). The lattice spacing at 0.235 nm which represents (001) plane was not observed in the HR-TEM image. The selected area electron diffraction (SAED) patterns of both un-doped and F-doped TiO$_2$ (F4-TiO$_2$) showed well-crystallized photocatalyst (Figure 4.24c,d). High crystalline TiO$_2$ was associated with increasing crystallite size and thus, narrowing of full width of half maximum (FWHM). This was clearly observed in F3-TiO$_2$ (Table 4.8). The SAED pattern confirmed the presence of {001} facet from the interfacial angle of (001) and (101) plane at 68.3° (Figure 4.24d) (Yang et al., 2008). This was also confirmed by observing two separate shapes of squares and compressed tetragonal bipyramids in Figure 4.24b. Using the evidence of {001} facet in Figure 4.24d, the schematic diagram of F4-TiO$_2$ was proposed (Figure 4.25a,b). Furthermore, the photocatalysts structures observed in FESEM (Figure 4.22) and HR-TEM (Figure 4.25b) of F4-TiO$_2$ were mostly

of spheres and less of squares and compressed truncated tetragonal bipyramids. Sphere shape morphology is associated with truncated tetragonal bipyramids with dominant {101} facets and less of {001} facets (Yu et al., 2014), and thus the majority of facets in F- doped TiO_2 were of {101} facets.
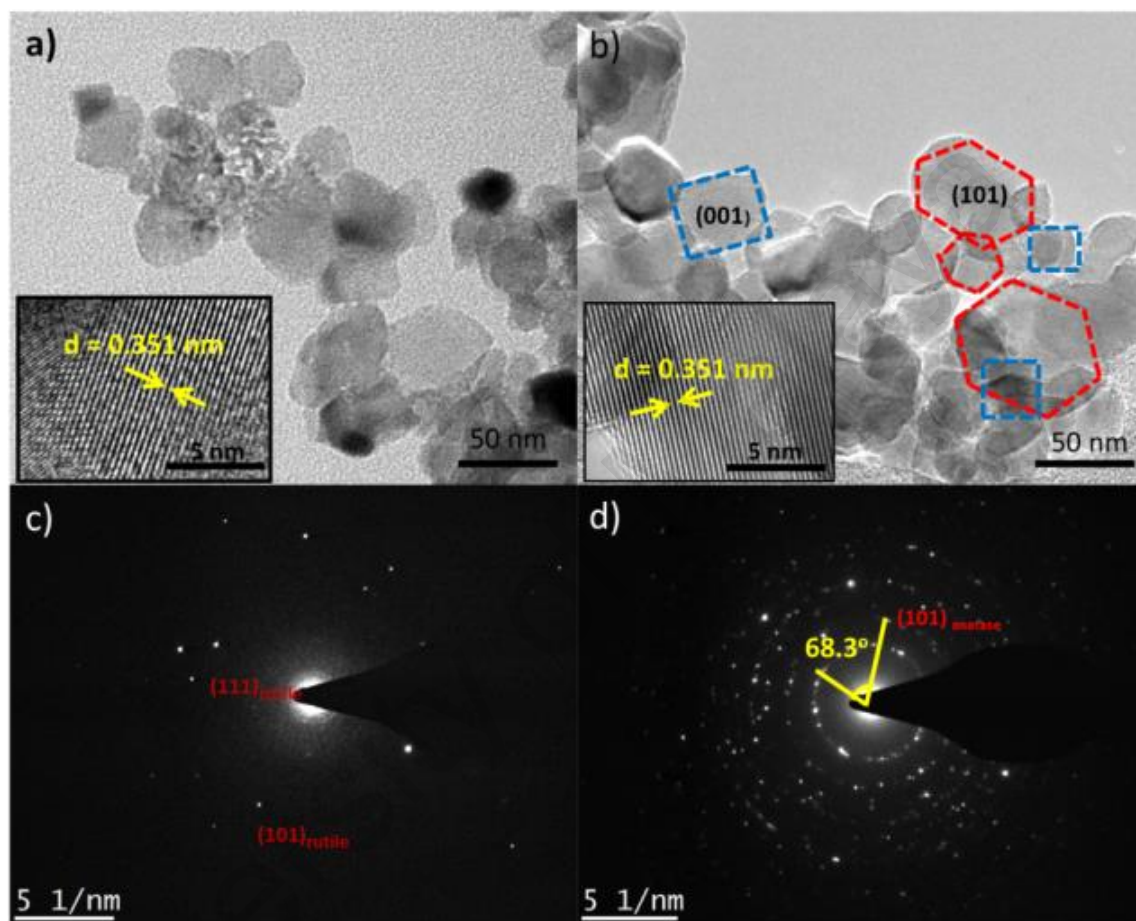
Figure 4.24: HR-TEM image with respective SAED pattern for a,c) un-doped TiO_2 (F0-TiO_2) and b,d) F4-TiO_2 (Inset: Enlarged lattice spacing images)
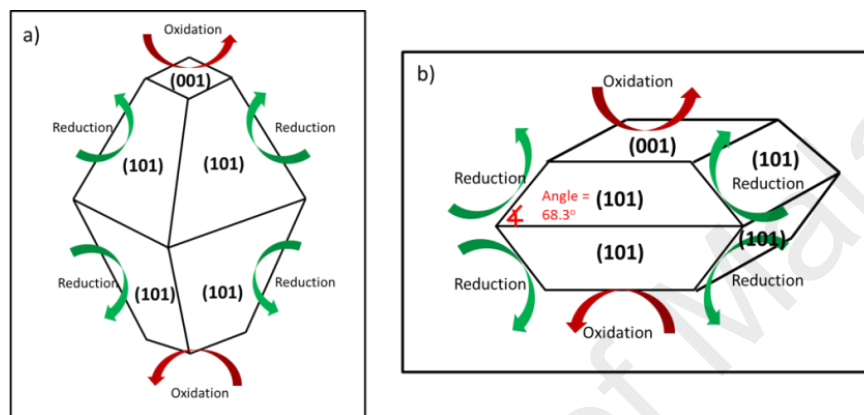
Figure 4.25: Proposed schematic structure of F4-TiO$_2$ for a) major structure and b) minor structure based on FESEM, HR-TEM (SAED) and XRD data of F-doped TiO$_2$ *(not drawn to scale)*

Table 4.8: Crystal phase ratio, crystallite size, plane with corresponding full width at half maximum (FWHM) and percentage of exposed surface active {001} facet of un-doped and F-doped TiO$_2$

Catalyst	Crystal phase ratio, wt %		Crystallite size, nm		Plane and Corresponding FWHM			Raman Count (a.u)		Percentage (%) of exposed {001} facets
	Anatase	Rutile	Anatase	Rutile	(101)	(004)	(200)	E$_g$ (414 cm^{-1})	A$_{1g}$ (515 cm^{-1})	(E$_g$/A$_{1g}$)*100%
F0-TiO$_2$	65	35	23.0	69.0	0.3542	0.4723	0.2755	21578	1574	7.36
F1-TiO$_2$	100	-	17.3	-	0.4723	0.2362	0.3149	16256	1294	8.00
F2-TiO$_2$	100	-	23.0	-	0.3542	0.2755	0.3936	29696	1966	6.62
F3-TiO$_2$	100	-	25.9	-	0.3149	0.3936	0.3936	14075	990	7.03
F4-TiO$_2$	100	-	18.8	-	0.4330	0.3149	0.5510	10267	721	7.02
F5-TiO$_2$	100	-	23.0	-	0.3542	0.6928	0.5510	11731	768	6.55

In un-doped TiO$_2$, two crystals phase of anatase and rutile were observed with calculated mass ratio of 65 : 35 using Spurr's equation (Figure 4.26a) (Spurr & Myers, 1957). Contrary to un-doped TiO$_2$, a single anatase phase was observed in all prepared F-doped TiO$_2$. The presence of F$^-$ ions adhered on the surface of TiO$_2$ was believed to accelerate the crystallization and growth of anatase TiO$_2$ due to *in situ* dissolution-recrystallization process (Yu et al., 2003). Contrary, the growth of rutile crystal phase is highly favored on defect-surfaces as the atoms possessed higher energy than those in the lattice. These surface defects, in turn, acts as a nucleation sites. The presence of F$^-$ ions hinders anatase-to-rutile crystal phase transformation due to reduced surface defects (Zhang, Li, Feng, Chen, & Li, 2006). The thermal property of TiO$_2$ also increased in F-doped TiO$_2$ and thus inhibits anatase to rutile phase transformation (Lv, Yu, et al., 2011). Therefore it was expected that the growth of rutile phase is hindered in F-doped TiO$_2$, calcined at the same temperature as un-doped TiO$_2$.

Yu et al (2015) observed increased crystallite size in F-doped TiO$_2$ using hydrofluoric acid, relative to un-doped TiO$_2$. In this work, the crystallinity and crystallite size varies in F-doped TiO$_2$ (Table 4.8) and were due to the different F$^-$ ions interactions with the medium during sol gel process and possibly limited accessibility of the bulkier form of F$^-$ ions (CF$_3$COO$^-$) during sol-gel. The type and concentration of F precursor also influences the properties of F-doped TiO$_2$ (Yu et al., 2014). In un-doped TiO$_2$, rutile crystal phase was observed in the absence of F$^-$ ions. Furthermore, TiO$_2$ prepared at low pH facilitate the growth of rutile and was aggravated in the absence of fluorine (Kim & Kwak, 2007). Other factors that affects crystal growth during sol gel process includes synthesis step, solvent, impurities, precursors, ageing and calcination process (Kim & Kwak, 2007; Samsudin, Hamid, Juan, & Basirun, 2015).

The FWHM of (004) and (200) planes were associated with TiO$_2$ anatase thickness in [001] direction and length in [100] direction respectively, as showed in Table 4.8 and

Figure 4.26b. The increased F$^-$ ions concentration in F-doped TiO$_2$ results to a decreased in both thickness and length of the catalyst structure. Moreover, the change of size in F-doped TiO$_2$ was shown to be erratic, and was similar to previous observation (Han et al., 2009), Thus, the change of size in F-doped TiO$_2$ was independent of F$^-$ ions concentration doped in TiO$_2$.

In Figure 4.27a, the XRD peaks were shown to shift slightly to higher Bragg angle in F-doped TiO$_2$ and was associated to oxygen vacancies due to F-doping (Ong et al., 2014), impurities (Hu et al., 2014) and {001} facets (Wei et al., 2012). Moreover, adhesion of F$^-$ ions is known to stabilize high surface energy of {001} facets during the synthesis step (Yu, Xiang, Ran, & Mann, 2010). Ethanol has been shown to play an important role in controlling the synthesis of TiO$_2$ with {001} facets as well (Xiang et al., 2011). Nevertheless, the growth of {001} facets was low, and hence, the majority of F-doped TiO$_2$ consists larger portion of {101} facets and supports the observed structure in FESEM and HR-TEM previously. In Figure 4.27b, the main Raman E$_g$ peak of anatase (at 144 cm^{-1}) shifted to higher frequency relative to F0-TiO$_2$. Such shift, coupled with peak broadening features oxygen vacancy in TiO$_2$ (Khan et al., 2014). Raman shift due to phonon confinement effect was absence as insignificant difference in crystallite size between un-doped and F-doped TiO$_2$ was obtained.
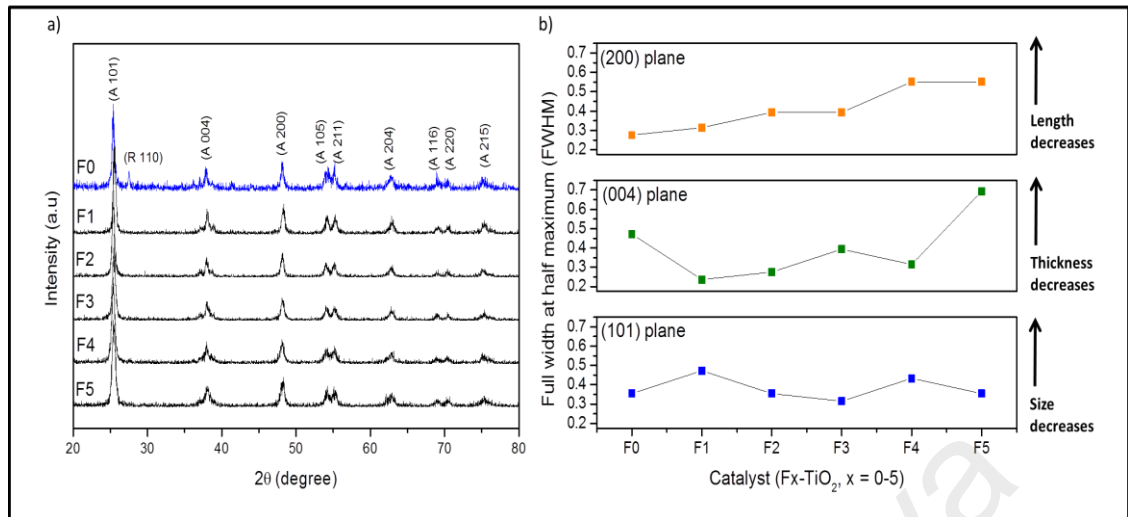
Fig 4.26: a) XRD pattern and b) FWHM data extraction for all prepared photocatalyst at different fluorine loading
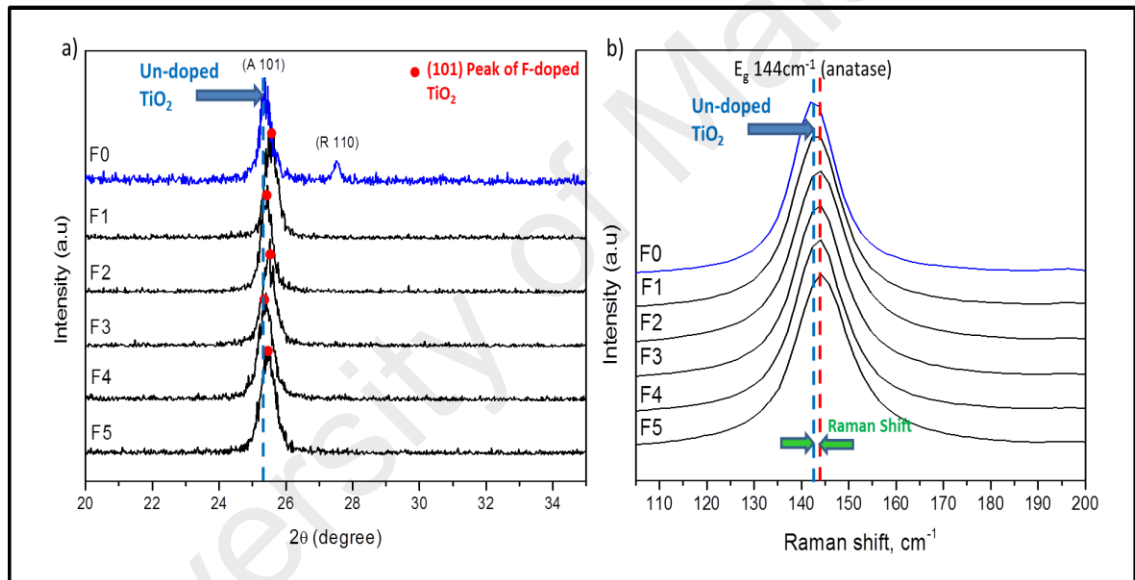
Figure 4.27: a) Enlarged (101) anatase plane of XRD and b) main E_g peak of Raman for all prepared photocatalyst (both showing peak shifts) at different fluorine loading

4.3.3 Light Absorption and photoluminescence behavior

Un-doped TiO_2 (F0-TiO_2) showed both UV and visible light absorption (Figure 4.28a). This was anticipated as rutile crystal phase in F0-TiO_2 has higher mass density than anatase, resulting to a more pronounced localization of 3d states and larger photon absorption due narrower band gap (Scanlon et al., 2013). F0-TiO_2 showed smallest band gap of 2.87 eV (Figure 4.28b) compared to single anatase and rutile crystal phase at 3.2 eV and 3.0 eV, respectively (Zhu & Gao, 2014). An increased in the band gap was

118

observed in all F-doped TiO_2 due to the absence of rutile crystal phase (Figure 4.28b). Thus, the type of crystal phase and ratio were shown to influence the band gap of TiO_2 (Scanlon et al., 2013). The presence of F^- ions in F-doped TiO_2 enhanced the light absorption intensity in the UV range, but showed weak visible light absorption and intensity (Figure 4.28a). Similar observation was observed in previous work (Khan et al., 2014), and thus fluorine was shown to improve the intrinsic UV-properties of TiO_2. The visible light absorption observed in F-doped TiO_2 (Figure 4.28aa) was triggered from extrinsic absorption owing to oxygen vacancies created by F-doping (Martyanov, Sitharaman Uma, Rodriguesa, & Klabundea, 2004). In F-doped TiO_2, the F 2p state is located below O 2p state and is less likely to affect TiO_2 optical properties (Kumar et al., 2013). However, charge imbalance caused by the absence of oxygen in TiO_2 forms Ti^{3+} and creates a shallow band below the conduction band and thus induced visible light absorption as well (Li & Liu, 2008). In F5-TiO_2, the band gap was the smallest relative to other F-doped TiO_2 due to the highest concentration of doped F. Higher concentration of F^- ions in TiO_2 results to larger oxygen vacancies, as evidenced by the largest shift in the XRD and Raman peaks. This was also observed in other prepared F-doped TiO_2 (Santana-Aranda et al., 2005; Sayilkan & Asilturk, 2005; Shahini et al., 2011).

The efficiency of charge carrier trapping, migration and transfer plus the fate of photo-generated electrons and holes pairs were analyzed using PL emission. Illumination with UV light results in broad visible PL arising from the recombination of oppositely charge carriers (Figure 4.28c). All of the prepared photocatalysts showed ligand to metal charge transfer (O^{2-} to Ti^{4+}) designated at 320 nm. A broadening of the PL spectrum was observed in F-doped TiO_2 with distinguished peaks at 450 nm, 500 nm, 530 nm, 550 nm and 650 nm. No PL peak was observed at 650 nm for un-doped TiO_2. The peak observed between 400 to 430 nm for all prepared photocatalysts

corresponds to a band gap between 2.87 eV (F0-TiO$_2$) and 3.03 eV (F5-TiO$_2$). The PL peak at 450 nm corresponds to self-trapped electrons, while 500 and 550 nm corresponds to defects or surface oxygen vacancies (Memesa et al., 2011). Interestingly, the PL spectrum was observed to red shift and was predominant in larger doped F-TiO$_2$. In previous work, the blue shift in the PL spectrum was assigned to the transformation of un-coordinated Ti^{3+} ions to surface oxygen vacancies and enhancement of green PL (mobile electron from CB to trapped holes 0.7-1.4 eV above the VB) (Jin, Liu, Lei, & Sun, 2015). As a red PL shift was observed for higher F-doped TiO$_2$, less un-coordinated Ti^{3+} ions were transformed to surface oxygen vacancies, and thus the enhancement of oxygen vacancies observed from the shift in XRD and Raman could be associated with bulk oxygen vacancies in TiO$_2$. Furthermore, the band gap in F5-TiO$_2$ was the smallest relative to other F-doped TiO$_2$, and this observation suggests larger concentration of Ti^{3+} under the conduction band, allowing larger absorption of visible light. In contrast to green PL, the PL peak at 650 nm represents red PL, which is the migration of trapped electrons located between 0.7 to1.4 eV under CB to VB holes (Dozzi et al., 2013). The above observation simply illustrated that the concentration of doped fluorine in TiO$_2$ played a significant role in determining electrons and holes recombination (Akplea et al., 2015). Furthermore, higher F-doped TiO$_2$ was shown to demonstrate good separation of electrons and holes, due to lower PL intensity. The slightly higher PL intensity observed in F5-TiO$_2$ compared to F4-TiO$_2$ could be the result of excessive oxygen vacancies, which acts a trapping site, and thus increase electrons and holes recombination (Rao & Okada, 2014).
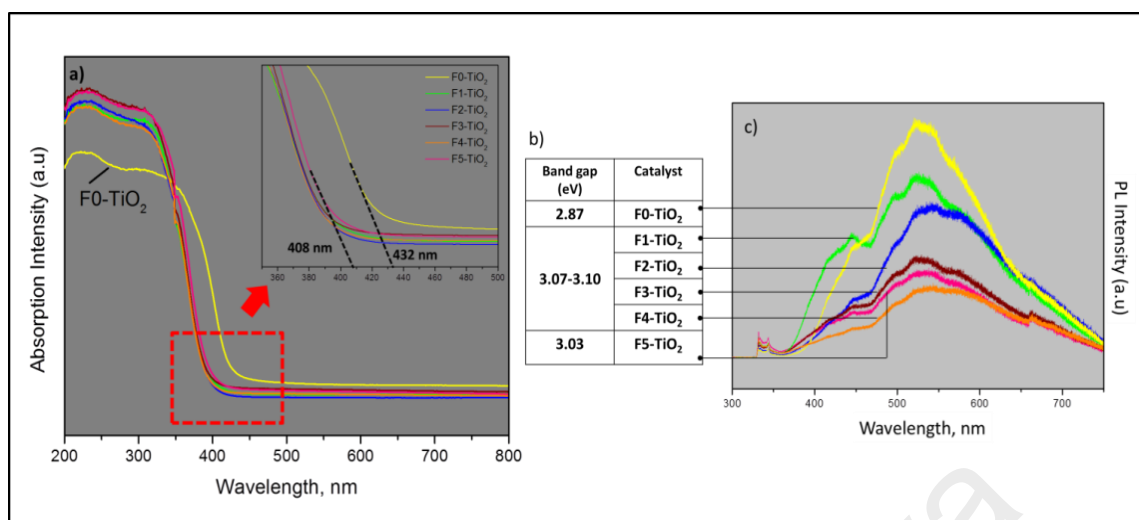
Figure 4.28: a) Full range absorption spectrum with enlarged view from 350 to 500 nm (inset), b) calculated band gap using K-M function and c) PL spectrum for all prepared photocatalyst at different fluorine loading

4.3.4 Surface characterization

The chemical state of un-doped TiO_2 (F0-TiO_2) and (F-doped TiO_2) F4-TiO_2 were evaluated and the individual spectrum of C 1s, F 1s, Ti 2p, O 1s and valence band was shown in Figure 4.29. The binding energy (E_g) of all elements were aligned with C 1s peak at 285 eV (C-H, C-C, C=C) corresponding to residual carbon from Ti and F precursor and adventitious hydrocarbon from the XPS instrument itself (Briggs, 1981). In the C 1s spectrum, the E_g at 286.7 eV and 288.8 eV belonged to C-OH and O-C=O bonds respectively. At E_g of 288.8 eV, the peak intensity was higher in F4-TiO_2 compared to F0-TiO_2 and was associated with residual organic complex not removed during calcination. This observation strongly explained the larger oxygen atomic concentration and decreased cumulative pore volume in F-doped TiO_2 (Table 4.7). No chemisorbed TFA molecules were present on TiO_2 surface due to the absence of peak at 292 eV (CF_2) and 294 eV (CF_3) (Ho et al., 2006).
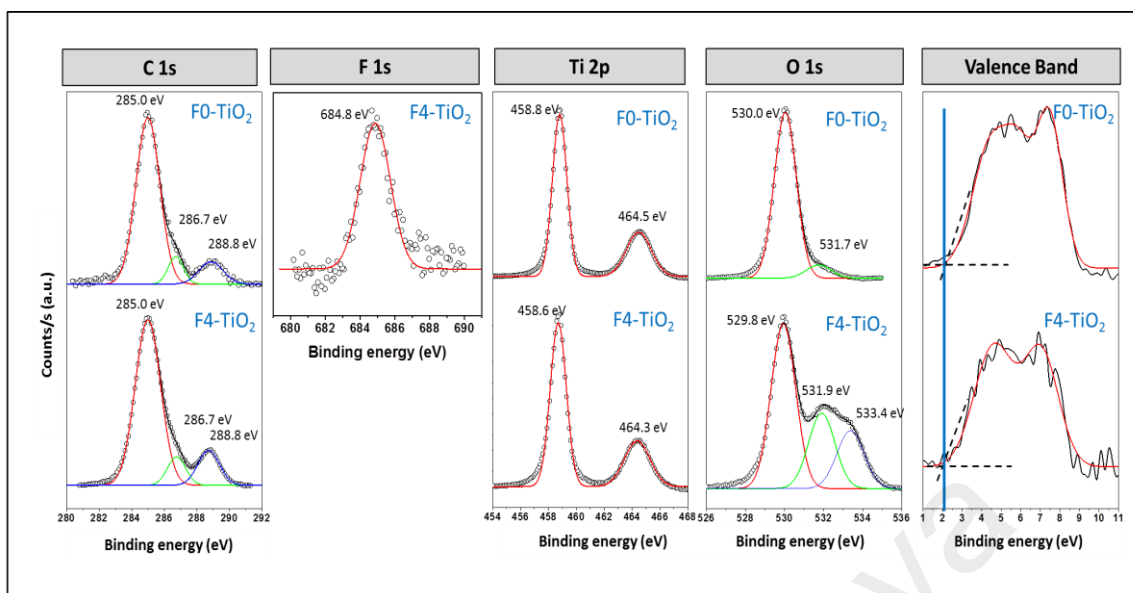
Figure 4.29: XPS spectra and valence band position for F0-TiO$_2$ and F4-TiO$_2$

In addition, no peak was also observed at 687.5 to 688.0 eV of the F 1s spectra which corresponds to CF$_3$ groups of chemisorbed TFA (Giannakopoulou, Todorova, Vaimakis, Ladas, & Trapalis, 2008). The only peak observed in the F 1s spectrum at 684.8 eV corresponded to physically adsorbed fluoride ions on TiO$_2$ surface or ligand exchange from ≡Ti-OH to ≡Ti-F (Lv, Yu, et al., 2011). Previous report demonstrated enhanced photocatalytic activity due to free ·OH radical formations as a result of ≡Ti-F bonds on F-TiO$_2$ surfaces (Lv, Cheng, Yu, & Liu, 2012). In the F 1s spectrum, no substituted F-doped TiO$_2$ was present (E$_g$ around 687.8 eV to 688.5 eV) and therefore eliminated the possibility of surface oxy-fluoride complex (E$_g$ at 683.6 eV) as well (Pelaez, de la Cruz, Stathatos, Falaras, & Dionysiou, 2009). Moreover, low-temperature heat treatment (500-700 °C) would typically form surface-fluorinated TiO$_2$, while substitutional F-doped TiO$_2$ is likely to form at higher calcination temperature of 900 °C (Padmanabhan et al., 2007). TiOF$_2$, which does not contributes to the photocatalytic activities (Samsudin, Hamid, Juan, Basirun, & Centi, 2015), was not present at E$_g$ of 685.3 eV to 685.5 eV (Li & Liu, 2008). Furthermore, the formation of TiOF$_2$ requires high concentration of fluorine doped in TiO$_2$ (Yu et al., 2015).

In Figure 4.29, Ti $2p_{3/2}$ and Ti $2p_{1/2}$ at ~458 eV and ~464 eV respectively, confirmed the presence of Ti^{4+} in both $F0\text{-}TiO_2$ and $F4\text{-}TiO_2$. No surface Ti^{3+} was detected at ~457.7 eV. Furthermore, surface Ti^{3+} is metastable and easily oxidized in air (O_2, H_2O, etc.) (Wang et al., 2013). Interestingly, there was a slight negative shift by ~0.2 eV in Ti 2p of $F4\text{-}TiO_2$ and was related to an increase in electron density of Ti atom. This observation cancelled out the possibility of titanium tetra-acetate complex, $Ti(CH_3COO)_4$ forming on the surface of TiO_2 as this would decrease the electron density of Ti due to higher electronegativity of acetate (CH_3COO^-) ion, and causes a positive Ti 2p shift instead. Therefore, our earlier observation in C 1s spectrum that evidences residual organic complex on the surface of F-doped TiO_2 was merely a weak physical absorption. Hence, the negative shift in Ti 2p was associated with surface O-Ti-F bonds formation. No surface Ti-O-F bond was present, as this would result in a positive shift in the Ti 2p binding energy.

The O 1s E_g at ~529 -530 eV and ~531-532 eV were observed in both $F0\text{-}TiO_2$ and $F4\text{-}TiO_2$. This E_g range corresponds to lattice oxygen (O^{2-}) and surface hydroxyl (OH) respectively (Liu et al., 2008). Additional E_g was observed in $F4\text{-}TiO_2$ at 533.4 eV, associated with organic C=O bond. As this peak was only observed in $F4\text{-}TiO_2$, it was attributed to residual TFA degradation products. There was no E_g peak at 535 eV associated with O-F_x bond. This was in agreement with our earlier observation confirming the absence of surface Ti-O-F bonds. Surprisingly, larger concentration of surface hydroxyls (OH) was observed in F-doped TiO_2 relative to un-doped TiO_2. This was related to the protonation of physically absorbed residual organic ions such as CH_3COO^- forming CH_3COOH on the surface of F-doped TiO_2.

In Figure 4.29, no shift in the valence band was observed in $F0\text{-}TiO_2$ and $F4\text{-}TiO_2$ as overlapping of the O 2p and F 2p energy level does not create new energy level above the valence band. Moreover, the valence band was not influenced by the ratio of {001}

and {101} facets as both facets have fairly similar valence band position (Yu et al., 2014), although {101} have a slightly higher CB position than {001} facets (Dozzi et al., 2013).

4.4 Nitrogen and fluorine co-doped TiO$_2$ (N,F-TiO$_2$)

4.4.1 Color, morphology and textural properties

The color of prepared N,F-TiO$_2$ photocatalyst was yellow, differently from the white color of un-doped TiO$_2$ and mono-doped TiO$_2$ with nitrogen and fluorine (Figure 4.30). This observation, which has been reported before (Kumar et al., 2013; Pelaez et al., 2009), simply demonstrates better ability of N,F-TiO$_2$ to absorb wider range of the solar light. The average particle size of un-doped TiO$_2$ was between 10 and 30 nm in diameter and increased up to 50 nm upon N and F incorporation (Figure 4.31a-c).

Figure 4.30: Appearance (color) of un-doped TiO$_2$, F-TiO$_2$, N-TiO$_2$ and N,F-TiO$_2$

Much interesting, the shape of particle was changed drastically. Un-doped TiO$_2$ showed irregular round-shape morphology with shape similar to truncated tetragonal bipyramid (Figure 4.31a). By increasing the dopant concentrations, it resulted to a progressive change of shape to compressed truncated bipyramid with profound edges (Figure 4.31b). Elongation of the compressed truncated bipyramid was observed (Figure 4.31c) generating an interfacial angle between {001} and {101} facets at 68.3° (Figure 4.32). At higher dopant concentrations, mixed morphologies of compressed truncated bipyramid and elongated compressed truncated bipyramid were present, both showing

the presence of {001} facets. For un-doped TiO$_2$, it was dominated by the thermodynamically stable {101} facets with less exposure of the {001} facets (Table 4.9).
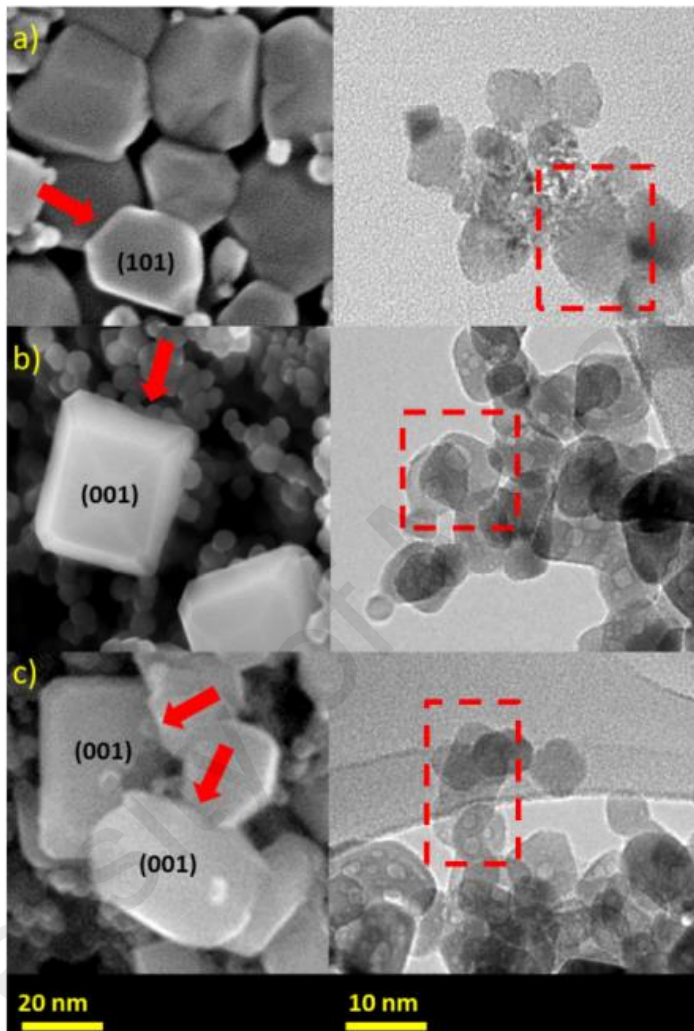
Figure 4.31: FESEM (left) and HR-TEM (right) images of a) Un-doped TiO$_2$ (NF0-TiO$_2$) b) NF1-TiO$_2$ and c) NF5-TiO$_2$
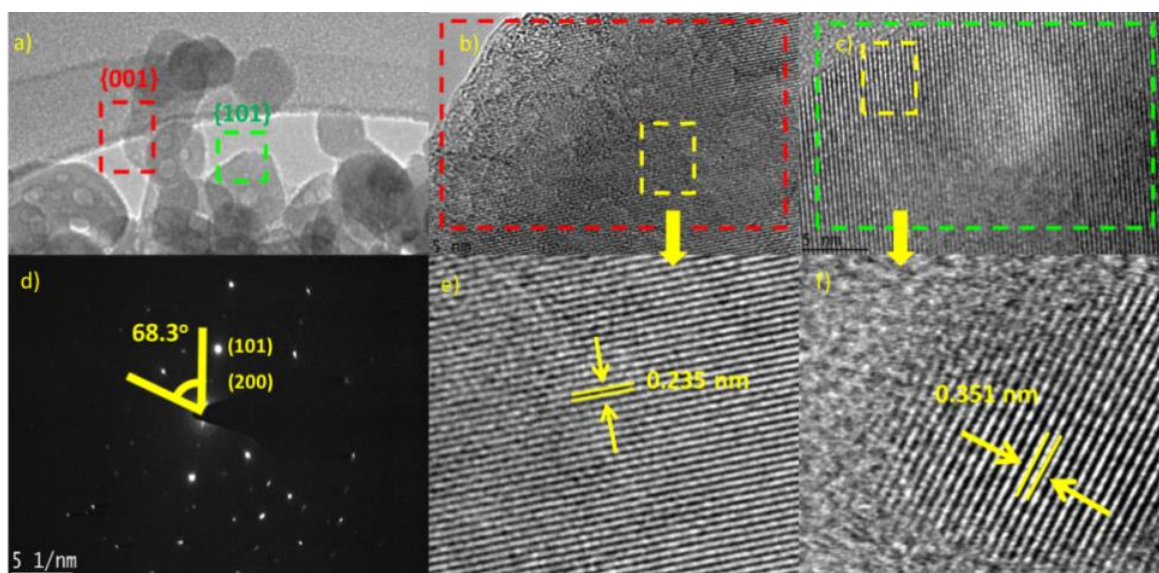
Figure 4.32: Images of NF5-TiO$_2$ showing a) HR-TEM image, b,e) Lattice spacing of 0.235 nm corresponding to (001) plane, c,f) Lattice spacing of 0.351 nm corresponding to (101) place and d) Selected Area Electron Diffraction (SAED) with an interfacial angle of 68.3°

Table 4.9: Corresponding FWHM, cystallite size (XRD analysis) and percentage of exposed {001} facets (Raman analysis) of un-doped and N,F-TiO$_2$

Catalyst	Dopant, wt%		Plane & Corresponding FWHM			Crystallite size, nm	% of exposed {001} facets
	N	F	(101)	(004)	(200)		
NF0-TiO$_2$	0.0	0.0	0.3936	0.3936	0.3149	20.7	5.8
NF1-TiO$_2$	2.7	0.8	0.2165	0.3149	0.2755	37.6	7.2
NF5-TiO$_2$	6.3	1.9	0.2755	0.3149	0.3936	29.6	11.0

Table 4.10: Textural properties of un-doped and N,F-TiO$_2$

Catalyst	BET surface area, m^2/g	SA$_{ext}$	Cumulative pore vol., cm^3/g	Average pore width, nm
NF0-TiO$_2$	38.8	0.990	0.134	11.1
NF1-TiO$_2$	14.3	0.509	0.150	15.0
NF2-TiO$_2$	23.1	0.703	0.104	18.2
NF3-TiO$_2$	30.2	0.676	0.132	17.5
NF4-TiO$_2$	51.5	0.465	0.187	15.4
NF5-TiO$_2$	55.0	0.854	0.269	17.0

The textural properties of N,F- TiO$_2$ were compared in Table 4.10. Data for the cumulative pore volume and average pore width were determined from the adsorption isotherms using the BJH (Barrett-Joyner-Halenda) method. The fraction of external

surface area or non micropore area (SA_{ext}) was calculated from the ratio of t-Plot external surface area divided by the Langmuir surface area. At low N and F loading, the pore volume decreased by half relative to un-doped TiO_2, followed by a drastic change in the surface area. Furthermore, the morphology of doped catalyst shown in Figures 4.31b and 4.31c demonstrated mixed particle shapes and sizes, which could imply different N and F interaction with TiO_2 at different loading. Previous observation for F-doped TiO_2 showed better morphology control at higher fluorine content (Figure 4.22, Table 4.6). Thus the decreased surface area in NF1-TiO_2 could imply that nitrogen doping was favored than fluorine at low dopant loading. Nitrogen-doped TiO_2 has been shown to have larger particle size, and subsequently smaller specific surface area (Yang et al., 2010). At higher N and F loading, the photocatalysts showed higher surface area, pore volume and average pore width with respect to un-doped TiO_2.

Nitrogen absorption-desorption isotherms of both samples were characterized by Type IV behavior and showed mesoporosity with an average pore width from 11.1 nm to 18.2 nm for un-doped and N,F-TiO_2 respectively(Figure 4.33). The pore shape was observed to change from cylindrical in un-doped to slits in N,F-TiO_2.
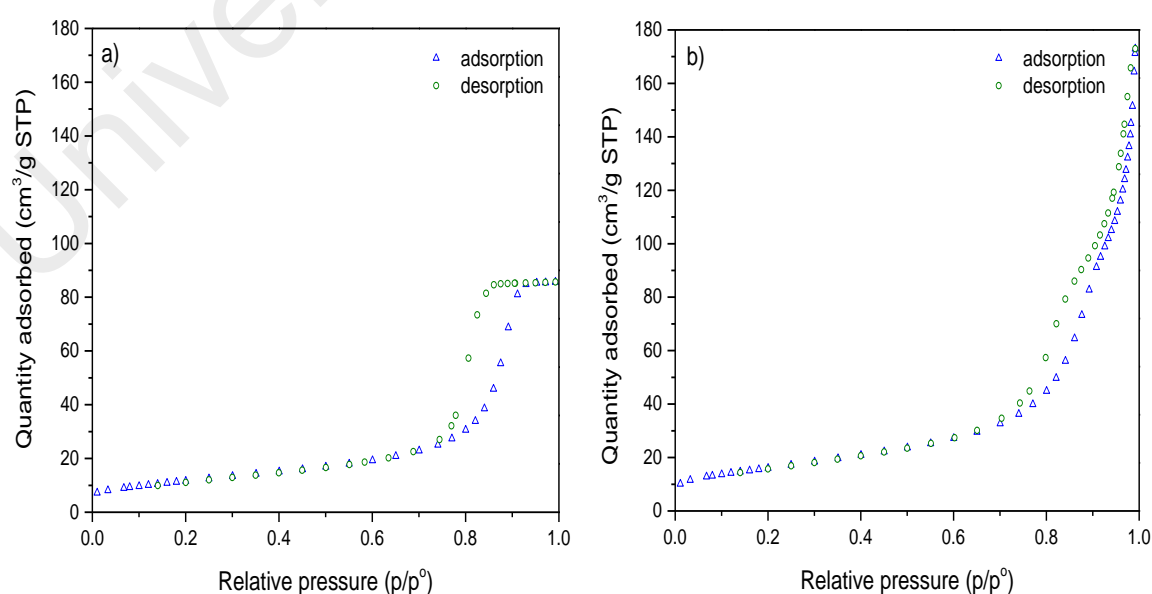
Figure 4.33: Nitrogen adsorption-desorption isotherm of a) NF0-TiO_2 and b) NF5-TiO_2

4.4.2 Structure and crystallinity

XRD data evidenced the presence of mixed anatase and rutile structure and single anatase structure respectively (Figure 4.34). The anatase and rutile crystal structure was according to JCPDS 84-1286 and JCPDS 34-0180 respectively. No shifts in the XRD peaks were observed before and after the doping process, indicating the absence of a significant change in the average unit cells of the crystal. An additional reflection at about 24° 2θ in Figure 4.34 was visible at higher N and F loading, corresponding to $TiOF_2$ (Lv, Yu, et al., 2011). A similar diffraction peak was also observed in previous work (Chen et al., 2008).

The typical crystallite size (determined using Scherer equation for XRD data) varies from 10 to 40 nm, supporting the findings in FESEM and HR-TEM data. Interestingly, a significant change in the crystal size was observed at lower N and F loading, from 20.7 nm (un-doped TiO_2) to 37.6 nm (NF1-TiO_2) (Table 4.9). However, as N and F loading increases, the crystallite size reduced to 29.6 nm and the intensity of [101] plane decreases, corresponding to the broadening of the full width at half maximum (FWHM). The thickness in [001] direction and length in [100] direction can be predicted from the full width at half-maximum (FWHM) of (004) diffraction peaks and (200) diffraction peaks respectively. In Table 4.9, NF1-TiO_2 results to an increased in thickness and length of the structure which corresponds to the narrowing of FWHM. Interestingly, at higher N and F loading, the thickness of N,F-TiO_2 crystals does not change but the length decreases corresponding to the broadening of FWHM of (200) diffraction reflection. This agrees with the HR-TEM observation from the blunt edges of truncated tetragonal bipyramid of un-doped TiO_2 to sharp edges of compressed truncated tetragonal bipyramid. There was an increment of {001} facets (having higher surface energy) exposure in N,F-TiO_2 relative to un-doped TiO_2 on increasing N and F loading and thus, facilitates the photocatalytic activity.
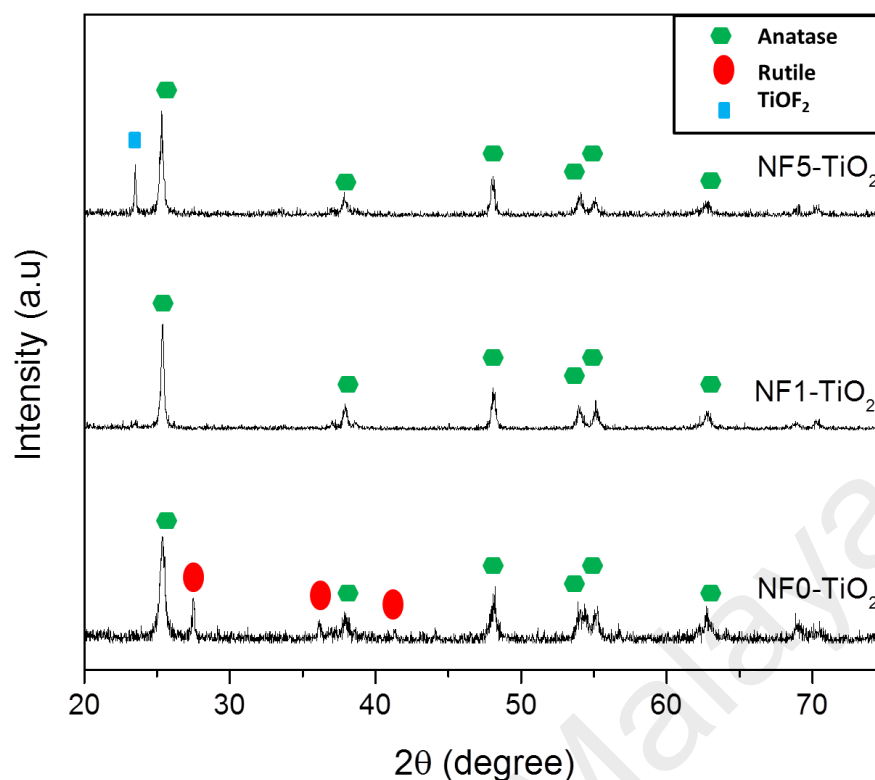
Figure 4.34: XRD patterns of NF0-TiO$_2$, NF1-TiO$_2$ and NF5-TiO$_2$

4.4.3 Surface characterization

XPS was used to analyze the surface state of both un-doped TiO$_2$ and N,F-TiO$_2$. The binding energy, E$_g$ for carbon at 284.9 eV indicates presence of surface adventitious carbon (Pelaez et al., 2009). A symmetrical F 1s spectra was observed in N,F-TiO$_2$ at E$_g$ of 684.8 eV and no other peak was observed (Figure 4.35a). E$_g$ within the range of 684.3 - 685.5 eV is consistently associated with F$^-$ ions physically adsorbed on the catalyst surface (Dozzi et al., 2013), which in high concentration could lead to the formation of TiOF$_2$ (Jiang et al., 2010). Binding energy, E$_g$ at 684.5 eV represents substitutional fluorine in TiO$_2$ (Ti-F-Ti bonds) (Wang et al., 2005), while higher E$_g$ (688.3 − 688.6 eV) was designated to substituted fluorine (Pelaez et al., 2009). A single E$_g$ peak was also observed for N 1s spectra at 400.2 eV and was attributed to molecularly chemisorbed γ-N$_2$ or interstitial doped nitrogen in TiO$_2$ (Figure 4.35b) (Viswanathan & Krishanmurthy, 2012). Substitutional N-atom (O-Ti-N bonds)

characterized by E_g ~ 396-397 eV was not present (Zheng-peng Wang et al., 2005). Viswanathan and Krishanmurthy (2012) reported that chemisorbed γ-N_2 was likely to present at high nitrogen loading and substitutional-doped at low nitrogen loading. However, the loading value for the transition was not indicated.

In this work, the EDX data indicates that the amount of nitrogen present in NF5-TiO_2 was approximately 6.9 wt %. A significant change in the crystal structure was expected if Ti-N bonds were present, suggesting that the majority of nitrogen doped remained as chemisorbed γ-N_2 and interstitial doping. Ti $2p_{3/2}$ and Ti $2p_{1/2}$ of un-doped TiO_2 appeared at 458.7 eV and 464.5 eV respectively, indicating the existence of Ti^{4+} (Figure 4.35c-d). A similar observation was made for N,F-TiO_2 however with a slight positive shift of 0.3 eV as compared to Ti 2p of un-doped TiO_2. This indicates clearly that nitrogen did not substitute lattice oxygen in TiO_2, forming O-Ti-N bonds. In fact, when O-Ti-N bond is present, the E_g of Ti 2p peak shifts negatively as it becomes electron enriched (Lin et al., 2007). No peak was observed at E_g 457.7 eV, which is a characteristic of Ti^{3+} (Xiong et al., 2012). This suggests that F^- ions mainly exist as surface fluorination, because substituted F-TiO_2 would require the formation of Ti^{3+}. $TiOF_2$, which is characterized at E_g of 684.0 (Lv, Yu, et al., 2011) and 685.3 to 685.5 eV (Li & Liu, 2008) was not observed. In both un-doped TiO_2 and N,F-TiO_2, the O 1s peak corresponds to lattice O^{2-} (lower E_g) and surface hydroxyl (higher E_g) as shown in Figure 4.35c-e (Liu et al., 2008). Interestingly, a slight positive shift of 0.2 eV was observed for N,F-TiO_2 indicating possible formation of Ti-O-F bonds. This also supports why the E_g of Ti 2p shifted positively (electron deficient). In conclusion, the doping elements in N,F-TiO_2, based on XPS results, were present mainly as chemisorbed γ-N_2 and surface fluorine ions.
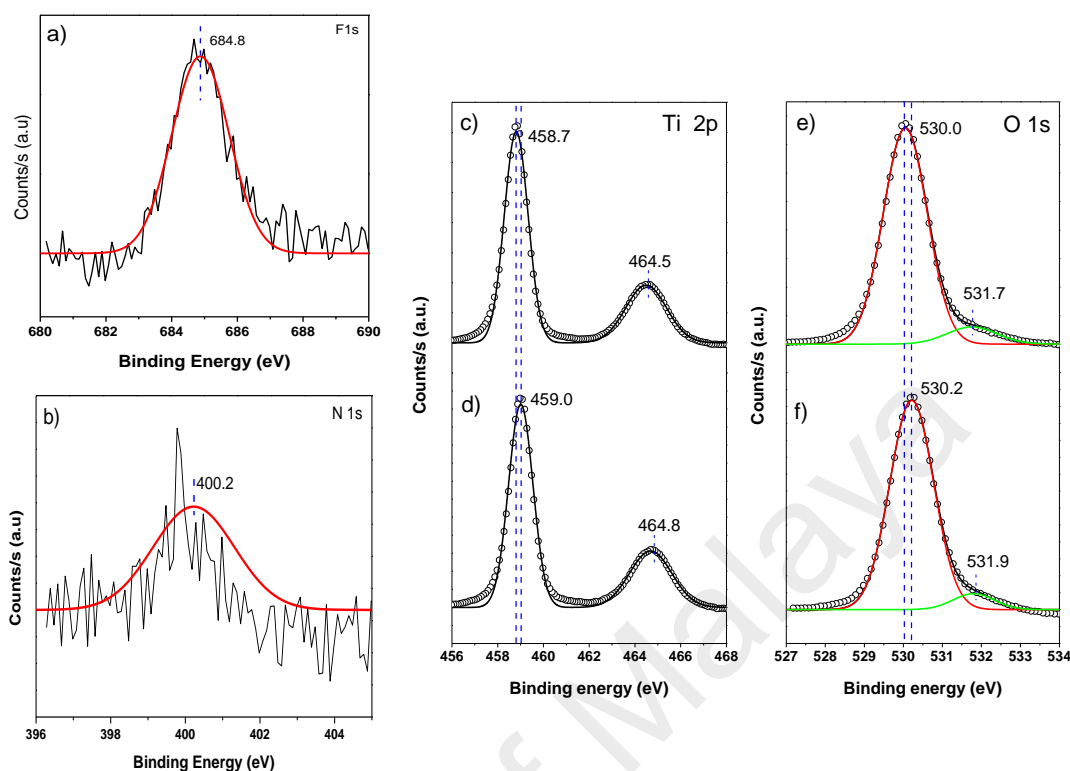
Figure 4.35: XPS spectra of a) F1s (N,F-TiO$_2$), b) N1s (N,F-TiO$_2$), c) Ti 2p (Un-doped TiO$_2$), d) Ti 2p (N,F-TiO$_2$), e) O1s (Un-doped TiO$_2$) and f) O1s (N,F-TiO$_2$)

4.4.4 Light absorption and photoluminescence behavior

The UV-visible reflectance spectra of N,F-TiO$_2$ photocatalysts showed the typical charge transfer bands of TiO$_2$ below about 320 nm, with the lowest charge transfer (LCT) due to ligand-to-metal (O^{2-}-Ti^{4+}) at about 315 nm (valence to conduction band) (Figure 4.36). In addition, it showed a clear additional band centered at about 425 nm, as found by other author for N,F-TiO$_2$ (Yang et al., 2010). Although debate exists on the nitrogen-incorporation in TiO$_2$, a reasonable interpretation of this band was the creation of N-state about 0.74 eV above the valence band, with thus reduced photon energy to populate the conduction band (Viswanathan & Krishanmurthy, 2012). The enhancement of {001} facets and color centre (yellow N,F-TiO$_2$ powder relative to white un-doped TiO$_2$ powder) also played important roles in extending the light

absorption towards the visible region coupled with the formation of oxygen vacancies due to N and F doping respectively (Dozzi et al., 2013).

In Figure 4.36, higher N and F loadings results to greater light absorption towards the visible region. In un-doped TiO_2, the visible light absorption was attributed to the present of rutile crystal phase decorating anatase TiO_2, however with lower range relative to N,F-TiO_2. The synergy between N and F in doped TiO_2 was shown to elevate the absorption intensity in the UV region which favors the photocatalytic activity (Kumar et al., 2013).
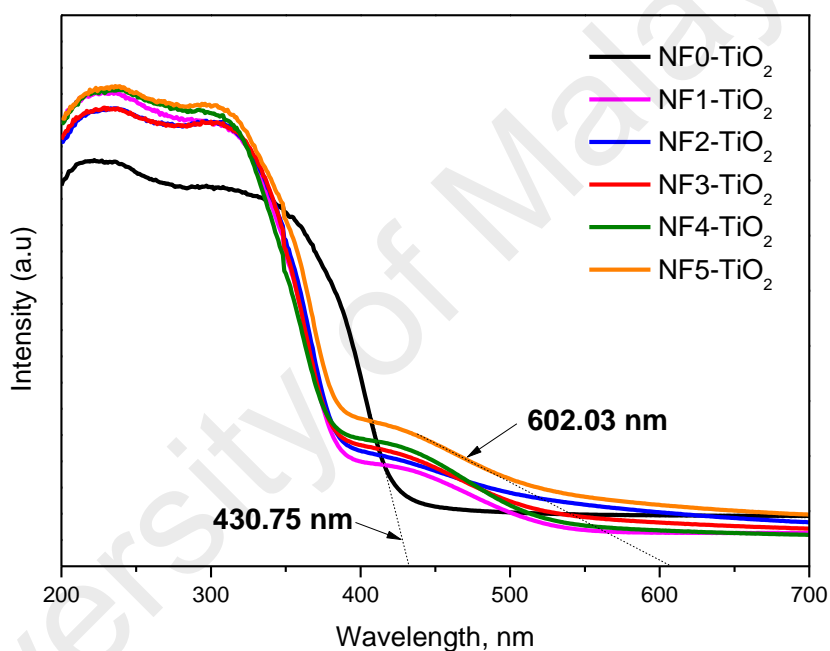
Figure 4.36: UV-visible diffuse reflectance spectra of all prepared photocatalysts

The normal emission of un-doped TiO_2 nanoparticles was dominated by PL arising from the recombination of trapped electrons with valence band holes, leading to a broad spectrum (Figure 4.37). Two distinctive PL patterns were observed in Figure 4.37a, demonstrating low and high PL intensity of N,F-TiO_2 relative to un-doped TiO_2. The lower intensity of the PL spectrum of N,F-TiO_2 with respect to un-doped TiO_2 indicates the introduction of an intermediate state between the conduction and valence bands of TiO_2. This is possibly related to the presence of F center (two trapped electrons) and F^+

center (one trapped electron) and also from the change in the morphology of the TiO_2 nanocrystals, from an irregular truncated tetragonal bipyramid to elongated truncated compressed tetragonal bipyramid morphology, as shown by SEM and HR-TEM images (Fig's 4.31, 4.32). The PL intensity at high N and F loading exceeded that of un-doped TiO_2, and was attributed to excessive oxygen vacancies acting as charge traps. In Figure 4.37b, both NF1-TiO_2 and NF2-TiO_2 PL peaks red shifted compared to un-doped TiO_2. This shift was related to the formation of defects in the form of Ti^{3+} and was able to facilitate the photocatalytic activity in the UV region (Xiong et al., 2012).

Also present was higher energy emission ("green PL") at about 530 nm (Jin et al., 2015), arising from the recombination of mobile electrons with trapped holes that was assigned to oxygen-vacancy color centers. In comparing the PL behavior of TiO_2 nanoparticles with that of TiO_2 nanotubes (TiO_2 nanotubes expose different crystal facets than those typically dominant in anatase nanoparticles), previous work showed that surface defects depends on the crystal facet and this may explain the differences observed in the PL emission intensity as well (Mercado, Seeley, Bandyopadhyay, Bose, & McHale, 2011). The increment of exposed {001} facets due to the change of morphology contributed a positive effect towards an efficient electrons and holes charge transfer, and facilitates enhanced photocatalytic activity (Ong et al., 2014).

Additional peaks at 625 nm and 675 nm of Figure 4.37b, were attributed to an impurity caused by either N or F doping because no similar peak was found in un-doped TiO_2. Similar finding was also reported by Li et al (2005). PL spectra thus indicate that in un-doped TiO_2, there was a higher tendency of radiative recombination in comparison to N,F-TiO_2, with thus a reduced formation of radicals on the catalyst surface.
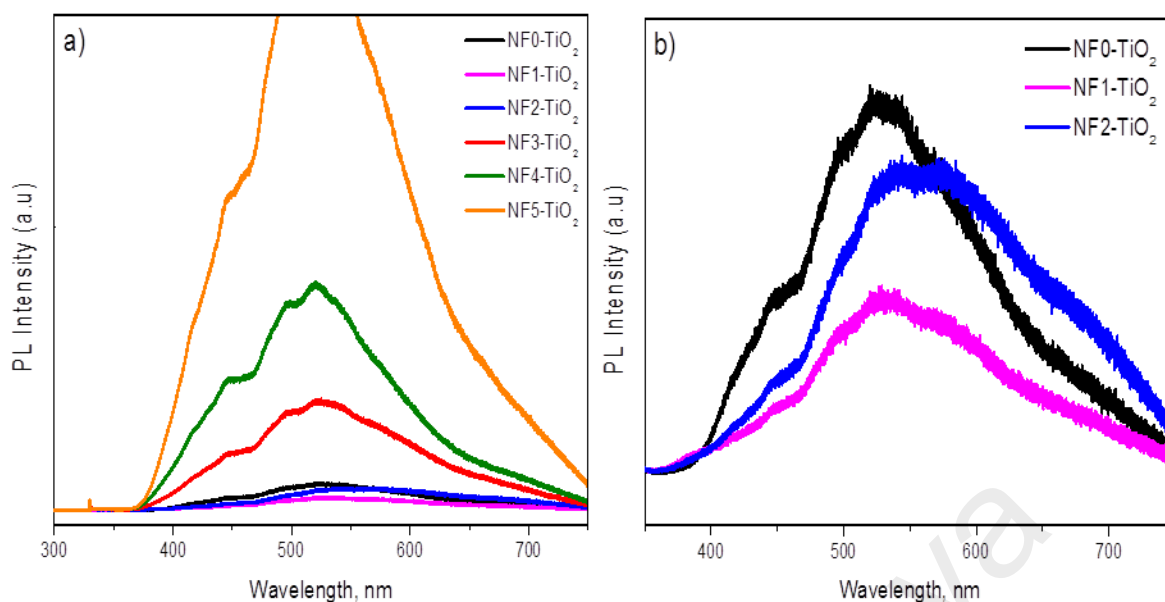
Figure 4.37: Photoluminescence spectra of a) all prepared photocatalysts and b) enlarged PL spectra of un-doped TiO_2 and N,F-TiO_2

4.5 Hydrogenated TiO₂ (H-TiO₂)

4.5.1 Color, morphology and textural properties

The change in color for hydrogenated TiO_2 indicates successful level of hydride-titanium bond formation of O-Ti-H linkages, via termination of surface dangling bonds (Chen et al., 2011). Un-hydrogenated TiO_2 appeared as white powder (Figure 4.38a) (Akpan & Hameed, 2010), while hydrogenated TiO_2 turned dark gray for H6-TiO_2 (Figure 4.38b) and bluish-gray for H12-TiO_2 (Figure 4.38c) and H24-TiO_2 (Figure 4.38d). Significant color changes were also observed in previous work for hydrogenated TiO_2 such as black (Chen et al., 2013), blue (Hamdy, Amrollahi, & Mul, 2012), light brown (Leshuk et al., 2013) and gray (Ramchiary & Samdarshi, 2014). However, a direct comparison was difficult as different synthesis and hydrogenation method were used. It was evident that hydrogenation affects the color of TiO_2 and thus its optical properties. However, it is in fact, the initial synthesis method used to prepare TiO_2 which influences any color changes of hydrogenated TiO_2. In previous work, different color of hydrogenated TiO_2 between light brown and white (negligible color change) was observed for TiO_2 synthesized using similar conditions (Leshuk et al., 2013).

Although, similar preparation method was used, the different order of chemicals introduced during sol gel leads to different color of hydrogenated TiO_2. The color of hydrogenated TiO_2 is influenced by the availability of surface dangling bonds (pre-existing reaction sites) and sol formation during sol-gel process (rapid precipitate gel governs high concentration of trapped incomplete hydrolyzed precursor in the gel's interior, thus hypothetically facilitates greater surface dangling bonds as compared to slow colloid/gel formation). Rapid precipitation of insoluble metal oxides network during sol-gel process typically yields TiO_2 with larger particle size as compared to controlled gel formation. This was influenced by pH, reactivity of metal oxides, solvent, water to alkoxide ratio, additives, chemical mixing routes and reaction condition (Samsudin et al., 2015; Shon et al., 2008).
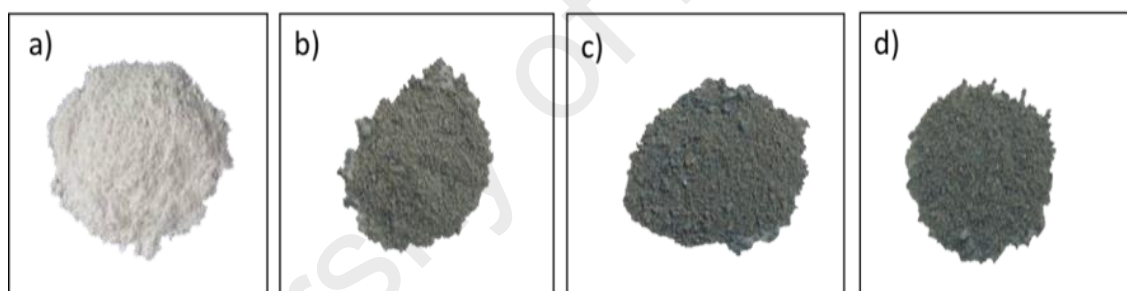
Figure 4.38: Powdered TiO_2 a) H0-TiO_2, b) H6-TiO_2, c) H12-TiO_2 and d) H24-TiO_2

In this work, an increased in hydrogenation duration leads to a slight change of hydrogenated TiO_2 color from dark gray to bluish-gray powder. The color change was attributed to the increased formation of O-Ti-H bonds in H12-TiO_2 and H24-TiO_2 and also Ti^{3+} in TiO_2 lattice (Wang, Yang, & Huang, 2015).

The morphology of un-hydrogenated TiO_2 (H0-TiO_2) and hydrogenated TiO_2 (H6-TiO_2, H12-TiO_2, H24-TiO_2) were observed under field emission scanning electron microscope (FESEM) at 20,000x magnification and showed significant differences in terms of particle shape and size uniformity (Figure 4.39). Well distributed and uniform particles size of 20-40 nm was observed in H0-TiO_2 (Figure 4.39a) with a truncated

tetragonal bipyramid structure (spheres with blunt edges and rhombuses). After 6h of hydrogenation process, the particle size of H6-TiO$_2$ increased significantly to 70 nm with a mixture of smaller particle sizes of 20 nm. Similar observation of particle size inhomogeneity was observed for longer hydrogenation period. It is interesting to observe mixed morphology for hydrogenated TiO$_2$ with emblematic features of 1) small spheres of truncated tetragonal bipyramid with blunt edges and 2) larger irregular distorted tetragonal bipyramid with defined cut edges. There was no vivid explanation for such irregular and defined cut edges of the larger particle, but could be the result of prolonged exposure of hydrogen under intense heat, which perturb the growth, orientation and kinetics of the TiO$_2$ crystal. In addition, the transformation of particle blunt edges to sharp edges was strongly affected by temperature and duration of the thermal treatment (Betzler et al., 2014). Inhomogeneous particle size of TiO$_2$ could be the result of different crystal phase composition as well (Paul & Choudhury, 2013). The non-stoichiometric ratio of titanium and oxygen atoms in hydrogenated TiO$_2$ showed oxygen deficiencies (Table 4.11). These oxygen vacancies served as electron donors and thus contributes to an enhanced photocatalytic properties (Cui et al., 2014).
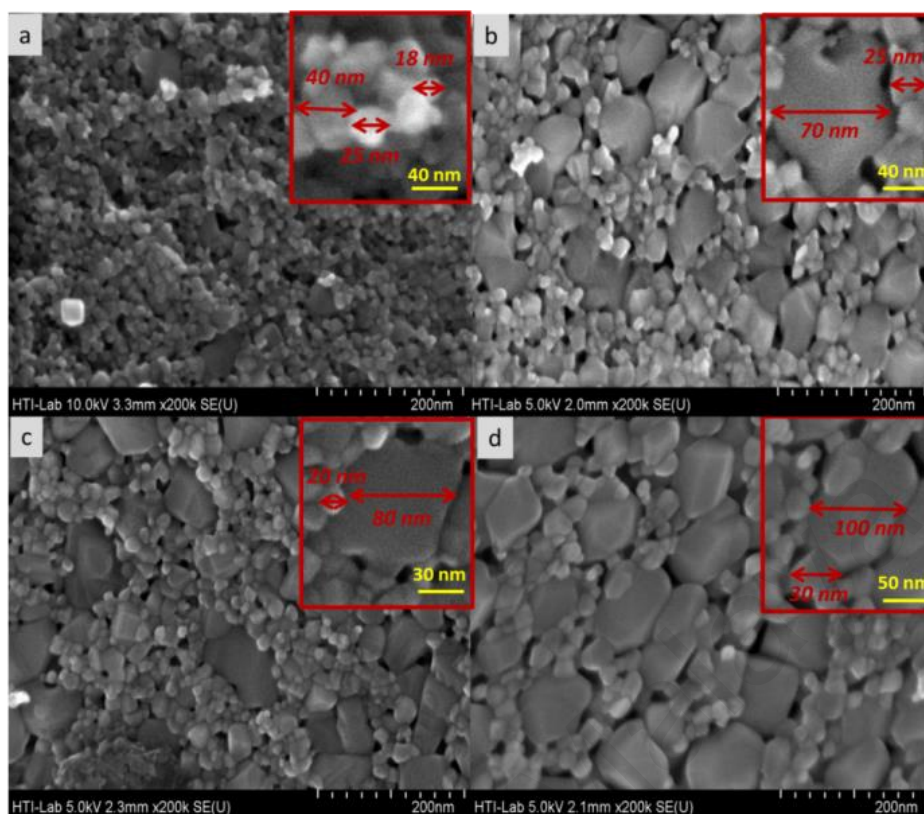
Figure 4.39: Surface morphology at 200,000x magnification for a) H0-TiO$_2$, b) H6-TiO$_2$, c) H12-TiO$_2$ and d) H24-TiO$_2$

Table 4.11: Elemental composition (EDX) of un-hydrogenated and hydrogenated TiO$_2$

Catalyst	Atomic composition (%)		Stoichiometric ratio	
	Titanium (Ti)	Oxygen (O)	Titanium (Ti)	Oxygen (O)
H0-TiO$_2$	31.79	68.21	1.00	2.14
H6-TiO$_2$	29.99	70.01	1.00	2.33
H12-TiO$_2$	41.76	58.24	1.00	1.39
H24-TiO$_2$	50.94	49.06	1.03	1.00

Under high resolution transmission electron microscopy (HR-TEM) analysis, well dispersed crystals with uniform size were observed in H0-TiO$_2$ (Figure 4.40ai). In hydrogenated TiO$_2$, there were a mixture of different crystal sizes (Figure 4.40bi,ci,di). The interplanar lattice spacing of anatase (0.325 nm) and rutile (0.169 nm) of (101) and (211) plane respectively, were shown in H0-TiO$_2$, with a clear boundary demarcation between anatase and rutile and confirms the presence of mixed crystal phase (Figure 4.40aii). The well resolved lattice arrangement showed good crystallinity throughout H0-TiO$_2$. As observed by others (Chen et al., 2013, 2011; Xia & Chen, 2013), hydrogenation of TiO$_2$ creates surface disorders on the crystal core due to the

termination of surface dangling bonds by hydride ions (Figure 4.40bii,cii,dii). The formation of O-Ti-H on TiO_2 surface were intensified for longer hydrogenation period, inducing disorder depth of 1.5 nm, 2.5 nm and 4.1 nm for H6-TiO_2, H12-TiO_2 and H24-TiO_2 respectively. This showed a linear relation between hydrogenation duration (at similar temperature) and surface disorder thickness. Furthermore, it was observed that surface disorders preferably grow on anatase boundaries as opposed to rutile due to the weaker thermo-stability of anatase crystal structure, which was easier deformed under heat stress (Hanaor & Sorell, 2010). The selected area electron diffraction (SAED) pattern of H0-TiO_2 illustrated high crystallinity with clear evidence of rutile planes (Figure 4.40e). For H12-TiO_2, the SAED pattern revealed slight amorphousity with clear presence of rings (Figure 4.40f), an indication of a semi-crystalline TiO_2 as a result of surface disorders as observed in the HR-TEM images.
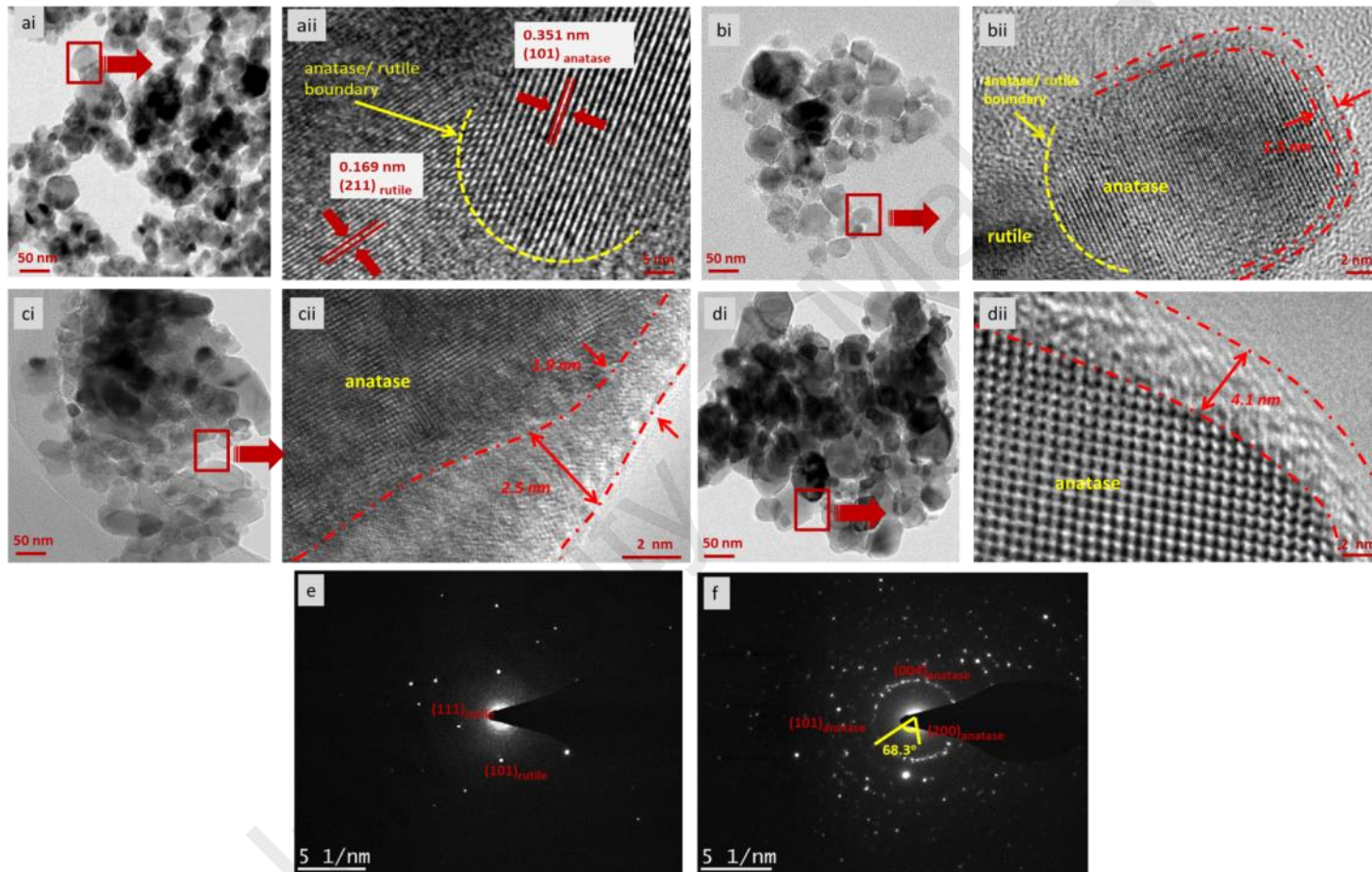
Figure 4.40: HR-TEM of H0-TiO$_2$ ai) particle dispersion, aii) anatase/ rutile boundary; H6-TiO$_2$ bi) particle dispersion, bii) surface disorders on anatase phase (thickness = 1.5nm); H12-TiO$_2$ ci) particle dispersion, cii) surface disorders on anatase phase (thickness = 1.8 nm - 2.9 nm); H24-TiO$_2$ di) particle dispersion, dii) surface disorders on anatase phase (thickness = 4.1 nm); e) SAED image of H0-TiO$_2$ and f) SAED image of H12-TiO$_2$.

All hydrogenated TiO₂ remained as mesoporous and was confirmed by type IV nitrogen absorption-desorption linear isotherm (Figure 4.41). The difference observed in the linear isotherm curve indicates morphology and structural changes. Less sharp increase of relative partial pressure between 0.5 and 0.7 p/p^o of nitrogen absorption showed for hydrogenated TiO₂ as compared to un-hydrogenated TiO₂ corresponded to poor homogeneity, which explained the presence of mixed morphology and less uniform particle sizes (Samsudin, Hamid, Juan, & Basirun, 2015). The particle size and textural properties of all prepared photocatalysts were shown in Table 4.12.
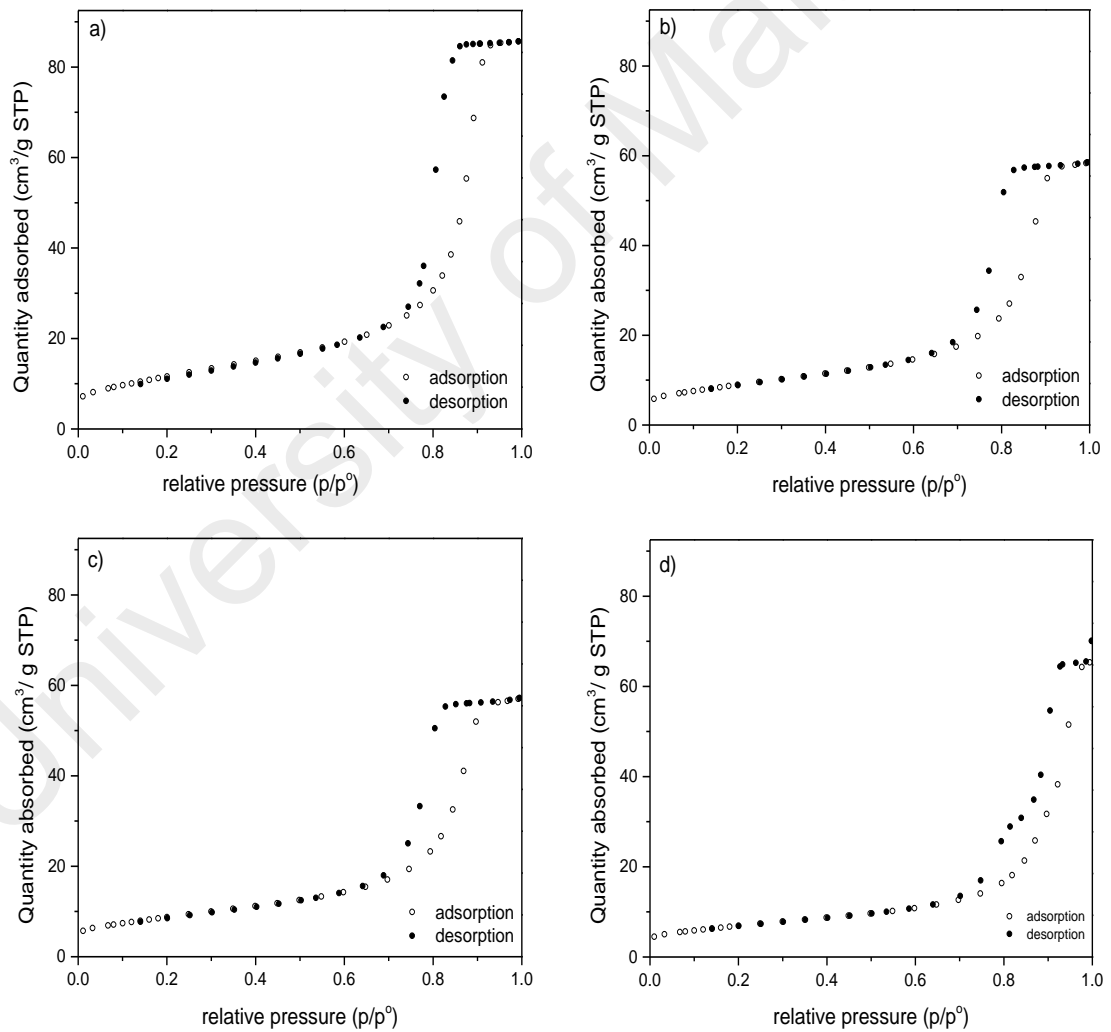
Figure 4.41: Nitrogen absorption/desorption linear isotherm for a) H0-TiO₂, b) H6-TiO₂, c) H12-TiO₂ and d) H24-TiO₂

Table 4.12: Particle size and textural properties of un-hydrogenated and hydrogenated TiO$_2$

Catalyst	[a]Particle size, nm	Multilayer surface area, m^2/g	External surface area ratio, SA$_{ext}$	Cumulative pore volume, cm^3/g	Average pore width, nm
H0-TiO$_2$	20-40	38.77	0.9900	0.133	11.1
H6-TiO$_2$	20-70	32.35	0.6849	0.090	10.2
H12-TiO$_2$	20-80	31.57	0.6822	0.088	10.2
H24-TiO$_2$	20-100	24.85	0.8186	0.100	15.5

4.5.2 Structure and crystallinity

It was observed that the crystal ratio of anatase and rutile were affected by hydrogenation duration. The growth of anatase to rutile was favored under reducing condition due to higher concentration of surface defects between anatase and rutile crystal boundaries (Hanaor & Sorell, 2010). At increased hydrogenation duration, the dominant (101) anatase XRD peak (Figure 4.42(left)) showed a decrease in crystallinity as a result of surface disorders (Kocemba, Nadajczyk, Rynkowski, & Maniukiewicz, 2014). Significant change in anatase and rutile crystallite size was also observed. Furthermore, structural and morphology change in [001] direction (thickness) and [100] direction (length) was visible from the corresponding change of FWHM of (004) and (200) diffraction peaks respectively. From Figure 4.42 (right), anatase (101) peak was observed to slightly shift towards higher Bragg's angle, and was dominant in H12-TiO$_2$. This phenomenon was attributed to the formation of Ti^{3+} in the TiO$_2$ lattice. Also, shifting towards higher Bragg's angle indicates smaller interplanar crystal spacing of {001} facets. The presence of {001} facets was further confirmed by the interfacial angle between {001} and {101} facets at 68.3° (Figure 4.40f) (Yang et al., 2008). However, the growth of {001} facets was marginal and inconsistent. The percentage (%) of {001} facets was estimated based on the data extracted from Raman (Figure 4.43).
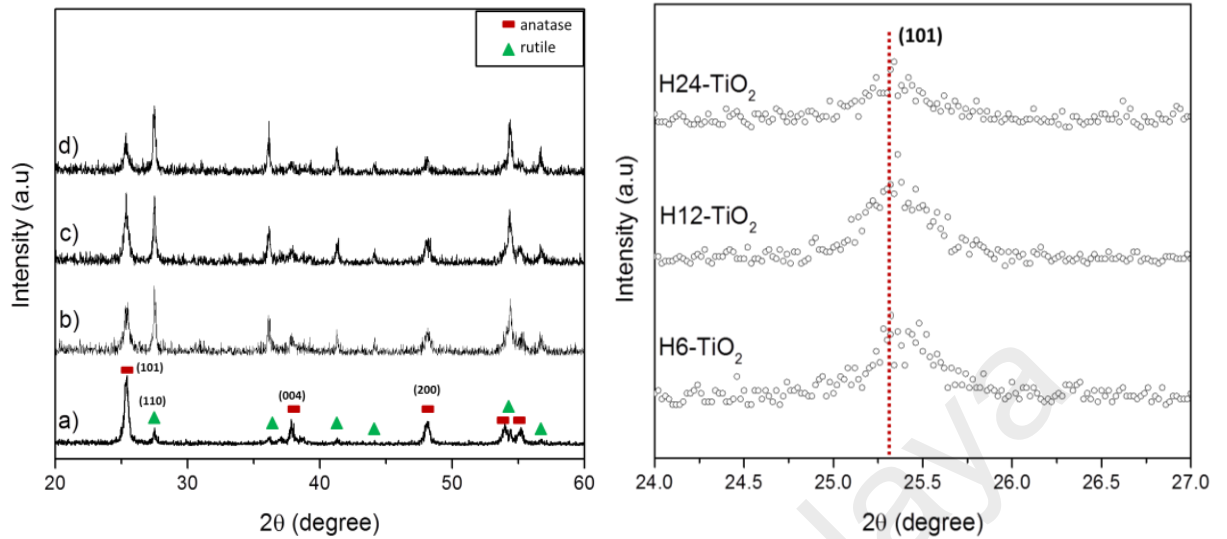
Figure 4.42: X-ray diffraction (XRD) spectra (left) for a) H0-TiO$_2$, b) H6-TiO$_2$, c) H12-TiO$_2$ and d) H24-TiO$_2$ and enlarged (101) anatase peak of hydrogenated TiO$_2$ (right)
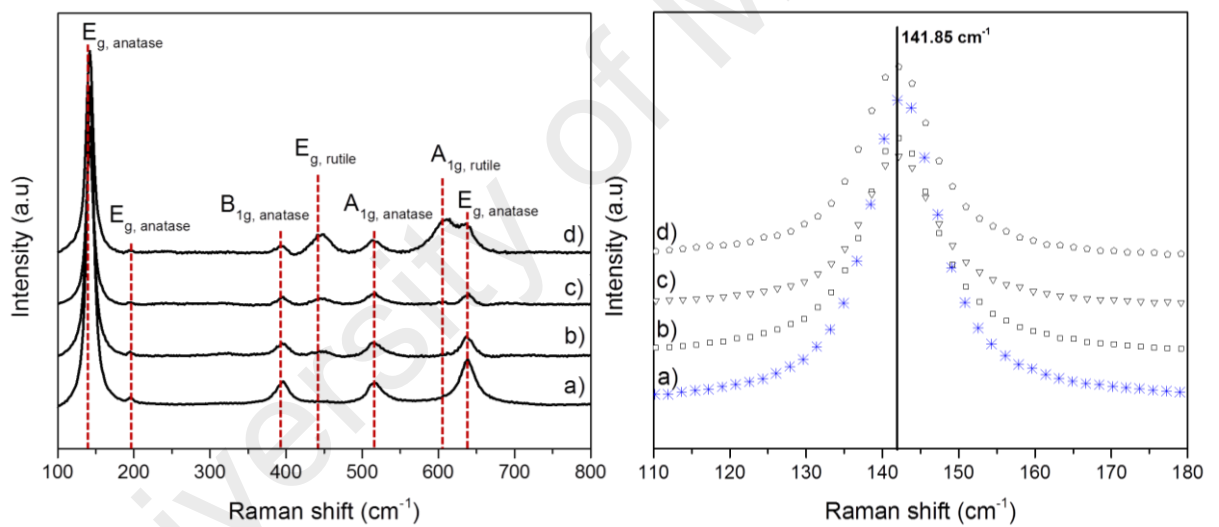
Figure 4.43: Raman spectra (left) of mixed phase anatase/rutile and enlarged E$_{1g}$ anatase peak (right) of a) H0-TiO$_2$, b) H6-TiO$_2$, c) H12-TiO$_2$ and d) H24-TiO$_2$

Table 4.13: Crystal phase ratio, crystallite size, plane with corresponding full width at half maximum (FWHM) and percentage of exposed surface active {001} facet of un-hydrogenated and hydrogenated TiO_2

Catalyst	Crystal phase ratio, wt%		Crystallite size, nm		Plane & Corresponding FWHM				% of exposed {001} facet
	Anatase	Rutile	Anatase	Rutile	(101)	(110)	(004)	(200)	
H0-TiO$_2$	65	35	23.0	69.3	0.3542	0.1181	0.4723	0.2755	7.36
H6-TiO$_2$	37	63	20.7	52.0	0.3936	0.1574	0.4723	0.4723	5.87
H12-TiO$_2$	40	60	29.6	52.1	0.2755	0.1574	0.4900	0.3936	7.29
H24-TiO$_2$	28	72	34.5	34.7	0.2362	0.2362	0.5112	0.6298	6.05

Raman was used to evaluate O-Ti-O coordination structure. Two distinctive features were observed; **1) weakening of anatase Raman active modes** (144 cm^{-1} (E$_g$), 197 cm^{-1} (E$_g$), 396 cm^{-1} (B$_{1g}$), 515 cm^{-1} (A$_{1g}$), 519 cm^{-1} (B$_{1g}$ superimposed with the A$_{1g}$ band) and 636 cm^{-1} (E$_g$)) and **2) strengthening of rutile Raman active modes** (447 cm^{-1} (E$_g$) and 608 cm^{-1} (A$_{1g}$)) as hydrogenation duration increases (Figure 4.43 (left)) (Wei et al., 2012). In Figure 4.43(right), the lowest frequency of E$_g$ anatase mode (144 cm^{-1}) slightly blue shifted to higher frequency, with peak broadening in all hydrogenated TiO$_2$ relative to H0-TiO$_2$. In previous works (Oshani et al., 2014; Wei et al., 2012), it was attributed to the presence of defects such as oxygen vacancies and also as a result of phonon confinement due to small size of nano-crystals. Regardless, the peak shifting remained insignificant and almost negligible, thus the presence of oxygen vacancies could not be confirmed by peak shifting, but was roughly shown by peak broadening. Longer hydrogenation duration leads to a broader peak, thus facilitates greater pools of oxygen vacancies. There was no presence of unidentifiable Raman peak prior to hydrogenation, which was in agreement with previous work (Leshuk et al., 2013).

The chemical bonds of un-hydrogenated and hydrogenated TiO$_2$ were examined under FTIR (Figure 4.44(left)) and showed clear evident of Ti-O bonds at 502.66 cm^{-1}. The integrity of Ti-O bonds remained even after intense hydrogenation of 24 h. There was a significant difference in the broad peak of surface hydroxyls group (hydrogen-bonded O-H band) of H0-TiO$_2$ as compared with all hydrogenated TiO$_2$ at 3418.27 cm^{-1}, whereby the corresponding peak area gradually decreases as hydrogenation duration increases. This is somehow expected, as continuous hydrogenation process would further eliminate more surface oxygen atoms, forming Ti-H bonds and surface disorders (Chen et al., 2013, 2012). The strength of terminal O-H at 3418.27 cm^{-1} of hydrogenated TiO$_2$ also illustrates the degree of hydrogen ion passivating O dangling bonds (Chen et al., 2012). If hydrogen ion were to passivate a significant amount of O

dangling bonds, an increased in the absorption peak at 3418.27 cm^{-1} would be noticeable. Hence, this further supports the presence of Ti-H bond, which concentration increases at longer hydrogen duration evidenced from the depth of the surface disorders in H24-TiO$_2$, as compared to H6-TiO$_2$ and H12-TiO$_2$ (Figure 4.44bii,cii,dii). In addition, the surface wettability was shown to be affected in hydrogenated TiO$_2$ (Xia & Chen, 2013). The Ti-OH bonds at 1631 cm^{-1} of all prepared photocatalyst showed marginal differences, and indicates that the internal hydroxyl groups were still well preserved. Small peak of free H$_2$O (3600 cm^{-1}) was observed for both un-hydrogenated and hydrogenated TiO$_2$ (Figure 4.44 (right)). Another interesting observation was an increase of peak area upon further hydrogenation at 3835.91 cm^{-1}, 3742.90 cm^{-1}, 2341.69 cm^{-1} and 1530.10 cm^{-1} and was also observed in un-hydrogenated TiO$_2$. According to Ramchiary and Samdarshi (2014), the bond vibration at 2341.69 cm^{-1} represents residual alkoxides group. Nonetheless, if this bond solely represent residual alkoxides group, the representative area was expected to remained or decreased under continuous heat stress, as the thermal stability of organic template (pluronic F127) or titanium precursor (TTIP) used in preparing TiO$_2$ were shown to be effectively removed between 200 to 500 $^{\circ}$C (Junpeng Wang et al., 2015). Hence, the increment of peak area was related to further polymerization of alkoxide group. This finding has not been reported in previous work. Another increased of peak at 1530.10 cm^{-1} was designated to surface disorders. Further examination of the FTIR spectra revealed proof which supports the peak shifting observed in XRD and Raman of hydrogenated TiO$_2$ relative to H0-TiO$_2$. As mentioned before, the peak shifting was related to the formation of oxygen vacancies and Ti^{3+}. This was well observed on the growing peak of 3835.91 cm^{-1} and 3742.90 cm^{-1} which corresponds to the increment of Ti^{3+}-OH (octahedral vacancies) (Ramchiary & Samdarshi, 2014). Being said, FTIR is a bulk analysis technique hence the observed Ti^{3+} represents accumulative surface and bulk Ti^{3+}. It has

been shown before that oxygen vacancies and Ti^{3+} increases with hydrogenation time (Haerudin, Bertel, & Kramer, 1998). The peak at 3685.12 cm^{-1} represent Ti^{4+}-OH (tetrahedral coordinated) of TiO_2, and imply preservation of TiO_2 crystalline core in the hydrogenated photocatalysts.
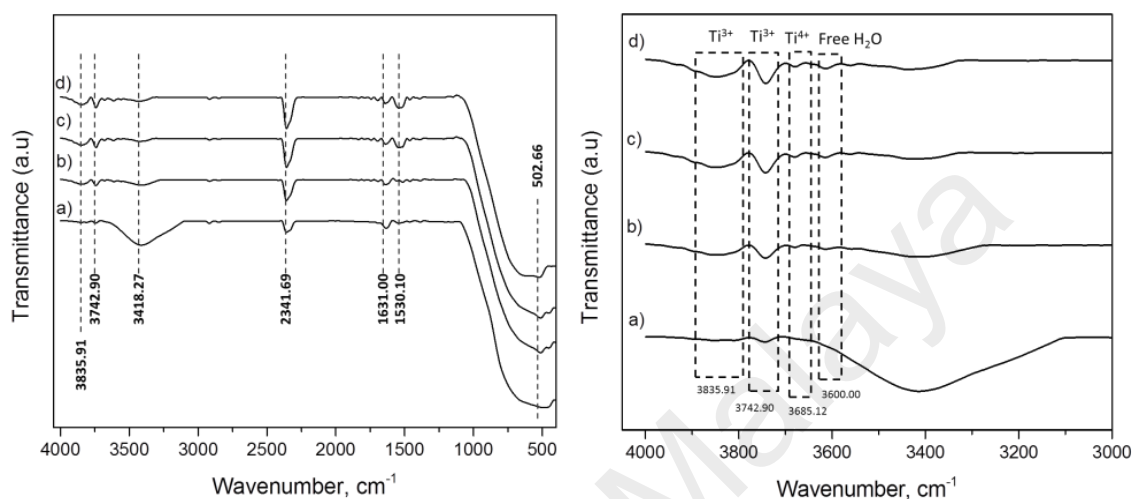
Figure 4.44: FTIR spectra for a) H0-TiO_2, b) H6-TiO_2, c) H12-TiO_2 and d) H24-TiO_2 (left; full spectra, right; enlarged spectra from 4000 – 3000 cm^{-1})

4.5.3 Light absorption and photoluminescence behavior

All prepared photocatalysts showed mixed crystal phase of anatase and rutile, readily promoting solar light absorption of both UV and visible region (Figure 4.45a). Single anatase crystal phase is only UV-activated due to its wide band gap of 3.2 eV (Samsudin et al., 2015), however the low surface energy of anatase reduces its ability to attract polar molecules, making it less hydrophilic (Buta et al., 2008). As for a single rutile crystal phase, it is activated under both UV and visible light due to lower band gap than 3.2 eV, however faced less affinity towards reduction of adsorbed molecular oxygen for radical generation. It was widely reported that mixed anatase and rutile crystal phase TiO_2 possessed greater ability to absorb light due to its smaller band gap, enhanced radical formation, and inhibits carrier charge recombination thus facilitates good photocatalytic response (Mohamed, Salleh, Jaafar, & Yusof, 2014).
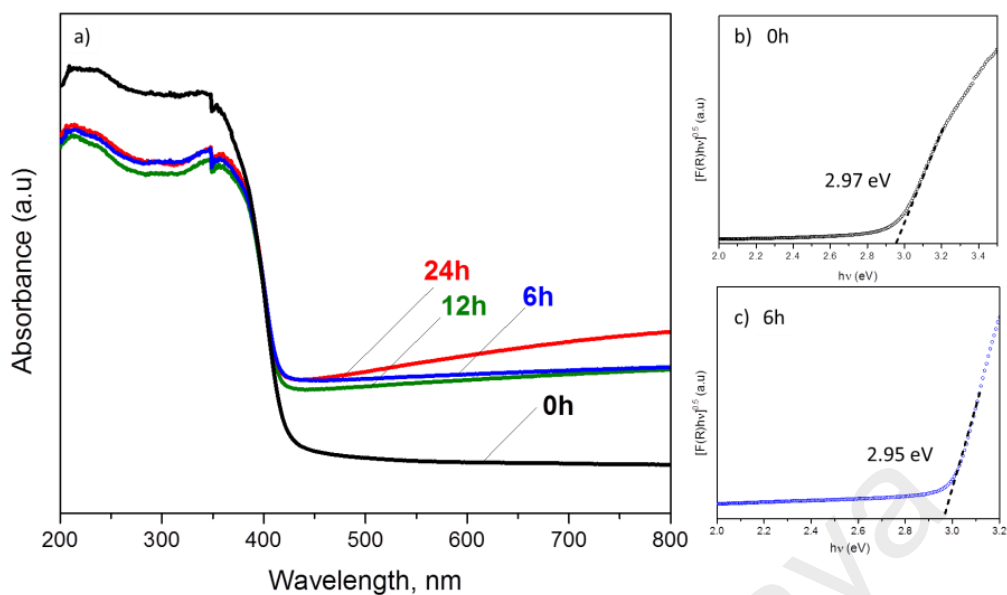
Figure 4.45: a) Absorption spectra of hydrogenated TiO₂ and un-hydrogenated TiO₂; K-M function showing calculated band gap interpolation for hydrogenation duration of b) 0h and c) 6h

All prepared photocatalysts showed ability to absorb light in both UV and visible region with varied intensities, while all hydrogenated TiO₂ showed extended light absorption towards the infrared region (Figure 4.45a). The UV intensity of hydrogenated TiO₂ reduces relative to un-hydrogenated TiO₂, but with increased light intensity in the visible and infrared region. The absorption spectra observed in Figure 4.45a differs from previous reported H-TiO₂. For example, Yan et al (2014) obtained increased UV intensity for shorter hydrogenation duration and the UV intensity gradually decreases at longer hydrogenation duration, Ramchiary and Samdarshi (2014) obtained increased light intensity in both UV and visible region and Teng et al (2014) obtained negligible change in the UV intensity, but very significant and sharp increase of visible and infrared light absorption. The different patterns of light absorption were narrowed down to the hydrogenation approach used in preparing hydrogenated TiO₂ (Leshuk et al., 2013). It was observed that similar pattern and intensity of visible and infrared light absorption as X Chen et al (2013) was found in H6-TiO₂, H12-TiO₂ and H24-TiO₂. Yan et al (2014) demonstrated that longer hydrogenation process results to color change from white, yellow, gray and black in hydrogenated TiO₂. Similar color of

147

hydrogenated TiO_2 does not necessarily govern similar optical behavior. Both hydrogenated TiO_2 prepared from previous work showed similar color of black photocatalysts, but with a completely different light absorption spectra (Chen et al., 2013, 2011; Yan et al., 2014). The final color of hydrogenated TiO_2 greatly depends on the hydrogenation approach as different approach was shown to govern different physico-chemical properties of hydrogenated TiO_2, especially on surface disorders and Ti^{3+}. The ability of any photocatalysts to absorb light vastly depends on the presence of oxygen vacancies as well (Teng et al., 2014). $H24-TiO_2$ showed largest visible and infrared light absorption relative to other hydrogenated TiO_2. Longer hydrogenation duration intensifies surface disorders, Ti^{3+} and oxygen vacancies (Chen et al., 2013; Yan et al., 2014; Zheng et al., 2012), which was responsible for the wider solar light absorption of $H24-TiO_2$. Surprisingly, the absorption intensity of $H12-TiO_2$ was slightly lower than $H6-TiO_2$ even though $H12-TiO_2$ was shown to have larger pools of oxygen vacancies and Ti^{3+}. A mixed anatase and rutile TiO_2 with larger rutile ratio typically results in enhanced solar light absorption (Hurum, Agrios, & Gray, 2003), however both $H6-TiO_2$ and $H12-TiO_2$ crystal ratio were almost similar. If oxygen vacancies and Ti^{3+} were the sole factors in enhancing solar light absorption, then we would observe a linear absorption trend with respect to hydrogenation duration. Ong et al (2014) reviewed that the increased light absorption was attributed and is a linear function with exposed {001} facets. And if so, $H12-TiO_2$ should show greatest absorption intensity as compared to $H6-TiO_2$ and $H24-TIO_2$ as it has the highest concentration of {001} facets as shown in Table 4.13, however this was not observed. According to (Wang et al., 2015), Ti^{3+} produces occupied states below the conduction band and enhances visible light absorption above 600 nm upon photo-excitation. Hence, the difference in light absorption between $H6-TiO_2$ and $H12-TiO_2$ could be due to the position and concentration of Ti^{3+} under the conduction band.

The photoluminescence spectra in Figure 4.46 demonstrate the efficiency of charge carrier trapping, migration and transfer plus the fate of photogenerated electrons and holes. The peak at 320 nm in all prepared photocatalysts represents ligand to metal charge transfer (O^{2-} to Ti^{4+}). All PL spectra showed peaks within 420 nm and 425 nm, corresponding to band gap reduction between 2.95 eV and 2.97 eV. H0-TiO$_2$ and H24-TiO$_2$ showed almost similar PL intensity, however the broader peak in H24-TiO$_2$ represents higher concentration of oxygen vacancies (Samsudin et al., 2015). The EDX data (Table 4.11) also confirmed larger oxygen atoms deficiencies in H24-TiO$_2$ relative to other prepared photocatalysts. Oxygen vacancy acts as an electron donor and enhances the photocatalytic activity. It has been explained that oxygen vacancies shifts the Fermi level closer to the conduction band, which further facilitates charge separation on the catalyst surface (Hu, 2012). However, an excessive amount of oxygen vacancies serves as charge traps centres. The PL peak at 450 nm represents self-trapped electrons (Haerudin et al., 1998), while 470 nm, 500 and 525 nm corresponds to defects or surface oxygen vacancies. Jin et al (2015) mentioned that a PL peak around ~525 nm (green band) is located on (101) plane surface and corresponds to surface oxygen vacancies. Furthermore, the peak of H6-TiO$_2$ and H12-TiO$_2$ was blue shifted relative to H0-TiO$_2$ and was attributed to the transformation of un-coordinated Ti^{3+} ions to surface oxygen vacancies. The peak at 550 nm represents oxygen vacancies which was responsible for visible and infrared light absorption (Teng et al., 2014). This peak was clearly seen in all of the hydrogenated TiO$_2$. A small peak at 575 nm, which was apparent in H6-TiO$_2$ represents additional defect site, attributed to the presence of Ti^{3+} (Jin et al., 2015). Although the PL spectrum cannot determine the actual position of oxygen vacancies (surface or bulk), it was assumed that H24-TiO$_2$ has the largest pool of bulk oxygen vacancies due to the high PL intensity (Kong et al., 2011). If we refer to the previous FTIR spectrum (Figure 4.44), H12-TiO$_2$ constitutes larger amount of

defects (in the form of Ti^{3+}) as opposed to H6-TiO_2. Therefore, the lower PL intensity in H12-TiO_2 was attributed to the higher exposed of {001} facets. The higher PL intensity of H6-TiO_2 was also correlated to the poor crystallinity relative to H12-TiO_2, which increases the probability of electrons and holes pair recombination (Memesa et al., 2011). It has been reported before that rutile with smaller grain size enables good separation of photogenerated electrons and holes (Wang et al., 2007). However, this was not observed in H24-TiO_2 which contained smallest size of rutile grains. Thus, there are many factors that contributes towards the separation of charge carriers such as {001} facets, oxygen vacancies, Ti^{3+}, size and crystal phase and ratio.
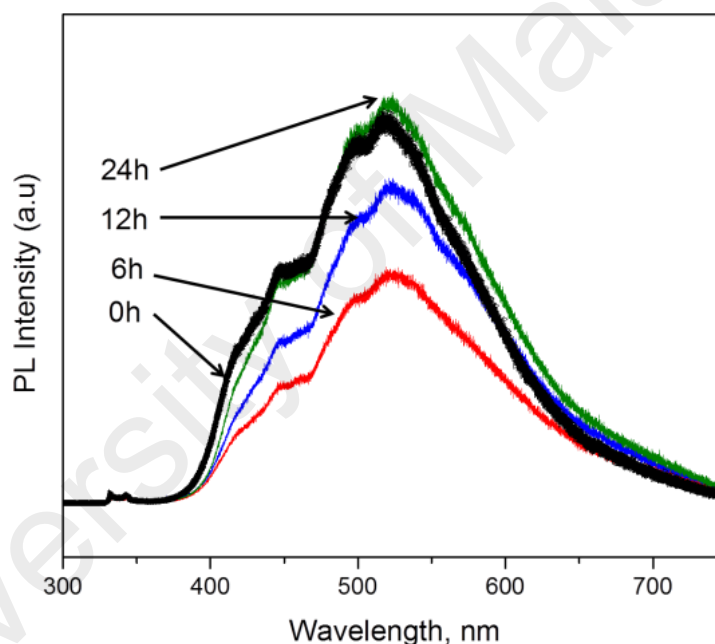
Figure 4.46: PL spectra of TiO_2 with different hydrogenation duration of 0 h, 6 h, 12 h and 24 h

4.5.4 Surface characterization

The chemical binding energy of un-hydrogenated and hydrogenated TiO_2 were analyzed, showing narrowing scans of Ti 2p state, O 1s state and valence band (VB) position (Figure 4.47). All prepared TiO_2 showed presence of Ti^{4+}-O bond in the Ti 2p spectrum (Figure 4.47a-d), with binding energy, E_g of ~ 458 eV and ~ 464 eV corresponding to Ti $2p_{3/2}$ and Ti $2p_{1/2}$ paramagnetic spins respectively (Chen et al., 2013,

2011). Surface Ti^{3+}, which is designated at E$_g$ of ~ 457 eV was not visible. Although previous data demonstrates the probability of surface Ti^{3+}, Wang et al (2013) stressed that the metastable Ti^{3+} is easily oxidized in air (O$_2$, H$_2$O, etc), and the process is further aggravated by TiO$_2$ surface disorders. An interesting observation to note was the systematic, but small E$_g$ shift to lower E$_g$ from H0-TiO$_2$, H6-TiO$_2$ and so on, for Ti 2p$_{3/2}$ and Ti 2p$_{1/2}$ peak. This was related to TiO$_2$ lattice substitution with hydrogen, creating O-Ti-H bonds on the surface. As oxygen is more electronegative than hydrogen, re-shifting of electrons density towards oxygen was expected thus increases the electron density of titanium. An electron rich Ti 2p would facilitate negative shifting towards lower E$_g$ (Samsudin, Hamid, Juan, Basirun, & Centi, 2015). Furthermore, this observation supports the decreasing area of surface hydroxyls group (OH) observed in Figure 4.47. It was postulated that H24-TiO$_2$ governs the highest concentration of surface Ti-H sites due to its largest surface disorders population. Although surface Ti^{3+} was not visible due to probable surface oxidation in air, XPS could still indicate the presence of Ti^{3+} by the blue shift of Ti 2p$_{3/2}$ peak to a lower E$_g$. Shifting to a lower E$_g$ demonstrates multiple oxidation states of Ti element. Junpeng Wang et al (2015) attributed this shift to the present of Ti^{3+}-O and Ti^{4+}-O bonds. The O 1s spectrum in Figure 4.47e-h at E$_g$ of ~530 eV and ~531-532 eV showed the presence of lattice O^{2-} and surface hydroxyl, O$_{OH}$ respectively, and was observed in all prepared photocatalysts. No absorbed H$_2$O was present at E$_g$ of ~532.7 eV (Liu et al., 2008). The slight shift in O 1s E$_g$ in hydrogenated TiO$_2$ relative to un-hydrogenated TiO$_2$, demonstrates different binding environment (Wang et al., 2015).
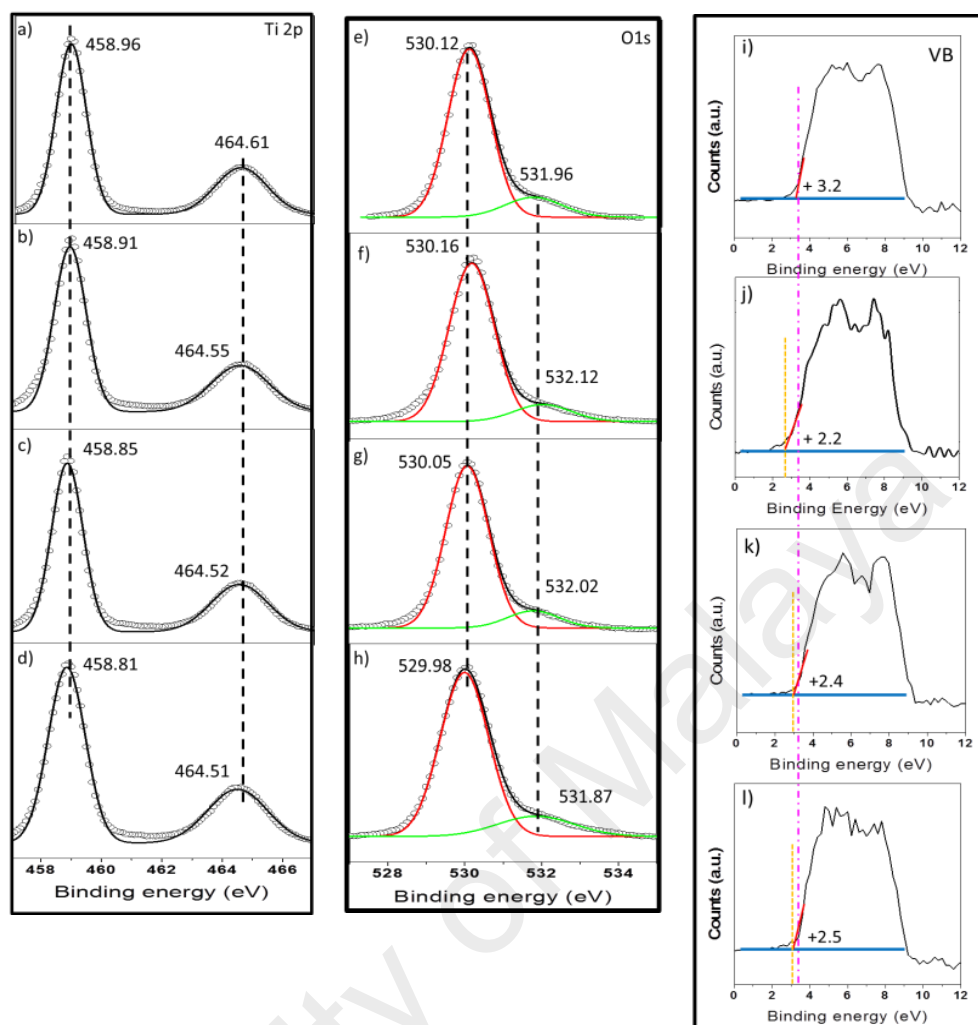
Figure 4.47: XPS spectra showing Ti 2p deconvoluted peak, O1s deconvoluted peak and valence band (VB) positioning of (a,e,i) 0h-TiO$_2$; (b,f,j) 6h-TiO$_2$; (c,g,k) 12h-TiO$_2$ and (d,h,l) 24h-TiO$_2$ respectively

The valence band tail states formation was also responsible for visible and infrared light absorption of hydrogenated TiO$_2$ (Teng et al., 2014). The valence band maxima of all photocatalysts were estimated by a linear extrapolation of the peaks with the baseline (Figure 4.47i-l). Interestingly, a negative shift of valence band by ~1.0 eV was observed for H6-TiO$_2$, and the shift reduced as hydrogenation duration increases. This was due to the greater formation of Ti^{3+} in H-TiO$_2$, analogous to previous finding (Chen et al., 2013; Zhu et al., 2013). Teng et al (2014) showed that the surface disorders created in hydrogenated TiO$_2$ formed an extended tail from the valence band and thus subsequent narrowing of the band gap. However, no drastic band gap narrowing was observed after

hydrogenation (Figure 4.45b,c). It was postulated that the valence band tail states formation might have a greater impact towards the fate of charge carriers and ability of TiO_2 to absorb solar light, as these were the significant changes observed in this study. The uplifting of the valence band corresponds to surface disorders, while the lowering of conduction band corresponds to oxygen vacancies and Ti^{3+} defect centers (Khan et al., 2014). As insignificant band gap change was observed in this work, it was assumed that the presence of Ti^{3+} were not large enough to have caused a dramatic change in the band gap. Similar observation was observed for hydrogenated TiO_2 in previous work (Leshuk et al., 2013). Furthermore, band gap narrowing due to Ti^{3+} was also difficult to measure (Cui et al., 2014). Despite no significant change in the band gap, the enhancement of solar light absorption for hydrogenated TiO_2 was attributed to the Ti^{3+} occupying the states below the conduction band, which prior to photo-excitation, induces light absorption for wavelength greater than 600 nm (Junpeng Wang et al., 2015).

4.6 Hydrogenated F-doped TiO_2

4.6.1 Color, morphology and textural properties

Un-doped TiO_2 (F127-TiO_2) and F4-TiO_2 were off-white and bright-white respectively (Figure 4.48a,b). On the contrary, H12-TiO_2 showed gray powder (Figure 4.48c), as a result of surface Ti-H bonds and Ti^{3+} (Chen et al., 2013, 2011; Cui et al., 2014). The hydrogenation process facilitates the formation of oxygen vacancies (color centers) in TiO_2 and contributes to a wide band absorption in the visible region, i.e. the gray color (Thompson & Jr., 2005). The color of all hydrogenated F-doped TiO_2 (HF6-TiO_2, HF12-TiO_2 and HF24-TiO_2) were almost similar to H-TiO_2 (Figure 4.48c-e). Thus, there was not an apparent difference in the visible-light absorption, when F-doped TiO_2 are hydrogenated with respect to hydrogenation of F127-TiO_2. Previous report

emphasized that the color of hydrogenated TiO_2 was influenced by the availability of surface dangling bonds (Leshuk et al., 2013). During the hydrogenation process, the dangling bonds on the catalyst surface were terminated by hydrogen forming O-Ti-H linkages which simultaneously modifies the color center of the catalyst. Extensive hydrogenation of F-TiO_2 (HF24-TiO_2) did not show significant color changes with respect to shorter treatments (HF6-TiO_2). Therefore the color (related to visible-light absorption) change was less likely depending from the creation of O-Ti-H linkages.
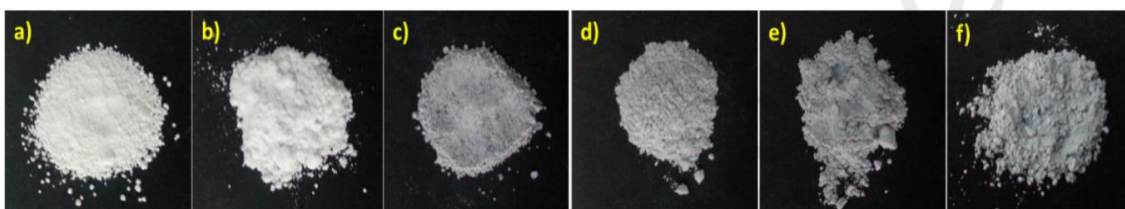
Figure 4.48: Color of a) F127-TiO_2, b) F4-TiO_2, c) H12-TiO_2, d) HF6-TiO_2, e) HF12-TiO_2 and f) HF24-TiO_2 photocatalysts

The morphologies of the photocatalysts were analyzed using field emission scanning electron microscope (FESEM) (Figure 4.49). The dominant morphologies of F127-TiO_2 and F4-TiO_2 were of spheres which emblements truncated tetragonal bipyramid structures. However, slightly higher particle agglomerations were observed in F4-TiO_2. This implies that different concentration of fluorine dopant in TiO_2 influences the catalyst surface charges, and thus its dispersion (Xue & Xu, 2013). Hydrogenation of TiO_2 (H12-TiO_2) remarkably affects the particle growth and size of TiO_2, giving rise to larger particles size of 20 to 80 nm in range (Figure 4.49c). H12-TiO_2 consisted of mixed morphologies of small spheres and larger particles with defined cut edges. Betzler et al (2014) demonstrated that temperature and prolonged heat treatment perturbed the growth, orientation and kinetics of TiO_2 crystal thus facilitates the change of spheres particle to sharp defined edges of TiO_2. Less change in the particle size and structure were observed in hydrogenated F-doped TiO_2 with respect to H12-TiO_2 (Figure 4.49d-f). A very interesting morphology was observed for the first time in HF6-

TiO$_2$ (Figure 4.49d), i.e. a uniform shape of concave umbrella around 30 nm in diameter (inset of Figure 4.49d). This morphology was not visible in HF12-TiO$_2$ and HF24-TiO$_2$. It was worth to mention that there were many factors affecting the growth mechanism of TiO$_2$ using sol-gel method which includes calcination temperature and duration, calcination medium (air, inert gases) and presence of impurities (Lv, Xiang, & Yu, 2011). In this work, similar calcination temperature and process conditions were employed. Initially, it was believed that hydrogenation of F-doped TiO$_2$ at high temperature (~500 °C) may have resulted to additional particles growth as observed in H12-TiO$_2$ (inset of Figure 4.49c). The presence of fluorine in the photocatalysts acts as an effective media to control the particle growths and structure of the catalysts from large defined cut edges to smaller uniform morphologies. Thus, the presence of concave umbrella morphology in HF6-TiO$_2$ could be the result of transient morphology changes due to the combined interactions of fluorine and hydrogen during the process. It was also observed that a complete uniform set of even morphologies were obtained for longer hydrogenation duration, which may indicate better equilibrium between fluorine and hydrogen synergies. Similar change in morphology from nanotubes to nanowires of TiO$_2$ was also observed before in the presence of fluorine, thus fluorine in TiO$_2$ is proven to participate in tuning the final morphology of the catalyst (Lv et al., 2012). In Table 4.14, the atomic concentration of fluorine decreases progressively from 1.82 at % in F4-TiO$_2$ to 0.54 at % in HF24-TiO$_2$. Hydrogenation thus removed part of the fluoride ions. In parallel, the oxygen to titanium ratio, initially higher in F4-TiO$_2$ than that of F127-TiO$_2$, progressively decreases with the time of hydrogenation and tend to reach the value of hydrogenated pure TiO$_2$. This was partly due to the removal of residual TFA degradation products during the hydrogenation process. The value of O/Ti surface ratio was also consistent with the creation of oxygen vacancies.
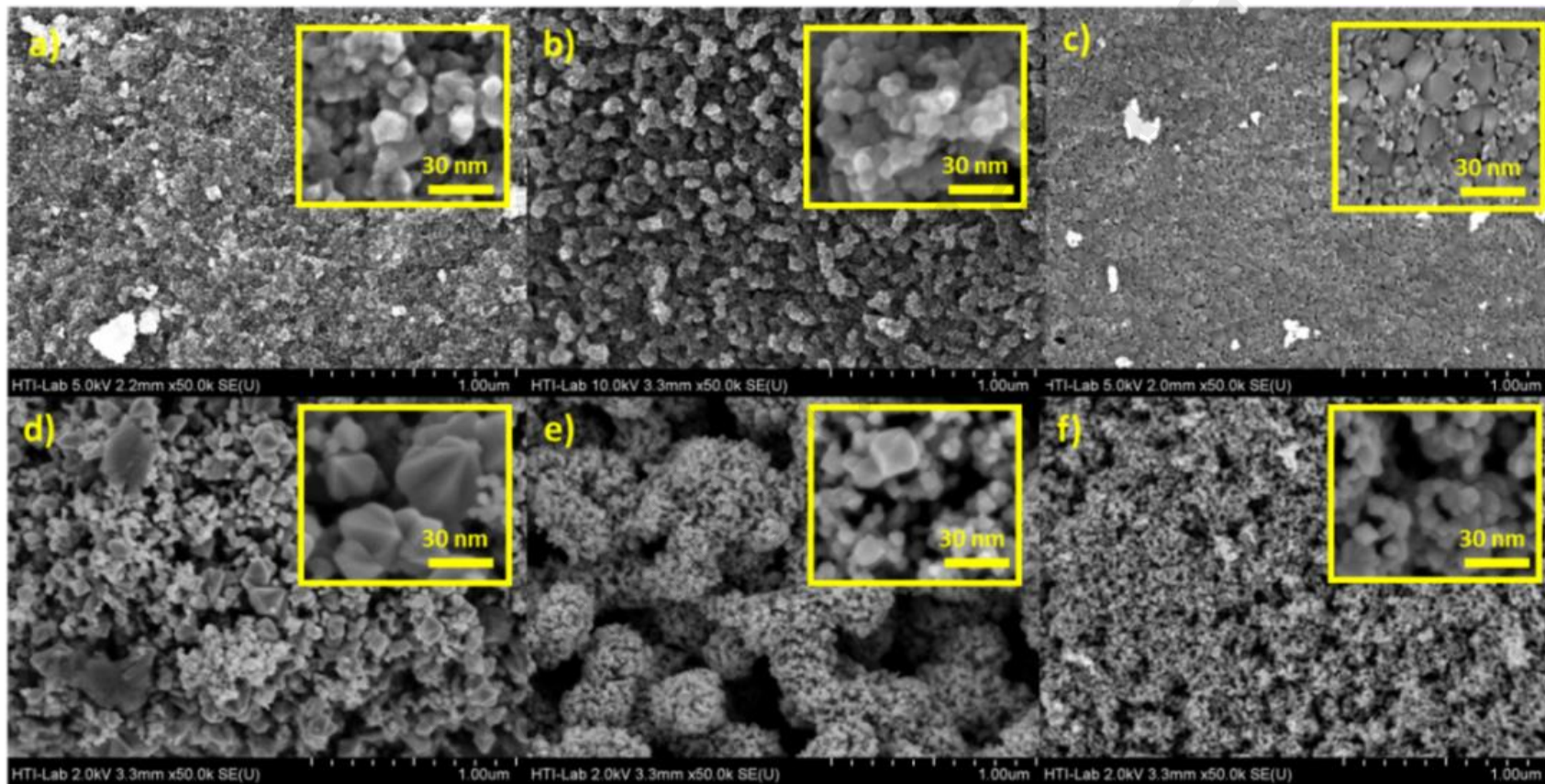
Figure 4.49: Morphology of a) F127-TiO$_2$, b) F4-TiO$_2$, c) H12-TiO$_2$, d) HF6-TiO$_2$, e) HF12-TiO$_2$ and f) HF24-TiO$_2$ at 50,000x magnification and enlarged image (inset)

Table 4.14: Atomic compositions (%) of $F127\text{-}TiO_2$, $F4\text{-}TiO_2$, $H12\text{-}TiO_2$ and hydrogenated F-doped TiO_2

Catalyst	Atomic composition (%)			Stoichiometric ratio	
	Titanium (Ti)	Oxygen (O)	Fluorine (F)	Titanium (Ti)	Oxygen (O)
$F127\text{-}TiO_2$	29.73	70.27	-	1.00	2.36
$F4\text{-}TiO_2$	22.89	75.28	1.82	1.00	3.29
$H12\text{-}TiO_2$	41.76	58.24	-	1.00	1.39
$HF6\text{-}TiO_2$	25.15	73.22	1.63	1.00	2.91
$HF12\text{-}TiO_2$	28.50	70.67	0.83	1.00	2.47
$HF24\text{-}TiO_2$	36.55	62.91	0.54	1.00	1.72

High resolution electron microscopy (HR-TEM) was used to evaluate the crystallinity, crystallite size, crystal shape, exposed facets and lattice spacing of the prepared photocatalysts (Figure 4.50). The crystallite size ranges from 20 to 80 nm in most of the photocatalysts, although $F127\text{-}TiO_2$, $H12\text{-}TiO_2$ and $HF24\text{-}TiO_2$ showed larger crystallite sizes. This was attributed to the higher particle growth rate in $F127\text{-}TiO_2$ and $H12\text{-}TiO_2$ samples, due to the absence of fluorine acting as morphology controlling agent. This was consistent with what is observed for $HF24\text{-}TiO_2$, where prolonged hydrogenation process removes a large part of fluoride ions. Various crystal structures were observed in all prepared photocatalysts: tetragonal bipyramid, truncated tetragonal bipyramid with and without (100) planes, compressed tetragonal bipyramid and rectangular cuboids.
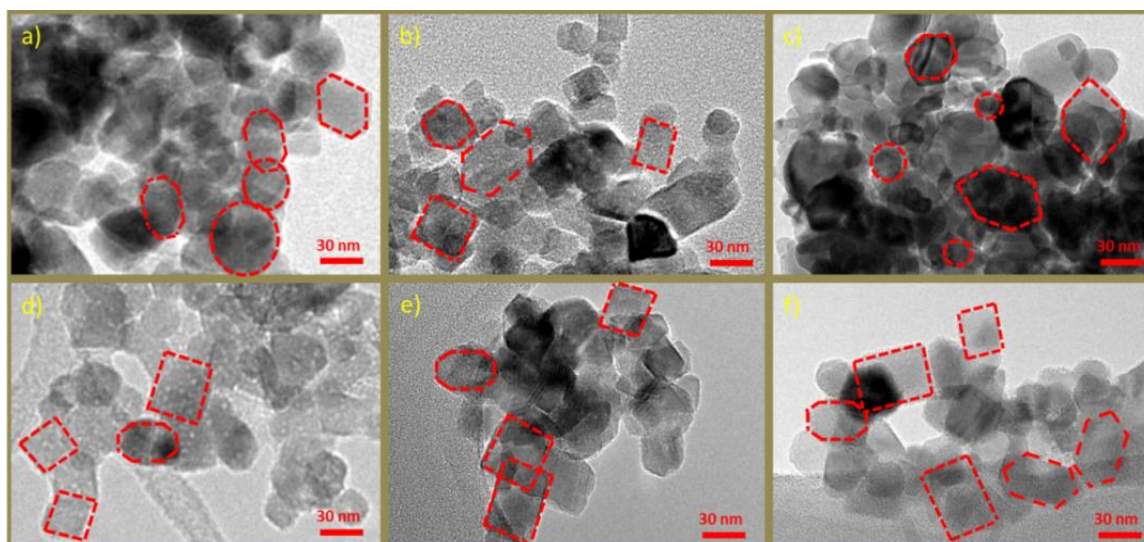
Figure 4.50: HR-TEM image of a) F127-TiO$_2$, b) F4-TiO$_2$, c) H12-TiO$_2$, d) HF6-TiO$_2$, e) HF12-TiO$_2$ and f) HF24-TiO$_2$

The schematic layouts of these crystal structures were illustrated in Figure 4.51. It was clear that fluorine is an efficient structure morphology agent as a more defined crystal shapes were observed in F4-TiO$_2$ with respect to F127-TiO$_2$ and H12-TiO$_2$. HR-TEM images showed in general, a low amount of crystal structures with highly exposed {001} facets. F4-TiO$_2$ showed the largest concentration of {001} facets and was confirmed by the highest value of lattice strains in the structure (Table 4.15). The average lattice strain decreases with hydrogenation time and tend to reach the value observed in H-TiO$_2$. Dozzi et al. indicates that high strained configuration was related to the preferential exposure of the {001} facets having high density of surface under-coordinated Ti atoms (Dozzi et al., 2013). H12-TiO$_2$ particles (Figure 4.51c) showed spherical structures in consistent with truncated tetragonal bipyramid structures (Samsudin, Hamid, Juan, Basirun, & Kandjani, 2015) and probably lower concentration of {001} facets in consistent with the lowest value of lattice strains. Hydrogenated F-doped TiO$_2$ showed presence of rectangular cuboids crystal structures and higher value of lattice strains.
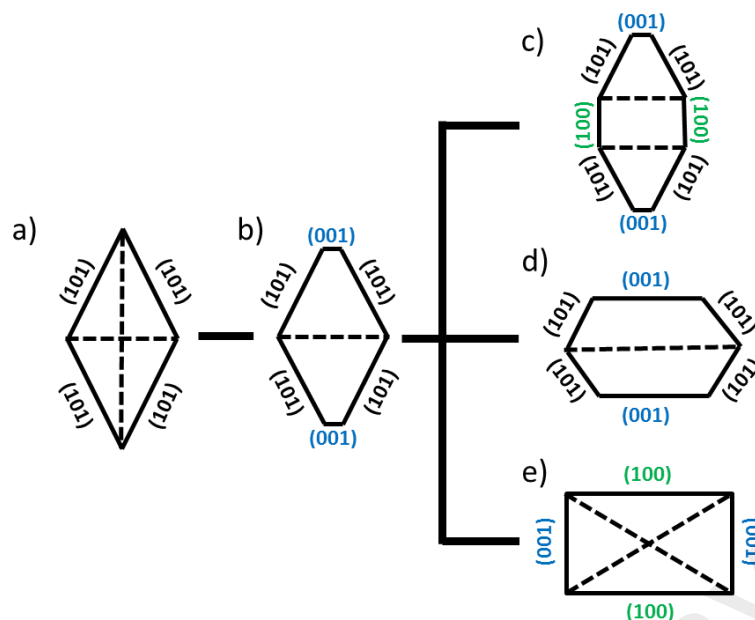
Figure 4.51: Schematic illustration of a) tetragonal bipyramid and shapes observed in all prepared photocatalyst of b) truncated tetragonal bipyramid, c) truncated tetragonal bipyramid with (100) planes, d) compressed tetragonal bipyramid and e) rectangular

F127-TiO$_2$ and hydrogenated F-doped TiO$_2$ showed crystalline structure with strong evidence of (101) plane and lattice spacing of 0.351 nm (Figure 4.52) (Segomotso et al., 2013). Figure 4.52b-d evidenced the presence of surface disorders in hydrogenated F-doped TiO$_2$ photocatalysts, consistent with literature data (Chen et al., 2013, 2011; Xia & Chen, 2013). Additional care was taken to avoid that the formation of surface disorder was related to an induced effect by the HR-TEM beam. The thickness of the disordered surface layer varied from 1.9 nm (Figure 4.40cii) to 1.7 nm, 2.0 nm and 2.5 nm in H12-TiO$_2$, HF6-TiO$_2$, HF12-TiO$_2$ and HF24-TiO$_2$ respectively. The formation of surface disordered layers after hydrogenation were related to the formation of surface Ti-H bonds on TiO$_2$ surface which reduces the surface crystallinity, consistent by the presence of semi-crystalline rings in the SAED pattern (inset of Figure 4.52c). Longer hydrogenation time induced larger degree of surface structural disorders due to higher concentration of surface Ti-H bonds.

The cumulative pore volume was larger in hydrogenated F-doped TiO$_2$ with respect to F-TiO$_2$ (Table 4.16). This was attributed to the removal of residual TFA degradation products during the hydrogenation process which caused pore blockages in F4-TiO$_2$

(Samsudin et al., 2016). The surface area of hydrogenated F-doped TiO_2 was twice larger with respect to $F4-TiO_2$ and was also larger than $F127-TiO_2$ and $H12-TiO_2$. This was analyzed using nitrogen absorption-desorption linear isotherms in Figure 4.53. All photocatalysts showed a type IV mesoporous linear isotherm. Both $F4-TiO_2$ and $H12-TiO_2$ did not result to high surface area photocatalysts, but the synergistic combination of fluorine and hydrogen in TiO_2 significantly increased the total surface area and average pore width of the photocatalyst (Table 4.15). Another interesting observation was the modification of pore shape from cylindrical in $F127-TiO_2$ and $H12-TiO_2$ to slits in $F4-TiO_2$ and hydrogenated F-doped TiO_2. Even after intense hydrogenation, the pore shape of hydrogenated F-doped TiO_2 remained similar to that in $F4-TiO_2$. Figure 4.53b,d-f showed that there was a sharp increase in the relative partial pressure between 0.5 and 0.7 p/p^o of nitrogen absorption on increasing the hydrogenation duration, which corresponds to homogeneous particle size and distributions.
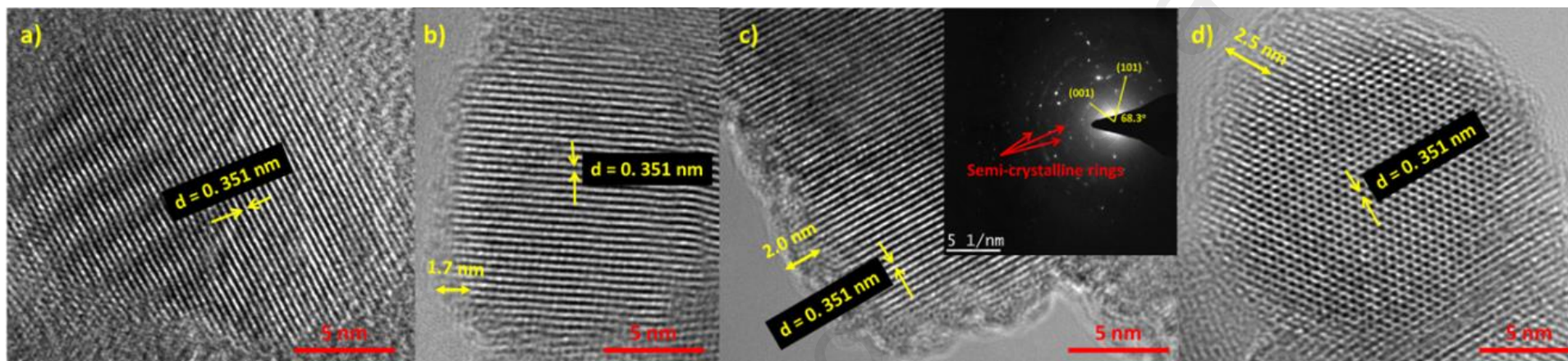
Figure 4.52: HR-TEM image of single crystal of a) un-doped TiO_2, b) HF6-TiO_2, c) HF12-TiO_2 and d) HF24-TiO_2 showing lattice spacing of (101) anatase plane and surface disorders in all hydrogenated F-doped TiO_2.
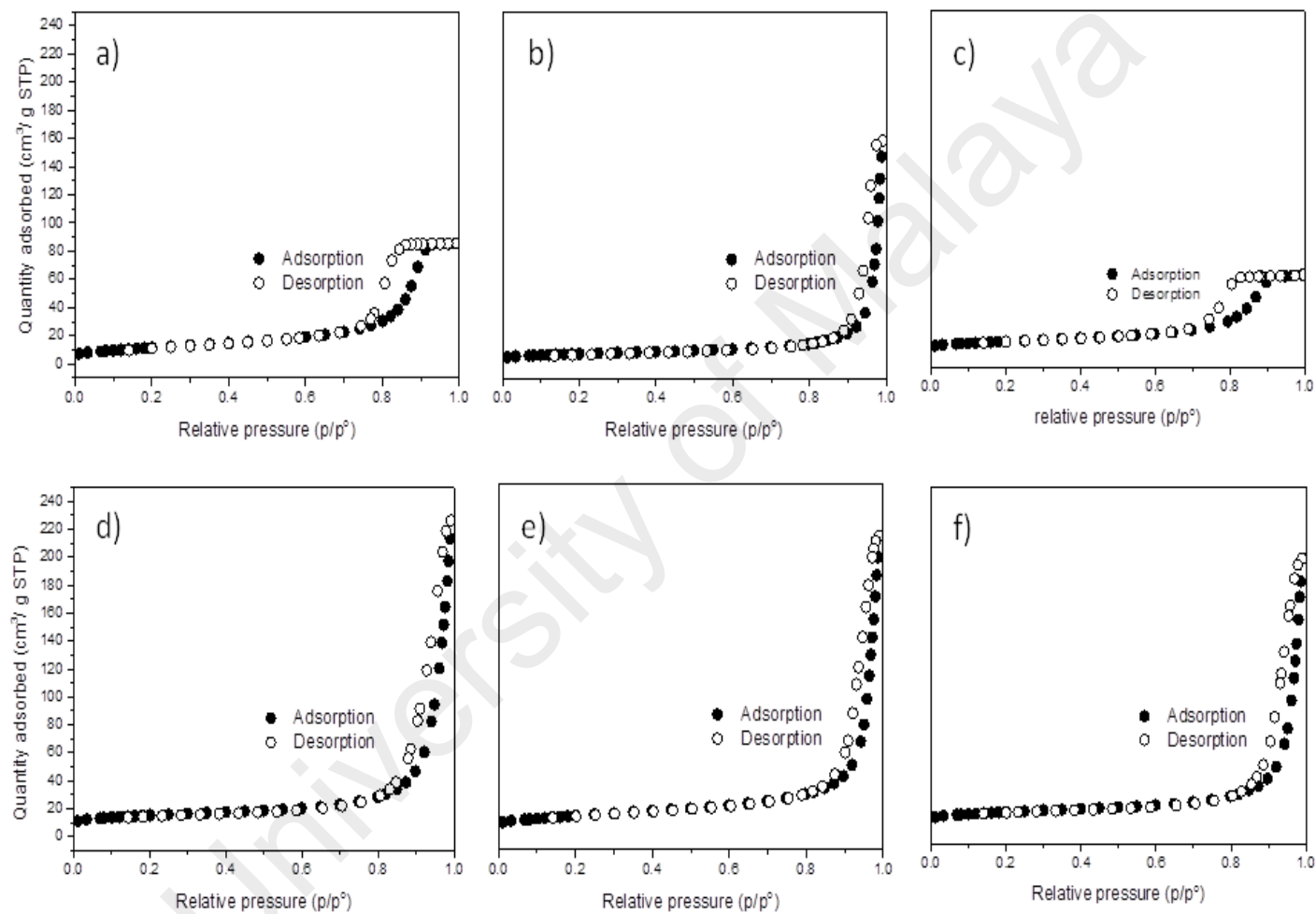
Figure 4.53: Nitrogen absorption-desorption linear isotherm plot of a) F127-TiO$_2$, b) F4-TiO$_2$, c) H12-TiO$_2$, d) HF6-TiO$_2$, e) HF12-TiO$_2$ and f) HF24-TiO$_2$

Table 4.15: Particle size and textural properties of un-doped TiO_2, F-doped TiO_2, hydrogenated TiO_2 and hydrogenated F-doped TiO_2

Catalyst	[a]Particle size, nm	Multilayer surface area, m^2/g	External surface area ratio, SA_{ext}	Cumulative pore volume, cm^3/g	Average pore width, nm
F127-TiO_2	20-40	38.77	0.9900	0.133	11.1
F4-TiO_2	10-50	24.65	0.2750	0.120	20.1
H12-TiO_2	20-80	31.57	0.6822	0.088	10.2
HF6-TiO_2	20-60	54.61	0.4753	0.346	25.6
HF12-TiO_2	20-60	50.34	0.6768	0.330	26.1
HF24-TiO_2	20-60	46.48	0.5444	0.303	26.4

4.6.2 Structure and crystallinity

F127-TiO$_2$ and H12-TiO$_2$ showed presence of mixed anatase and rutile crystal phases (Figure 4.54). In F4-TiO$_2$ and all hydrogenated F-doped TiO$_2$, a single anatase phase was observed (Table 4.16). The presence of fluoride ions stabilizes anatase TiO$_2$ and inhibits anatase to rutile crystal phase transformation (Lv, Xiang, et al., 2011). The transformation was instead favored by hydrogenation treatment (H12-TiO$_2$), likely because the creation of oxygen vacancies due to the hydrogenation process, which acts as a nucleation site for anatase to rutile crystal phase conversion. Table 4.16 reports the FWHM of (004) plane corresponding to the thickness in [001] direction of TiO$_2$ crystals. Differently from the trend observed for (101) plane in hydrogenated F-doped TiO$_2$, which was consistent with the increase in the average crystallite size (Table 4.16), the FWHM of (004) plane passed through a maximum. The Bragg's angle at (101) plane was right shifted towards higher value and was roughly observed in all photocatalysts relative to F127-TiO$_2$ (Figure 4.54). Shifting to higher Bragg's angle indicates smaller interplanar spacing and presence of high energy {001} facets (Ong et al., 2014). Significant shifting was observed in F4-TiO$_2$ and hydrogenated F-doped TiO$_2$ which was further confirmed by the interfacial angle between {001} and {101} facets at 68.3° (inset of Figure 4.52c). This phenomenon was also attributed to the formation of Ti^{3+} in TiO$_2$ (Wei et al., 2012).

Raman was used to evaluate TiO$_2$ lattice vibrational mode (Figure 4.55). A distinctive anatase feature at 144 cm^{-1} (Eg), 197 cm^{-1} (E$_g$), 396 cm^{-1} (B$_{1g}$), 515 cm^{-1} (A$_{1g}$), 519 cm^{-1} (B$_{1g}$ superimposed with the A$_{1g}$ band) and 636 cm^{-1} (E$_g$) were observed in all prepared photocatalysts. In H12-TiO$_2$ (Figure 4.55c (left)), a small peak at 447 cm^{-1} (E$_g$) represents rutile. In the enlarged Raman spectra at 144 cm^{-1}, a gradual shift to higher frequency (blue shift) was observed. This shift was triggered by defects such as oxygen vacancies and Ti^{3+} (Khan et al., 2014). H12-TiO$_2$ showed a red shift at 144 cm^{-1}

band, indicating that the frequency of phonons interacting with incident photons decreases. This fact may indicate a reduced number of surface defects, but this was in contrast with the experimental observation of relevant surface disorders in H12-TiO₂, as shown in HR-TEM images (Figure 4.40). Thus, the slight red shift in H12-TiO₂ could be associated with tensile strains and structural changes due to the formation of surface disorders (Scepanovic, G.-Brojcin, D.-Mitrovic, & Popovic, 2009). In F4-TiO₂ and hydrogenated F-doped TiO₂, insignificant {001} facets growth was observed relative to F127-TiO₂, even under the presence of fluorine (Table 4.17). This was attributed to the limited accessibility of bulk CF₃COO⁻ ions binding onto Ti-O-Ti polymer during the sol gel process for the development of {001} facets (Samsudin et al., 2016; Yu et al., 2014). This also explained the less dramatic change in morphology in F4-TiO₂ prepared using trifluoroacetic acid as opposed to other fluorine precursor such as hydrofluoric acid (Ong et al., 2014).
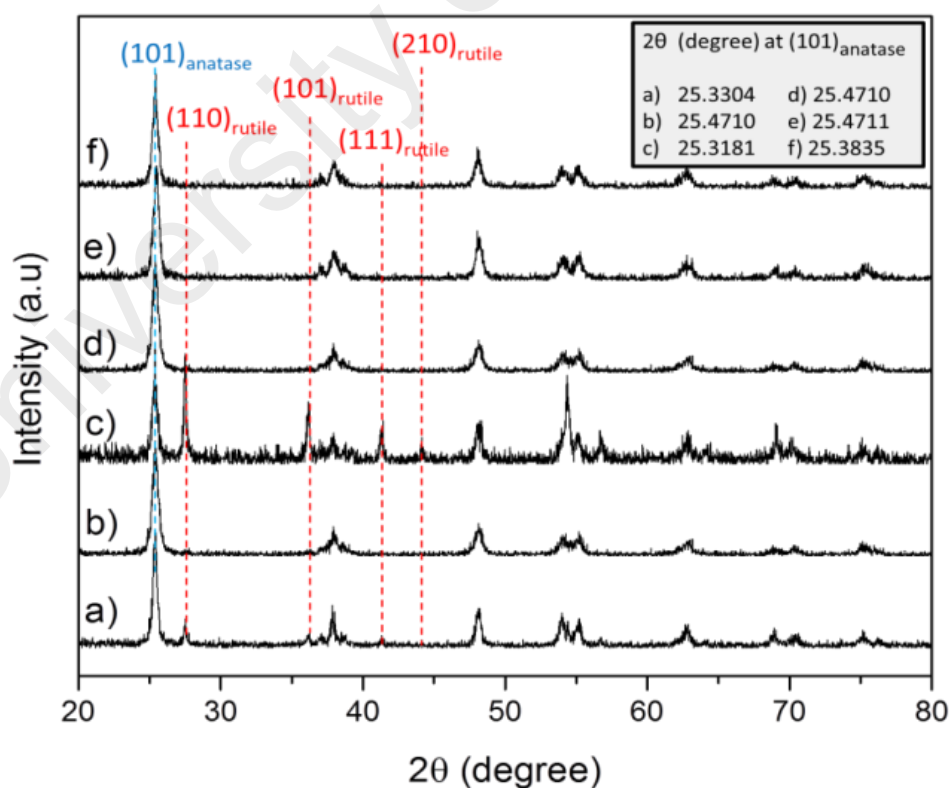
Figure 4.54: XRD spectra of a) F127-TiO₂, b) F4-TiO₂, c) H12-TiO₂, d) HF6-TiO₂, e) HF12-TiO₂ and f) HF24-TiO₂ with inset showing corresponding 2θ degree at (101) anatase plane
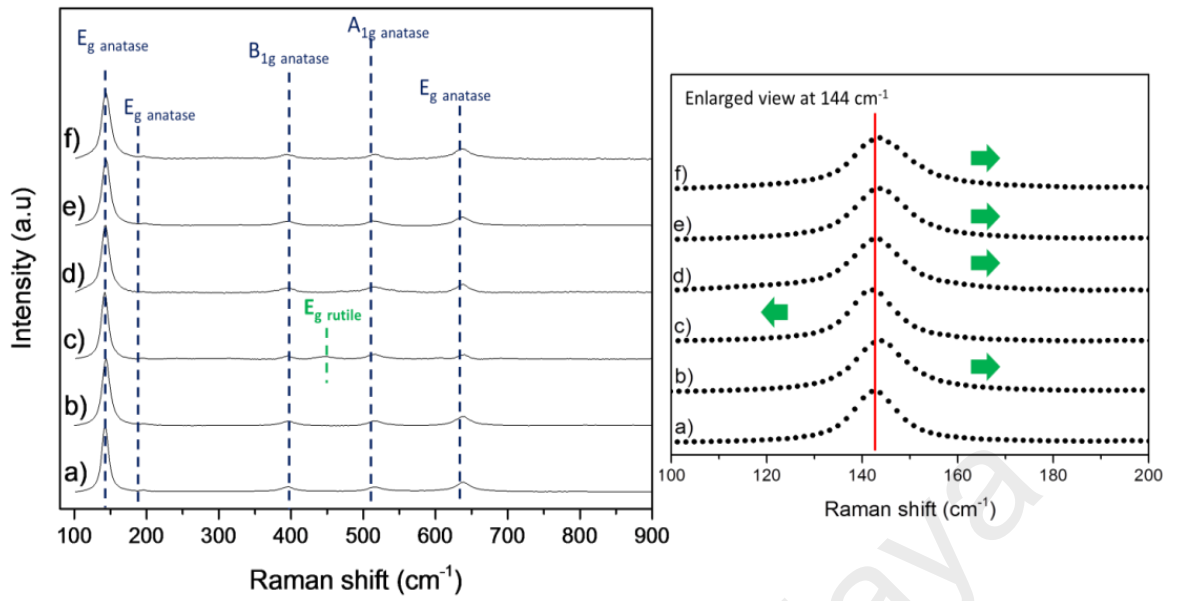
Figure 4.55: Raman spectra for a) F127-TiO$_2$, b) F4-TiO$_2$, c) H12-TiO$_2$, d) HF6-TiO$_2$, e) HF12-TiO$_2$ and f) HF24-TiO$_2$ and enlarged Raman spectra at 144cm^{-1} of anatase

Table 4.16: Crystal phase ratio, crystallite size and plane with corresponding full width at half maximum (FWHM) of un-doped TiO_2, F-doped TiO_2, hydrogenated TiO_2 and hydrogenated F-doped TiO_2

Catalyst	Crystal phase ratio, wt%		Crystallite size, nm		Plane & Corresponding FWHM				Williamson-Hall Plot (Average lattice strain)
	Anatase	Rutile	Anatase	Rutile	(101)	(110)	(004)	(200)	%
F127-TiO_2	65	35	23.0	69.3	0.3542	0.1181	0.4723	0.2755	0.4207
F4-TiO_2	100	-	18.8	-	0.4330	-	0.3149	0.5510	0.5310
H12-TiO_2	40	60	29.6	52.1	0.2755	0.1574	0.4900	0.3936	0.3315
HF6-TiO_2	100	-	19.0	-	0.4282	-	0.3149	0.4755	0.4707
HF12-TiO_2	100	-	25.9	-	0.3149	-	0.4723	0.4723	0.4419
HF24-TiO_2	100	-	51.7	-	0.1574	-	0.3542	0.3926	0.4043

The FTIR spectra were reported in Figure 4.56a-f. The intensity of the peaks at 3722 cm^{-1} and 3825 cm^{-1} gradually decreases with duration of hydrogenation in F-doped TiO_2 (Figure 4.56d-f). FTIR is a useful tool to evaluate the presence of Ti^{3+} ions in TiO_2 however it does not differentiate surface or bulk Ti^{3+} ions (Samsudin, Hamid, Juan, Basirun, & Kandjani, 2015). In Figure 4.56, the peak at 3410 cm^{-1} represents surface bonded hydroxyl groups. Surface fluorination slightly decreases the intensity of this peak, while hydrogenation nearly completely reduces the intensity of this peak. The intensity also decreases as a function of hydrogenation time in F-doped TiO_2. Furthermore, there was a slight red shift at the stretching vibration of Ti-O-Ti from 591 cm^{-1} to a lower frequency in F4-TiO_2 and hydrogenated F-doped TiO_2. Previous work attributed this red shift to the interfacial interaction between another compound with TiO_2 which further enhances the photo-generated electrons transfer and photocatalytic activity (Lu, Zhang, & Wan, 2015). In this work, it may be related to the presence of surface fluorination on TiO_2.
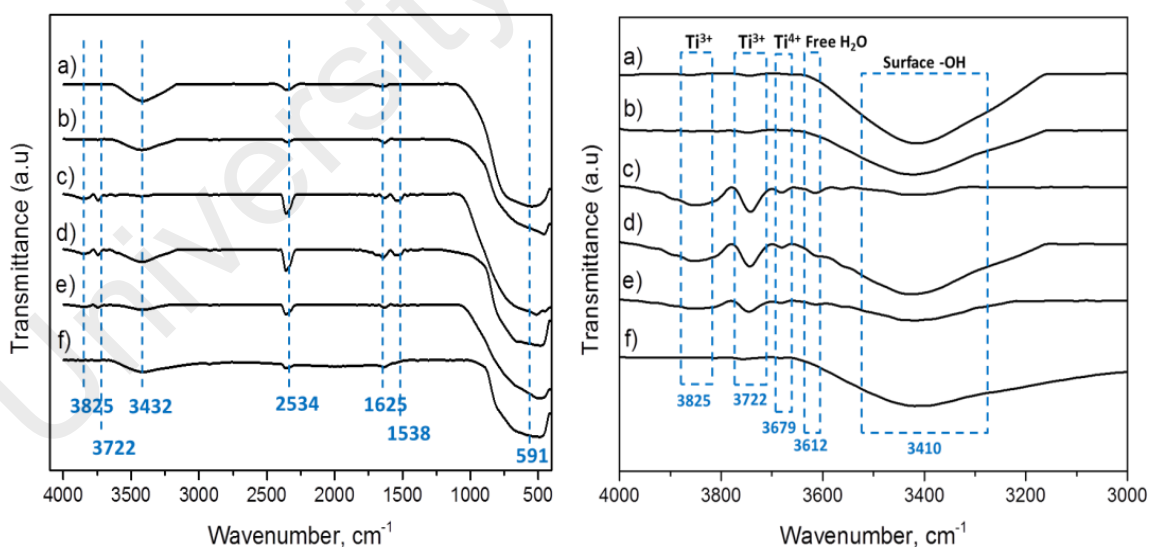
Figure 4.56: FTIR spectra for a) F127-TiO_2, b) F4-TiO_2, c) H12-TiO_2, d) HF6-TiO_2, e) HF12-TiO_2 and f) HF24-TiO_2 and enlarged FTIR spectra from 4000 to 3000 cm^{-1}

4.6.3 Light absorption and photoluminescence behavior

The optical properties of the prepared photocatalysts were reported in Figure 4.57, while the calculated band gap calculated from these spectra were reported in Table 4.17. Both F127-TiO$_2$ and H12-TiO$_2$ showed UV and visible light absorption, but the light absorption of H12-TiO$_2$ was extended towards the infrared region as well. TiO$_2$ absorbs majorly in the UV region and corresponds to a band gap of 2.94 eV, which was likely due to the presence of small rutile crystals decorating the anatase crystals. In H12-TiO$_2$, the visible and infra-red light absorption was attributed to surface disorders, oxygen vacancies and Ti^{3+} (Chen et al., 2011; Samsudin, Hamid, Juan, Basirun, & Kandjani, 2015). H12-TiO$_2$ showed apparently a decreased intensity of bands in the UV region, likely due to the presence of disorders. Contrary to F127-TiO$_2$ and H12-TiO$_2$, F4-TiO$_2$ majorly absorbs in the UV region, with an apparent intensification of bands. For hydrogenated F-doped TiO$_2$, the optical spectra were similar to that of H12-TiO$_2$, but with higher absorption intensity in the infrared region especially in HF12-TiO$_2$ and HF24-TiO$_2$. H-TiO$_2$ and HF6-TiO$_2$ showed similar spectra in the visible and infra-red regions, but the latter showed a more intense band in the UV region, likely due to fluorine.

The efficiency of charge carrier trapping, transport and transfer to the catalyst surface were analyzed by photoluminescence (PL) (Figure 4.57 (right)). Ligand to metal charge transfer (O^{2-} to Ti^{4+}) was observed in all photocatalysts below 350 nm. F127-TiO$_2$ showed poorest electrons and holes separation signatured by its high PL intensity. The doping of TiO$_2$ with F (F-TiO$_2$) strongly depresses the PL intensity, in agreement with the effect of highly electronegative fluorine to increase the lifetime of electrons on the catalyst surface. Furthermore, a right shift in the PL spectra was observed for F4-TiO$_2$ with respect to F127-TiO$_2$, likely due to the presence of Ti^{3+} ions. It is also worth to note that the PL peak of F4-TiO$_2$ was the broadest due to the larger concentration of

surface oxygen vacancies. Hydrogenation (H12-TiO₂) partially suppresses the PL intensity (Figure 4.57 (right)), due to the abundant presence of charge traps related to the high concentration of defects. The higher PL intensity in HF24-TiO₂ could be the result of excessive surface disorders that leads to additional defects and acts as charge carrier traps. In addition, the larger surface disorders on HF24-TiO₂ results to a decreased in TiO₂ crystallinity and thus results to higher PL intensity (Yang et al., 2014).
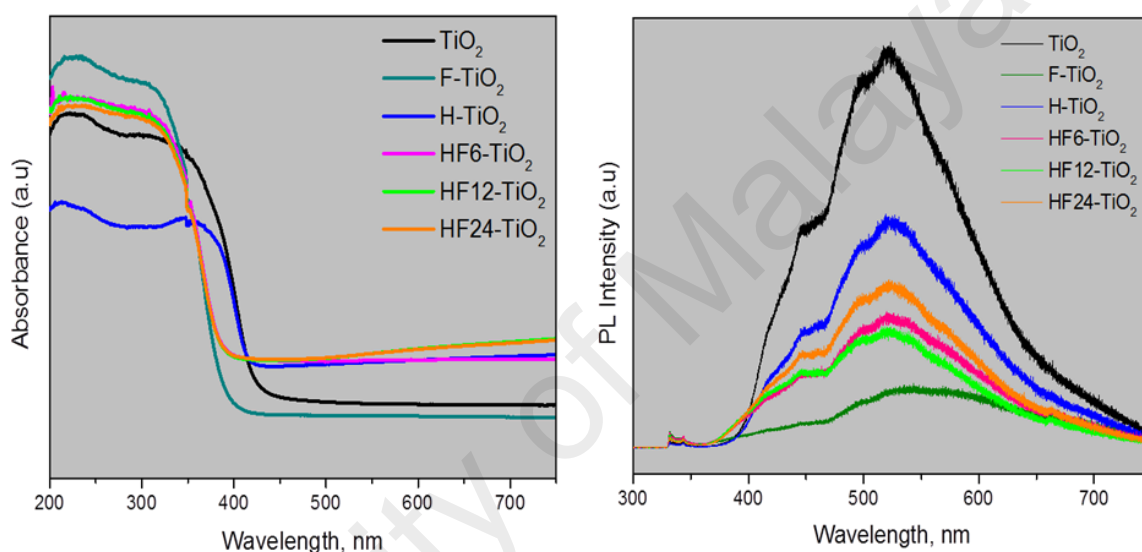
Figure 4.57: Absorption and photoluminescence spectra of all prepared photocatalyst

Table 4.17: Percentage (%) of exposed {001} facets and band gap calculated using Tauc Plot function of un-doped TiO₂, F-doped TiO₂, hydrogenated TiO₂ and hydrogenated F-doped TiO₂

Catalyst	Raman Intensity		% of exposed {001} facet	Band gap (eV)
	E_g (144 cm^{-1})	A_{1g} (515 cm^{-1})		
F127-TiO₂	21578	1574	7.36	2.94
F4-TiO₂	10267	721	7.02	3.18
H12-TiO₂	7569	551	7.29	2.96
HF6-TiO₂	8482	691	8.15	3.17
HF12-TiO₂	7219	540	7.48	3.18
HF24-TiO₂	4837	310	6.42	3.23

Another factor that affect the electrons and holes recombination is the concentration of {001} facets. Larger concentration of {001} facets inhibits electrons and holes recombination due to the creation of surface hetero-junctions between {001} and {101}

facets in TiO₂ (Carp et al., 2004; Samsudin et al., 2016; Yu, Low, Xiao, Zhou, & Jaroniec, 2014). The largest concentration of {001} facets was observed in HF6-TiO₂ sample, although probably the concentration of {001} facets were not large enough to cause any significant change in the PL intensity. The peaks at 400 to 430 nm in the PL spectra were related to defect states. Self-trapped electrons were observed in all photocatalysts at 450 nm (Memesa et al., 2011). Surface oxygen vacancy that is located under (101) planes was represented by PL peak at 470, 500 and 525 nm (Dozzi et al., 2013; Jin et al., 2015). These surface oxygen vacancies acts as electron donors and enhance the photocatalytic activity of TiO₂. HF6-TiO₂, HF12-TiO₂ and HF24-TiO₂ showed a peak at 500 nm, likely associated to oxygen vacancies responsible for visible and infrared light absorption. The PL peak at 600 nm was classified as a red PL and represents un-coordinated surface Ti^{3+} ions (Jin et al., 2015). Interestingly a new peak at 675 nm was present in all hydrogenated F-doped TiO₂ and was attributed to additional formation of surface Ti^{3+}. This peak was not observed in hydrogenated TiO₂, which was prepared in the absence of fluorine. Thus, this new finding could be linked to the synergistic combination of fluorine and hydrogen in the modified TiO₂.

4.6.4 Surface characterization

Figure 4.58 shows the C1s spectrum of TiO₂ and hydrogenated F-doped TiO₂ prepared at 6h, 12h and 24h. The peaks at ~286 eV and ~288-290 eV represents C-OH and O-C=O respectively. Interestingly in HF6-TiO₂, the corresponding peak area at ~286 eV increases and was attributed to enhanced surface hydroxyl groups bonded to the carbon atoms. In HF6-TiO₂, HF12-TiO₂ and HF24-TiO₂, the corresponding peak area at ~288 to 290 eV decreases as hydrogenation time increases. Adsorbed CH_3COO^- species (residual from the preparation) were also gradually removed from the photocatalyst surface as a function of hydrogenation time. This was consistent with the data on porosity whereby H24-TiO₂ showed the highest value (Table 4.15). During

hydrogenation, surface oxygen atoms were gradually removed from the photocatalyst surface as observed in the EDX data (Table 4.14). Data in Figure 4.58 also evidenced that residual adsorbed TFA was not present on the photocatalyst surface, because peaks at ~292 eV and ~294 eV (CF_2 and CF_3 bonds, respectively) were absent.
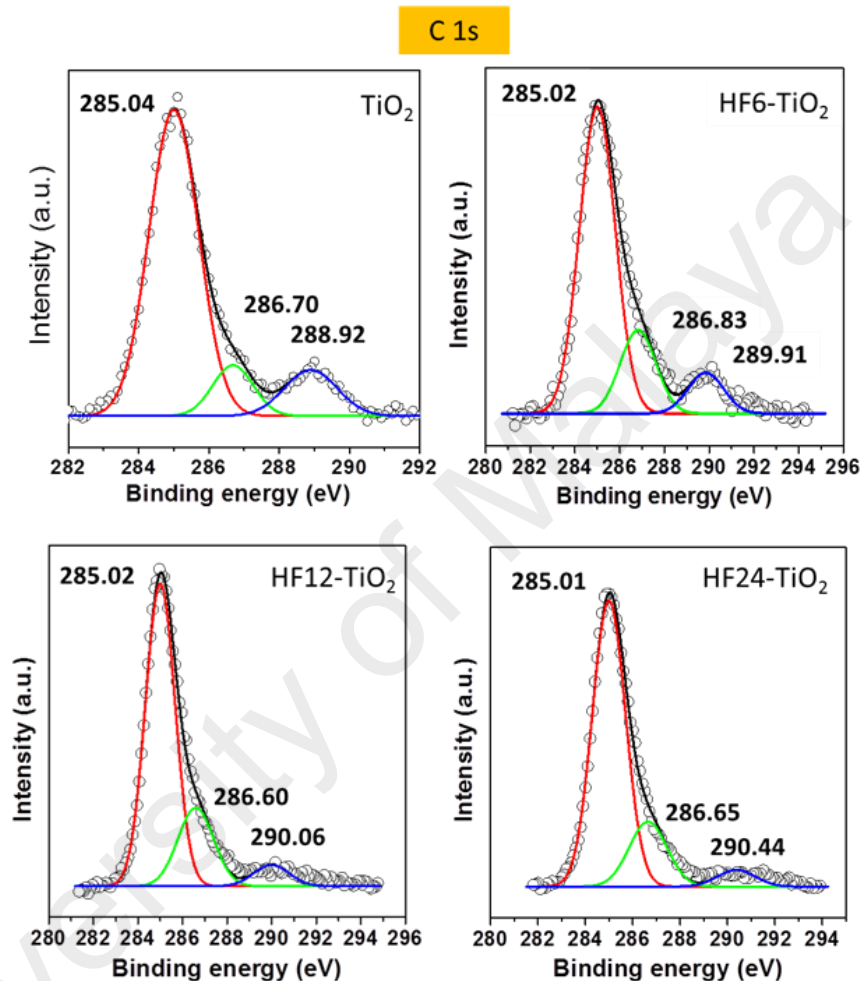
Figure 4.58: XPS spectrum showing C 1s band position for un-doped TiO_2 and hydrogenated F-doped TiO_2 photocatalysts

Figure 4.59 shows the XPS F 1s spectrum of F4-TiO$_2$ and hydrogenated F-doped TiO$_2$ samples. The position of fluorine in F-TiO$_2$ evidences the replacement of hydroxyls group with fluorine forming ≡Ti-F species (Lv, Yu, et al., 2011). The hydrogenation of F-TiO$_2$ decreases progressively the intensity of this peak, although slightly shifting to higher E$_g$. This indicates removal of the fluoride ions from the catalyst and complete removal was observed in HF24-TiO$_2$. The XPS F 1s peak in HF6-TiO$_2$ and HF12-TiO$_2$ was observed at 685.74 and 685.96 eV respectively. This value is close to that of TiOF$_2$ (685.3 to 685.5 eV) (Li & Liu, 2008), but no evidence were found of this species. The Ti 2p spectrum of un-doped TiO$_2$ and hydrogenated F-doped TiO$_2$ clearly shows Ti^{4+}-O bonds at ~ 458 to 459 eV and ~ 464 to 465 eV which corresponds to Ti 2p$_{3/2}$ and Ti 2p$_{1/2}$ paramagnetic spins respectively (Chen et al., 2013, 2011; Lim et al., 2005). Surface Ti^{2+} and Ti^{3+} species were not present (E$_g$ at 455 eV and 457 eV) (Lee & Lee, 2008). In addition, these states are metastable and easily oxidized in air. Ti 2p peaks gradually shifts to higher E$_g$ relative to un-doped TiO$_2$ which was an indication of different Ti binding environments. Although the F 1s spectra showed no presence of fluorine on the HF24-TiO$_2$ surface, EDX data indicates presence of fluorine, likely in bulk form (Table 4.14). The fluorine atom was less likely to be in the form of Ti-F-Ti, as FTIR did not show any increment of Ti^{3+} as hydrogenation of F-doped TiO$_2$ progresses (Figure 4.56d,e,f (right)).

Both F127-TiO$_2$ and hydrogenated F-doped TiO$_2$ shows presence of lattice oxygen, O^{2-} and surface hydroxyl, O$_{OH}$ at E$_g$ of ~530 eV and ~531 eV respectively (Karaman et al., 2013). In hydrogenated F-doped TiO$_2$, the O 1s E$_g$ was right shifted by approximately 1 eV in HF6-TiO$_2$ and gradually decreased again to a lower E$_g$ value. The physically absorbed fluorine forming Ti-O-F bonds decreased the electron density of oxygen, thus increases the E$_g$. As hydrogenation progresses, fluorine were gradually removed from the surface or less likely, migrates deeper into bulk TiO$_2$. The increased

in oxygen electron density was attributed to the larger surface disorders forming O-Ti-H. Previous work attributes E_g at 532.7 eV to adsorbed H_2O (Liu et al., 2008). Hence there was a probability that the E_g at ~532 eV in hydrogenated F-doped TiO_2 represents surface hydroxyls and also absorbed H_2O. The change of O 1s E_g in hydrogenated F-doped TiO_2 implies different binding environment as a result of continuous hydrogenation of F-TiO_2. The thickness of the surface disordered layer increases from 1.7 nm to 2.5 nm in HF24-TiO_2. Furthermore, large presence of surface disorders results to a decrease in the E_g of O 1s as well (Samsudin, Hamid, Juan, Basirun, & Kandjani, 2015).

The valence band maximum of un-doped TiO_2 and hydrogenated F-doped TiO_2 was determined by linear extrapolation of the peaks to the baseline as shown in Figure 4.59. Uplifting of the valence band (towards negative E_g) and lowering of the conduction band were due to the presence of surface disorders and Ti^{3+} and oxygen vacancies respectively (Oshani et al., 2014). Relative to F127-TiO_2, a significant uplifting of the valence band by 0.25 eV was observed in HF6-TiO_2. Surprisingly, no further uplifting of the valence band was observed in HF12-TiO_2 and HF24-TiO_2. The presence of fluorine in hydrogenated F-doped TiO_2 influences likely the position of the valence band. It is also worth to mention that no significant band gap narrowing was observed (Table 4.17). Thus the ability of hydrogenated F-doped TiO_2 to absorb visible and infrared light was attributed to the formation of oxygen vacancies and Ti^{3+} occupying the states below the conduction band. This was consistent with the presence of an additional PL peak at 675 in hydrogenated F-doped TiO_2 (Figure 4.57 (right)) and was related to the presence of additional Ti^{3+} sites deriving from the synergistic effect of fluorine and hydrogen in the modified TiO_2.
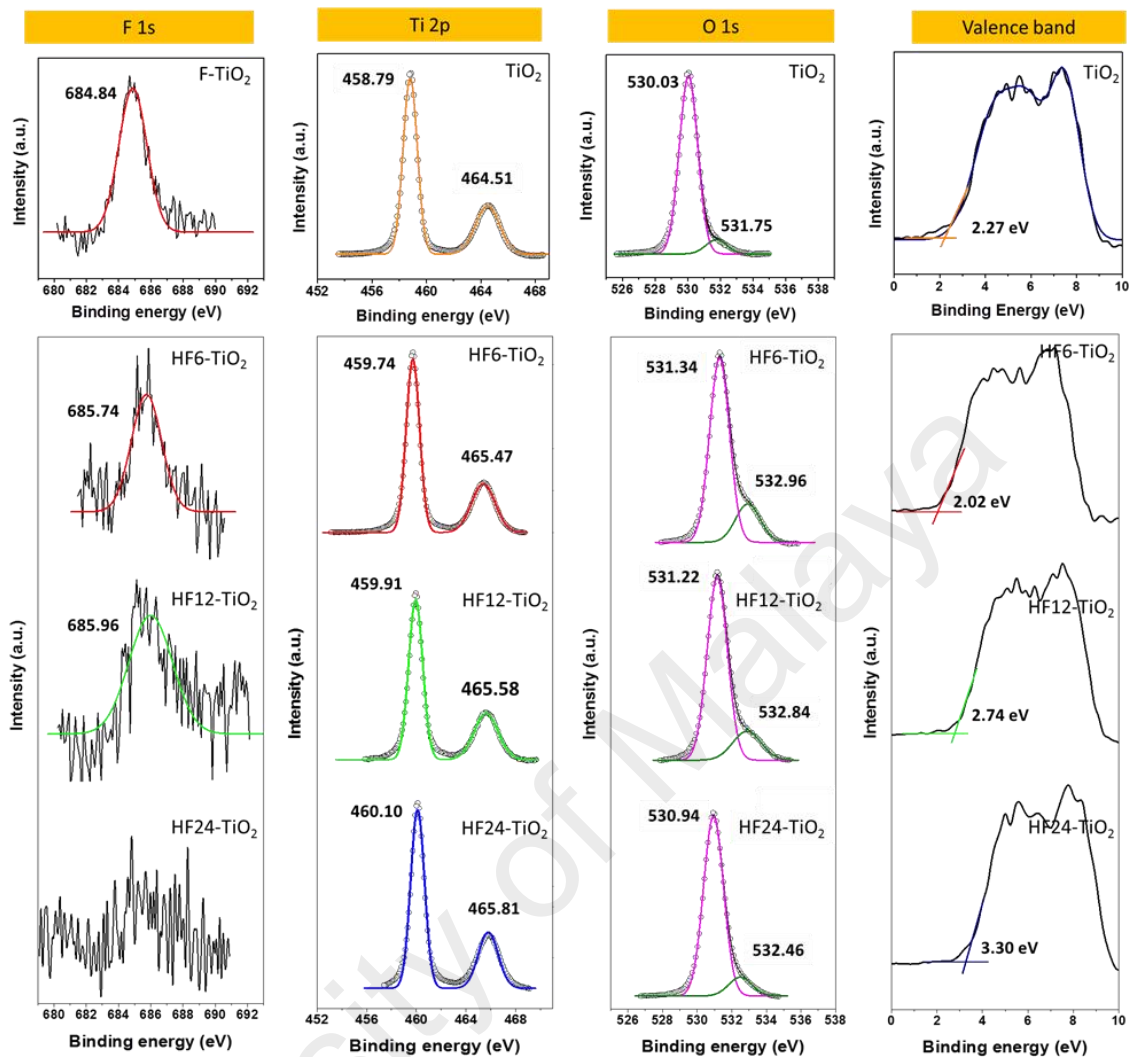
Figure 4.59: XPS spectrum showing F1s, Ti 2p, O 1s and valence band position for un-doped TiO_2 and hydrogenated F-doped TiO_2 photocatalysts

4.7 Preliminary investigation on photocatalytic reaction parameters

The photocatalytic degradation of atrazine is greatly driven by the availability of surface active radicals. The formation of hydroxyl radicals, $\cdot$OH is highly favored in most photocatalytic activity as it has the highest oxidizing potential relative to other radicals such as superoxide anion radicals, $\cdot O_2^-$ (Samsudin et al., 2015). In Figure 1.2, $\cdot$OH radicals are produced at the valence band (VB) from the oxidization of surface-bound OH or absorbed H_2O. At the conduction band (CB) band, additional $\cdot$OH radicals are also formed by the reduction of H_2O_2 generated from two $\cdot$OOH radicals. It has been reported before that TiO_2 with {101} facets facilitate surface photo-reduction while {001} facets facilitate surface photo-oxidation (Hu, Li, & Yu, 2010). In all of the prepared photocatalysts, the estimated ratio of exposed high energy {001} facets are lower than {101} facets. Therefore, it was assumed that the majority of the $\cdot$OH radicals were formed from the reduction of H_2O_2 at the CB. The photocatalytic degradation activity is greatly influenced by the amount of photocatalyst used, initial pollutant concentration and pH of the environment (Gaya & Abdullah, 2008). These factors were further investigated to determine the optimum photocatalytic condition and were used to effectively assess the prepared photocatalysts.

4.7.1 Catalyst loading

The presence of light scattering due to the differences in particle characteristics may affect the results in a slurry batch-type photocatalytic experiments. This could lead to a less accurate estimation of the differences in the rate constants of atrazine depletion between F127-TiO_2 and doped TiO_2. Therefore, the kinetics of atrazine removal was studied as a function of the catalyst concentration in solution. Even if kinetics should not formally depend on this aspect, the concentration of catalyst in the solution affects the amount of photons reaching the catalyst due to light scattering effects or other physico-chemical phenomena not related to the intrinsic activity of the photocatalyst. It

was observed that both F127-TiO$_2$ and N,F-TiO$_2$ showed maximum atrazine removal of about 0.5 g/l of photocatalyst loading (Figure 4.60).
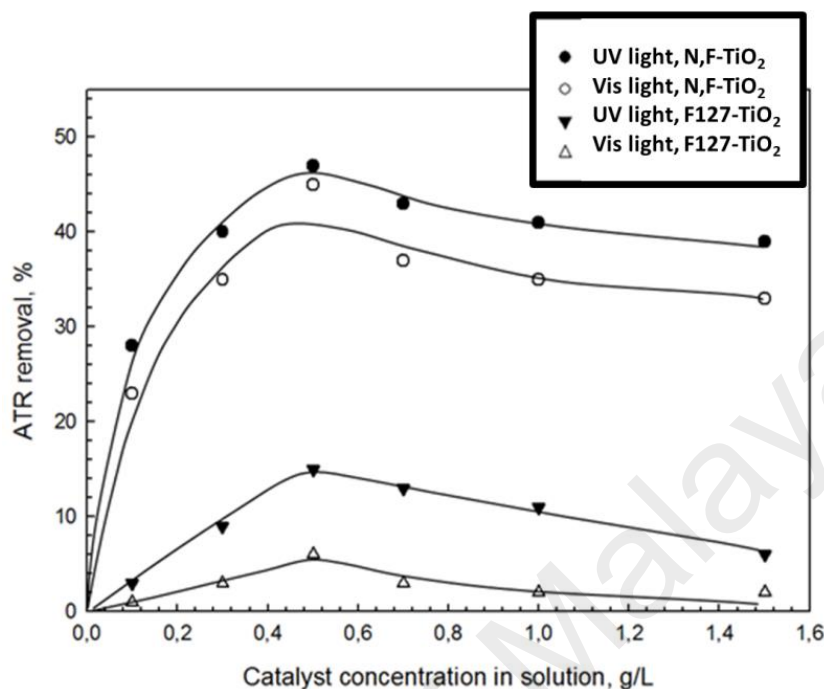
Figure 4.60: Influence of F127-TiO$_2$ and N,F-TiO$_2$ loading on the photodegradation of atrazine. Reaction conditions: initial atrazine concentration = 2 mg/l; irradiation time = 360 min; stirring speed = 400 rpm; pH = 7.3

The presence of a maximum in atrazine removal at the same catalyst loading indicates that the eventual differences in the photocatalysts were minor and allow a reliable comparison using the same photocatalyst amount of about 0.5 g/l. On increasing the amount of catalyst in the solution, there was an increase of the fraction of light reaching the photocatalyst surface, and promotes enhanced efficiency in generating the ·OH radicals responsible for the photocatalytic activity. However, this also increases light scattering by the solid particles and the rate of quenching of charge separation due to suspended particles collision. Being the maximum related to the physico-chemical phenomena of light scattering and particle collision, it may also depend on the particle characteristics as well, such as shape, size, wettability which may increase aggregation, etc., besides due to the photoreactor characteristics.

On the other hand, by fixing the catalyst concentration in solution, it was reliable to derive the first order rate constant of atrazine depletion. As expected, first-order rate constant of F127-TiO$_2$ was strongly depressed under visible-light irradiation (rate is about 80 % less of that with UV-light), while the decrease in the case of N,F-TiO$_2$ was only about 17 % (Table 4.18).

Table 4.18: First order rate constant (k) for F127-TiO$_2$ and N,F-TiO$_2$ under visible and UV-light irradiation

Catalyst	k (UV-light)	k (Visible-light)
F127-TiO$_2$	0.53E-3	0.11E-3
N,F-TiO$_2$	1.90E-3	1.58E-3

It may be observed that the rate constant with visible light for N,F-TiO$_2$ was significantly higher than that of F127-TiO$_2$ with UV-light. This was somehow expected as N,F-TiO$_2$ photocatalyst has been numerously reported to govern higher photocatalytic rate relative to un-doped TiO$_2$ (Wang et al., 2005; Wu et al., 2010). This was attributed to enhanced solar light absorption, charge carriers mobility, smaller band gap and presence of surface defects.

4.7.2 Initial atrazine concentration

The effect of the initial atrazine concentration on the apparent first order rate constant was shown in Figure 4.61 for F127-TiO$_2$ and N,F-TiO$_2$. There was a linear decrease in the rate constant on increasing the initial atrazine concentration. At higher substrate (atrazine) concentration, the photons originating from the source of lights were absorbed by the pollutant and less towards the surface of the photocatalysts. In return, less ·OH radicals were formed which eventually decreases the rate of atrazine degradation. In this aspect, larger concentration of catalyst (more than 0.5 mg/l) was necessary and thus longer reaction duration. In Figure 4.61, extrapolation to zero atrazine concentration may allow evaluating the intrinsic catalyst activity. Data in Table

4.19 evidenced that the intrinsic activity, extrapolated at zero atrazine concentration, was about 1.7 times higher in N,F-TiO$_2$ with respect to F127-TiO$_2$. With respect to this finding, the proposed initial atrazine concentration was fixed 0.5 mg/l throughout the remaining experiments.
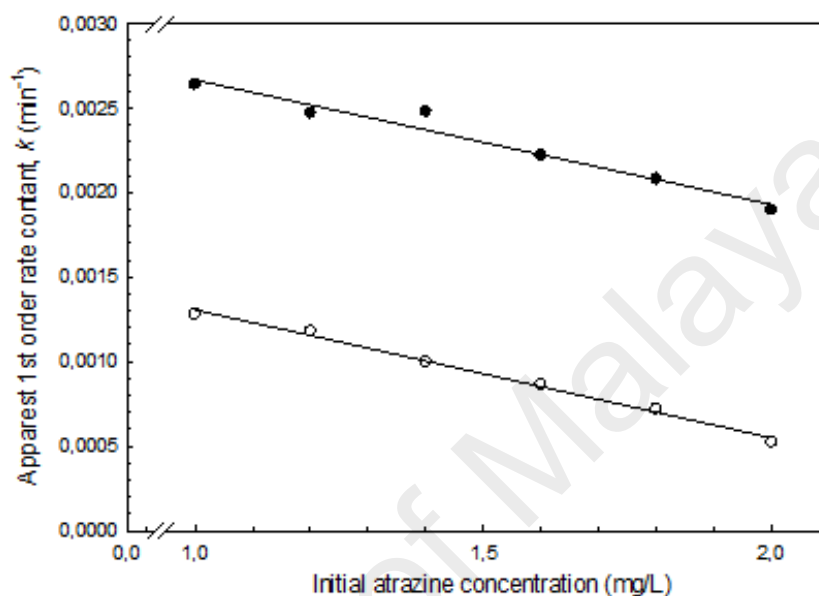
Figure 4.61: Dependence from the initial atrazine concentration of the apparent 1st order rate constant of atrazine depletion using F127-TiO$_2$ (open symbol) and N,F-TiO$_2$ (solid symbol) photocatalysts. Reaction conditions: catalyst concentration = 0.5 g/l; light source = UV light; irradiation time = 360 min; stirring speed = 400 rpm; pH = 7.3

Table 4.19: Fitting parameters for linear dependence of data reported in Figure 4.61

Catalyst	Slope	K at [ATR]$_o$ = 0	R^2
F127-TiO$_2$	-7.6E-4 ± 3.9E-5	2.06E-3 ± 4.6E-5	0.9938
N,F-TiO$_2$	-7.4E-4 ± 7.6E-5	3.40E-3 ± 1.2E-5	0.9595

4.7.3 pH and isoelectric point (IEP)

The measured isoelectric point (IEP) of F127-TiO$_2$ and N,F-TiO$_2$ was around 6.4 and 5.8 respectively, and similar IEP was observed in other work for N and F doping in TiO$_2$ (Meng, Chen, Wang, Ding, & Shan, 2009; Stewart, 2009). The initial pH of atrazine solution was measured at 7.3 and thus, based on Figure 4.62, the surface charge of both catalysts in this condition was negatively charged. As the molecular structure of

atrazine consists of multiple lone pairs, it may be easily protonated (atrazine is a base with pKa = 1.7). Hence in the present of protons, the substrate becomes positively charged. Thus, the negatively charged photocatalysts surface and positively charged atrazine molecules favored surface absorption to a certain extent.
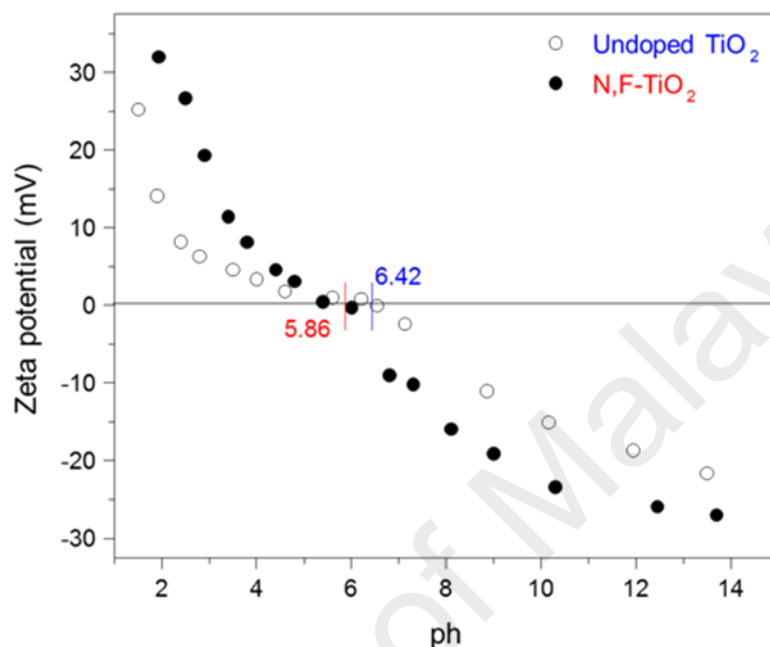
Figure 4.62: Isoelectric point (IEP) from pH 2 to pH 14 for un-doped TiO_2 ($F127$-TiO_2) and N,F-TiO_2

The evaluation of pH on the rate of atrazine depletion is important to understand whether there is any impact on the adsorption properties and catalyst surface charge. Figure 4.63 reports the photocatalytic response of $F127$-TiO_2 and N,F-TiO_2 from the pH range of 3 to 10. The change of atrazine removal as a function of time for each reaction condition were elaborated to derive the apparent 1st order rate constant which was also plotted in Figure 4.63. Almost a similar pattern was observed for both photocatalysts, which demonstrates no major differences in the IEP value even after N and F doping.

At acidic condition, the major oxidation species are the photo-generated holes on the catalyst surface, whereby at higher pH (pH 7 and above), the major oxidation species are the hydroxyl radicals (Li, Zhu, Chen, Li, & Zhang, 2011). Poor activity was observed in acidic condition (pH below 7) for both $F127$-TiO_2 and N,F-TiO_2. In acidic condition, $F127$-TiO_2 and N,F-TiO_2 photocatalysts surface were positively charged and

the lone pairs located at the N-ring and alkylamino chains of atrazine was also protonated with thus an inhibition on atrazine adsorption. On the other hand, this result confirmed the absence of homogeneous reactions, due to F^- leaching, differently from earlier observation for phenol degradation in acidic conditions by F- doped TiO_2 (Sahoo & Gupta, 2012). Above the threshold of IEP, e.g. when the surface of TiO_2 becomes negatively charged, the photocatalysts starts to be active in atrazine photodegradation, with a maximum activity in alkaline condition. This fact evidences clearly that adsorption of atrazine was a pre-requirement for the photocatalytic degradation and that homogeneous reactions (bulk liquid phase) were negligible. The higher concentrations of hydroxyl ions available at higher pH values were oxidized by the photo-excited holes in TiO_2 to form hydroxyl radicals ($\cdot OH$), thereby enhances the photo-degradation rate. On the other hand, the standard reduction potential of hydroxyl radicals decreases from 2.7 eV in acidic solution to 1.8 eV in neutral conditions and further decreases in basic conditions (Gajjela et al., 2010). It was thus quite reasonable to have a maximum in the rate of photo-degradation of atrazine with the change of pH. There was also a probability of atrazine de-protonation at very basic condition which may perturb the catalyst/substrate absorption efficiency. Nevertheless, at the de-protonated condition, the photocatalytic activity may proceeds via electrons (lone pairs) of atrazine towards the empty Ti 3d orbital of TiO_2. Additionally, the availability of photo-excited electrons on TiO_2 surface may react with the hydrogen atom of atrazine structure as well. Both of these scenarios triggers the catalytic surface reaction. It was worth to mention that the photocatalytic activity worsens at pH above 9 due to the repulsion of the excessive hydroxyl ions in the solution with the negatively charged surface of TiO_2. Regardless, N,F-TiO_2 showed a specific activity about 2 to 3 times higher than F127-TiO_2, further confirming previous indications of the higher intrinsic activity of the N,F-TiO_2.
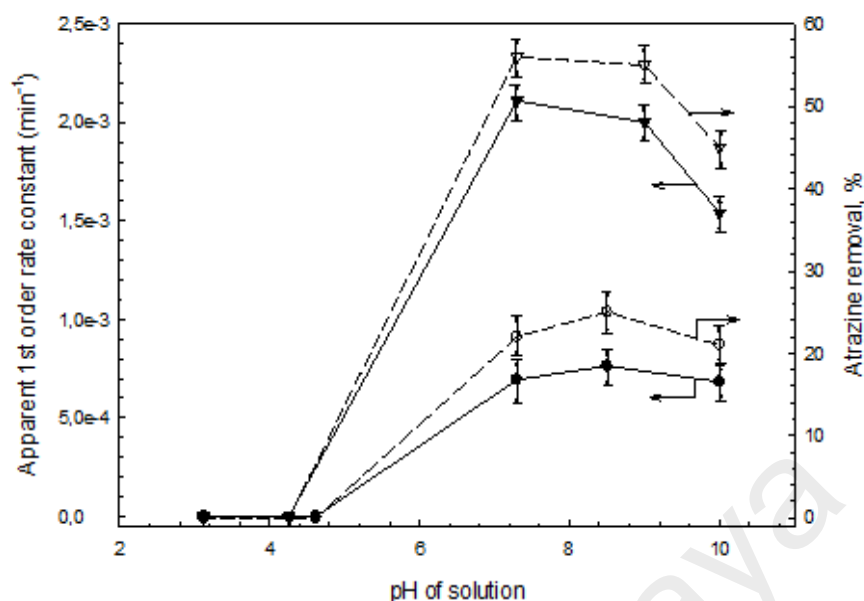
Figure 4.63: Effect of pH on atrazine removal and apparent 1st order rate constant of ATR depletion using F127-TiO$_2$ (circle symbol) and N,F-TiO$_2$ (triangle symbol) photocatalysts. Symbols = solid symbols (atrazine removal), open symbols (rate constant). Reaction conditions: initial atrazine concentration = 2 mg/l; catalyst loading = 0.5 g/l; light source = UV light; irradiation time = 360 min; stirring speed = 400 rpm; pH = 7.3

4.8 Photocatalytic degradation of atrazine using optimum reaction conditions

The photocatalytic degradation of atrazine using an initial concentration of 0.5 mg/l was evaluated using 0.5 g/l of catalyst loading and the results for the activities under both UV and visible light are displayed in Table 4.20. In addition, the normalized rate constant per surface area (k/S.A) are also included to investigate the impact of photocatalyst surface area towards the photocatalytic degradation of atrazine. For anionic-doped and hydrogenated TiO$_2$, the chosen photocatalysts used to evaluate the catalytic activity was based on the lowest PL intensity and thus a valid comparison in their activities could be made. Prior to the photocatalytic degradation activity, the catalyst was left in the dark to reached absorption-desorption equilibrium. For all of the analyzed photocatalysts, the reaction follows a first order rate of reaction derived from Eq. 3.1 and Eq. 3.2. A first order rate of reaction was confirmed by plotting a linear graph of ln [atrazine] versus time as shown in Figure 4.64.

Table 4.20: First order rate constant (k) and normalized rate constant per surface area (k/S.A) under UV and visible light irradiation

Catalyst	Surface area (m^2/g)	$[ATR]_o$	UV light			Visible light		
			k	k/S.A	R^2	k	k/S.A	R^2
TiO_2 (no surfactant)	30.46	0.81	1.4E-3	0.04	0.963	1.3E-3	0.04	0.980
$F127-TiO_2$*	38.77	0.87	2.3E-3	0.06	0.970	1.8E-3	0.05	0.986
$N1-TiO_2$	30.32	0.96	2.0E-3	0.07	0.991	9.2E-3	0.30	0.975
$F4-TiO_2$	24.65	0.83	2.8E-3	0.11	0.989	1.3E-3	0.05	0.968
$NF1-TiO_2$	14.30	0.87	11.2E-3	0.78	0.980	10.9E-3	0.76	0.992
$H12-TiO_2$	31.57	0.76	7.4E-3	0.23	0.993	7.0E-3	0.22	0.990
$HF6-TiO_2$	54.61	0.91	13.5E-3	0.25	0.972	12.1E-3	0.22	0.964
$HF12-TiO_2$	50.34	0.89	17.4E-3	0.35	0.988	15.3E-3	0.30	0.989
$HF24-TiO_2$	46.48	0.87	11.9E-3	0.26	0.996	10.4E-3	0.22	0.985

* $F127-TiO_2$ is also denoted as $N0-TiO_2$, $F0-TiO_2$, $NF0-TiO_2$, $H0-TiO_2$ and $HF0-TiO_2$.

4.8.1 Surfactant-modified TiO₂ (F127-TiO₂)

Referring to Figure 4.64 and Table 4.20, it was observed that the rate constant of atrazine degradation using F127-TiO$_2$ was roughly 1.5 to 1.7 times higher than TiO$_2$ prepared without surfactant. This observation confirmed that F127-TiO$_2$ is a better photocatalyst. Figure 4.64 shows that the photocatalytic activity progresses under both UV and visible light, however with a lower degradation rate under visible light. Overall, the main factor in the enhancement of the photo-kinetics in F127-TiO$_2$ was related to the change of structure induced by pluronic F127.
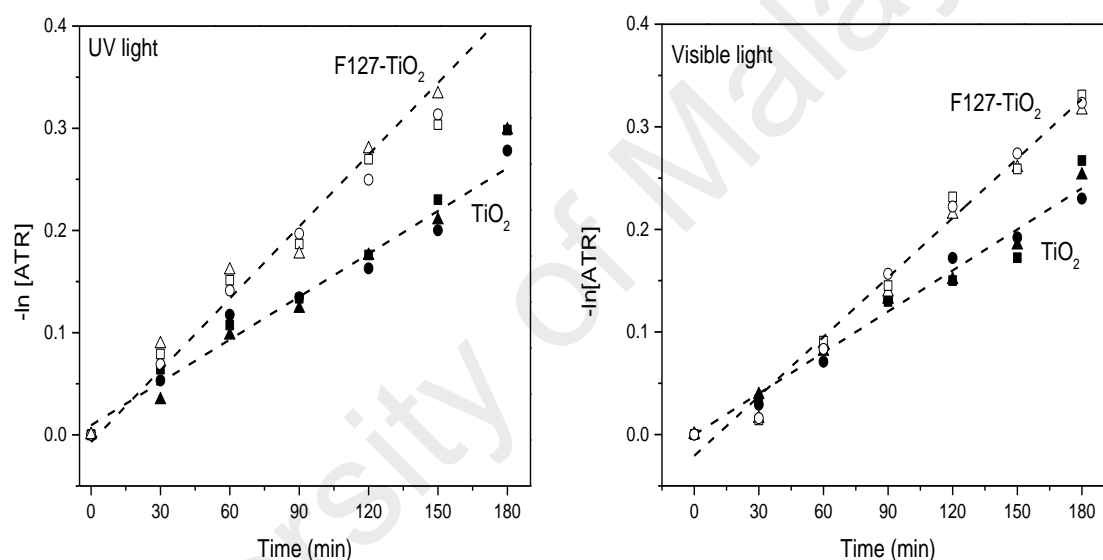
Figure 4.64: First order graph for the photo-degradation of atrazine using TiO$_2$ (solid symbols) and F127-TiO$_2$ (open symbols). Different symbols indicate three repeated tests. Reaction conditions: initial atrazine concentration = 0.5 mg/l; catalyst loading = 0.5 g/l; light source = UV and visible light; irradiation time = 180 min; stirring speed = 420 rpm; pH = 7.3

F127-TiO$_2$ also proved to sustained high reusability up to 8 consecutive cycles, suggesting good photocatalyst stability as compared to TiO$_2$, which, performance starts to deteriorate after the 3rd and 6th cycle (Figure 4.65). The normalized rate constant per surface area (Table 4.20) implies that the photocatalytic degradation activity was less likely to be influenced by the larger surface area of F127-TiO$_2$. Thus, a couple of factors were responsible for the photocatalytic enhancements in F127-TiO$_2$ which includes 1) greater mobility of electrons and holes pairs to the catalyst surface due to

184

smaller crystallite size and low PL intensity, 2) enhanced surface morphology with reactive {001} facets and 3) synergy of mixed crystal phase of anatase and rutile via surface hetero-junctions.
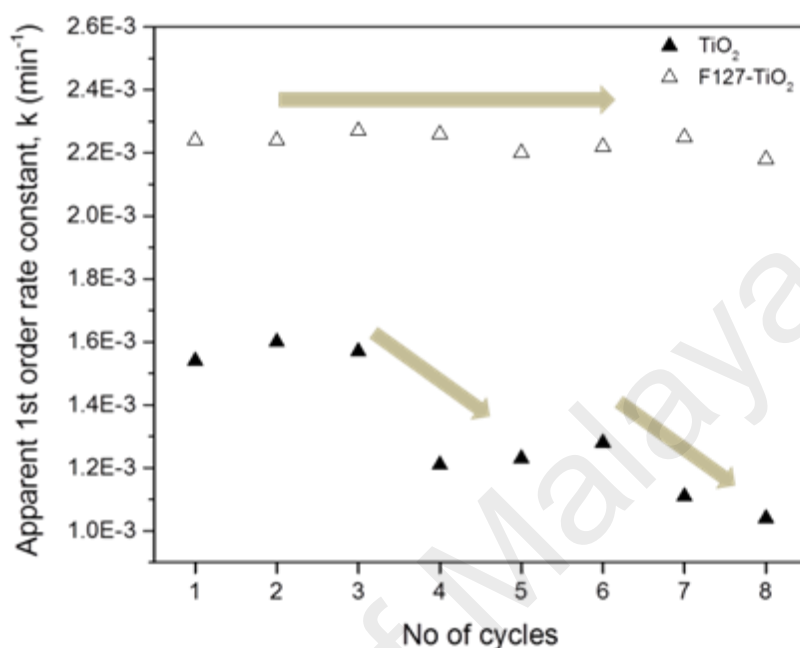
Figure 4.65: TiO_2 and $F127-TiO_2$ photocatalysts reusability test (similar condition as in Figure 4.64; light source = UV light)

4.8.2 Anionic-doped TiO₂

4.8.2.1 Nitrogen-doped TiO₂ (N-TiO₂)

N-TiO_2 demonstrates better photocatalytic activity than N0-TiO_2 ($F127-TiO_2$) but not under both light regions (Table 4.20). N-TiO_2 shows superior photocatalytic enhancement under visible light by approximately 5.1 times relative to N0-TiO_2 but yield poorer performance under UV light. Additional impurity state located 0.74 eV above the valence band coupled with oxygen vacancies in N-TiO_2 (Section 4.2.4, Figure 4.19), facilitates visible light absorption and thus more photons are absorbed on the catalysts surface (Section 4.2.5, Figure 4.20). In addition, the improved N-TiO_2 crystallinity aids good charge carrier mobility (Section 4.2.5, Figure 4.21). In N-TiO_2, only a single anatase phase was observed which increases the catalyst affinity towards oxygen molecules for the generation of superoxide radicals. Figure 4.66 illustrates the photocatalytic activity of N-TiO_2 under visible light using TiO_2 doped with different N-

loadings. It was observed that the first order of reaction constants was dependent on the amount of nitrogen loaded onto TiO_2. Optimum activity was achieved at low nitrogen loading (N1-TiO_2) and was attributed to the photocatalyst having better particles distribution and lowest PL intensity relative to other N-TiO_2 (Section 4.2.5, Figure 4.21).
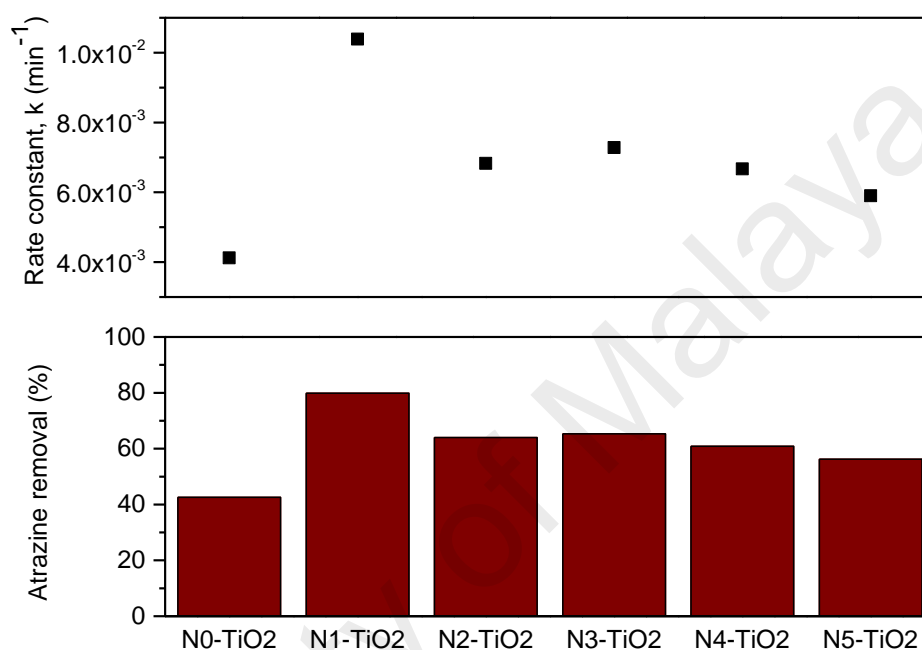
Figure 4.66: Atrazine removal (%) and corresponding first order rate constant for TiO_2 prepared using different nitrogen loading (source of light: visible light; N0 as F127-TiO_2)

Higher nitrogen loading does not necessarily favor the photocatalytic reaction due to the rapid electrons and holes recombination as shown in Figure 4.21 (Shon et al., 2008). This phenomenon explained in section 4.2.5, concluded that the necessity of slow electrons and holes recombination as well having the ability to absorb large concentration of photons were important. In table 4.20, the UV photocatalytic activity of N1-TiO_2 was lower than in N0-TiO_2. This observation was supported by the decreased in the UV light absorption intensity relative to N0-TiO_2 (Section 4.2.5, Figure 4.20), however the difference was insignificant. Lower photocatalytic activity in the UV region was obtained for TiO_2 prepared at higher N loading due to the decreased in the

UV absorption intensity. It is worth to mention that although N-doping exaggerates light absorption towards the visible region by forming impurities energy level and oxygen vacancies, it played a lesser role towards the UV-photo activity. This may be attributed to the presence of surface defects, thus perturbation on the UV-intrinsic properties of the catalyst (Nosaka et al., 2005). Overall, N0-TiO$_2$ shows weaker performance as the absorption of photons in the visible region was poorer; hence less light was absorbed to generate active radicals for the photo-degradation activity. The normalized rate constant per surface area also implies that the photocatalytic degradation activity was less likely to be influenced by the larger surface area of N0-TiO$_2$. In Table 4.20, N1-TiO$_2$ possessed similar surface area to TiO$_2$ prepared without surfactant, but demonstrated significant difference in the photocatalytic activity. Thus, surface area has a minor effect towards the enhancement of the photocatalytic activity.

4.8.2.2 Fluorine-doped TiO$_2$ (F-TiO$_2$)

In F-TiO$_2$, the surface is acidic owing to the stronger electronegativity and polarizing effect of fluorine forming ≡Ti-F bonds (Khan et al., 2014). Although high surface acidity favors specific organic pollutant absorptions (Pathak & Dikshit, 2011), the pH of industrial wastewater fluctuates depending on its chemical composition. Therefore, relating the photocatalytic activity of atrazine with the isoelectric point (IEP) of the catalyst is important. As a result of enhanced surface acidity in F-TiO$_2$, the IEP is expected to reduce to a lower pH value. In previous work, the IEP was observed to change from pH 6 in un-doped TiO$_2$ to pH 3 in F-doped TiO$_2$ (Park et al., 2013). In Figure 4.62, the reported IEP for un-doped TiO$_2$ (F127-TiO$_2$) was 6.4. As the initial pH of aqueous atrazine is 7.3, F-TiO$_2$ is monopolized by a negatively charged surface and thus, enhances absorption of the protonated atrazine substrates.

F-TiO$_2$ shows better photocatalytic response than F0-TiO$_2$ (F127-TiO$_2$) (Table 4.20). This was attributed to larger concentration of oxygen vacancies, Ti^{3+} and

187

effective hindrance of electrons and holes recombination as explained in section 4.3.3. The changed of pore shape from cylindrical to slits in F-TiO$_2$ (Section 4.3.1, Figure 4.23) improves the mobility of photo-excited charges and subsequently facilitates radical formation. Surface fluorination generates free ·OH radicals and are more active compared to surface-bound ·OH radicals formed on F0-TiO$_2$ (Wu et al., 2010). The formation of ·OH radical on fluorine-modified catalyst surfaces are illustrated in Figure 4.67. Furthermore, the redox potential of free ·OH radicals (ca. 2.3 V vs NHE at pH 7) in solution is larger than that of surface-bound ·OH radicals on TiO$_2$ (1.5-1.7 vs. NHE at pH 7) (Wu et al., 2010). For low concentration of organic pollutant, the photocatalytic activity is greatly driven by ·OH radicals rather than photo-generated holes, and thus can be associated with this work (Segomotso et al., 2013).
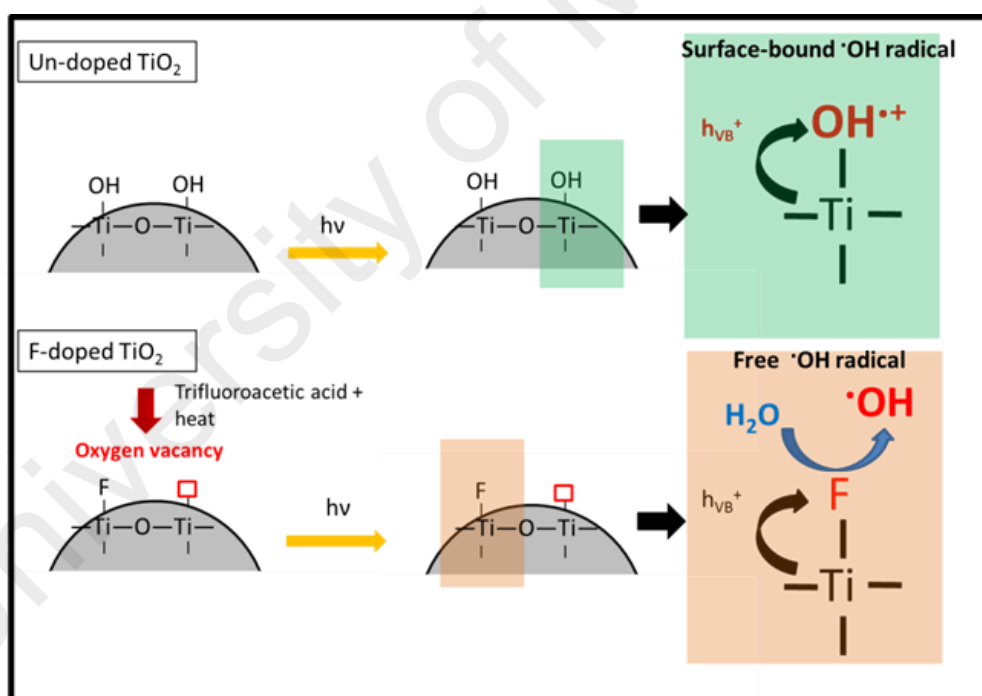
Figure 4.67: Schematic diagram showing formation of surface-bound and free hydroxyl radicals on un-doped and F-TiO$_2$

The photocatalytic activity of all F-TiO$_2$ were better under UV light than visible light, and was attributed to the enhanced UV absorption intensity (Section 4.3.3, Figure 4.28) good crystallinity. In addition, the enhanced photocatalytic activity observed in F-

TiO$_2$ was less likely due to the presence of {001} facets as growth were insignificant (Section 4.3.2, Table 4.8). Previous work demonstrates that large concentration of {001} facets activate UV-photoactivity (Yang et al., 2008). Hence, the photocatalytic mechanism was believed to occur via photo-reduction on the surface of {101} facets (Dozzi et al., 2013).

In Table 4.20, a distinctive gap between the rate constants were observed for activity under UV and visible light irradiation. F4-TiO$_2$ showed better photoactivity under UV light while F0-TiO$_2$ under visible light. In Figure 4.68a, the visible light absorption of F0-TiO$_2$ significantly red-shifted to 432 nm. Larger absorption of light facilitates greater production of surface radicals and thus enhances the photocatalytic activity under the visible region for F0-TiO$_2$ (Chen, Li, Gratzel, Kostecki, & Mao, 2014). Additionally, the visible light activities observed in F0-TiO$_2$ and all doped-TiO$_2$ were triggered by rutile crystal phase and extrinsic light absorption due to oxygen vacancies, respectively (Dozzi & Selli, 2013).

In F-TiO$_2$, optimum activity was achieved at high fluorine loading due to the enhanced inhibition of electrons and holes separation as a result of TiO$_2$ surface modifications (Section 4.3.0: surface wettability, crystal structure, single anatase phase, formation of free hydroxyl radicals, slits pore shape and oxygen vacancies). In this work, no F$^-$ ions were leached into the environment throughout the photocatalytic activity of F-doped TiO$_2$ and thus activity in homogeneous phase was negligible.
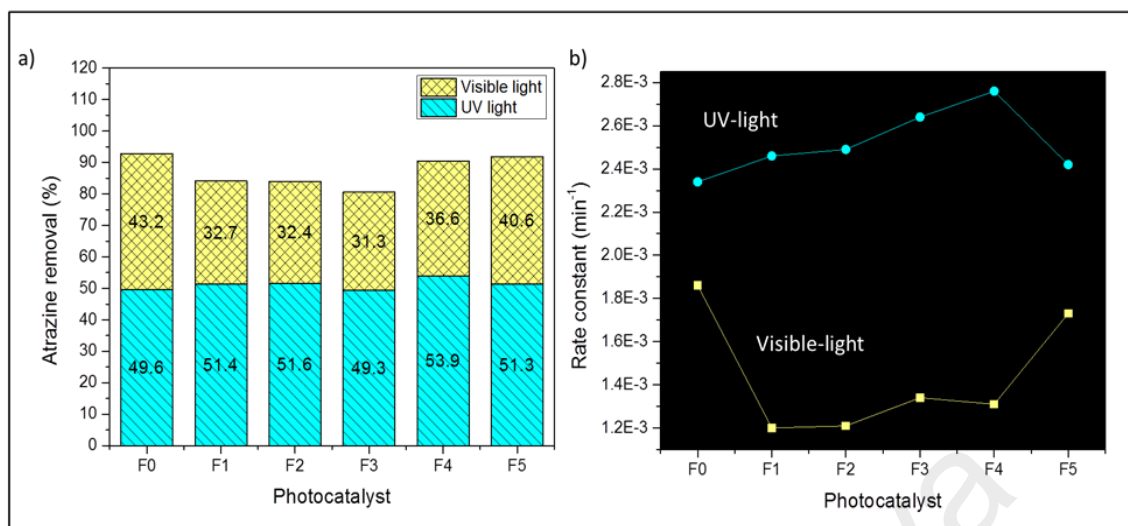
Figure 4.68: a) Atrazine removal (%) and b) corresponding rate constant irradiated under both UV and Visible light for all prepared photocatalyst at different fluorine loading (F0 as F127-TiO$_2$)

4.8.2.3 Nitrogen,fluorine co-doped TiO$_2$ (N,F-TiO$_2$)

The synergy between nitrogen and fluorine in TiO$_2$ (N,F-TiO$_2$) was shown to enormously improve the photocatalytic degradation of atrazine under both UV and visible light region (Figure 4.69). In Table 4.20, the activities of N,F-TiO$_2$ relative to mono-doped TiO$_2$ (nitrogen or fluorine doped) were enhanced by a factor of 4.0 to 5.6 (UV light) and 1.7 to 8.3 (visible lights) respectively. Clearly, the synergy between N and F enables greater photocatalytic activity improvement in the visible region. Moreover, the activity enhancement in N,F-TiO$_2$ was not influenced by the surface area. Figure 4.69 shows that the highest normalized rate constant was achieved using N,F-TiO$_2$, although the surface area was small relative to other photocatalysts. Interestingly, F127-TiO$_2$ shows poorer catalytic activity despite having a surface area larger by 63% than N,F-TiO$_2$.

190
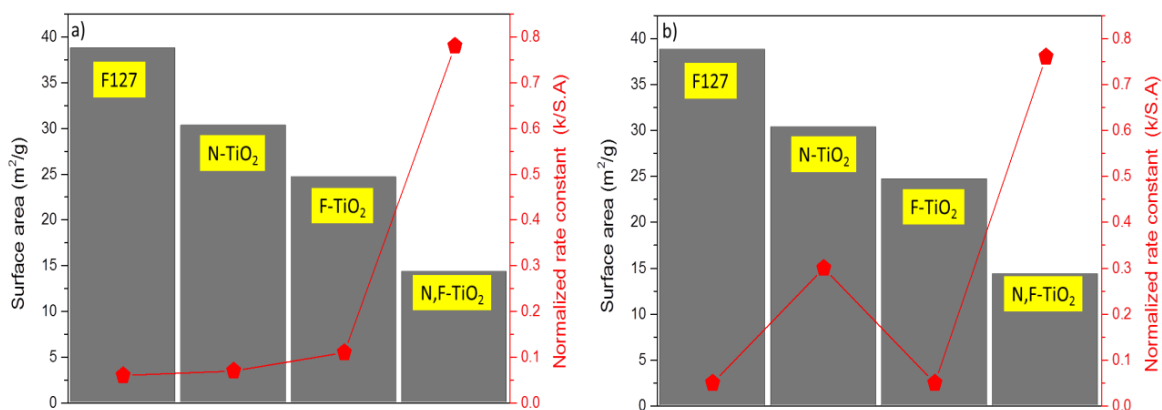
Figure 4.69: Surface area and corresponding normalized rate constant for F127-TiO$_2$ and anionic mono-doped and co-doped TiO$_2$ under a) UV light and b) visible light irradiation

The contribution factors towards the photocatalytic activity enhancement in N,F-TiO$_2$ are ruled down to 1) different morphology with larger ratio of high surface energy facets, 2) greater light absorption intensity in UV and visible regions, 3) improved photonic efficiency (able to absorb more photons in the visible light region) due to Ti^{3+} defects, 4) smaller band gap due to the formation of impurity energy levels, 5) higher crystallinity and 6) oxygen vacancies color centers. All of these factors were explained in section 4.4. F-TiO$_2$ and N,F-TiO$_2$ demonstrates slit pore shapes (Figure 4.23, Figure 4.33), therefore the charge carriers mobility are with less restriction as compared to N-TiO$_2$ (Figure 4.13). However, Figure 4.37 shows worsen electrons and holes separation for TiO$_2$ prepared at high N and F loading as indicated by the high PL intensity. Hence, it can be hypothesized that good photocatalytic activity occurs at low dopant concentration of N and F in TiO$_2$ due to less defects acting as charge traps. This also implies that larger absorption of light does not necessarily improved the photocatalytic activity. Although the atomic concentration of nitrogen in N1-TiO$_2$ (8.86 at %) and fluorine in F4-TiO$_2$ (1.82 at %) were larger than N,F-TiO$_2$ (N at 2.7 at%, F at 0.8 at%), it implies that an optimum condition exists for the synergies between the N and F dopants with respect to the photocatalytic activity.

The prepared N,F-TiO$_2$ using higher N and F loading results to an additional peak at about 24° 2θ representing TiOF$_2$ (Section 4.4.2, Figure 4.34c; Figure 4.70a). Prior to the photocatalytic activity, the photocatalyst was stirred under darkness to optimize atrazine absorption on its surface. Figure 4.70b and Figure 4.70c shows no similar peak of TiOF$_2$ at 24° 2θ after absorption in darkness and after the photocatalytic activity. It can be concluded that TiOF$_2$ was less likely to contribute to the photocatalytic degradation of atrazine, as disappearance of its diffraction peak was observed from the initial stage of the experiment (atrazine absorption in darkness), and atrazine was still degraded under the absence of TiOF$_2$ with consistent reusability rate (Figure 4.71).
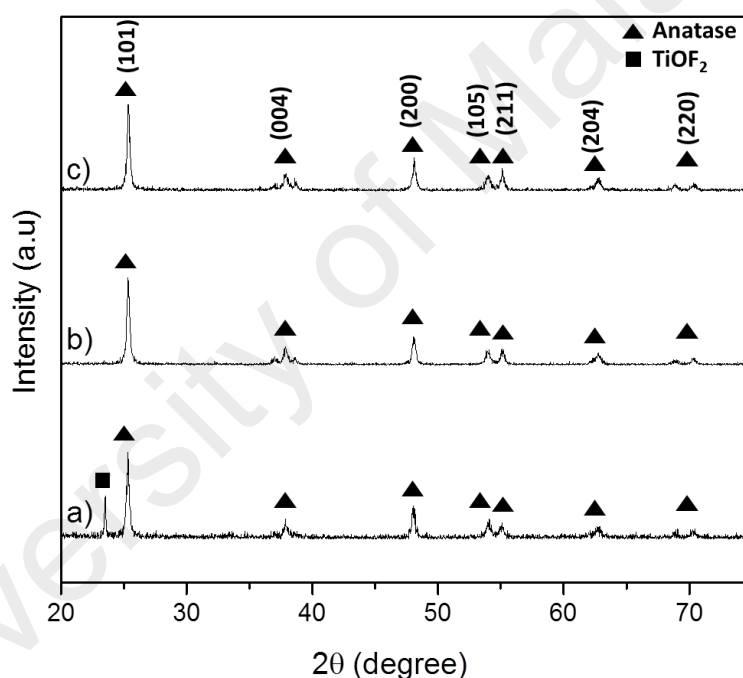
Figure 4.70: XRD Pattern of NF5-TiO$_2$ at a) As-synthesized, b) after 60 min under darkness and c) after catalytic reaction under UV light

The stability of the performances of NF5-TiO$_2$ photocatalyst in sixth consecutive cycles indicates that at least within the range examined, there was a good reproducibility of the performances in consecutive cycles of reaction. The diffraction peaks of anatase remained significantly crystalline after prolonged UV irradiation, indicating sustainable structural stability of NF5-TiO$_2$. Furthermore, no F$^-$ ions leaching

was observed in the solution, hence the disappearance of $TiOF_2$ peak was probably due to the amorphization and redistribution on the photocatalyst surface.
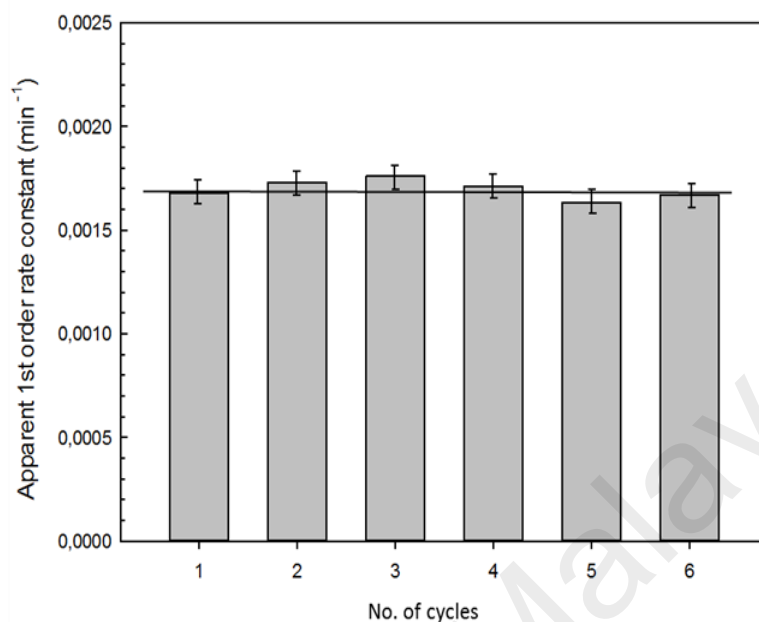
Figure 4.71: NF5-TiO_2 photocatalyst reusability test. Reaction conditions: catalyst amount = 0.5 g/l; initial atrazine concentration = 2 mg/l; light source = UV light; irradiation time = 360 min; stirring speed = 420 rpm; pH = 7.3

4.8.3 Hydrogenated TiO_2 (H-TiO_2)

The first order rate constant of all prepared H-TiO_2 for atrazine degradation is illustrated in Table 4.21 and Figure 4.72. The photocatalytic activity of H-TiO_2 was more superior under UV light relative to visible light. Hydrogenation of TiO_2 induces the formation of Ti^{3+} as shown in Figure 4.44. However, Ti^{3+} is UV photo-active and has poor visible-light photocatalytic activity. According to Xiong et al (2012), Ti^{3+} serves as an electron donor and no free holes is generated upon visible light irradiation and thus exhibit no photocatalytic activity. Therefore, any visible light activities were attributed to the presence of oxygen vacancies and rutile crystal phase in the hydrogenated TiO_2. Moreover, H0-TiO_2 shows lower photocatalytic activity in the UV region despite having higher UV light absorption intensity (Section 4.5.3, Figure 4.45). This implies that a greater role was played by surface defects to accomodate the higher activity in H-TiO_2 (Park et al., 2013).

Table 4.21: First order rate constant (k) for atrazine degradation using H-TiO$_2$ (H0 as F127-TiO$_2$)

Catalyst	[ATR]$_o$	k (UV light)	R^2 (UV light)	k (Vis light)	R^2 (Vis light)
H0-TiO$_2$	0.87	2.3E-3	0.970	1.8E-3	0.986
H6-TiO$_2$	0.93	5.6E-3	0.965	4.7E-3	0.962
H12-TiO$_2$	0.94	7.4E-3	0.994	7.0E-3	0.991
H24-TiO$_2$	0.95	5.3E-3	0.983	4.3E-3	0.976

The enhanced activity of H-TiO$_2$ in the visible region was due to the higher photon flux on the photocatalyst surface which facilitates more production of surface ·OH radicals (Chen et al., 2014). In Table 4.20, H12-TiO$_2$ shows the highest rate constant under both light region as a result of a more effective charge carrier separations relative to other hydrogenated catalysts (Section 4.5.3, Figure 4.46). Referring to Table 4.20, H12-TiO$_2$ and N1-TiO$_2$ shows almost similar surface area but the normalized degradation rate constant was larger in the former. Thus, the effect of surface area towards the photocatalytic activity played a lesser role.
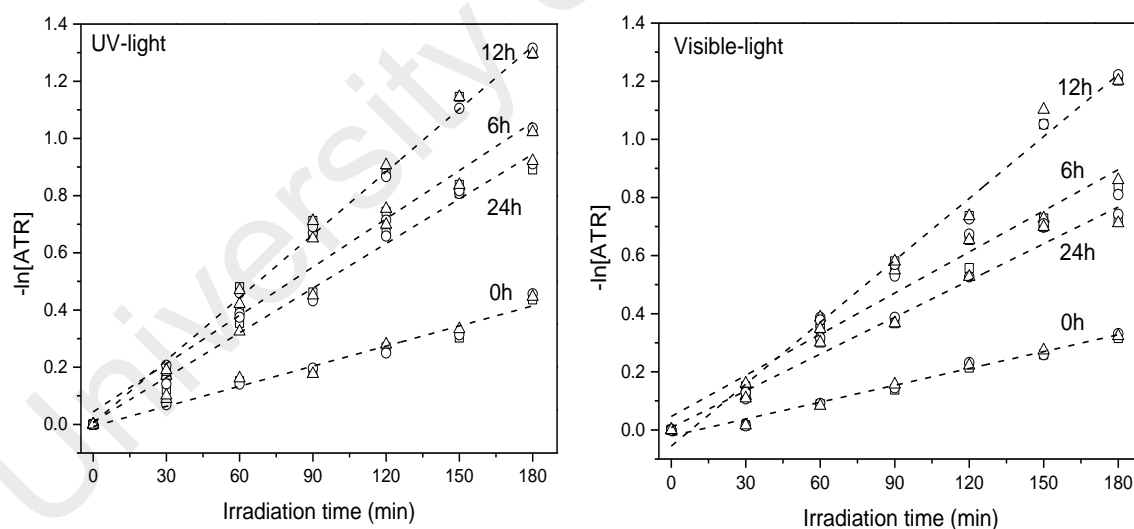
Figure 4.72: First order rate of reaction graph for the photodegradation of atrazine using hydrogenated TiO$_2$ at 0h, 6h, 12h and 24h. Different symbols indicate utilized three repeated tests. Reaction conditions: initial atrazine concentration = 0.5 mg/L; catalyst loading = 0.5 g/L; light source = UV and visible light; irradiation time = 180 min; stirring speed = 420 rpm; pH = 7.2

In Table 4.20 and 4.21, all of the prepared H-TiO$_2$ photocatalysts shows higher rate constant than N-TiO$_2$ and F-TiO$_2$. As observed in section 4.2 and 4.3, both of these

mono-doped photocatalysts shows a single anatase phase whereby all of the prepared H-TiO$_2$ shows mixed anatase and rutile phase (Section 4.5.2, Table 4.13). This could imply that a minor role was played by the mixed crystal phase via surface heterojunctions. The presence of surface heterojunctions aids in the mobility of charge carriers and thus, facilitates the photocatalytic activity (Carp et al., 2004). Other factors such as surface disorders, {001} exposed facets, charge carriers separation and light absorption also contributes to the photodegradation rate of atrazine. In H24-TiO$_2$, the excessive oxygen vacancies acts as charge traps and obstruct the formation of ·OH radicals (Naldoni et al., 2012). It is worth to note that wider solar light absorption and largest amount of surface disorders as shown in H24-TiO$_2$ does not necessarily governs enhanced photocatalytic activity.

As shown in Figure 4.73, F127-TiO$_2$ was negatively charged above slightly neutral pH (initial pH of experiment in this study is 7.3). This condition facilitates atrazine absorption on the negatively charged surface of hydrogenated TiO$_2$. Ti-H bonds that were present on the surface of hydrogenated TiO$_2$ might enhance the surface basicity (tendency to donate electrons) of TiO$_2$ and shifts the isoelectric point towards larger pH value. However, minor effect on the iso-electric point was observed between F127-TiO$_2$ and H-TiO$_2$. In this work, the photocatalytic degradation of atrazine was successful under the influence of hydrogenated TiO$_2$. However, the IEP of H-TiO$_2$ was close to the value of atrazine aqueous solution (pH at 7.3). Exceeding the pH value of 7.3 would not favor the photocatalytic activity due to repulsions between the positively charged photocatalysts and atrazine molecules.
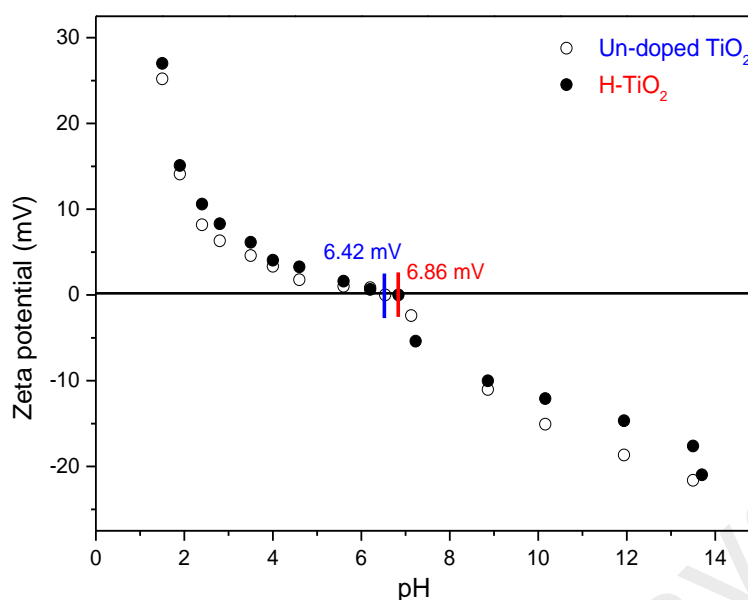
Figure 4.73: Point of zero charge (PZC) from pH 2 to pH 14 for un-doped TiO$_2$ and H-TiO$_2$

4.8.4 Hydrogenated fluorine-doped TiO$_2$ (HF-TiO$_2$)

The photocatalytic activity of hydrogenated F-doped TiO$_2$ was investigated under UV and visible light (Figure 4.74). The photocatalytic activity was higher under UV light relative to visible light irradiation. Amongst all photocatalysts, HF12-TiO$_2$ shows the best performance in removing atrazine (Figure 4.74, Table 4.20). Although the PL intensity of HF12-TiO$_2$ was slightly higher than F-TiO$_2$ (Section 4.6.3, Figure 4.57(right)), the presence of surface disorders on HF12-TiO$_2$ serves as additional active sites for surface photocatalytic reaction (Zheng et al., 2012). In addition, residual adsorbed TFA on the surface of F-TiO$_2$ limits the direct contact of photo-excited carrier charges with the electrons donors and acceptor. This explained the low activity of F-TiO$_2$ although it possessed the highest UV absorption intensity (Section 4.6.3, Figure 4.57 (left)). Atrazine removal rate observed in HF12-TiO$_2$ was higher by a factor of 6 and 12 under UV and visible light respectively, relative to F-TiO$_2$ (Table 4.20). The photocatalytic activity enhancement under visible light was attributed to the ability of HF12-TiO$_2$ to absorb wider range of light coupled with surface defects (surface disorders and oxygen vacancies). In F-TiO$_2$, the presence of low visible light activity

196

was attributed to extrinsic light absorption as a result of oxygen vacancies (Dozzi & Selli, 2013).

In addition, the pore shape from cylindrical to slits in hydrogenated F-doped TiO_2 was believed to accelerate surface contacts between charge carriers with electron donors and acceptors and thus generates larger concentration of surface radicals. All photocatalysts that possessed cylindrical pore shapes shows weaker photocatalytic performance than those with slits.
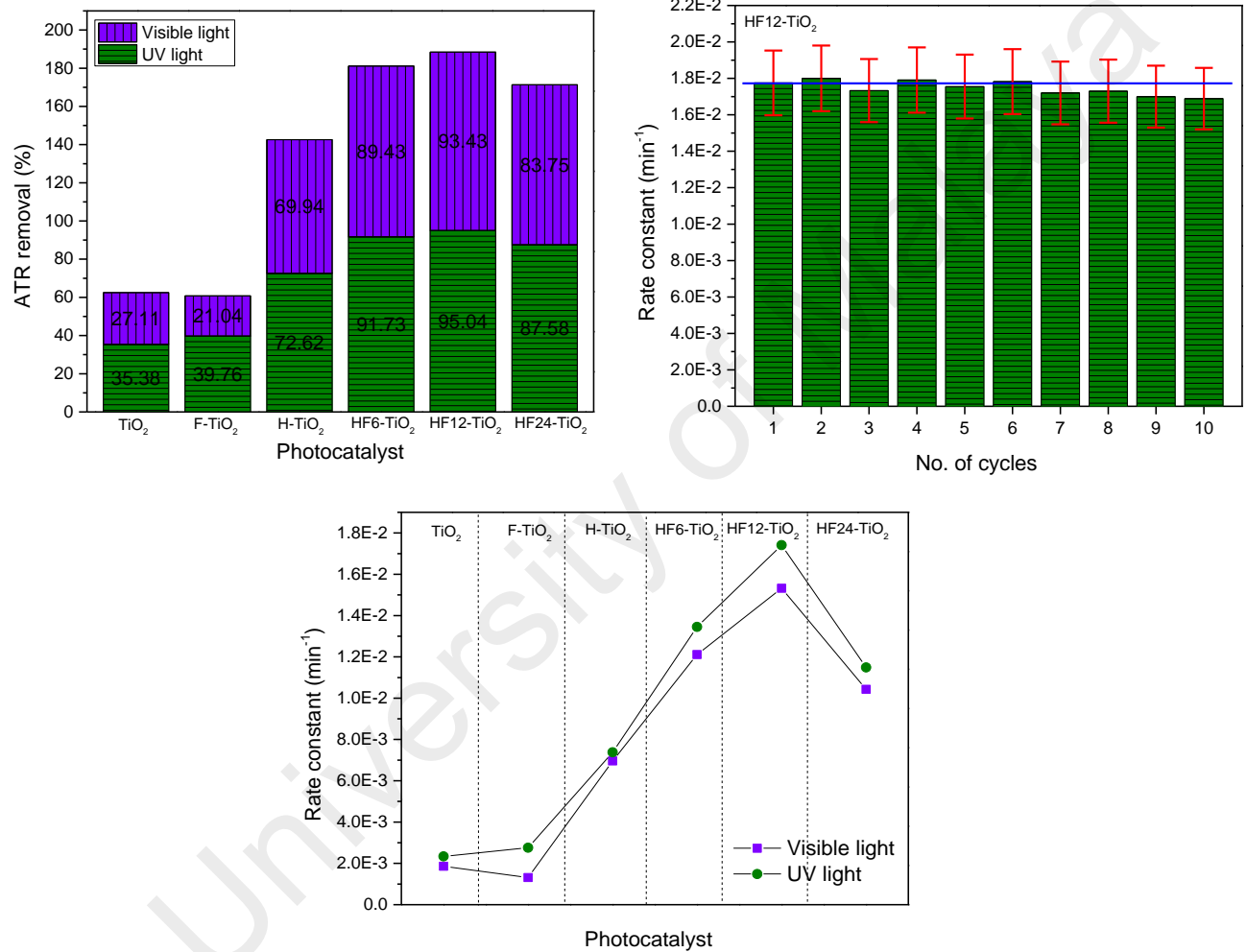
Figure 4.74: Photocatalytic degradation of atrazine showing percentage of removal and corresponding rate constant and catalyst reusability test

The photocatalytic activity of hydrogenated F-doped TiO_2 was also greater than H-TiO_2 although both photocatalysts had almost similar thickness of surface disorders (H12 at 2.5 nm; HF12 at 2.0 nm). Thus the thickness of surface disorders does not determine the rate of atrazine degradation. Hydrogenated F-doped TiO_2 shows superior surface hydrophilicity due to the larger presence of surface hydroxyl groups relative to H-TiO_2 (Section 4.6.2, Figure 4.56d-f). In addition, hydrogenated F-doped photocatalyst shows efficient electrons and holes separation as a result of highly electronegative fluorine decorating the photocatalyst surface. In H-TiO_2, higher PL intensity was observed due to the larger particle size (20 nm larger than HF-TiO_2). Larger particle size creates more room for charge traps and subsequent electrons and holes recombination (Zhang, Wang, Zakaria, & Ying, 1998). Furthermore, excessive concentration of Ti^{3+} in H-TiO_2 could act as charge carrier trapping sites and thus reduce the formation of active radicals on the photocatalyst surface. Ti^{3+} being only UV photo-active compensate to higher activity in the UV region especially for H-TiO_2 and HF-TiO_2 (Table 4.20, Figure 4.74). Although N,F-TiO_2 shows high UV activity (Table 4.20), it was attributed to the presence of {001} facets rather than Ti^{3+}.

Comparing the photocatalytic activity of all hydrogenated F-doped TiO_2, HF12-TiO_2 shows the most prominent activity. The lower photocatalytic activity in HF6-TiO_2 was attributed to excessive amount of Ti^{3+} acting as charge carriers trapping site (Naldoni et al., 2012). Furthermore, HF6-TiO_2 shows poorer visible and infrared absorption relative to HF12-TiO_2. In HF24-TiO_2, the performance deteriorates due to decreasing concentration of Ti^{3+} and thus fewer electrons are available on the catalyst surface to take part in forming active radicals. In a photocatalytic degradation activity, the surface charge of the catalyst plays an important role as the degradation of pollutants is surface-oriented. As a result of hydrogen and F-doping synergies, larger presence of hydroxyls group was observed on the catalyst surface, increasing surface wettability

(Section 4.6.2, Figure 4.56). However, the hydroxyl groups on the photocatalyst surface are deprotonated in alkaline environment, resulting to a negatively charged surface. Furthermore, the presence of surface disorders as a result of Ti-H bonds increases the basicity of the catalyst surface, and thus governs a negatively charged surface as well. A negatively charged surface has higher tendency to attract the positively charged protonated atrazine molecules and facilitate surface photocatalytic degradation activity. Overall, this suggests that the photocatalytic activities in hydrogenated F-doped TiO_2 were driven by various factors such as formation of surface disorders, impurities states due to F dopant (impurities), oxygen vacancies, pore shape, charge carriers recombination, surface charges and Ti^{3+} defects.

Summarizing the data in Table 4.20, it was clear that the concentration and position of fluorine, as well as hydrogenation duration influences the physico-chemical properties of TiO_2. Furthermore, the involvement of fluorine and hydrogen in modifying TiO_2 initiates a positive synergy and further enhances the photocatalytic degradation of atrazine. The stability of HF12-TiO_2 was shown in Figure 4.74 for 10th consecutive cycles. The photocatalytic performance slightly decreases after the 7th cycles by 5 %. However, the degradation rate constant remains superior and exceeds the rate constant of HF6-TiO_2 and HF24-TiO_2. This indicates good photocatalyst stability in HF12-TiO_2. In addition, Figure 4.75 shows the preservation of surface disorders on the HF12-TiO_2 surface after 10th cycles of photocatalytic degradation activity.
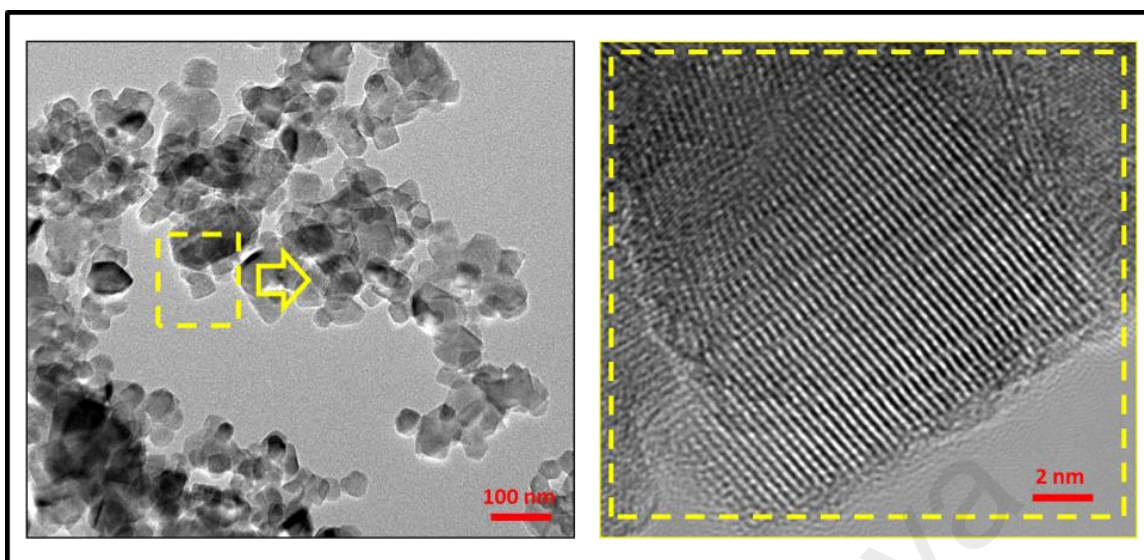
Figure 4.75: HR-TEM image of hydrogenated F-doped TiO_2 (HF12-TiO_2) after 10th consecutive cycles of photocatalytic activity

4.8.5 Other hydrogenated anionic-doped TiO_2

Hydrogenated N-doped TiO_2 and hydrogenated N,F co-doped TiO_2 were also prepared using similar condition as HF12-TiO_2, but was expected not to show promising result, attributed to the significantly high PL intensity (Figure 4.76). High PL intensity results to rapid electrons and holes recombination and thus deteriorates the overall photocatalytic activity. It was postulated that an excessive number of defects were present in HN12-TiO_2 and HNF12-TiO_2, which acts as charge traps and inhibits the formation of surface radicals. Other factors that might lead to high PL intensity includes 1) poor synergy between dopants and hydrogenation process, 2) large particle size, 3) stunted growth of high energy facets and 4) low porosity.
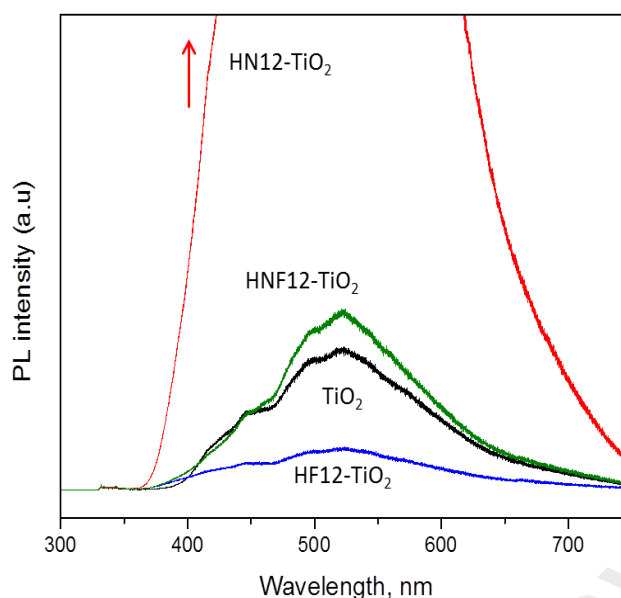
Figure 4.76: Photoluminescence spectra of hydrogenated F-doped TiO_2, N-doped TiO_2, N,F co-doped TiO_2 for 12 h relative to un-hydrogenated TiO_2

4.8.6 Comparison of all prepared photocatalysts

The sequence of photocatalytic degradation rate of atrazine was as followed; Hydrogenated F-doped TiO_2 > N,F co-doped TiO_2 > Hydrogenated TiO_2 > N-doped TiO_2 > F-doped TiO_2 > TiO_2 with surfactant > TiO_2 without surfactant (Figure 4.77). Within 180 min of photocatalytic activity, more than 95 % of 0.5 mg/l atrazine was removed using hydrogenated F-doped TiO_2, which meets the environmental requirement. Atrazine removal was shown to exceed those of N,F co-doped TiO_2 (85 %), hydrogenated TiO_2 (70 %), N-doped TiO_2 (70 %), F-doped TiO_2 (40 %) and F127-TiO_2 (35 %).
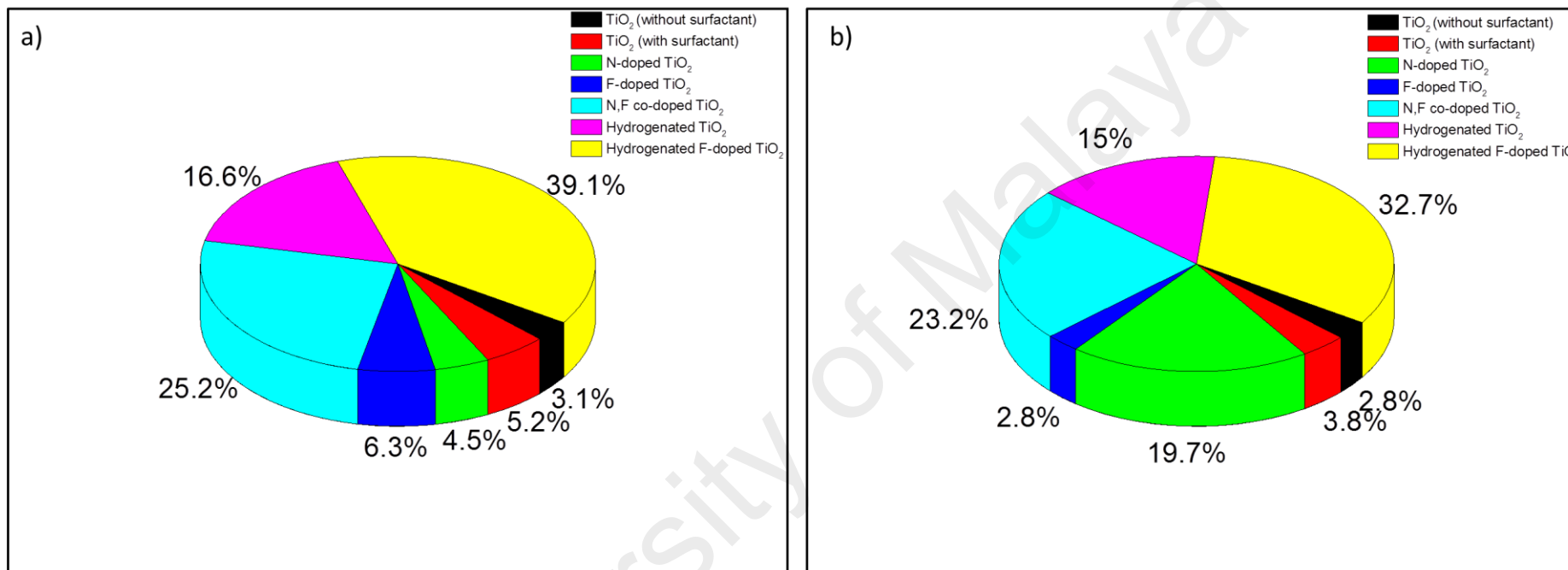
Figure 4.77: Overall photocatalytic activity for atrazine degradation under a) UV light ($\lambda < 350$ nm) and b) visible light (λ at 420 to 1000 nm)

4.9 Photocatalytic degradation pathway of atrazine pollutant

The reaction network for the photo-degradation of atrazine was analyzed using the reaction intermediates by HPLCMS/MS. Table 4.22 reports atrazine degradation intermediates observed using N-TiO$_2$ catalyst. Based on LCMS/MS peaks, a total of 8 degradation intermediates were observed, which enables the plotting of potential degradation pathway (Figure 4.78). The obtained m/z at 215.7 shows presence of atrazine after 180 min of catalytic reaction and indicates incomplete removal of atrazine. The degradation pathway involves dehalogenation of chlorine at position two with a hydroxyl group, oxidation of alkyl side chain, further dealkylation and deamination. The degradation processes includes the formation of hydroxyatrazine, deethylatrazine, desethylhydroxyatrazine, deisopropylatrazine, deethyldeisopropylatrazine, ammelide and ammeline (Mc Murray et al., 2006). The degradation pathway leads to a final amino group displacement with hydroxyl and forms a stable intermediate of cyanuric acid at m/z 129.1.

Table 4.23 reports the identified intermediates and relative mass (m/z) value observed using N,F-TiO$_2$ catalyst. Out of the 15 degradation intermediates identified, one compound was not earlier reported in literature: 2-hydroxy-4-(2-hydroxyethylamino)-6-amino at m/z 171.17. Based on these observed intermediates throughout the photocatalytic reaction, the degradation pathways was proposed. The two figures refer to one possible pathway with dehalogenation as primary step (Figure 4.79) and another pathway with dealkylation as primary step (Figure 4.80). Full atrazine degradation involves oxidation of alkyl side chain, dehalogenation of chlorine, further dealkylation and deamination. Both pathways of transformation leads to a final displacement of amino group by hydroxyl forming a stable intermediate: cyanuric acid (m/z 129.08). The difference in surface properties of prepared photocatalysts was less

likely to influence the type and distribution of atrazine degradation intermediates, but

affects the photocatalytic degradation rate (Table 4.20).

Table 4.22: Atrazine degradation intermediates by LCMS/MS using N-TiO$_2$ photocatalyst

Mass spectra,	Abbreviatio	Compound
215.7	CIET	2-chloro-4-ethylamino-6-isopropylamino-s-triazine
197.3	HEIT	2-hydroxy-4-ethylamino-6-isopropylamino-s-
197.2	HEAcT	2-hydroxy-4-ethylamino-6-acetamido-s-triazine
155.2	HEAT	2-hydroxy-4-ethylamino-6-amino-s-triazine
127.1	HAAT	2-hydroxy-4,6-diamino-s-triazine (ammeline)
169.2	HAIT	2-hydroxy-4-amino-6-isopropylamino-s-triazine
128.1	OOAT	2,6-hydroxy-4-amino-s-triazine (ammelide)
129.1	OOOT	2,4,6-triols-s-triazine (cyanuric acid)

[a] MS analysis in +ve ion mode

Table 4.23: Atrazine degradation intermediates by LCMS/MS using NF-TiO$_2$ photocatalyst

Compound	Mass spectrum (m/z)[a]
2-chloro-4-ethylamino-6-isopropylamino-s-triazine (atrazine)	215.70
2-chloro-4-acetamido-6-isopropylamino-s-triazine	229.67
2-chloro-4-amino-6-isopropylamino-s-triazine	187.64
Unknown	185.62
2-chloro-4-amino-6-acetamido-s-triazine	187.59
2-chloro-4-acetamido-6-amino-s-triazine	187.59
Unknown	213.67
2-chloro-4,6-diamino-s-triazine	145.56
2-hydroxy-4-ethylamino-6-isopropylamino-s-triazine	197.25
2-hydroxy-4-ethylamino-6-acetamido-s-triazine	197.20
2-hydroxy-4-amino-6-isopropylamino-s-triazine	169.19
2-hydroxy-4-ethylamino-6-amino-s-triazine	155.17
2-hydroxy-4-(2-hydroxyethyl amino)-6-amino-s-triazine	171.17
2-hydroxy-4,6-diamino-s-triazine (ammeline)	127.12
2,6-hydroxy-4-amino-s-triazine (ammelide)	128.10
2,4,6-triols-s-triazine (cyanuric acid)	129.08

[a] MS analysis in +ve ion mode
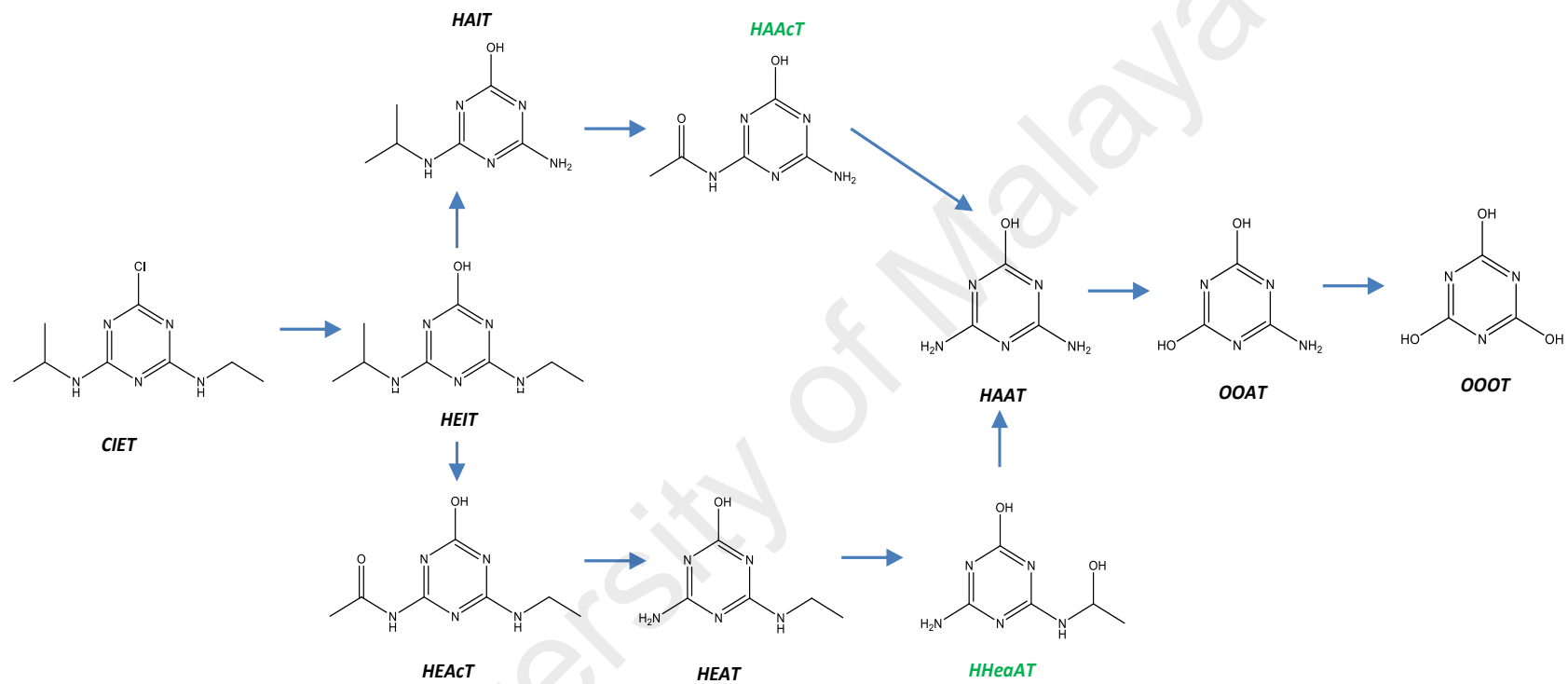
Figure 4.78: Proposed degradation pathway of atrazine using N-TiO$_2$ (HAAct and HHeaAT were absence and not detected by LCMS/MS)
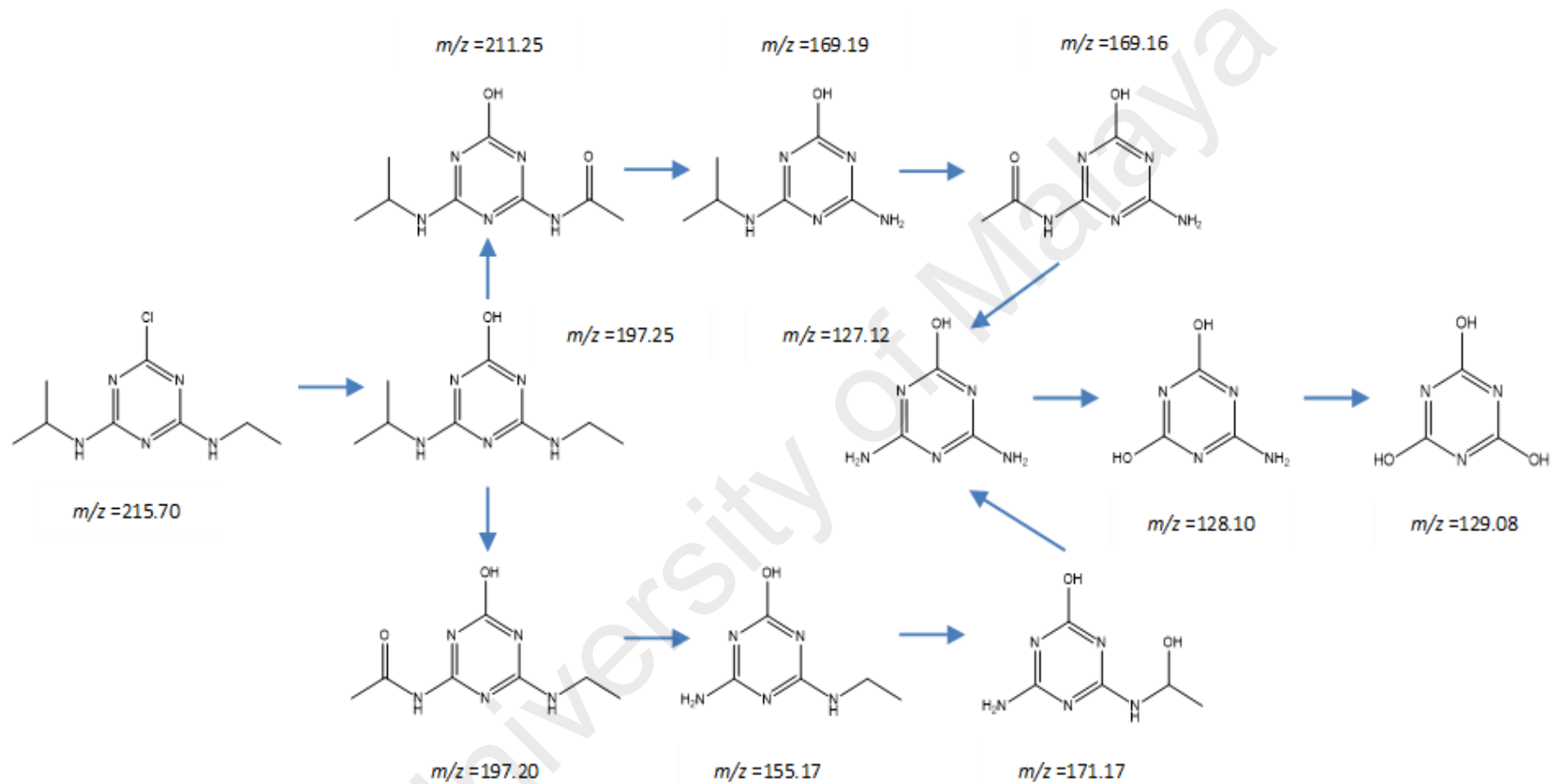
Figure 4.79: Proposed degradation pathway of atrazine using N,F-TiO$_2$ (Pathway 1; dehalogenation as primary step). The mass spectrum, m/z 211.25 and 169.16 were not detected by LCMS/MS
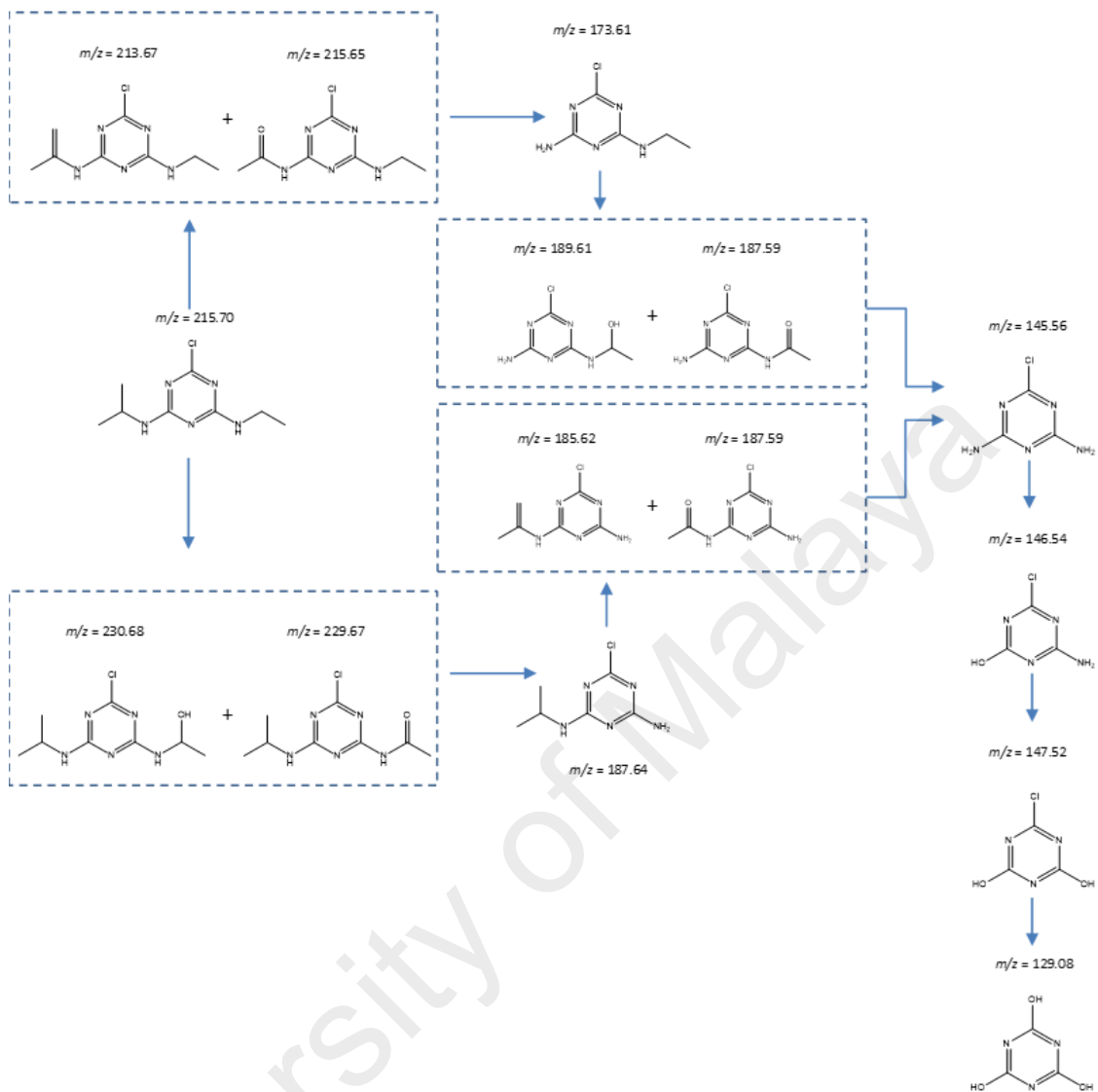
Figure 4.80: Possible degradation pathway of atrazine using N,F-TiO$_2$ (Pathway 2; dealkylation as primary step). The mass spectrum, m/z 230.68, 215.65, 173.61, 189.61, 146.54 and 147.52 were not detected by LCMS/MS

CHAPTER 5: CONCLUSION AND RECOMMENDATION

5.1 Conclusion

A novel, highly active photocatalyst for the photocatalytic degradation of atrazine under solar light was successfully developed. The photocatalyst, namely hydrogenated F-doped TiO_2 showed excellent electrons and holes separation and improved solar light absorption covering UV, visible and near infra-red light. Complete 0.5 mg/l atrazine removal (more than 95 %) was achieved in less than 180 min under solar light irradiation using minimal amount of photocatalyst at 0.5 g/l. High degradation rate was achieved following large concentration of radicals during the photocatalytic reaction. These radicals took part in the redox reaction, breaking down atrazine into non-hazardous cyanuric acid. In this work, atrazine is degraded following two pathways; 1) dehalogenation or 2) dealkylation process. It has been shown that the type and distribution of intermediates products were not influenced by the different surface properties of TiO_2. However, different surface properties of TiO_2 were shown to significantly influence the photocatalytic activity and degradation rate of atrazine.

Hydrogenated F-doped TiO_2 showed superior photocatalytic activity improvement relative to all of the other prepared photocatalysts as a result of hydrogenation and F-doping synergies. This was related to the favorable surface active sites (oxygen vacancies, Ti^{3+} and surface disorders), improved light absorption intensity and range covering UV, visible and infrared region, efficient electrons and holes separation, enhanced thermal stability, slits pore shape, uniform particle size and distribution and improved surface hydrophilicity. Re-engineering the photocatalyst surface by hydrogenation creates surface disorders which maximizes solar light absorption. Greater optical response was facilitated by the presence of oxygen vacancies and Ti^{3+} as well. This observation indicates that wide range of light absorption was possible without narrowing of the band gap. The mobility of the charge carriers were also not affected

due to the preservation of hydrogenated TiO$_2$ crystalline core. The presence of $\equiv$Ti-F, $\equiv$Ti-OH, $\equiv$Ti-O$_{vacancy}$ and $\equiv$Ti-H species decorating the surface of hydrogenated F-doped TiO$_2$ were shown to enhance the photocatalytic activity by facilitating the formation of radicals. Contrary to hydrogenated TiO$_2$ prepared without fluorine, the results showed poorer photocatalytic performance. This was attributed to the weaker thermal stability, excessive particle growth and irregular morphology. This limitation was removed by inserting fluorine in hydrogenated TiO$_2$.

The importance of surfactant was also stressed. TiO$_2$ prepared by using surfactant demonstrated homogeneous morphology and particle size, larger surface area and improved charge carriers separations relative to TiO$_2$ prepared without surfactant. Pluronic F127 is a non-ionic surfactant which does not dissociate in an aqueous sol-gel process and possessed lower sensitivity towards electrolytes. During the sol-gel process, the hydrophilic (ethylene oxide) and hydrophobic (alkyl groups) of the surfactant binds to similar groups in TiO$_2$ polymers which enables efficient control of the growth, shape and porosity of the photocatalyst. TiO$_2$ photocatalyst that was prepared without surfactant demonstrated irregular morphology of large particles and rapid electrons and holes recombination relative to F127-TiO$_2$.

Introducing nitrogen as dopant enables visible light absorption and reduces particle agglomeration. The presence of nitrogen in N-doped TiO$_2$ retards anatase to rutile crystal phase transformation and controls charge carrier recombination. In the prepared N-doped TiO$_2$, the chemical states showed interstitial and chemisorbed gamma–N$_2$. This leads to the formation of new impurity energy states 0.2 to 0.4 eV above the valence band acting as additional layer of electrons. These electrons require less energy to be photo-excited to the conduction band and thus, the application of N-doped TiO$_2$ under visible light was possible. The presence of oxygen vacancies in N-doped TiO$_2$

also acts as active sites and facilitates the photocatalytic activity however enhancement was not observed under the UV region.

The prepared F-doped TiO_2 showed slight photocatalytic improvement in the UV region relative to N-doped TiO_2 but poor activity in the visible region. F-doped TiO_2 demonstrates superior electrons and holes separation as a result of highly electronegative doped fluorine decorating the catalyst surface. Furthermore, fluorine was able to tune TiO_2 pore shape from cylindrical to slits and thus provides better mobility of charge carriers. In F-doped TiO_2, the visible light absorption was triggered by the presence of oxygen vacancies but due to the low concentration of oxygen vacancies, it played a lesser role in the visible light photocatalytic activity. No significant change in the band gap was observed in F-doped TiO_2 as the energy state of F 2p is located under the O 2p of TiO_2 conduction band. Thus fluorine is a useful mediator to improve TiO_2 surface acidity, retardation of rutile crystal growth and charge carriers recombination. However, F-doped TiO_2 is a poor candidate in absorbing visible light, and thus limits its activity in the UV region only.

The synergy between nitrogen and fluorine in co-doped TiO_2 showed remarkable photocatalytic improvement in both UV and visible light range. This was attributed to enhanced surface area, exposed high energy facets, slits pore shape, single anatase crystal phase, narrowing of band gap and inhibition of electrons and holes recombination. It was observed that the growth of high energy {001} facets was the most promising in N,F co-doped TiO_2 relative to other prepared photocatalysts. This was attributed to the availability of fluoride ions as single F^- from the dissociation of ammonium fluoride compared CF_3COO^- from trifluoroacetic acid. Thus absorbed surface fluoride on TiO_2 enables great tuning of high energy facets during the sol-gel process. Nevertheless, the growth of this facet remained insignificant and thus the formation of facets hetero-junctions between {001} and {101} were less likely to

contribute to the enhanced catalytic activity in N,F co-doped TiO_2. The photocatalytic activity of N,F co-doped TiO_2 was limited to only UV and certain portion of the visible light.

This research concluded the importance of TiO_2 properties towards the photocatalytic degradation of atrazine. The properties includes defects (dopant, oxygen vacancies, Ti^{3+}, surface disorders), morphology (shape, size, distribution), crystallinity, crystal structure and ratio, exposed crystal facets, textural properties (surface area, pore volume, pore size and pore shape), photoluminescence effect (charge carriers trapping, migration and transfer), optical properties (color, light absorption, band gap), hydrophilicity and surface charge. In overall, all of the objectives of this research work were met successfully.

5.2 Recommendations

A few strategies could be employed to widen the application of hydrogenated F-doped TiO_2 for water treatment by using thin films or membranes. The handling of thin films is much easier compared to TiO_2 powder in terms of separation and recovery. Thin film with a thickness less than 100 nm can be achieved via spin coating technique, where the prepared TiO_2 powder is mixed with a suitable film forming solvent before the spinning process. Another alternative is to prepare F-doped TiO_2 as sol-gel precursors followed by spin or dip coating on a substrate before subjecting the thin film for annealing and hydrogenation process. Hydrogenated F-doped TiO_2 nanotubes is also possible by preparing F-doped TiO_2 nanotubes by anodization technique followed by annealing and hydrogenation process. Hydrogenated F-doped TiO_2 can also be prepared in the form of nanofibre membrane which possesses a dual function as a filter and as a photocatalyst. Contrary to TiO_2 powder, the poor photocatalyst separation and low recovery are minimized.

Since hydrogenated F-doped TiO_2 is a highly active photocatalyst, it can be tested and optimized for different types of s-triazine herbicides such as simazine, trietazine, prometon and prometryn. These herbicides are also listed as recalcitrant water pollutants. The photocatalytic experiment variables such as initial pollutant concentration, catalyst loading, pH, light source and duration can be optimized by using central composite design (CCD) coupled with response surface methodology (RSM). This is an effective method to roughly estimate the optimum conditions required to achieve the highest photocatalytic degradation using hydrogenated F-doped TiO_2.

REFERENCES

Abou-Helal, M. O., & Seeber, W. T. (2002). Preparation of TiO_2 thin films by spray pyrolysis to be used as a photocatalyst. *Applied Surface Science*, *195*(1-4), 53–62.

Agarwala, S., & Ho, G. W. (2009). Synthesis and tuning of ordering and crystallinity of mesoporous titanium dioxide film. *Materials Letters*, *63*, 1624–1627.

Ahmad, A., Tan, L., & Abd Shukor, S. (2008). Dimethoate and atrazine retention from aqueous solution by nanofiltration membranes. *Journal of Hazardous Materials*, *151*(1), 71–77.

Ahmed, L. M., Ivanova, I., Hussein, F. H., & Bahnemann, D. W. (2014). Role of platinum deposited on TiO2 in photocatalytic methanol oxidation and dehydrogenation reactions. *International Journal of Photoenergy*, *2014*, 1–9.

Ahmed, S., Rasul, M. G., Martens, W. N., Brown, R., & Hashib, M. A. (2010). Heterogeneous photocatalytic degradation of phenols in wastewater: A review on current status and developments. *Desalination*, *261*(1-2), 3–18.

Akpan, U. G., & Hameed, B. H. (2010). Applied Catalysis A : General The advancements in sol – gel method of doped-TiO_2 photocatalysts. *Applied Catalysis A: General*, *375*, 1–11.

Akplea, M. S., Lowa, J., Qin, Z., Wageh, S., Al-Ghamdi, A. A., Yua, J., & Liu, S. (2015). Nitrogen-doped TiO_2 microsheets with enhanced visible-light photocatalytic activity for CO_2 reduction. *Chinese Journal of Catalysis*, *36*(12), 2127–2134.

Aktar, M. W., Sengupta, D., & Ashim, C. (2009). Impact of pesticides use in agriculture: their benefits and hazards. *Interdisciplinary Toxicology*, *2*(1), 1–12.

Almajdalawi, S., Pavlinek, V., Mrlik, M., Cheng, Q., Piyamanocha, P., Pastorek, M., & Stenicka, M. (2013). Solvothermal synthesis of different TiO_2 and their electrorheological characteristics. *Journal of Physics: Conference Series*, *412*(012004), 1–7.

Ananpattarachai, J., Kajitvichyanukul, P., & Seraphin, S. (2009). Visible light absorption ability and photocatalytic oxidation activity of various interstitial N-doped TiO_2 prepared from different nitrogen dopants. *Journal of Hazardous Materials*, *168*(1), 253–261.

Andersen, J., Pelaez, M., Guay, L., Zhang, Z., O'Shea, K., & Dionysiou, D. D. (2013). NF-TiO_2 photocatalysis of amitrole and atrazine with addition of oxidants under simulated solar light: emerging synergies, degradation intermediates, and reusable attributes. *Journal of Hazardous Materials*, *260*, 569–575.

Antonelli, D. M., & Ying, J. K. (1995). Synthesis of hexagonally packed mesoporous TiO_2 by a modified sol-gel method. *Angewandte Chemie (International Ed. in English)*, *18*, 2014–2017.

Arora, S. (2014). Textile Dyes: It's impact on environment and its treatment. *Journal of Bioremediation & Biodegradation*, *5*(3), 1.

Asahi, R., Morikawa, T., Ohwaki, T., Aoki, K., & Taga, Y. (2001). Visible-light photocatalysis in nitrogen-doped titanium oxides. *Science*, *293*(5528), 269–271.

Avasarala, B. K., Tirukkovalluri, S. R., & Bojja, S. (2011). Photocatalytic degradation of monocrotophos pesticide-An endocrine disruptor by magnesium doped titania. *Journal of Hazardous Materials*, *186*(2-3), 1234–1240.

Avasarala, B. K., Tirukkovalluri, S. R., & Bojja, S. (2016). Magnesium Doped Titania for Photocatalytic Degradation of Dyes in Visible Light. *Journal of Environmental & Analytical Toxicology*, *06*(02), 1–8.

Azlan, A., Khoo, H. E., Idris, M. A., Ismail, A., & Razman, M. R. (2011). Evaluation of minerals content of drinking water in Malaysia. *Scientific World Journal*, (403574), 1–10.

Bae, J.-Y., Yun, T.-K., Ahn, K.-S., & Kim, J.-H. (2010). Visible-photoresponsive Nitrogen-Doped Mesoporous TiO$_2$ Films for Photoelectrochemical Cells. *Bulletin of the Korean Chemical Society*, *31*(4), 925–928.

Balasubramanian, G., Dionysiou, D., Suidan, M., Baudin, I., & Laine, J. (2004). Evaluating the activities of immobilized TiO$_2$ powder films for the photocatalytic degradation of organic contaminants in water. *Applied Catalysis B: Environmental*, *47*(2), 73–84.

Barndõk, H., Peláez, M., Han, C., & Platten, W. E. (2013). Photocatalytic degradation of contaminants of concern with composite NF-TiO$_2$ films under visible and solar light. *Environental Science and Pollution Research*, *20*, 3582–3591.

Betzler, S. B., Wisnet, A., Breitbach, B., Mitterbauer, C., Weickert, J., Schmidt-Mended, L., & Scheu, C. (2014). Template-free synthesis of novel, highly-ordered 3D hierarchical Nb$_3$O$_7$(OH) superstructures with semiconductive and photoactive properties. *Journal of Materials Chemistry A*, *2*, 12005–12013.

Beutler, C., & Shaer, T. (2013). *2015 Annual Drinking Water Quality Report*.

Bhatkhande, D. S., Pangarkar, V. G., & Beenackers, A. (2002). Photocatalytic degradation for environmental applications - a review. *Journal of Chemical Technology & Biotechnology*, *77*(1), 102–116.

Bourne, J. R., & Davey, R. J. (1976). The role of solvent-solute interactions in determining crystal growth mechanisms from solution. II. The growth kinetics of hexamethylene tetramine. *Journal of Crystal Growth*, *36*(2), 287–296.

Briggs, D. (1981). Physical Electronics Division. In *Handbook of X-ray photoelectron spectroscopy* (pp. 149–190). John Wiley & Sons, Ltd.

Brinker, C. J., & Schunk, P. R. (1992). Review of sol-gel thin film formation. *Journal of Non-Crystalline Solids*, *148&147*, 424–436.

Brune, D., Hellborg, R., Whitlow, H. J., & Hunderi, O. (1997). Electrical and magnetic properties of thin films. In *Surface Characterization: A User's Sourcebook* (pp. 539–540). Wiley-VCH.

Buta, E. V., Pascariu, P., Prihor, F., Vlad, L., Pohoata, V., Apetrei, R., … Mardare, D. (2008). Characterization of sputtered TiO$_2$ thin films. In *SCIENTIFIC ANNALS of "Alexandru Ioan Cuza din Iaşi" University* (pp. 1–6).

Byranvand, M. M., Kharat, a N., Fatholahi, L., & Beiranvand, Z. M. (2013). A Review on Synthesis of Nano-TiO$_2$ via Different Methods. *Journal of Nanostructures*, *3*, 1–9.

Carp, O., Huisman, C. L., & Reller, A. (2004). Photoinduced reactivity of titanium dioxide. *Progress in Solid State Chemistry*, *32*(1-2), 33–177.

Chaudhary, V., Srivastava, A. K., & Kumar, J. (2011). On the Sol-gel Synthesis and Characterization of Titanium Oxide Nanoparticles. *Materials Research Society Symposium Proceedings*, *1352*, 10–24.

Chen, D., Jiang, Z., Geng, J., Zhu, J., & Yang, D. (2008). A facile method to synthesize nitrogen and fluorine co-doped TiO2 nanoparticles by pyrolysis of $(NH_4)_2TiF_6$. *Journal of Nanoparticle Research*, *11*(2), 303–313.

Chen, H. (2008). *Dye sensitized solar cells*. *Dye Sensitized Solar Cells Using Zinc Oxide Nanotips and Gallium-doped Zinc Films*. The State University of New Jersey.

Chen, H., Yu, S.-M., Shin, D.-W., & Yoo, J.-B. (2010). Solvothermal Synthesis and Characterization of Chalcopyrite CuInSe2 Nanoparticles. *Nanoscale Research Letters*, *5*(1), 217–223.

Chen, X., Li, C., Gratzel, M., Kostecki, R., & Mao, S. S. (2014). Nanomaterials for renewable energy production and storage. *Chemical Society Reviews*, *41*, 7909–7937.

Chen, X., Li, C., Grätzel, M., Kostecki, R., & Mao, S. S. (2012). Titanium dioxide nanomaterials: synthesis, properties, modifications, and applications. *Chemical Society Reviews*, *41*(23), 7909–7937.

Chen, X., Liu, L., Liu, Z., Marcus, M. a, Wang, W.-C., Oyler, N. a, … Mao, S. S. (2013). Properties of disorder-engineered black titanium dioxide nanoparticles through hydrogenation. *Scientific Reports*, *3*, 15101–15107.

Chen, X., Liu, L., Yu, P. Y., & Mao, S. S. (2011). Increasing solar absorption for photocatalysis with black hydrogenated titanium dioxide nanocrystals. *Science*, *331*(6018), 746–750.

Choi, J., Cho, S. H., Kim, T. H., & Lee, S. W. (2011). Comparison of Sonochemistry Method and Sol-Gel Method for the Fabrication of TiO$_2$ Powder. *Materials Science Forum*, *695*, 109–112.

218

Collings, A. F., & Gwan, P. B. (2010). Ultrasonic destruction of pesticides contaminants in slurries. *Ultrasonic Sonochemistry*, *17*, 1–3.

Colmenares, J. C., Luque, R., Campelo, J. M., Colmenares, F., Karpiński, Z., & Romero, A. A. (2009). Nanostructured photocatalysts and their applications in the photocatalytic transformation of lignocellulosic biomass: An overview. *Materials*, *2*(4), 2228–2258.

Conde-Gallardo, A., Guerrero, M., Castillo, N., Soto, A. B., Fragoso, R., & Cabanas-Moreno, J. G. (2005). TiO_2 anatase thin films deposited by spray pyrolysis of an aerosol of titanium diisopropoxide. *Thin Solid Films*, *473*(1), 68–73.

Cong, Y., Zhang, J., Chen, F., & Anpo, M. (2007). Synthesis and Characterization of Nitrogen-Doped TiO_2 Nanophotocatalyst with High Visible Light Activity. *Journal of Physical Chemistry C*, *111*, 6976–6982.

Cui, H., Zhao, W., Yang, C., Yin, H., Lin, T., Shan, Y., … Huang, F. (2014). Black TiO_2 nanotube arrays for high-efficiency photoelectrochemical water-splitting. *Journal of Materials Chemistry A*, *2*(23), 8612–8616.

Czoska, A. M., Livraghi, S., Chiesa, M., Giamello, E., Agnoli, S., Granozzi, G., … Pacchioni, G. (2008). The nature of defects in fluorine-doped TiO_2. *Journal of Physical Chemistry C*, *112*(24), 8951–8956.

D. Eder, & Windle, A. H. (2008). Morphology control of CNT-TiO_2 hybrid materials and rutile nanotubes. *Journal of Materials Chemistry*, *18*, 2036–2043.

Dar, M. I., Chandiran, A. K., Grätzel, M., Nazeeruddin, M. K., & Shivashankar, S. a. (2014). Controlled synthesis of TiO_2 nanoparticles and nanospheres using a microwave assisted approach for their application in dye-sensitized solar cells. *Journal of Materials Chemistry A*, *2*, 1662–1667.

Dawe, D., Stamoulis, K., & Wiebe, K. (2011). *The State of Food Insecurity in the World: How does international price volatility affect domestic economies and food security? FOOD AND AGRICULTURE ORGANIZATION OF THE UNITED NATIONS*.

Dawei Gong, Grimesa, C. A., Varghesea, O. K., Hua, W., Singha, R. S., Chena, Z., & Dickey, E. C. (2001). Titanium oxide nanotube arrays prepared by anodic oxidation. *Journal of Materials Research*, *16*(12), 3331–3334.

Deng, Y., Cal, Y., Sun, Z., Liu, J., Liu, C., Wei, J., … Zhao, D. (2010). Multifuntional mesoporous composite microsphere with well-designed nanostructure: A highly integrated catalyst system. *Journal of American Chemical Society*, *132*, 8466–8473.

Dozzi, M., Andrea, C., Ohtani, B., Valentini, G., & Selli, E. (2013). Fluorine-Doped TiO$_2$ Materials : Photocatalytic Activity vs Time- Resolved Photoluminescence. *The Journal of Physical Chemistry*, *117*, 25586–25595.

Dozzi, M., & Selli, E. (2013). Specific Facets-Dominated Anatase TiO$_2$: Fluorine-Mediated Synthesis and Photoactivity. *Catalysts*, *3*(2), 455–485.

Dunnill, C. W., Aiken, Z. A., Kafizas, A., Pratten, J., Wilson, M., Morgan, D. J., & Parkin, I. P. (2009). White light induced photocatalytic activity of sulfur-doped TiO$_2$ thin films and their potential for antibacterial application. *Journal of Materials Chemistry*, *19*(46), 8747–8754.

Echavia, G. R. M., Matzusawa, F., & Negishi, N. (2009). Photocatalytic degradation of organophosphate and phosphonoglycine pesticides using TiO$_2$ immobilized on silica gel. *Chemosphere*, *76*(5), 595–600.

Emeline, A. V., Kuznetsov, V. N., Rybchuk, V. K., & Serpone, N. (2008). Visible-Light-Active Titania Photocatalysts: The Case of N-Doped TiO_2s—Properties and Some Fundamental Issues. *International Journal of Photoenergy*, *2008*(258394), 1–19.

Fenner, K., Canonica, S., Wackett, L. P., & Elsner, M. (2013). Evaluating Pesticide Degradation in the Environment: Blind Spots and Emerging Opportunities. *Science*, *341*(6147), 752–758.

Fujishima, A., & Honda, K. (1972). Electrochemical Photolysis of Water at a Semiconductor Electrode. *Nature*, *238*(5358), 37–38.

Fujishima, A., Rao, T. N., & Tryk, D. A. (2000). Titanium dioxide photocatalysis. *Journal of Photochemistry and Photobiology C: Photochemistry Reviews*, *1*, 1–21.

Gajjela, S. R., Ananthanarayanan, K., Yap, C., Gratzel, M., & Balaya, P. (2010). Synthesis of mesoporous titanium dioxide by soft template based approach: characterization and application in dye-sensitized solar cells. *Energy & Environmental Science*, *3*, 838–845.

Galarneau, A., Villemot, F., Rodriguez, J., Fajula, F., & Coasne, B. (2014). Validity of the t-plot Method to Assess Microporosity in Hierarchical Micro/Mesoporous Materials. *Langmuir*, *30*(44), 13266–13274.

Ganesh, I., Gupta, A. K., Kumar, P. P., Sekhar, P. S. C., Radha, K., Padmanabham, G., & Sundararajan, G. (2012). Preparation and characterization of Co-doped TiO2 materials for solar light induced current and photocatalytic applications. *Materials Chemistry and Physics*, *135*(1), 220–234.

Gaya, U. I. (2014). Principles of heterogeneous photocatalysis. In *Heterogeneous Photocatalysis Using Inorganic Semiconductor Solids* (pp. 26–27). Springer.

Gaya, U. I., & Abdullah, A. H. (2008). Heterogeneous photocatalytic degradation of organic contaminants over titanium dioxide: A review of fundamentals, progress and problems. *Journal of Photochemistry and Photobiology C: Photochemistry Reviews*, *9*(1), 1–12.

Giannakopoulou, T., Todorova, N., Vaimakis, T., Ladas, S., & Trapalis, C. (2008). Study of Fluorine-Doped TiO_2 Sol-Gel Thin Coatings. *Journal of Solar Energy Engineering*, *130*(4), 1–5.

Gole, J. L., Stout, J. D., Burda, C., Lou, Y., & Chen, X. (2004). Highly Efficient Formation of Visible Light Tunable $TiO_{2-x}N_x$ Photocatalysts and Their Transformation at the Nanoscale. *The Journal of Physical Chemistry B*, *108*(4), 1230–1240. doi:10.1021/jp030843n

Gopal, N. O., Lo, H. H., Ke, T. F., Lee, C. H., Chou, C. C., Wu, J. De, … Ke, S. C. (2012). Visible light active phosphorus-doped TiO_2 nanoparticles: An EPR evidence for the enhanced charge separation. *Journal of Physical Chemistry C*, *116*(30), 16191–16197.

Gratzel, M. (2001). Photoelectrochemical cells. *Nature*, *414*, 338–344.

Gupta, S. M., & Tripathi, M. (2011). A review of TiO_2 nanoparticles. *Chinese Science Bulletin*, *56*(16), 1639–1657.

Haerudin, H., Bertel, S., & Kramer, R. (1998). Surface stoichiometry of titanium suboxide: Part I Volumetric and FTIR study. *Journal of Chemical Society Faraday Transition*, *94*(10), 1481–1487.

Hamdy, M. S., Amrollahi, R., & Mul, G. (2012). Surface Ti^{3+} containing (blue) titania: A unique photocatalyst with high activity and selectivity in visible light-stimulated selective oxidation. *ACS Catalysis*, *2*(12), 2641–2647.

Han, X., Kuang, Q., Jin, M., Xie, Z., & Zheng, L. (2009). Synthesis of titania nanosheets with a high percentage of exposed (001) facets and related photocatalytic properties. *Journal of the American Chemical Society*, *131*(9), 3152–3153.

Hanaor, D., Michelazzi, M., Leonelli, C., & Sorrell, C. C. (2012). The effects of carboxylic acids on the aqueous dispersion and electrophoretic deposition of ZrO_2. *Journal of the European Ceramic Society*, *32*(1), 235–244.

Hanaor, D., & Sorell, C. (2010). Review of the anatase to rutile phase transformation. *Journal of Materials Science*, *46*(4), 855–874.

Harris, J., & McCartor, A. (2011). *The World'S Worst Toxic Pollution Problems Report 2011*. *Blacksmith Institute*. Retrieved from www.worstpolluted.org

Hashimoto, K., Irie, H., & Fujishima, A. (2006). TiO_2 Photocatalysis : A Historical Overview and Future Prospects. *Japanese Journal of Applied Physics*, *44*(12), 8269–8285.

Hassanjani-Roshan, A., Kazemzadeh, S. M., Vaezi, M. R., & Shokuhfar, A. (2011). The effect of sonication power on the sonochemical synthesis of titania nanoparticles. *Journal of Ceramic Processing Research*, *12*(3), 299–303.

He, T., & Yao, J. (2006). Photochromism in composite and hybrid materials based on transition-metal oxides and polyoxometalates. *Progress in Materials Science*, *51*(6), 810–879.

Hequet, V., Gonzalez, C., & Cloirec, P. Le. (2001). Photochemical process for atrazine degradation methodological approach. *Water Resources*, *35*(18), 4253–4260.

Ho, W., Yu, J. C., & Lee, S. (2006). Low-temperature hydrothermal synthesis of S-doped TiO_2 with visible light photocatalytic activity. *Journal of Solid State Chemistry*, *179*(4), 1171–1176.

Hu, C., Lu, T., Chen, F., & Zhang, R. (2013). A brief review of graphene–metal oxide composites synthesis and applications in photocatalysis. *Journal of the Chinese Advanced Materials Society*, *1*(1), 21–39.

Hu, L., Wang, J., Zhang, J., Zhang, Q., & Liu, Z. (2014). An N-doped anatase/rutile TiO_2 hybrid from low-temperature direct nitridization: enhanced photoactivity under UV-/visible-light. *RSC Adv.*, *4*(1), 420–427.

Hu, X., Li, G., & Yu, J. C. (2010). Design, fabrication, and modification of nanostructures semiconductor materials for environmental and energy applications. *Langmuir*, *26*, 3031–3039.

Hu, Y. H. (2012). A highly efficient photocatalyst--hydrogenated black TiO_2 for the photocatalytic splitting of water. *Angewandte Chemie (International Ed. in English)*, *51*(50), 12410–12412.

Hurum, D. C., Agrios, A. G., & Gray, K. A. (2003). Explaining the enhanced photocatalytic activity of Degussa P25 mixed-phase TiO_2 using EPR. *Journal of Physical Chemistry B*, *107*, 4545–4549.

Hyeun, K. J. (2013). Photocatalysts for Hydrogen Production from Solar Water Splitting. *Clean Technology*, *19*(3), 191–200.

Ichimura, A. S., Mack, B., Usmani, S. M., & Mars, D. (2012). Direct synthesis of anatase films with ~100% (001) facets and [001] preferred orientation. *Chemistry of Materials*, *24*(12), 2324–2329.

J. Lee, Lee, S. J., Han, W. B., Jeon, H., Park, J., Kim, H., … Jeon, H. (2012). Effect of crystal structure and grain size on photo-catalytic activities of remote-plasma atomic layer deposited titanium oxide thin film. *Journal of Solid State Science and Technology*, *1*(4), 63–69.

Jiang, L.C., & Zhang, W. D. (2009). Electrodeposition of TiO_2 nanoparticles on multiwalled carbon nanotube arrays for hydrogen peroxide sensing. *Electroanalysis*, *21*(8), 988–993.

Jiang, J., Oberdosrster, G., Elder, A., Gelein, R., Mercer, P., & Biswas, P. (2010). Does nanoparticles activity depend upon size and crystal phase. *Nanotoxicology*, *2*(1), 33–42.

Jin, C., Liu, B., Lei, Z., & Sun, J. (2015). Structure and photoluminescence of the TiO_2 films grown by atomic layer deposition using tetrakis-dimethylamino titanium and ozone. *Nanoscale Research Letters*, *10*, 95–104.

Jollie, D. M., & Harrison, P. G. (1997). An in situ IR study of the thermal decomposition of trifluoroacetic acid. *Journal of the Chemical Society, Perkin Transactions 2*, (8), 1571–1576.

Jusof Khadidi, M. H., & Hamid, E. A. (2013). A New Flocculant-Coagulant with Potential Use for Industrial Wastewater Treatment. In *2nd International Conference on Environment, Energy and Biotechnology* (Vol. 51, pp. 139–142).

Karaman, M., Sariipek, F., Koysuren, O., & Yildiz, H. B. (2013). Template assisted synthesis of photocatalytic titanium dioxide nanotubes by hot filament chemical vapor deposition method. *Applied Surface Science*, *283*, 993–998.

Karuppuchamy, S., Andou, Y., & Endo, T. (2012). Preparation of nanostructured TiO_2 photoelectrode for flexible dye-sensitized solar cell applications. *Applied Nanoscience*, *3*(4), 291–293.

Kasuga, T., Hiramatsu, M., Hoson, A., Sekino, T., & Niihara, K. (2007). Formation of titanium oxide nanotube. *Langmuir*, *14*(12), 3160–3163.

Kaur, T., Sraw, A., Wanchoo, R. K., & Toor, A. P. (2016). Visible–Light Induced Photocatalytic Degradation of Fungicide with Fe and Si Doped TiO$_2$ Nanoparticles. *Materials Today: Proceedings*, *3*(2), 354–361.

Khan, J. A., Han, C., Shah, N. S., Khan, H. M., Nadagouda, M. N., Likodimos, V., … Dionysiou, D. D. (2014). Ultraviolet-visible light sensitive high surface area phosphorous fluorine co-doped TiO$_2$ nanoparticles for the degradation of atrazine in water. *Environmental Engineering Science*, *31*(7), 435–446.

Khan, M. M., Ansari, S. A., Pradhan, D., Ansari, M. O., Han, D. H., Leea, J., & Cho, M. H. (2014). Band gap engineered TiO$_2$ nanoparticles for visible light induced photoelectrochemical and photocatalytic studies,. *Journal of Materials Chemistry A*, *2*, 637–644.

Kim, D. S., & Kwak, S.-Y. (2007). The hydrothermal synthesis of mesoporous TiO$_2$ with high crystallinity, thermal stability, large surface area, and enhanced photocatalytic activity. *Applied Catalysis A: General*, *323*, 110–118.

Klaus, D. S. (2016). Carbon Nanomaterials Sourcebook. In *Carbon Nanomaterials Sourcebook: Nanoparticles, Nanocapsules, Nanofibres, Nanoporous structures, and Nanocomposites (Volume 2)* (pp. 221–223). CRC Press.

Kocemba, I., Nadajczyk, J., Rynkowski, J., & Maniukiewicz, W. (2014). The effect of pretreatment conditions on structural, morphological and catalytic properties of TiO2. *Applied Surface Science*, *288*, 90–97.

Kong, M., Li, Y., Chen, X., Tian, T., Fang, P., Zheng, F., & Zhao, X. (2011). Tuning the relative concentration ratio of bulk defects to surface defects in TiO$_2$ nanocrystals leads to high photocatalytic efficiency. *Journal of American Chemical Society*, *164*, 16414–16417.

Konstantinou, I. K., & Albanis, T. A. (2003). Photocatalytic transformation of pesticides in aqueous titanium dioxide suspensions using artificial and solar light : intermediates and degradation pathways. *Applied Catalysis B: Environmental*, *42*, 319–335.

Konstantinou, I. K., Sakellarides, T. M., Sakkas, V. A., & Albanis, T. A. (2001). Photocatalytic Degradation of Selected s-Triazine Herbicides and Organophosphorus Insecticides over Aqueous TiO_2 Suspensions. *Environmental Science and Technology*, *35*(2), 398–405.

Kumar, N., Maitra, U., Hegde, V. I., Waghmare, U. V, Sundaresan, A., & Rao, C. N. R. (2013). Synthesis, characterization, photocatalysis, and varied properties of TiO_2 cosubstituted with nitrogen and fluorine. *Inorganic Chemistry*, *52*(18), 10512–1-519

Kwamman, T., & Smith, S. M. (2012). Low Temperature Solvolthermally Synthesized Nitrogen-Fluorine Doped TiO_2 for Methyl Orange Photodegradation. *Advanced Materials Research*, *488-489*, 98–102.

Lee, K. B., & Lee, K. H. (2008). Ti-O binding states of resistive switching TiO2 thin films prepared by reactive magnetron sputtering. *Journal of the Korean Physical Society*, *53*(4), 1996–2001.

Leshuk, T., Parviz, R., Everett, P., Krishnakumar, H., Varin, R. a, & Gu, F. (2013). Photocatalytic activity of hydrogenated TiO_2. *ACS Applied Materials & Interfaces*, *5*(6), 1892–1895.

Li, D., Haneda, H., Hishita, S., Ohashi, N., & Labhsetwar, N. K. (2005). Fluorine-doped TiO_2 powders prepared by spray pyrolysis and their improved photocatalytic activity for decomposition of gas-phase acetaldehyde. *Journal of Fluorine Chemistry*, *126*, 69–77.

Li, G., Zhu, M., Chen, J., Li, Y., & Zhang, X. (2011). Production and contribution of hydroxyl radicals between the DSA anode and water interface. *Journal of Environmental Sciences*, *23*(5), 744–748.

Li, S., Zhang, G., Guo, D., Yu, L., & Zhang, W. (2009). Anodization Fabrication of Highly Ordered TiO_2 Nanotubes. *The Journal of Physical Chemistry C*, *113*(29), 12759–12765.

Li, X., & Liu, S. (2008). Characterization of Visible Light Response N-F Codoped TiO_2 Photocatalyst Prepared by Acid Catalyzed Hydrolysis. *Acta Physica-Chimica Sinica*, *24*(11), 2019–2024.

Li, Y., Bastakoti, B. P., Imura, M., Hwang, S. M., Sun, Z., Kim, J. H., … Yamauchi, Y. (2014). Synthesis of mesoporous TiO_2/SiO_2 hybrid films as an efficient photocatalyst by polymeric micelle assembly. *Chemistry A European Journal*, *20*, 6027–6032.

Lim, Y., Jeong, J., An, J., Jeon, Y., Jeon, K., & K. (2005). Nickel-doped titanium oxide films prepared by chemical solution deposition. *Journal Of Ceramic Processing Research*, *6*(4), 302–304.

Lin, L., Zheng, R. Y., Xie, J. L., Zhu, Y. X., & Xie, Y. C. (2007). Synthesis and characterization of phosphor and nitrogen co-doped titania. *Applied Catalysis B: Environmental*, *76*(1-2), 196–202.

Lin, T., Yang, C., Wang, Z., Yin, H., Lü, X., Huang, F., … Jiang, M. (2014). Effective nonmetal incorporation in black titania with enhanced solar energy utilization. *Energy & Environmental Science*, *7*(3), 967–972.

Liu, C., Cheng, W., Sheng, Y., & Li, L. (2009). Atrazine degradation in solar irradiation/S-doped titanium dioxide treatment. In *3rd International Conference on Bioinformatics and Biomedical Engineering (iCBBE 2009),* (pp. 1–4).

Liu, C., Tang, X., Mo, C., & Qiang, Z. (2008). Characterization and activity of visible-light-driven TiO_2 photocatalyst codoped with nitrogen and cerium. *Journal of Solid State Chemistry*, *181*(4), 913–919.

Liu, M., Piao, L., Lu, W., Ju, S., Zhao, L., Zhou, C., … Wang, W. (2010). Flower-like TiO_2 nanostructures with exposed {001} faacets: Facile synthesis and enhanced photocatalysis. *Nanoscale*, *2*, 1115–1117.

Liu, S., Wu, J., Liu, X., & Jiang, R. (2010). TiO_2/V–TiO_2 composite photocatalysts with an n–n heterojunction semiconductor structure. *Journal of Molecular Catalysis A: Chemical*, *332*(1-2), 84–92.

Liu, Y., Chen, X., Li, J., & Burda, C. (2005). Photocatalytic degradation of azo dyes by nitrogen-doped TiO_2 nanocatalysts. *Chemosphere*, *61*(1), 11–18.

Livraghi, S., Paganini, M. C., Giamello, E., Selloni, A., Valentin, C. Di, & Pacchioni, G. (2006). Origin of Photoactivity of Nitrogen-Doped Titanium Dioxide under Visible Light. *Journal of American Chemical Society*, *128*(21), 15666–15671.

López-Muñoz, M. J., Aguado, J., & Revilla, A. (2011). Photocatalytic removal of s-triazines: Evaluation of operational parameters. *Catalysis Today*, *161*(1), 153–162.

Loryuenyonga, V., Angamnuaysiria, K., Sukcharoenponga, J., & Suwannasria, A. (2012). Sol-gel template synthesis and photocatalytic behaviour of anatase titania nanoparticles. *Science Asia*, *38*, 301–306.

Lu, D., Zhang, G., & Wan, Z. (2015). Visible-light-driven g-C_3N_4/Ti^{3+} TiO_2 photocatalyst co-exposed {001} and {101} facets and its enhanced photocatalytic activities for organic pollutant degradation and Cr(VI) reduction. *Applied Surface Science*, *358*, 223–230.

Lu, J., Dai, Y., Jin, H., & Huang, B. (2011). Effective increasing of optical absorption and energy conversion efficiency of anatase TiO_2 nanocrystals by hydrogenation. *Physical Chemistry Chemical Physics : PCCP*, *13*(40), 18063–18068.

Lucky, R. A., Sui, R. H., Lo, J. M. H., & Charpentier, P. A. (2010). Effect of solvent on the crystal growth of one-dimensional ZrO_2–TiO_2 nanostructures. *Crystal Growth and Design*, *10*(4), 1598–1604.

Luo, H., Wang, C., & Yan, Y. (2003). Synthesis of mesostructured titania with controlled crystalline framework. *Chemistry of Materials*, *15*, 3841–3846.

Lv, K., Cheng, B., Yu, J., & Liu, G. (2012). Fluorine ions-mediated morphology control of anatase TiO_2 with enhanced photocatalytic activity. *Physical Chemistry Chemical Physics*, *14*(16), 5349–5362.

Lv, K., Xiang, Q., & Yu, J. (2011). Effect of calcination temperature on morphology and photocatalytic activity of anatase TiO_2 nanosheets with exposed {001} facets. *Applied Catalysis B: Environmental*, *104*(3-4), 275–281.

Lv, K., Yu, J., Cui, L., Chen, S., & Li, M. (2011). Preparation of thermally stable anatase TiO_2 photocatalyst from $TiOF_2$ precursor and its photocatalytic activity. *Journal of Alloys and Compounds*, *509*(13), 4557–4562.

Ma, X. Y., Chen, Z. G., Hartono, S. B., Jiang, H. B., Zou, J., Qiao, S. Z., & Yang, H. G. (2010). Fabrication of uniform anatase TiO2 particles exposed by {001} facets. *Chemical Communications (Cambridge, England)*, *46*, 6608–6610.

Mahata, S., Mahato, S. S., Nandi, M. M., & Mondal, B. (2011). Synthesis of TiO_2 nanoparticles by hydrolysis and peptization of titanium isopropoxide solution. In *AIP Conference Proceedings* (Vol. 1461, pp. 225–228).

Martyanov, I. N., Sitharaman Uma, A., Rodriguesa, S., & Klabundea, K. J. (2004). Structural defects cause TiO_2-based photocatalysts to be active in visible light. *Chemical Communications*, *21*, 2476–2477.

Maruyama, T., & Tabata, K. (1990). Fluorine-doped tin dioxide thin films prepared by chemical vapor deposition. *Journal of Applied Physics*, *68*(8), 4282–4285.

Mc Murray, T., Dunlop, P., & Byrne, J. (2006). The photocatalytic degradation of atrazine on nanoparticulate TiO_2 films. *Journal of Photochemistry and Photobiology A: Chemistry*, *182*(1), 43–51.

Memesa, M., Lenz, S., Emmerling, S. G. J., Nett, S., Perlich, J., Müller-Buschbaum, P., & Gutmann, J. S. (2011). Morphology and photoluminescence study of titania nanoparticles. *Colloid and Polymer Science*, *289*, 943–953.

Meng, Y., Chen, J., Wang, Y., Ding, H., & Shan, Y. (2009). (N, F)-codoped TiO_2 Nanocrystals as Visible Light-activated Photocatalyst. *J. Mater. Sci. Technol.*, *25*(1), 73–76.

Mercado, C., Seeley, Z., Bandyopadhyay, A., Bose, S., & McHale, J. (2011). Photoluminescence of dense nanocrystalline titanium dioxide thing films: Effect of doping and thickness and relation to gas sensing. *ACS Applied Materials & Interfaces*, *3*, 2281–2288.

Minero, C., Pelizzetti, E., Malato, S., & Blanc, J. (1996). Large solar plant photocatalytic water decontamination : Degradation of atrazine. *Solar Energy*, *56*(5), 411–419.

Mohamed, M. A., Salleh, W. N. W., Jaafar, J., & Yusof, N. (2014). Preparation and photocatalytic activity of mixed phase anatase/ rutile TiO_2 nanoparticles for phenol degradation. *Advances in Polymeric Membrane Research*, *70*(2), 65–70.

Mohamed, R. M., McKinney, D. L., & Sigmund, W. M. (2012). Enhanced nanocatalysts. *Materials Science and Engineering: R: Reports*, *73*(1), 1–13.

Morikawa, T., Asahi, R., Ohwaki, T., Aoki, K., Suzuki, K., & Taga, Y. (2005). Visible-light Photocatalyst - Nitrogen-doped Titanium Dioxide. *R&D Review of Toyota CDRL*, *40*(3), 45–50.

Murugan, A. V., Samuel, V., & Ravi, V. (2006). Synthesis of nanocrystalline anatase TiO_2 by microwave hydrothermal method. *Materials Letters*, *60*(4), 479–480.

Nainani, R., Thakur, P., & Chaskar, M. (2012). Synthesis of Silver Doped TiO_2 Nanoparticles for the Improved Photocatalytic Degradation of Methyl Orange. *Journal of Materials Science and Engineering B*, *2*(1), 52–58.

Naldoni, A., Allieta, M., Santangelo, S., Marelli, M., Fabbri, F., Cappelli, S., … Dal Santo, V. (2012). Effect of nature and location of defects on bandgap narrowing in black TiO_2 nanoparticles. *Journal of the American Chemical Society*, *134*(18), 7600–7603.

Nam, C. T., Yang, W. D., & Duc, L. M. (2013). Solvothermal synthesis of TiO_2 photocatalysts in ketone solvents with low boiling points. *Journal of Nanomaterials*, *2013*, 1–11.

National Water-Quality Assessment (NAWQA) Program. (2013). *U. S Geological Survery (USGS)*.

Nav́o, J. A., Colón, G., Trillas, M., Peral, J., Domènech, X., Testa, J. J., … Litter, M. I. (1998). Heterogeneous photocatalytic reactions of nitrite oxidation and Cr(VI) reduction on iron-doped titania prepared by the wet impregnation method. *Applied Catalysis B: Environmental*, *16*(2), 187–196.

Neppolian, B., Choi, H., & Sakthivel, S. (2002). Solar light induced and TiO_2 assisted degradation of textile dye reactive blue 4. *Chemosphere*, *46*, 1173–1181.

Nguyen Phan, T. D., Pham, H. D., Viet Cuong, T., Jung Kim, E., Kim, S., & Woo Shin, E. (2009). A simple hydrothermal preparation of TiO_2 nanomaterials using concentrated hydrochloric acid. *Journal of Crystal Growth*, *312*(1), 79–85.

Nosaka, Y., Matsushita, M., Nishino, J., & Nosaka, A. Y. (2005). Nitrogen-doped titanium dioxide photocatalysts for visible response prepared by using organic compounds. *Science and Technology of Advanced Materials*, *6*(2), 143–148.

Oh, Y., & Jenks, W. S. (2004). Photocatalytic degradation of a cyanuric acid , a recalcitrant species. *Journal of Photochemistry and Photobiology A: Chemistry*, *162*, 323–328.

Oja, I., Mere, a., Krunks, M., Solterbeck, C.-H., & Es-Souni, M. (2004). Properties of TiO_2 Films Prepared by the Spray Pyrolysis Method. *Solid State Phenomena*, *99-100*, 259–264.

Okuya, M., Nakade, K., & Kaneko, S. (2002). Porous TiO_2 thin films synthesized by a spray pyrolysis deposition (SPD) technique and their application to dye-sensitized solar cells. *Solar Energy Materials and Solar Cells*, *70*(4), 425–435.

Olayini, A. O., Ramli, M. F., & Sood, A. M. (2013). Agricultural Land Use in Malaysia : an Historical Overview and Implications for Food Security. *Bulgarian Journal of Agricultural Science*, *19*(1), 60–69.

Ong, W.-J., Tan, L.-L., Chai, S.-P., Yong, S.-T., & Mohamed, A. R. (2014). Highly reactive {001} facets of TiO_2-based composites: synthesis, formation mechanism and characterization. *Nanoscale*, *6*(4), 1946–2008.

Orikawa, T. M., Sahi, R. A., & Hwaki, T. O. (2001). Band-Gap Narrowing of Titanium Dioxide by Nitrogen Doping Band-Gap Narrowing of Titanium Dioxide by Nitrogen Doping. *The Japan Society of Applied Physics*, *40*(6A), 561–563.

Oshani, F., Marandi, R., Rasouli, S., & Farhoud, M. K. (2014). Photocatalytic investigations of TiO_2-P25 nanocomposite thin films prepared by peroxotitanic acid modified sol-gel method. *Applied Surface Science*, *311*, 308–313.

Oveisi, H., Suzuki, N., Beitollahi, A., & Yamauchi, Y. (2010). Aerosol-assisted fabrication of mesoporous titania spheres with crystallized anatase structures and investigation of their photocatalytic properties. *Journal of Sol-Gel Science and Technology*, *56*, 212–218.

Padmanabhan, S. C., Pillai, S. C., Colreavy, J., Balakrishnan, S., Mccormack, D. E., Perova, T. S., … Kelly, J. M. (2007). A Simple Sol - Gel Processing for the Development of High-Temperature Stable Photoactive Anatase Titania. *Chemistry of Materials*, *19*(11), 4474–4481.

Paola, A. Di, Bellardita, M., & Palmisano, L. (2013). Brookite, the Least Known TiO_2 Photocatalyst. *Catalysts*, *3*(1), 36–73.

Park, H., Park, Y., Kim, W., & Choi, W. (2013). Surface modification of TiO_2 photocatalyst for environmental applications. *Journal of Photochemistry and Photobiology C: Photochemistry Reviews*, *15*(1), 1–20.

Parra, S., Elena Stanca, S., Guasaquillo, I., & Ravindranathan Thampi, K. (2004). Photocatalytic degradation of atrazine using suspended and supported TiO_2. *Applied Catalysis B: Environmental*, *51*(2), 107–116.

Parra, S., Olivero, J., & Pulgarin, C. (2002). Relationships between physicochemical properties and photoreactivity of four biorecalcitrant phenylurea herbicides in aqueous TiO_2 suspension, *36*, 75–85.

Pathak, R. K., & Dikshit, A. K. (2011). Various method for atrazine removal. In *International Conference on Life Science and Technology (IPCBEE) 3* (pp. 19– 22).

Patterson, A. L. (1939). The Scherrer Formula for X-Ray Particle Size Determination. *Physical Review Letters*, *56*(10), 978–981.

Paul, S., & Chouhury, A. (2013). Investigation of the optical property and photocatalytic activity of mixed phase nanocrystalline titania. *Applied Nanoscience*, *4*(7), 839–847.

Pelaez, M., de la Cruz, A. a., Stathatos, E., Falaras, P., & Dionysiou, D. D. (2009). Visible light-activated N-F-codoped TiO₂ nanoparticles for the photocatalytic degradation of microcystin-LR in water. *Catalysis Today*, *144*(1-2), 19–25.

Pelizzeti, E., Mauriono, V., Minero, C., Carlin, V., Pramauro, E., Zerbinati, O., & L. Tosato, M. (1990). Photocatalytic Degradation of Atrazine and Other s-Triazine Herbicides. *Environmental Science and Technology*, *24*, 1559–1565.

Peng, T., Zhao, D., Dai, K., Shi, W., & Hirao, K. (2005). Synthesis of titanium dioxide nanoparticles with mesoporous anatase wall and high photocatalytic activity. *Journal of Physical Chemistry B*, *109*, 4947–4952.

Pillai, S. C., McCormack, D., & Colreavy, J. (2007). A Simple Sol-Gel Processing for the Development of High-Temperature Stable Photoactive Anatase Titania. *American Chemical Society*, *19*(18), 4474–4481.

Plakas, K. V., Karabelas, a. J., Wintgens, T., & Melin, T. (2006). A study of selected herbicides retention by nanofiltration membranes—The role of organic fouling. *Journal of Membrane Science*, *284*(1-2), 291–300.

235

Plummer, B. (2013). We've covered the world in pesticides. Is that a problem? Retrieved from https://www.washingtonpost.com/news/wonk/wp/2013/08/18/the-world-uses-billions-of-pounds-of-pesticides-each-year-is-that-a-problem/

Pookmanee, P., & Phanichphant, S. (2009). Titanium dioxide powder prepared by a sol-gel method. *Journal of Ceramic Processing Research*, *10*(2), 167–170.

Prabhu, Y. T., & Rao, K. V. (2014). X-Ray Analysis by Williamson-Hall and Size-Strain Plot Methods of ZnO Nanoparticles with Fuel Variation. *World Journal of Nano Science and Engineering*, *4*(March), 21–28.

Ramchiary, A., & Samdarshi, S. K. (2014). High visible light activity of hydrogenated structure-engineered mixed phase titania photocatalyst. *Chemical Physics Letters*, *597*, 63–68.

Rao, K. V., & Rajendar, V. (2015). TiO_2 nanoparticles: Synthesized by simpple microwave - assisted method using room temperature ionic liquids. *International Journal of Multidisciplinary Advanced Research Trends*, *II*(I), 241–246.

Rao, R., & Okada, T. (2014). Effect of oxygen pressure on photoluminescence spectra and hall coefficients. In *ZnO Nanocrystals and Allied Materials* (pp. 95–96). Springer.

Reddy, K. M., Manorama, S. V., & Reddy, A. R. (2003). Bandgap studies on anatase titanium dioxide nanoparticles. *Materials Chemistry and Physics*, *78*(1), 239–245.

Regulska, E., Małgorzata Bruś, D., & Karpińska, J. (2013). Photocatalytic decolourization of direct yellow 9 on titanium and zinc oxides. *International Journal of Photoenergy*, *2013*(975356), 1–9.

Ribaudo, M., & Bouzaher, A. (1994). *Atrazine : Environmental Characteristics and Economics of Management. Agricultural Economic Report*.

Rosborg, I., Nihlgard, B., Gerhadsson, L., & Sverdrup, H. (2006). Concentrations of inorganic elements in 20 municipal waters in Sweden before and after treatment − links to human health. *Environmental Geochemistry and Health*, *28*(3), 215–229.

Rosendo López, & Gómez, R. (2012). Band-gap energy estimation from diffuse reflectance measurements on sol–gel and commercial TiO_2: a comparative study. *Journal of Sol-Gel Science and Technology*, *61*(1), 1–7.

Rovelli, L., & Thampi, K. R. (2015). Solar water splitting using semiconductor systems. In J. Sa (Ed.), *Fuel Production with Heterogeneous Catalysis* (pp. 11–12). CRC Press.

Rozhkova, E. A., & Ariga, K. (2015). Soft X-ray microscopy and electronic structure of 3d transition metal compounds in artifical photosynthesis materials. In *From Molecules to Materials: Pathways to Artificial Photosynthesis* (pp. 276–277). Springer.

Ruslimie, C. A., Razali, H., & M.Khairul, W. (2011). Catalytic Study on TiO_2 Photocatalyst Synthesised Via Microemulsion Method on Atrazine. *Sains Malaysiana*, *40*(8), 897–902.

Sahoo, C., & Gupta, A. K. (2012). Optimization of photocatalytic degradation of methyl blue using silver ion doped titanium dioxide by combination of experimental design and response surface approach. *Journal of Hazardous Materials*, *215-216*, 302–310.

Samsudin, E. M., Abd Hamid, S. B., Juan, J. C., Basirun, W. J., Kandjani, A. E., & Bhargava, S. K. (2015). Controlled nitrogen insertion in titanium dioxide for optimal photocatalytic degradation of atrazine. *RSC Adv.*, *5*(55), 44041–44052.

Samsudin, E. M., Goh, S. N., Wu, T. Y., Ling, T. T., Hamid, S. B. A., & Juan, J. C. (2015). Evaluation on the photocatalytic degradation activity of reactive blue 4 using pure anatase nano-TiO₂. *Sains Malaysiana*, *44*(7), 1011–1019.

Samsudin, E. M., Hamid, S. B. A., Juan, J. C., & Basirun, W. J. (2015). Influence of triblock copolymer (pluronic F127) on enhancing the physico-chemical properties and photocatalytic response of mesoporous TiO₂. *Applied Surface Science*, *355*, 959–968.

Samsudin, E. M., Hamid, S. B. A., Juan, J. C., Basirun, W. J., & Centi, G. (2015). Enhancement of the intrinsic photocatalytic activity of TiO₂ in the degradation of 1,3,5-triazine herbicides by doping with N,F. *Chemical Engineering Journal*, *280*, 330–343.

Samsudin, E. M., Hamid, S. B. A., Juan, J. C., Basirun, W. J., & Kandjani, A. E. (2015). Surface modification of mixed-phase hydrogenated TiO₂ and corresponding photocatalytic response. *Applied Surface Science*, *359*, 883–896.

Samsudin, E. M., Hamid, S. B. A., Juan, J. C., Basirun, W. J., Kandjani, A. E., & Bhargava, S. K. (2016). Effective role of trifluoroacetic acid (TFA) to enhance the photocatalytic activity of F-doped TiO₂ prepared by modified sol–gel method. *Applied Surface Science*, *365*, 57–68.

Samsudin, E. M., Soo, C. W., Abd Hamid, S. B., Basiron, W. J., Lai, C. W., Lai, C. W., … Juan, J. C. (2015). Synthesis and Characterization of TiO2 Nanoparticles via Alternative Sol-Gel Preparation Routes. *Advanced Materials Research*, *1087*, 191–196.

Santacruz-Chavez, J. A., Oros-Ruiz, S., Prado, B., & Zanella, R. (2015). Photocatalytic degradation of atrazine using TiO₂ superficially modified with metallic nanoparticles. *Journal of Environmental Chemical Engineering*, *3*(4), 3055–3061.

Santana-Aranda, M. A., M.Moran-Pineda, Hernandez, J., & Castillo, S. (2005). Physical properties of TiO$_2$ prepared by sol-gel under different pH conditions for photocatalysis. *Sociedad Mexicana de Ciencia Y Technologia de Superficies Y Materiales*, *18*(1), 46–49.

Sathish, M., Viswanathan, B., Viswanath, R. P., & Gopinath, C. S. (2005). Synthesis , Characterization, Electronic Structure, and Photocatalytic Activity of Nitrogen-Doped TiO2 Nanocatalyst. *Chemistry and Materials*, *17*(10), 6349–6353.

Sayilkan, F., & Asilturk, M. (2005). Characterization of TiO$_2$ Synthesized in Alcohol by a Sol-Gel Process: The Effects of Annealing Temperature and Acid Catalyst. *Turkish Journal of Chemistry*, *29*(2005), 697–706.

Scanlon, D. O., Dunnill, C. W., Buckeridge, J., Shevlin, S. A., Logsdail, A. J., Woodley, S. M., … Sokol, A. A. (2013). Band alignment of rutile and anatase TiO$_2$. *Nature Materials*, *12*(9), 798–801.

Scepanovic, M. J., G.-Brojcin, M., D.-Mitrovic, Z. D., & Popovic, Z. V. (2009). Characterization of anatase TiO$_2$ nanopowder by variable-temperature raman spectroscopy. *Science of Sintering*, *41*, 67–73.

Schneider, J., Matsuoka, M., Takeuchi, M., Zhang, J., Horiuchi, Y., Anpo, M., & Bahnemann, D. V. (2014). Understanding TiO$_2$ photocatalysis : Mechanisms and materials. *Chemical Reviews*, *114*, 9919–9986.

Segomotso, B., Niu, Y., Nasir, M., Tian, B., & Zhang, J. (2013). The study of visible light active bismuth modified nitrogen doped titanium dioxide photocatalysts: role of bismuth. *Applied Surface Science*, *264*, 139–147.

Shahini, S., Askari, M., & Sadrnezhaad, S. K. (2011). Gel-sol synthesis and aging effect on highly crystalline anatase nanopowder. *Bulletin of Materials Science*, *34*(6), 1189–1195.

Shon, H., Phuntsho, S., Okour, Y., Cho, D.-L., Kim, K. S., Li, H.-J., … Kim, J.-H. (2008). Visible Light Responsive Titanium Dioxide (TiO$_2$). *Journal of Korean Industrial Engineering Chemistry*, *19*(1), 1–16.

Simonsen, M. E., & Søgaard, E. G. (2009). Sol–gel reactions of titanium alkoxides and water: influence of pH and alkoxy group on cluster formation and properties of the resulting products. *Journal of Sol-Gel Science and Technology*, *53*(3), 485–497.

Smarsly, B., Grosso, D., Brezesinski, T., Pinna, N., Boissiere, C., Antonietti, M., & Sanzhez, C. (2008). Highly crystalline cubic mesoporous TiO$_2$ with 10-nm pore diameter made with a new block copolymer template. *Chemistry of Materials*, *16*, 2948–2952.

Spurr, R. A., & Myers, H. (1957). Quantitative Analysis of Anatase-Rutile Mixtures with an X-Ray Diffractometer. *Analytical Chemistry*, *29*(5), 760–762.

Sreekantan, S., Hazan, R., & Lockman, Z. (2009). Photoactivity of anatase-rutile TiO$_2$ nanotubes formed by anodization method. *Thin Solid Films*, *518*(1), 16–21.

Stewart, L. K. (2009). *Tungsten trioxide and titanium dioxide photocatalytic degradations of quinoline*. Iowa State University.

Su, C., Hong, B.-Y., & Tseng, C.-M. (2004). Sol–gel preparation and photocatalysis of titanium dioxide. *Catalysis Today*, *96*(3), 119–126.

Su, Z., & Zhou, W. (2011). Formation, morphology control and applications of anodic TiO$_2$ nanotube arrays. *Journal of Materials Chemistry*, *21*(25), 8955–8970.

Sun, H., Wang, C., Pang, S., Li, X., Tao, Y., Tang, H., & Liu, M. (2008). Photocatalytic TiO2 films prepared by chemical vapor deposition at atmosphere pressure. *Journal of Non-Crystalline Solids*, *354*(12-13), 1440–1443.

Sun, J., Qiao, L., Sun, S., & Wang, G. (2008). Photocatalytic degradation of Orange G on nitrogen-doped TiO_2 catalysts under visible light and sunlight irradiation. *Journal of Hazardous Materials*, *155*(1-2), 312–319.

Sung, C., Ho, J., Kim, D., Cho, S., & Oh, W. (2010). Reaction morphology and the effect of pH on the preparation of TiO_2 nanoparticles by a sol-gel method. *Journal of Ceramic Processing Research*, *11*(6), 736–741.

Supriyo Bandyopadhyay. (2002). Interaction of light with matter: Absorption and emission processes. In *Physics of Nanostructured Solid State Devices* (pp. 259–260). Springer.

Tan, H., Zhao, Z., Zhu, W., Coker, E. N., Li, B., Zheng, M., … Sun, Z. (2014). Oxygen Vacancy Enhanced Photocatalytic Activity of Pervoskite $SrTiO_3$. *Applied Materials and Interfaces*, *6*(21), 19184–19190.

Tarver, T. (2008). Ensuring water quality. *Food Technology*, *62*(1), 38–42.

Teimouri, M., Aberoomand, P., Moradi, S., Zhalechin, M., & Piramoon, S. (2012). Synthesis of Nickel-doped TiO_2 nano crystalline by the sol-gel method and influence of ultrasonic irradiation for the photo catalytic degradation of Tartrazine dye. In *Proceedings of the 4th International Conference on Nanostructures (ICNS4)* (pp. 994–995).

Teng, F., Li, M., Gao, C., Zhang, G., Zhang, P., Wang, Y., … Xie, E. (2014). Preparation of black TiO_2 by hydrogen plasma assisted chemical vapor deposition and its photocatalytic activity. *Applied Catalysis B: Environmental*, *148-149*, 339–343.

Thakare, S. R., & Bhave, N. S. (2005). Photocatalytic degradation of Thiram (Fungicides) under visible light irradiation. *E-Journal of Chemistry*, *2*(1), 62–69.

Thompson, T. L., & Jr., J. T. Y. (2005). TiO$_2$-based photocatalysis: surface defects, oxygen and charge transfer. In *Topics in Catalysis* (Vol. 35, pp. 197–210). Springer.

Thuy, N. M., Van, D. Q., & Hai, L. T. H. (2012). The Visible Light Activity of the TiO$_2$ and TiO2 : V4+ Photocatalyst. *Nanomaterials and Nanotechnology*, *2*(14), 1–8.

Tian, B., Qian, Y., Hu, B., Sun, J., & Du, Z. (2012). Synthesis and characterization of nitrogen-doped titanium dioxide nanomaterials derived from nanotube sodium titanate precursor. *Journal of Materials Research*, *27*(18), 2408–2416.

Tian, F., Zhang, Y., Zhang, J., & Pan, C. (2012). Raman Spectroscopy : A New Approach to Measure the Percentage of Anatase TiO$_2$ Exposed (001) Facets. *Journal of Physical Chemistry C*, *116*(001), 7515–7519.

Tongpool, R., & Setwong, K. (2008). Sulfur doping and its effect on TiO$_2$ photoactivity. *Songklanakarin J. Sci. Technol.*, *30*(2), 201–206.

Tsai, C. Y., Hsi, H. C., Kuo, T. H., Chang, Y. M., & Liou, J. H. (2013). Preparation of Cu-doped TiO$_2$ photocatalyst with thermal plasma torch for low-concentration mercury removal. *Aerosol and Air Quality Research*, *13*(2), 639–648.

Umar, A. A., Yusri, M., Rahman, A., Saad, S. K., & Salleh, M. M. (2012). Effect of NH$_3$ Concentration on the Performance of Nitrogen doped TiO$_2$ Photoelectrochemical Cell. *International Journal of Electrochemistry and Science*, *7*, 7855–7865.

Varghese, O. K., Mor, G. K., Grimes, C. A., Paulose, M., & Mukherjee, N. (2004). A titania nanotube array room temperature sensor for selective detection of hydrogen at low concentrations. *Nanotechnology*, *4*(7), 733–737.

Vijayalaxmi, R., & Rajendran, V. (2012). Synthesis and characterization of nano-TiO_2 via different methods. *Journal of Applied Sciences and Research*, *4*(2), 1183–1190.

Viswanathan, B., & Krishanmurthy, K. R. (2012). Nitrogen Incorporation in TiO_2: Does It Make a Visible Light Photo-Active Material? *International Journal of Photoenergy*, *2012*, 1–10.

Wall, T. (2012). *The Millennium Development Goals Report 2012*. *United Nations*.

Wang, G., Huang, B., Li, Z., Lou, Z., Wang, Z., Dai, Y., & Whangbo, M.-H. (2015). Synthesis and characterization of ZnS with controlled amount of S vacancies for photocatalytic H_2 production under visible light. *Scientific Reports*, *5*, 8544–8551.

Wang, H., Song, Y., Liu, W., Yao, S., & Zhang, W. (2013). Template synthesis and characterization of TiO_2 nanotube arrays by the electrodeposition method. *Materials Letters*, *93*, 319–321.

Wang, H., Zheng, L., Liu, C., Liu, Y., Luan, C., Cheng, H., … Bello, I. (2011). Rapid Microwave Synthesis of Porous TiO_2 Spheres and Their Applications in Dye-Sensitized Solar Cells. *The Journal of Physical Chemistry C*, *115*(21), 10419–10425.

Wang, J., Tafen, D. N., Lewis, J. P., Hong, Z., Manivannan, A., Zhi, M., … Wu, N. (2009). Origin of Photocatalytic Activity of Nitrogen-Doped TiO_2 Nanobelts. *Journal of American Chemical Society*, *131*(13), 12290–12297.

Wang, J., Yang, P., & Huang, B. (2015). Self-doped TiO$_{2-x}$ nanowires with enhanced photocatalytic activity: facile synthesis and effect of the Ti^{3+}. *Applied Surface Science*, *356*, 391–398.

Wang, Q., Chen, C., Ma, W., Zhu, H., & Zhao, J. (2009). Pivotal role of fluorine in tuning band structure and visible-light photocatalytic activity of nitrogen-doped TiO$_2$. *Chemistry - A European Journal*, *15*(19), 4765–4769.

Wang, W., Lu, C., Ni, Y., Su, M., & Xu, Z. (2012). A new sight on hydrogenation of F and N-F doped {001} facets dominated anatase TiO$_2$ for efficient visible light photocatalyst. *Applied Catalysis B: Environmental*, *127*, 28–35.

Wang, W.-N., Widiyastuti, W., Ogi, T., Lenggoro, I. W., & Okuyama, K. (2007). Correlations between crystallite/particle size and photoluminescence properties of submicrometer phosphors. *Chemistry of Materials*, *19*(7), 1723–1730.

Wang, X., Tian, J., Fei, C., Lv, L., Wang, Y., & Cao, G. (2015). Rapid construction of TiO$_2$ aggregates using microwave assisted synthesis and its application for dye-sensitized solar cells. *RSC Adv.*, *5*(12), 8622–8629.

Wang, Y., He, Y., Lai, Q., & Fan, M. (2014). Review of the progress in preparing nano TiO$_2$: An important environmental engineering material. *Journal of Environmental Sciences (China)*, *26*, 2139–2177.

Wang, Z., Xu, J., Cai, W., Zhou, B., He, Z., Cai, C., & Hong, X. (2005). Visible light induced photodegradation of organic pollutants on nitrogen and fluorine co-doped TiO$_2$ photocatalyst. *Journal of Environmental Sciences (China)*, *17*(1), 76–80.

Wang, Z., Yang, C., Lin, T., Yin, H., Chen, P., Wan, D., … Jiang, M. (2013). H-Doped Black Titania with Very High Solar Absorption and Excellent Photocatalysis Enhanced by Localized Surface Plasmon Resonance. *Advanced Functional Materials*, *23*(43), 5444–5450.

Wang, Z., Yang, C., Lin, T., Yin, H., Chen, P., Wan, D., … Jiang, M. (2013). Visible-light photocatalytic, solar thermal and photoelectrochemical properties of aluminium-reduced black titania. *Energy & Environmental Science*, *6*(10), 3007–3014.

Wang, Z., Zhang, F., Yang, Y., Cui, J., Sun, Q., & Guan, N. (2006). One-pot synthesis of visible-light-responsive. *Chinese Journal of Catalysis*, *27*, 1091–1095.

Warwick, M. E., Dunnill, C. W., Goodall, J., Darr, J. A., & Binions, R. (2011). Hybrid chemical vapour and nanoceramic aerosol assisted deposition for multifunctional nanocomposite thin films. *Thin Solid Films*, *519*(18), 5942–5948.

Wei, F., Ni, L., & Cui, P. (2008). Preparation and characterization of N-S-codoped TiO_2 photocatalyst and its photocatalytic activity. *Journal of Hazardous Materials*, *156*(1-3), 135–140.

Wei, W., Yaru, N., Chunhua, L., & Zhongzi, X. (2012). Hydrogenation of TiO_2 nanosheets with exposed {001} facets for enhanced photocatalytc activity. *RSC Advances*, *2*(22), 8286–8288.

Wu, H., Lin, Y., & Lin, S. (2013). Mechanisms of Visible Light Photocatalysis in N-Doped Anatase TiO_2 with Oxygen Vacancies from GGA + U Calculations. *International Journal of Photoenergy*, (289328), 1–7.

Wu, M., Quirindongo, M., Sass, J., & Wetzler, A. (2010). *Still Poisoning the Well*. *Natural Resources Defense Council*.

Wu, T., Lin, T., Zhao, J., Hidaka, H., & Serpone, N. (1999). TiO_2-assisted photodegradation of dyes. 9. Photooxidation of a squarylium cyanine dye in aqueous dispersions under visible light irradiation. *Environ Sci Technol*, *33*, 1379–1387.

Wu, Y., Xing, M., Tian, B., Zhang, J., & Chen, F. (2010). Preparation of nitrogen and fluorine co-doped mesoporous TiO_2 microsphere and photodegradation of acid orange 7 under visible light. *Chemical Engineering Journal*, *162*(2), 710–717.

Xia, T., & Chen, X. (2013). Revealing the structural properties of hydrogenated black TiO_2 nanocrystals. *Journal of Materials Chemistry A*, *1*(9), 2983–2989.

Xiang, Q., & Yu, J. (2011). Photocatalytic activity of hierarchical flower-like TiO_2 superstructures with dominant {001} facets. *Chinese Journal of Catalysis*, *32*(4), 525–531.

Xiang, Q., Yu, J., & Jaroniec, M. (2012). Graphene-based semiconductor photocatalysts. *Chemical Society Reviews*, *41*, 782–796.

Xiang, Q., Yu, J., Wang, W., & Jaroniec, M. (2011). Nitrogen self-doped nanosized TiO_2 sheets with exposed {001} facets for enhanced visible-light photocatalytic activity. *Chemical Communications*, *47*(24), 6906–6908.

Xiong, L.-B., Li, J.-L., Yang, B., & Yu, Y. (2012). Ti^{3+} in the Surface of Titanium Dioxide: Generation, Properties and Photocatalytic Application. *Journal of Nanomaterials*, *2012*(831524), 1–13.

Xue, C., & Xu, T. (2013). Fluorine-free synthesis of large ZSM-39 crystals incorporated with alkaline earth metals in an environment-friendly system. *Materials Letters*, *112*, 200–202.

Yan, Y., Han, M., Konkin, A., Koppe, T., Wang, D., Andreu, T., … Schaaf, P. (2014). Slightly hydrogenated TiO_2 with enhanced photocatalytic performance. *Journal of Materials Chemistry A*, *2*(32), 12708–12716.

Yang, G., Jiang, Z., Shi, H., Xiao, T., & Yang, Z. (2010). Preparation of highly visible-light active N-doped TiO_2 photocatalyst. *Journal of Materials Chemistry*, *20*, 5301–5309.

Yang, H. G., Sun, C. H., Qiao, S. Z., Zou, J., Liu, G., Smith, S. C., … Lu, G. Q. (2008). Anatase TiO_2 single crystals with a large percentage of reactive facets. *Nature*, *453*, 638–641.

Yang, L., Luo, S., Cai, Q., & Yao, S. (2010). A review on TiO_2 nanotube arrays: fabrication, properties, and sensing applications. *Chinese Science Bulletin*, *55*(4-5), 331–338.

Yang, Y., Zhang, T., Le, L., Ruan, X., Fang, P., Pan, C., … Weia, J. (2014). Quick and Facile Preparation of Visible light-Driven TiO_2 Photocatalyst with High Absorption and Photocatalytic Activity. *Scientific Reports*, *4*, 1–7.

Yu, H. K., Yi, G. R., Kang, J. H., Cho, Y. S., Manoharan, V. N., Pine, D. J., & Yang, S. M. (2008). Surfactant-assisted synthesis of uniform titania microspheres and their clusters. *Chemistry of Materials*, *20*(8), 2704–2710.

Yu, J. C., Ho, W., Yu, J., Hark, S. ., & Iu, K. (2003). Effects of Trifluoroacetic Acid Modification on the Surface Microstructures and Photocatalytic Activity of Mesoporous TiO_2 Thin Films. *Langmuir*, *19*, 3889–3896.

Yu, J. C., Jiaguo, Wingkei, Zitao, & Lizhi. (2002). Effects of F-Doping on the Photocatalytic Activity and Microstructures of Nanocrystalline TiO_2 Powders. *Chemistry of Materials*, *14*(9), 3808–3816.

Yu, J. C., Zhang, L., & Yu, J. (2002). Direct Sonochemical Preparation and Characterization of Highly Active Mesoporous TiO_2 with a Bicrystalline Framework. *Chemistry of Materials*, *14*(11), 4647–4653.

Yu, J., Low, J., Xiao, W., Zhou, P., & Jaroniec, M. (2014). Enhanced Photocatalytic CO_2-Reduction Activity of Anatase TiO_2 by Coexposed {001} and {101} Facets. *Journal of the American Chemical Society*, *136*(25), 8839–8842.

Yu, J., Wang, W., Cheng, B., & Su, B. L. (2009). Enhancement of photocatalytic activity of Mesporous TiO_2 powders by hydrothermal surface fluorination treatment. *Journal of Physical Chemistry C*, *113*(16), 6743–6750.

Yu, J., Xiang, Q., Ran, J., & Mann, S. (2010). One-step hydrothermal fabrication and photocatalytic activity of surface-fluorinated TiO_2 hollow microspheres and tabular anatase single micro-crystals with high-energy facets. *CrystEngComm*, *12*, 872–879.

Yu, X., Jeon, B., & Kim, Y. K. (2015). Dominant influence of the surface on the photoactivity of shape-controlled anatase TiO_2 nanocrystals. *ACS Catalysis*, *5*(6), 3316–3322.

Zadaka, D., Nir, S., Radian, A., & Mishael, Y. G. (2008). Atrazine removal from water by polycation–clay composites: Effect of dissolved organic matter and comparison to activated carbon. *Water Research*, *43*(3), 677–683.

Zahraa, O., Sauvanaud, L., Hamard, G., & Bouchy, M. (2003). Kinetics of atrazine degradation by photocatalytic process in aqueous solution. *International Journal of Photoenergy*, *05*(14), 87–93.

Zaleska, A. (2008). Doped-TiO_2 : A Review. *Recent Patents on Engineering*, *2*(1), 157–164.

Zeghbroeck, B. Van. (2011). Principles of Semiconductor Devices. Retrieved April 23, 2016, from http://ecee.colorado.edu/~bart/book/book/title.htm

Zhang, J., Li, M., Feng, Z., Chen, J., & Li, C. (2006). UV Raman spectroscopic study on TiO$_2$. I. Phase transformation at the surface and in the bulk. *Journal of Physical Chemistry B*, *110*(2), 927–935.

Zhang, W., Zou, L., Lewis, R., & Dionysio, D. (2014). A Review of Visible-Light Sensitive TiO$_2$ Synthesis via Sol-Gel N-Doping for the Degradation of Dissolved Organic Compounds in Wastewater Treatment. *Journal of Materials Science and Chemical Engineering*, *2*, 28–40.

Zhang, Y., Wu, H., & Liu, P. (2014). Enhanced transformation of atrazine by high efficient visible light-driven N, S-codoped TiO$_2$ nanowires photocatalysts. *International Journal of Photoenergy*, *2014*(425836), 1–8.

Zhang, Z., Wang, C.-C., Zakaria, R., & Ying, J. Y. (1998). Role of Particle Size in Nanocrystalline TiO$_2$-Based Photocatalysts. *Journal of Physical Chemistry B*, *102*(52), 10871–10878.

Zheng, Z., Huang, B., Lu, J., Wang, Z., Qin, X., Zhang, X., … Whangbo, M.-H. (2012). Hydrogenated titania: synergy of surface modification and morphology improvement for enhanced photocatalytic activity. *Chemical Communications*, *48*(46), 5733–5735.

Zhou, J. K., Lv, L., Yu, J., Li, H. L., Guo, P. Z., Sun, H., & Zhao, X. S. (2008). Synthesis of self-organized polycrystalline F-doped TiO$_2$ hollow microspheres and their photocatalytic activity under visible light. *Journal of Physical Chemistry C*, *112*(14), 5316–5321.

Zhu, G., Lin, T., Lü, X., Zhao, W., Yang, C., Wang, Z., … Lin, J. (2013). Black brookite titania with high solar absorption and excellent photocatalytic performance. *Journal of Materials Chemistry A*, *1*(34), 9650–9653.

Zhu, T., & Gao, S.-P. (2014). The stability, electronic structure, and optical property of TiO$_2$ polymorphs. *Journal of Physical Chemistry C*, *18*(2), 11385–11396.

Zhu, W.-D., Wang, C.-W., Chen, J.-B., Li, D.-S., Zhou, F., & Zhang, H.-L. (2012). Enhanced field emission from hydrogenated TiO$_2$ nanotube arrays. *Nanotechnology*, *23*(45), 455204–455210.

LIST OF PUBLICATIONS

1. **Samsudin, E. M**., Soo, C. W., Abd Hamid, S. B., Basiron, W. J., Lai, C. W., Lai, C. W., … Juan, J. C. (2015). Synthesis and Characterization of TiO_2 Nanoparticles via Alternative Sol-Gel Preparation Routes. Advanced Materials Research, 1087, 191–196.

2. **Samsudin, E. M**., Abd Hamid, S. B., Juan, J. C., Basirun, W. J., Kandjani, A. E., & Bhargava, S. K. (2015). Controlled nitrogen insertion in titanium dioxide for optimal photocatalytic degradation of atrazine. RSC Adv., 5(55), 44041–44052.

3. **Samsudin, E. M**., Goh, S. N., Wu, T. Y., Ling, T. T., Hamid, S. B. A., & Juan, J. C. (2015). Evaluation on the photocatalytic degradation activity of reactive blue 4 using pure anatase nano-TiO_2. Sains Malaysiana, 44(7), 1011–1019.

4. **Samsudin, E. M**., Hamid, S. B. A., Juan, J. C., Basirun, W. J., & Centi, G. (2015). Enhancement of the intrinsic photocatalytic activity of TiO_2 in the degradation of 1,3,5-triazine herbicides by doping with N,F. Chemical Engineering Journal, 280, 330–343.

5. **Samsudin, E. M**., Hamid, S. B. A., Juan, J. C., & Basirun, W. J. (2015). Influence of triblock copolymer (pluronic F127) on enhancing the physico-chemical properties and photocatalytic response of mesoporous TiO_2. Applied Surface Science, 355, 959–968.

6. **Samsudin, E. M**., Hamid, S. B. A., Juan, J. C., Basirun, W. J., & Kandjani, A. E. (2015). Surface modification of mixed-phase hydrogenated TiO_2 and corresponding photocatalytic response. Applied Surface Science, 359, 883–896.

7. Lai, C. W., **Samsudin, E. M**., & Juan, J. C. (2015). Improved Photocatalytic Oxidation of Organic Dye Using One-Dimensional Titania Nanotubes. Advanced Materials Research, 1087, 186–190.

8. **Samsudin, E. M**., Hamid, S. B. A., Juan, J. C., Basirun, W. J., Kandjani, A. E., & Bhargava, S. K. (2016). Effective role of trifluoroacetic acid (TFA) to enhance the photocatalytic activity of F-doped TiO_2 prepared by modified sol–gel method. Applied Surface Science, 365, 57–68.

9. **Samsudin, E. M**., Abd Hamid, S. B., Juan, J. C., Basirun, W. J., & Centi, G. (2016). Synergetic effects in novel hydrogenated F-doped TiO_2 photocatalysts. Applied Surface Science, 370, 380–393.

LIST OF CONFERENCE PROCEEDINGS

1. **International Conference on X-Ray & Related Technique in Research and Industry (ICXRI 2014)**
   (Johor Bahru, MALAYSIAN, 11-13th August 2014)
   Emy Marlina Samsudin, Sharifah Bee Abd Hamid, Wan Jefrey Basirun, Soo Chan Wai, Juan Joon Ching, 2014, Synthesis and Characterization of TiO_2 nanoparticles via alternative sol gel preparation.

2. **International Conference on X-Ray & Related Technique in Research and Industry (ICXRI 2014)**
   (Johor Bahru, MALAYSIA, 11-13th August 2014)
   Chin Wei Lai, Emy Marlina Samsudin, Joon Ching Juan, 2014, Improved Photocatalytic Oxidation of Organic Dye using One-Dimensional Titania nanotubes.

3. **International Conference on Chemistry and Environmental Sciences Research 2014 (ICCESR 2014)**
   (Penang, MALAYSIA, 18-19th September 2014)
   Emy Marlina Samsudin, Sharifah Bee Abd Hamid, Wan Jefrey Basirun, Juan Joon Ching, 2014, The photocatalytic degradation of atrazine by $N,F-TiO_2$ mesoporous nanoparticles.

4. **18th Malaysian International Chemical Congress (18MICC 2014)**
   (Kuala Lumpur, MALAYSIA, 4th November 2014)
   Emy Marlina Samsudin, Sharifah Bee Abd Hamid, Wan Jefrey Basirun, Juan Joon Ching, 2014, Photocatalytic Degradation of Atrazine using Nitrogen-doped TiO_2 Nanoparticles: Effect of Dopants.

LIST OF PATENTS

1. PHOTOREACTOR DESIGN FOR THE TREATMENT OF FLUID, Patent, <u>PI 2015702766</u>, 2015, (National).